Title

Structure-Property Relationships of Conjugated Polymers and Conjugated Oligoelectrolytes for Optoelectronic and Biocatalysis Applications

Author

Fronk, Stephanie

Publication Date

2017

UNIVERSITY OF CALIFORNIA

Santa Barbara

Structure-Property Relationships of Conjugated Polymers and Conjugated Oligoelectrolytes for Optoelectronic and Biocatalysis Applications

A dissertation submitted in partial satisfaction of the
requirements for the degree Doctor of Philosophy
in Chemistry

by

Stephanie Fronk

Committee in charge:
Professor Guillermo Bazan, Chair
Professor Steven Buratto
Professor Craig Hawker
Professor Michael Chabinyc

June 2017

The dissertation of Stephanie Fronk is approved.

Michael Chabinyc

Craig Hawker

Steven Buratto

Guillermo Bazan, Committee Chair

May 2017

Structure-Property Relationships of Conjugated Polymers and Conjugated Oligoelectrolytes

for Optoelectronic and Biocatalysis Applications

ACKNOWLEDGEMENTS

I want to dedicate this work to my parents, Jayne and Laurence Fronk. They gave unfailing support during my graduate work: encouraged me when times were tough, shared in the joy of my successes, and never stopped believing that I would succeed. I could not have earned my doctorate without them. I also want to thank the rest of my family for supporting me and believing in me, especially my sister, Jill, and brother Chris.

I want to thank my adviser, Prof. Gui Bazan, for providing guidance and support through the process. I appreciate the opportunity to pursue interested research and develop further as a scientist. I would like to thank my entire committee: Prof. Craig Hawker, Prof. Steven Buratto, and Prof. Michael Chabynic. I greatly appreciate the administrative and general support of the UCSB Chemistry Department Staff and the Shared Facilities staff, in particular Dr. James Pavolvich and Dr. Rachel Brehens.

My CPOS colleagues have become my friends and I greatly appreciate the fun times we had together, having people to discuss ideas, and help on various projects. In particular, I want to think Dr. Cheng-Kang Mai and Dr. Ming Wang for teaching me all I know of synthetic chemistry. I have enjoyed spending these five years getting to know all of you.

Last, but not least, I want to thank the Santa Barbara running community. The Santa Barbara Running and Racing team and the Santa Barbara trail runners have been a source of support and encouragement throughout this process. The miles and miles we ran together and the friendships I developed will stay with me. Their support really helped me through the rough patches.

VITA OF Stephanie Fronk
May 2017

EDUCATION

Bachelor of Science in Chemistry, University of Chicago, June 2010 (with honors)
Bachelor of Arts in Political Science, University of Chicago, June 2010 (with honors)
Doctor of Philosophy in Chemistry, University of California, Santa Barbara, June 2017

PROFESSIONAL EMPLOYMENT

2010-2012: R&D Chemist, Collins Ink, Cincinnati, OH

2012-2013, 2017: Teaching Assistant, Department of Chemistry, University of California, Santa Barbara

PUBLICATIONS

N. A. Yufa, **S. L. Fronk**, S. B. Darling, R. Divan, W. A. Lopes and S. J. Sibener. Modifying Metal-Polymer Nanostructures Using UV Exposure, Soft Matter, 2009, 5, 1683-1686.

N. A. Yufa, **S. L. Fronk**, S. J. Rosenthal, Seth B. Darling, W.A. Lopes, and S. J. Sibener. Self-Assembled Monolayer-Modified Block Copolymers for Chemical Surface Nanopatterning, Materials Chemistry and Physics, 2011, 125, 382-385.

C-K. Mai, R. A. Schlitz, G. M. Su, D. Spitzer, X. Wang, **S. L. Fronk**, D. G. Cahill, M. L. Chabinyc, and G. C. Bazan. Side-Chain Effects on the Conductivity, Morphology, and Thermoelectric Properties of Self-Doped Narrow-Band-Gap Conjugated Polyelectrolytes. Journal of the American Chemical Society, 2014, 136, 13478-13481.

C-K. Mai, B. Russ, **S. L. Fronk**, N. Hu, M. B. Chan-Park, J. J. Urban, R. A. Segalman, M. L. Chabinyc, and G. C. Bazan. Varying the ionic functionalities of conjugated polyelectrolytes leads to both p- and n-type carbon nanotube composites for flexible thermoelectric. Energy and Environmental Science, 2015, 8, 2341-2346.

S. L. Fronk, C-K. Mai, M. Ford, R. P. Noland, and G. C. Bazan. End-Group-Mediated Aggregation of Poly(3-hexylthiophene). Macromolecules, 2015, 48, 6224-6232.

C-K. Mai, T. Arai, X. Liu, **S. L. Fronk**, G. M. Su, R. A. Segalman, M. L. Chabinyc, G. C. Bazan. Electrical Properties of Doped Conjugated Polyelectrolytes with Modulated Density of the Ionic Functionalities. Chemical Communications, 2015, 51, 17607-17610.

B. Russ, M. J. Robb, B. C. Popere, E. E. Perry, C-K. Mai, **S. L. Fronk**, S. N. Patel, T. E. Mates, G. C. Bazan, J. J. Urban, M. L. Chabinyc, C. J. Hawker, R. A. Segalman. Tethered Tertiary Amines as Solid-State n-type Dopants for Solution Processable Organic Semiconductors. Chemical Science, 2016, 7, 1914-1919.

S. L. Fronk, M. Wang, M. Ford, J. Coughlin, C-K. Mai, G. C. Bazan. Effect of Chiral 2-Ethylhexyl Side Chains on Chiroptical Properties of the Narrow Bandgap Conjugated Polymers PCPDTBT and PCDTPT. Chemical Science, 2016, 7, 5313-5321.

Y. Shi, C-K. Mai, **S. L. Fronk**, Y. Chen, G. C. Bazan. Optical Properties of Benzotriazole-Based Conjugated Polyelectrolytes. Macromolecules, 2016, 49, 6343-6349.

M. Wang, H. Wang, M. Ford, J. Yuan, C-K. Mai, S. L. Fronk, G. C. Bazan. Influence of Molecular Structure on the Performance of Low V_{oc} Loss Polymer Solar Cells. J. Mater. Chem. A, 2016, 4, 15232-15239.

S. L. Fronk, Y. Shi, M. Siefrid, C-K. Mai, C. McDowell, G. C. Bazan. Chiroptical Properties of a Benzotriazole-Thiophene Copolymer Bearing Chiral Ethylhexyl Side Chains. Macromolecules, 2016, 49, 9301-9308.

V. V. Brus, M. A. Gluba, C-K. Mai, **S. L. Fronk**, J. Rappich, N. H. Nickel, G. C. Bazan. Conjugated Polyelectrolyte/Graphene Hetero-Bilayer Nanocomposites Exhibit Temperature Switchable Type of Conductivity. Adv. Electron. Mater. 2017, 3, 1600515.

AWARDS

NSF REU Program, University of Chicago, 2008, 2009

NSF Research Fellowship Honorable Mention, Santa Barbara, 2013

Department of Chemistry, Outstanding Service to the Department, University of California, Santa Barbara, 2014, 2015, 2016

FIELDS OF STUDY

Major Field: Organic Materials Chemistry

Studies in synthesis and characterization of end-functionalized P3HT

Studies in structure-property relationships of donor-acceptor copolymers containing chiral ethylhexyl side chains

Studies in accelerating biocatalysis using membrane-spanning conjugated oligoelectrolytes

Studies in formation and characterization of tunable diblock copolymer thin films

ABSTRACT

Structure-Property Relationships of Conjugated Polymers and Conjugated Oligoelectrolytes for Optoelectronic and Biocatalysis Applications

by

Stephanie Fronk

What happens if you introduce a chiral side chain to a conjugated polymer backbone? The conjugated polymer is forced to answer the question: to twist or not to twist? The ability of conjugated polymers to form helical nanostructures depends on the molecular structure of the conjugated backbone. Two conjugated polymers, PCPDTBT* and PCDTPT*, containing chiral side chains, were synthesized in order to study their secondary structures using circular dichroism (CD) spectroscopy. PCPDTBT* provides a strong chiral response. However, the single structural difference of the substitution of a nitrogen atom on the PCDTPT* monomer for a –CH group on the PCPDTBT* monomer decreases the CD signal, indicating a less chiral aggregation. Theoretical calculations suggest the CDT-PT monomer has a higher rotational barrier compared to the CDT-BT monomer. This higher barrier to rotation provides an explanation for the planar conformation of the PCDTPT backbone, its promising transistor performance, and the inability of PCDTPT* to form a helical nanostructure.

Where did that chiral side chain come from anyway? Biocatalysts, such as Baker's yeast, contain enzymes particularly suited to synthesizing chiral molecules such as chiral side chains. Biocatalysis is advantageous for chemical production as reaction conditions tend to be mild and environmentally-friendly. However, the cell membrane can often act as a barrier; preventing the starting material from entering the cell and the product from leaving. Just as conjugated polymers can be forced into unnatural structures, yeast can be forced to perform biocatalysis. Conjugated oligoelectrolytes (COEs) provide a potential solution based on their ability to intercalate into membranes, resulting in cell membrane permeabilization. Yeast cells were stained with these molecules and used in a model biocatalysis reaction (the conversion of fumaric acid to L-malic acid) where membrane diffusion is known to be the limiting step. As the number of phenylenevinylene units in the conjugated backbone is increased, the permeabilization ability of the COE decreases, along with the biocatalytic yield. The highest improvement utilized DSBN+, containing the smallest number of phenylenevinylene units, to achieve 4.5 times greater yield compared to a control reaction with unpermeabilized cells. If this result proves to be generalizable, a variety of reactions, with applications from pharmaceuticals to nanoparticles, could benefit from a simple and easy-to-use method of biocatalysis acceleration.

TABLE OF CONTENTS

LIST OF FIGURES

I. Controlled Synthesis of Poly(3-hexylthiophene) with Functionalization of a Single Chain End for Optoelectronic Applications

A. Background

Conjugated polymers have found applications as organic semiconductors for organic field effect transistors (OFETS),[1-7] organic light emitting diodes (OLEDs),[8-13] and organic solar cells (OSC).[14-17] The molecular structure of the monomer units consists of a connected π-system which allows electron delocalization along the polymer backbone.[18-19] This conjugated system can be described energetically by the highest occupied molecular orbital (HOMO) and lowest unoccupied molecular orbital (LUMO).[20-21] The offset between the HOMO and LUMO is the energy bandgap, such that materials with relatively small bandgaps are classified as semiconductors.[18-19,21] A conjugated polymer can absorb light with energies equal to or greater than its bandgap, often these wavelengths are in the visible range.[21-22] When a conjugated polymer absorbs light at these wavelengths, an electron is excited from the HOMO to the LUMO in a $\pi \rightarrow \pi^*$ transition, creating an electron-hole pair (exciton).[21,23-24] The electron can relax back down to the ground state or, with additional energy input, the exciton can separate into a free electron and a free hole.[21,25-27] Charge transport along the conjugated backbone or between polymer chains enables these materials to serve as the active layer in OFETs and OSCs.[28-32]

Conjugated polymers are of particular interest as optoelectronic materials based on their potential for solution processing.[33-35] Solution processing is advantageous from a manufacturing perspective, based on lower costs and ease of deposition.[33-35] The presence of side chains attached to the conjugated polymer backbone allows these polymers to be dissolved in a variety of organic solvents.[36-39] Alkyl and alkoxy side chains have little effect on the energy levels of the conjugated polymer but do influence its solubility and solid-state packing.[36-39] Devices such as OFETs and OSCs are solid state devices and therefore depend on polymer packing in thin films.[38,40] Previous work has explored the structure-property relationships of the choice of side chain and conjugated backbone on their packing structure in the solid state using X-ray techniques, AFM, and electron microscopy techniques to name a few.[41-44]

Poly(3-hexylthiophene) is one of the original, high performing conjugated polymers and thus it's fundamental properties and application in devices have been well studied in the literature.[45-48] A thorough review is not possible here. P3HT has continued to be studied based on its role as a model system[45-48] and the potential for low cost scale up.[49-50] There exist a variety of methods for synthesizing P3HT, including gringard metathesis polymerization,[51-53] Stille and Suzuki coupling polymerization,[54-56] direct heteroarylation polymerization,[57] and electrochemical polymerization.[58-59] Specifically, synthesis of regioregular-P3HT, where monomer units have head-to-tail coupling with respect to the side chain, is desirable as rr-P3HT provides more favorable packing structures in thin films due to ease of access to low energy planar conformations.[60-63] More recent efforts, such as the one described in the following sections, focus on catalyst-transfer polymerization where a desired functional group is transferred from the catalyst to one end of the polymer chain.[64-66]

Organic solar cells, containing P3HT as the donor material and phenyl C_{61} butyric acid methyl ester (PCBM) as the acceptor material, provided promising performance in early bulk heterojunction (BHJ) organic photovoltaic (OPV) devices.[45-48] Bulk heterojunction solar cells contain an active layer composed of a donor (P3HT) and an acceptor

(PCBM).[16,44-46] Extensive research has explored optimizing processing conditions to achieve morphologies amenable to efficient charge separation and transport.[67-70] P3HT is the light absorbing material.[21] Excitons generated on P3HT travel to an interface with PCBM where, ideally, they separate into free charges and are collected at the device electrodes.[71-74] Forming the ideal morphology where charge separation and charge transport are highly efficient is a challenge facing the OPV community.[75-76] Thus understanding the organization of these materials both separately and as blends in solution and in thin films is essential.

The goal of this chapter is the development of structure-property relationships through the modification of the end-group of P3HT. By modulating a single functional group of a material, the effect of that group on the resulting material properties can be studied. Below, applying a specific end-group to P3HT enables three different applications. First, the influence of the hydrophobicity vs. hydrophilicity of the end-group is found to influence P3HT aggregation properties in solution and thin films when P3HT chains are functionalized with either C_{60} or dye molecule.[77] Second, P3HT is functionalized with a surface binding group to enable single-molecule microscopy (publication in progress). Third, a PEG chain is attached to the end of a P3HT chain with the aim of producing micelles capable of being imaged by fluorescence microscopy for drug delivery (unpublished work).

B. End-Group Mediated Aggregation of Poly(3-hexylthiophene)

1. Introduction

Much of the interest in organic semiconductors arises from the possibility of manufacturing optoelectronic devices via solution deposition methods.[33-35] In order to realize the advantages of solution-processing, it is necessary to understand how to control and ultimately optimize the resulting thin film device morphology.[78-81] For example, thin film morphology control is essential in applications such as organic photovoltaics and field effect transistors, due to the impact of interchain contacts and large-scale phase separation on charge carrier mobility and photophysical processes.[82-84] One method of influencing the organization of conjugated polymers in the solid state is through pre-aggregation of the chains in solution and understanding polymer-solvent interactions is thus critical in this respect.[85-87]

P3HT is a well studied conjugated polymer.[44-45] Synthetic methods for achieving well-defined, regio-regular P3HT have been developed, such as the Kumada-coupling living polymerization (GRIM method), which provide control over molecular weight, dispersity, and regioregularity.[51,65,88] This method can be extended to provide control of the end-group.[89-91] P3HT is readily dissolved in organic solvents, such as chloroform and chlorobenzene, and is known to form different thin film morphologies depending upon solution-processing conditions. Such morphologies include for example well-defined "whiskers," formed by cooling P3HT solutions in cyclohexanone,[92] and long rectangular parallelepipeds, formed when a large volume fraction of hexane nucleates aggregate growth in solution via favorable π-π interactions.[93] P3HT is also known to form a fibrillar structure when deposited from solutions of ortho-dichlorobenzene where the size of the nanofiber increases with increasing volume fraction of non-solvent hexane.[70] Similar nanowire morphologies are observed with the addition of small amounts of poor solvents, such as acetonitrile; however, round nanometer-sized aggregates are seen upon addition of larger amounts of acetonitrile.[86] Further work has shown higher boiling point solvents or post-deposition annealing increases the overlap between neighboring nanorods.[94]

General methods previously used to modify conjugated polymer structures in the solid state include solvent choice, solvent additives, and thermal annealing.[95-96] The first two methods address the self-assembly of P3HT in solution in order to influence organization in the solid state based on extrinsic factors. Intrinsic factors such as the modification of the P3HT structure also influence self-assembly.[97] This approach has been proven by previous work on side-chain engineering[98-100] and variations in polymer molecular weight.[69] Varying the side chain composition is known to influence solubility and molecular ordering in the solid state.[98] Modification of the P3HT end-group from a bromide to an alcohol to a methyl group to a fluorinated alkyl chain, has resulted morphology improvements in bulk-heterojunction solar cells when blended with $PC_{60}BM$.[101-102]

Another strategy for tuning the self-assembly properties of P3HT is post-polymerization chemical modification through synthetic methods such as click chemistry[103-104] and esterification reactions.[105-106] Click chemistry provides an efficient synthetic technique for linking two chemical structures.[107] Relevant advantages include high yields and mild reaction conditions. Click chemistry has thus been used to synthesize diblock copolymers,[88,108-110] modify polymer side-chains,[111-112] and provide end-functionalization to establish the method particularly useful for synthesizing asymmetric polymer architectures.[113-114]

In this work, we provide details on the synthesis of two functionalized P3HT derivatives with different end-groups, including a fullerene derivative, (P3HT-C_{60}) and sulforhodamine 101 dye (P3HT-Dye), via the azide-alkyne Huisgen cycloaddition. We also examine how the choice of end-group impacts aggregation tendencies in solution, as probed by dynamic light scattering and absorption spectroscopy measurements. Using a case study comparing non-functionalized P3HT and P3HT-C_{60}, characterization of thin films with absorption spectroscopy and GIWAXS measurements provides insight into differences in the resulting solid state organizations.

2. Synthesis

Kumada-coupling living polymerization (GRIM method) was used to synthesize P3HT (Scheme 1-1) because of its ability to control molecular weight characteristics and backbone regioregularity.[52,115-116] Use of specific, well-defined catalysts allows one to control the functional group present on one end of the polymer chain.[116] Nickel catalysts containing a bidentate phosphine ligand, a bromide, and an aryl group can be used to initiate the polymerization through transfer of the aryl group to the active monomer.[64,117] Catalyst **2** was chosen for this application. Its structure contains a triisopropylsilyl (TIPS)-protected ethynyl phenyl ring as the aryl group for transfer to the polymer chain end. The incorporation of a protected alkyne moiety provides a functionality suitable for click reaction after deprotection. A monomer-to-catalyst ratio of 40:1 was used to obtain P3HT with good solubility (20 mg/mL) in solvents such as $CHCl_3$, toluene, and THF. The reaction was quenched using ethyl magnesium bromide with the goal of incorporating an ethyl functional group at the second polymer chain end.

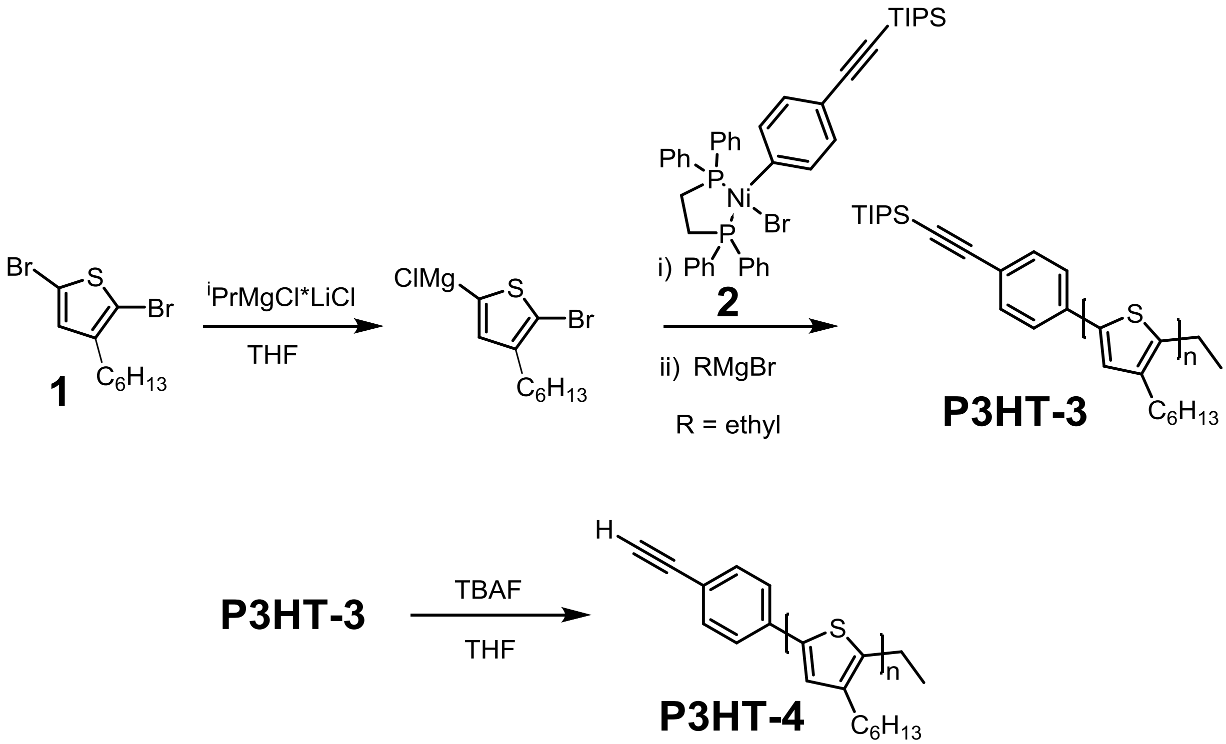

Scheme 1-1. Polymerization of 2,5-dibromo-3-hexylthiophene using initiator **2** to yield P3HT-**3** and subsequent deprotection to the ethynyl-terminated P3HT-**4**, which is suitable for click reactions.

The product obtained after polymerization and isolation, *i.e.* P3HT-**3** in Scheme 1-1, was characterized by using ^{1}H NMR spectroscopy and MALDI-TOF. ^{1}H NMR spectroscopy (Figure S1-1A) shows a doublet at 1.1 ppm corresponding to the methyl protons on the TIPS-protected-ethynyl group which indicates incorporation of the desired end-group on the polymer chain. A peak at 2.7 ppm represents the methylene group on the hexyl side chain adjacent to the thiophene ring. As expected from the monomer-to-catalyst ratio, comparing the integrated intensity of the methylene peak and the TIPS peak provides a ratio of 2:0.45, which corresponds to polymer chains with approximately an average of 40 repeat units.

MALDI-TOF mass spectrometry was used to identify polymer end-groups.[118] The MALDI mass distribution is shown in Figure 1-1A, where the correct repeat spacing of the peaks of 166 mass units is observed. The highest intensity peak corresponds to a degree of polymerization of 40, confirming the ^{1}H NMR spectroscopy analysis. MALDI end-group analysis confirms the presence of the TIPS-protected ethynylbenzene moiety on each polymer chain. However, there are two sets of peaks present in the mass distribution curve that can be reasonably attributed to two different functional groups on the chain end opposite the TIPS-ethynyl functionality. From the mass of the products, it was determined that these end-groups are the desired ethyl group and also hydrogen. The ratio of ethyl-to-hydrogen termination is 3.5:1. Hydrogen-termination during Kumada coupling has been observed previously by Kang et al.[53] However, hydrogen-terminated P3HT chains do not interfere with the end-group functionalization via click chemistry in subsequent transformations.

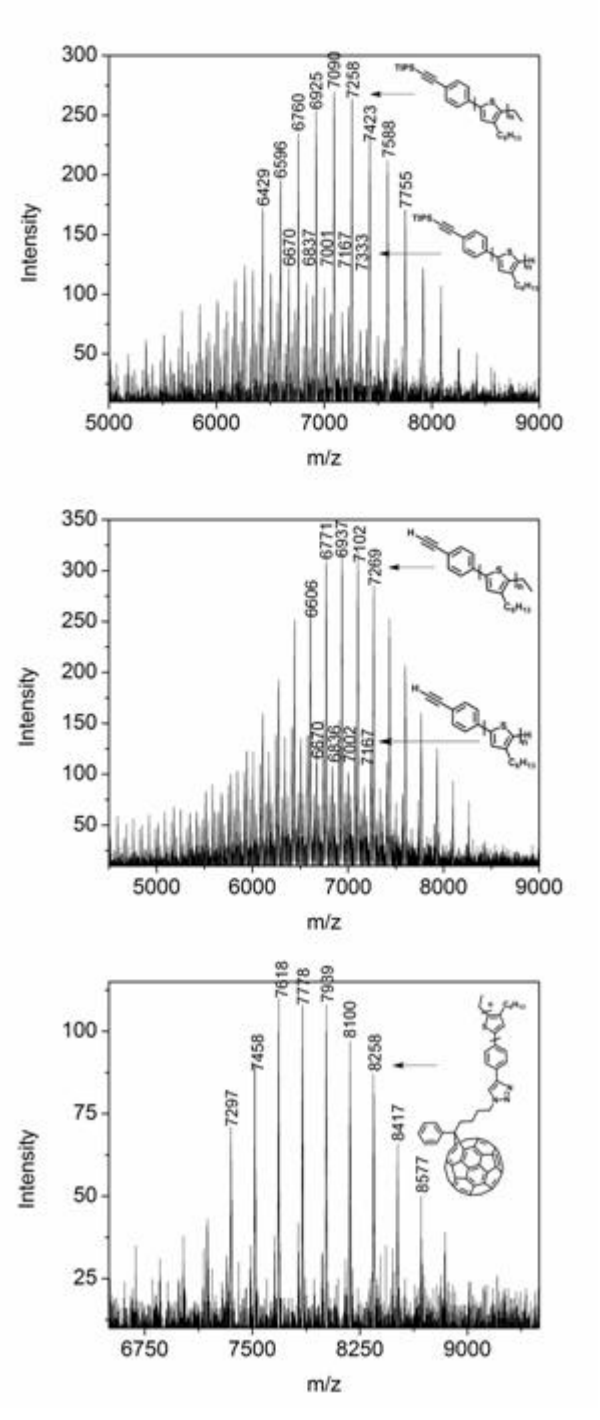

Figure 1-1. MALDI spectra of a) TIPS-protected-ethynyl-phenyl terminated P3HT (P3HT-**3**), b) ethynyl-phenyl terminated P3HT (P3HT-**4**), and c) **P3HT-C_{60}**.

The TIPS protecting group is easily removed under basic conditions using tetrabutylammonium fluoride at room temperature to yield the deprotected polymer, P3HT-**4** in Scheme 1-1. ^1H NMR spectroscopy (Figure S1-1B) is consistent with the removal of the TIPS group through the disappearance of the peak at 1.1 ppm and the concomitant appearance of the ethynyl peak at 3.1 ppm. MALDI end-group analysis (Figure 1-1B) is also in accord with the presence of terminal ethynyl groups. This chemical transformation thus renders the chain end of P3HT readily available for click coupling.

A fullerene derivative and a sulforhodamine 101 dye were chosen for coupling with P3HT because of their contrasting chemical properties. Sulforhodamine 101 is optically active in the visible region of the spectrum and can be identified by UV-Vis spectroscopy. The chemical properties and solubility of the two end-group molecules are also significantly different. The fullerene cage is a large hydrophobic moiety that is soluble in nonpolar organic solvents, whereas sulforhodamine 101 dye is hydrophilic and soluble in polar solvents. Comparing the two different end-groups provides a method for studying to what extent each end-group can be used to tune the aggregation properties of the polymer chains in media of different polarity.

The azide derivative of $PC_{60}BM$, compound **8** in Scheme 1-2, was synthesized using a procedure modified from the literature.[119] A three step procedure (Scheme 1-2) was used starting with the conversion of the commercially-available fullerene derivative, **5**, to the alcohol, **6**, using diisobutylaluminum hydride (DIBAL-H).[120] Compound **6** was converted to the tosylate, **7**, which was then subjected to NaN_3 in a mixture of toluene:DMF (3:1) to provide the azide, **8**. This choice of solvent mixture enables enough solubility of the fullerene derivative and facilitates nucleophilic displacement. It is worth noting that the target compound **8** is not stable upon storage and thus it was used in the next step without further purification. The azide derivative of sulforhodamine 101 dye, *i. e.* compound **9** in Scheme 2, is commercially available.

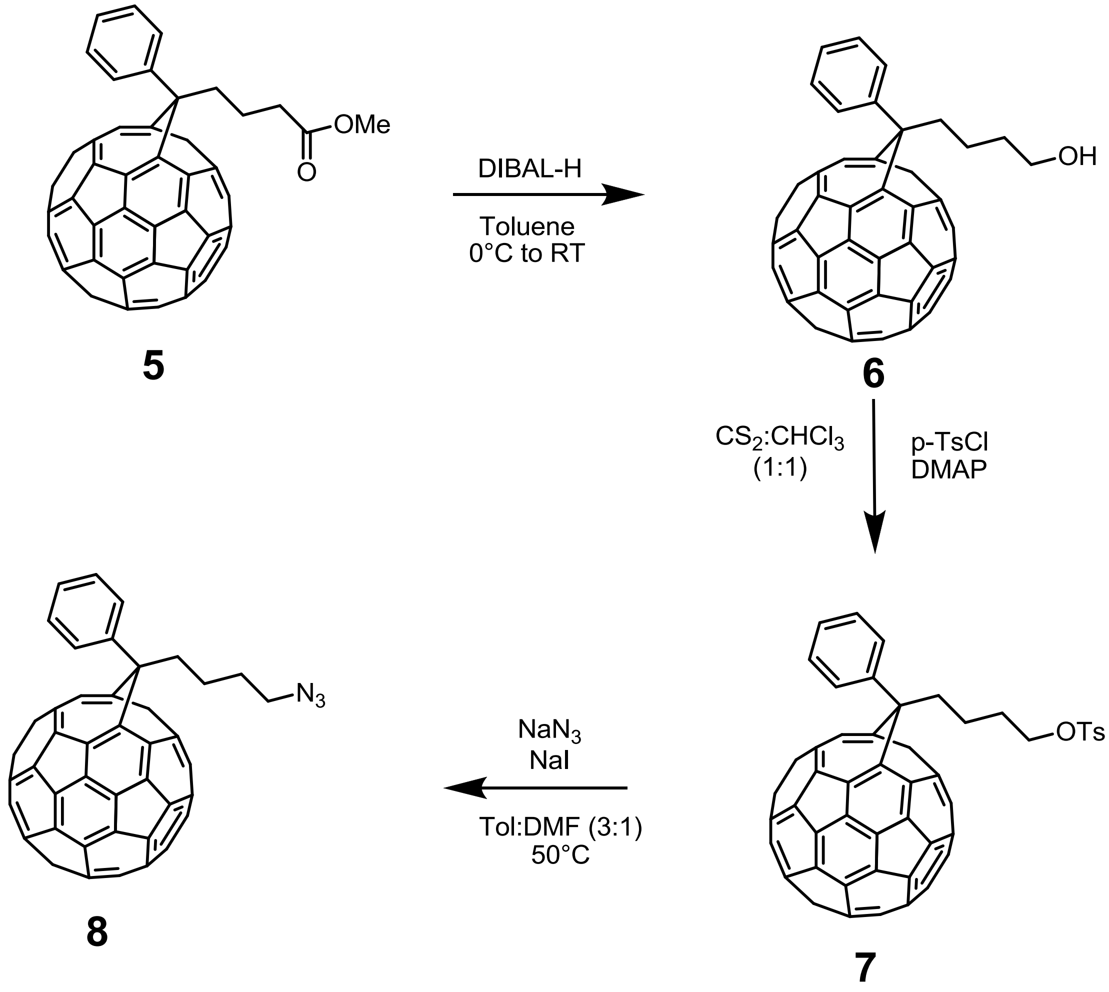

Scheme 1-2. Synthesis of azide-containing fullerene derivative, **8**.

Copper-catalyzed azide-alkyne click reactions (Scheme 1-3) were performed to couple both **9** and **8** with ethynyl-terminated P3HT-**4** resulting in **P3HT-Dye** and **P3HT-C$_{60}$**, respectively. The ^{1}H NMR spectrum of **P3HT-C$_{60}$** (Figure S1-1C) shows a peak at 7.7 ppm corresponding to the hydrogen on the triazole ring. Characterization by MALDI (Figure 1-1C) shows that the peak spacing of about 166 mass units remains the same as the parent polymer, P3HT-**4**. Analysis of the end-groups confirms the successful tethering of the fullerene to every polymer chain. The ionic functionality on sulforhodamine 101 gives rise to fragmentation in the MALDI spectrum such that a clean mass distribution could not be obtained (Figure S1-4). Following a thorough wash of the resulting product with methanol to remove any unattached sulforhodamine 101 dye, the UV-Vis spectrum (Figure S1-5) in THF shows both the P3HT peak at 450 nm and the sulforhodamine 101 dye peak at 580 nm.

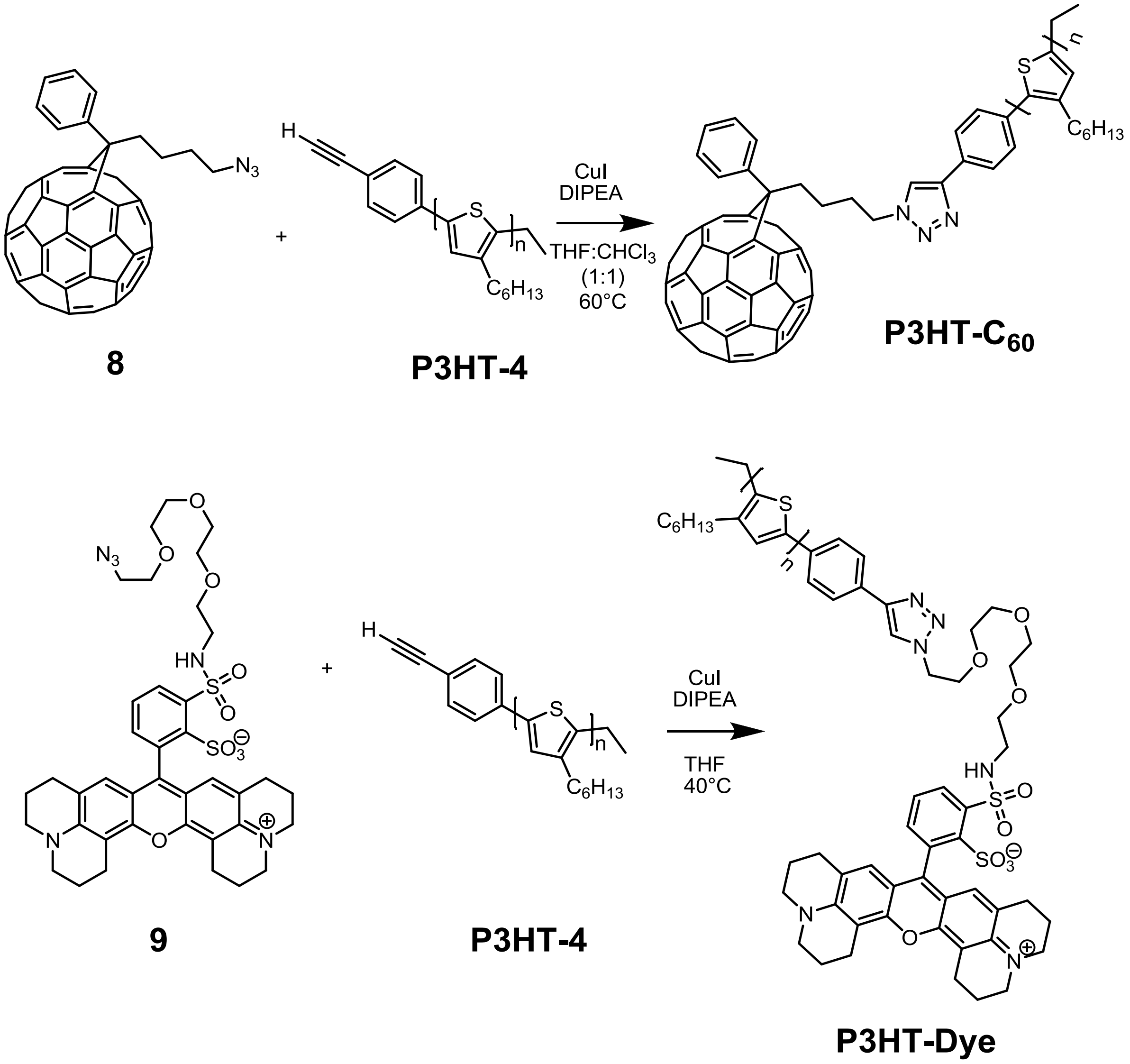

Scheme 1-3. Synthesis and molecular structures of the two end-functionalized P3HT derivatives **P3HT-C$_{60}$** and **P3HT-Dye**.

3. Solution Properties via Dynamic Light Scattering

The particle size of **P3HT-C_{60}**, **P3HT-Dye**, and the parent non-functionalized P3HT-**3** were studied using dynamic light scattering, (DLS). DLS is a powerful technique for comparing the degree of aggregation between different materials through analysis of their hydrodynamic radii.[121-123] P3HT has previously been studied in this way.[124-125] To maintain consistency, the non-functionalized P3HT, namely P3HT-**3**, used in these experiments came from the same batch used to synthesize **P3HT-C_{60}** and **P3HT-Dye**. DLS involves a multistep process to determine the hydrodynamic radius (R_{hyd}) of the macromolecules. Laser light hits the solution, which causes the light to scatter due to the Brownian motion of the particles. The intensity of the light fluctuations is measured to produce an intensity curve. An autocorrelation function is determined to fit the data. The diffusion coefficient is extracted from the autocorrelation function and R_{hyd} is calculated using the Stokes-Einstein equation.[126-127]

Measurements were taken in three different solvent systems with increasing solvent polarity: THF, THF:methanol (8:2), and THF:methanol (1:1). The concentration (14 μM) used in experiments proved sufficiently high to obtain a useful signal-to-noise ratio and to result in aggregation of polymer chains in each solvent system. At lower concentrations, the autocorrelation function does not show the expected scattering decay but instead shows incoherent scattering due to the solvent. Further experimental details are provided in the SI.

The R_{hyd} values obtained through DLS analysis are summarized in Table 1-1. A similar R_{hyd} is observed for P3HT-**3**, **P3HT-C_{60}**, and **P3HT-Dye** when dissolved in THF, ~ 90 nm. When the percentage of MeOH is increased, all three materials show an increase in R_{hyd}. Specifically, the R_{hyd} of P3HT-**3** increases from 90 nm in THF, to 180 nm in THF:MeOH

(8:2), and ultimately 438 nm in THF:MeOH (1:1). **P3HT-C_{60}** exhibits an increase from 90 nm in THF to 161 nm in THF:MeOH (8:2) to 675 nm in THF:MeOH (1:1). The R_{hyd} of **P3HT-Dye** increases from 92 nm in THF to 115 nm in THF:MeOH (8:2) to 303 nm in THF:MeOH (1:1). At a 1:1 ratio of THF to MeOH, the R_{hyd} of **P3HT-Dye** (303 nm) is smaller than that of P3HT-**3** (438 nm) whereas that of **P3HT-C_{60}** (675 nm) is larger than P3HT-**3**.

Table 1-1. Hydrodynamic radii of P3HT-**3**, **P3HT-C_{60}**, and **P3HT-Dye**.

Solvent	Radii (nm)		
	P3HT-3	**P3HT-C_{60}**	**P3HT-Dye**
THF	90	90	92
THF:MeOH (8:2)	180	161	115
THF:MeOH (1:1)	438	675	303

Interactions between P3HT, the end-groups, and the solvent contribute to a plausible explanation of the DLS data. Interactions with the solvent are governed by the solubility of each component of a given material in that solvent. These parameters have been previously studied for P3HT and $PC_{61}BM$.[128-131] P3HT can be well-dissolved in THF; however, MeOH is a poor solvent.[129] When MeOH is added to THF, the solubility of P3HT decreases and there is a greater likelihood of polymer chain aggregation and ultimately precipitation out of solution. Individual P3HT chains tend to form energetically-favorable π-stacked conformations during aggregation.[132] These favorable interchain interactions further promote aggregation in a poor solvent. Through the increase in R_{hyd}, the DLS data confirm an increase in P3HT-**3** aggregate size with increasing volume fraction of MeOH.

When attached to the end of a P3HT chain, C_{60} functions as a large hydrophobic group with the potential to influence the solubility of the dyad. $PC_{60}BM$ can be dissolved in THF but not MeOH.[133] Based on the interactions of the two components with the solvent, the size of the **P3HT-C_{60}** aggregates would be expected to increase as the volume fraction of

MeOH relative to THF is increased, in agreement with the experimental data. The R_{hyd} of **P3HT-C$_{60}$** THF:MeOH (8:2) falls nicely between that of THF and THF:MeOH (1:1). In the case of the THF:MeOH (1:1) solvent mixture, **P3HT-C$_{60}$** aggregates are larger (675 nm) than both P3HT-**3** (438 nm) and **P3HT-Dye** (303 nm) aggregates. The exact differences in aggregate morphology cannot be determined solely from the data gathered here. However there are two potential morphological explanations. First, the bulky fullerene end-group could disrupt the local packing structure of the P3HT chains. Less ordered packing could result in a larger particle size. Second, the addition of hydrophobic C$_{60}$ to P3HT decreases the material's solubility in MeOH as compared to non-functionalized P3HT-**3**, further favoring aggregation.

Sulforhodamine 101, in contrast to P3HT and C$_{60}$, is more readily dissolved in both MeOH and THF. When sulforhodamine 101 is connected to the end of P3HT, it acts as a hydrophilic end-group and causes the solubility properties of the molecule to change relative to its non-functionalized P3HT-**3** counterpart. The solubility of **P3HT-Dye** is expected to be higher in THF:MeOH mixtures relative to non-functionalized P3HT-**3**. The size of the **P3HT-Dye** aggregate is expected to be smaller than that of non-functionalized P3HT-**3** as the amount of MeOH is increased; a hypothesis that is confirmed by the DLS data. Despite the good solubility properties of sulforhodamine 101 in MeOH, the predominant P3HT component continues to influence the aggregate size in solution. Poor solubility in MeOH and strong π-stacking of P3HT contribute to an increase in the **P3HT-Dye** aggregate size as the amount of MeOH is increased.

4. Solution Properties via Absorption and Emission Spectroscopy Measurements

Absorption spectroscopy can also be used to probe the presence of aggregation.[134-135] UV-Vis spectroscopy measurements were taken in the same three solvent systems used for DLS. Each molecule was tested at multiple concentrations to probe the effect of concentration on absorption. The results shown here correspond to measurements performed at room temperature at a concentration of 0.75 μM. Emission spectra were also measured at room temperature at a concentration of 0.75 μM in THF. Representative absorption spectra are shown in Figure 1-2 and representative emission spectra are shown in Figure S1-8.

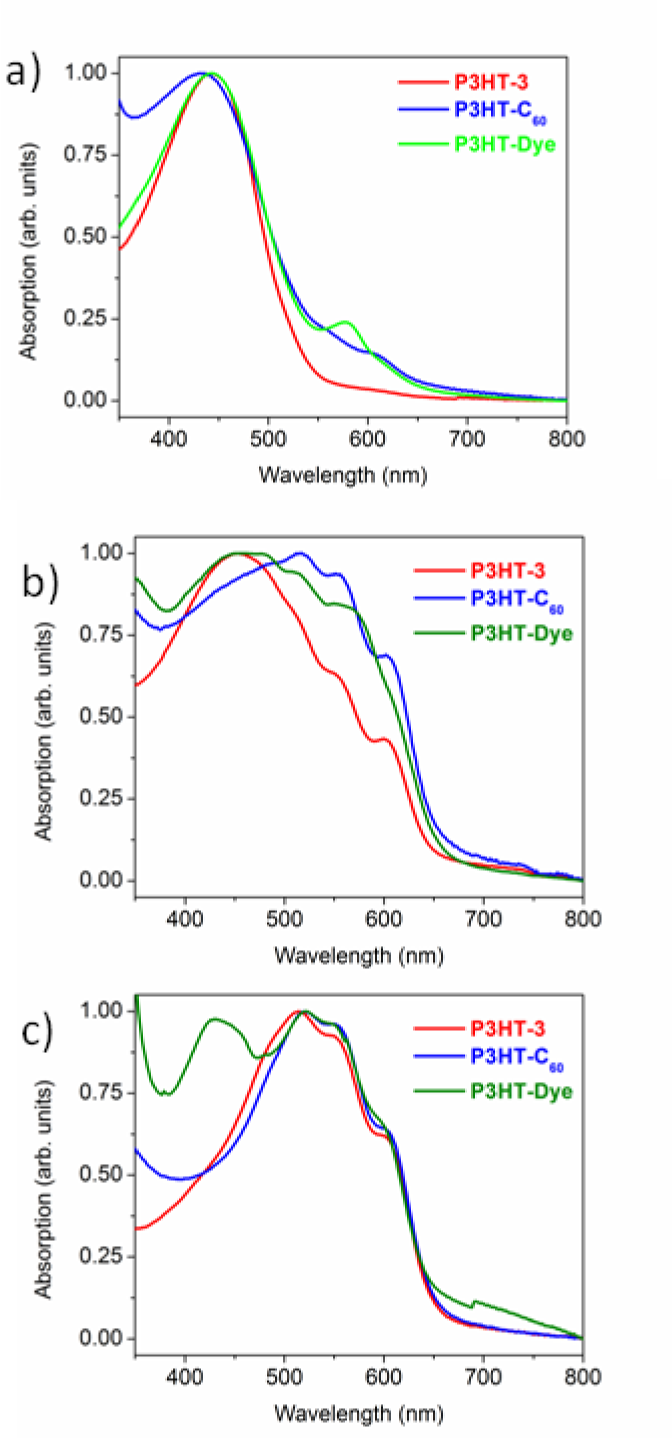

Figure 1-2. Absorption spectra of P3HT-**3**, **P3HT-C$_{60}$**, and **P3HT-Dye** in a) THF, b) THF:MeOH (8:2), and c) THF:MeOH (1:1). All measurements were taken with a concentration of 0.75 µM at room temperature. Results have been normalized based on the maximum absorption.

The absorption spectrum of P3HT-**3** in THF exhibits a featureless band with a maximum at 450 nm, as expected from literature precedent.[136] **P3HT-C$_{60}$** and **P3HT-Dye** in THF also exhibit absorption profiles corresponding to well-dissolved polymer chains. However, **P3HT-C_{60}** and **P3HT-Dye** exhibit weak absorption peaks at longer wavelengths corresponding to interchain interactions from aggregation[137-138] and dye absorption respectively. Overall, absorption in THF solutions agrees with the DLS data, where all three materials exhibit similar R_{hyd} values. The THF:MeOH (8:2) solvent mixture serves as a transition between THF and THF:MeOH (1:1). The absorption profile of P3HT-**3** maintains a major peak at approximately 450 nm, whereas the absorption maximum of **P3HT-C_{60}** is red-shifted to about 515 nm. Both P3HT-**3** and **P3HT-C_{60}** begin to exhibit aggregation peaks at approximately 550 nm and 600 nm. **P3HT-Dye** also maintains a major peak at 450 nm but the dye peak at 580 nm becomes more prominent compared to absorption in THF. These data indicate that the three materials exhibit a greater degree of aggregation and increased electron delocalization from π-stacking with the addition of methanol.

In THF:MeOH (1:1), both P3HT-**3** and **P3HT-C_{60}** show a red-shift in absorption and aggregation peaks. These results agree with the increasing R_{hyd} of P3HT-**3** and **P3HT-C_{60}** with the addition of methanol. The absorption spectrum of **P3HT-Dye** in THF:MeOH (1:1) reveals a peak at 450 nm corresponding to well-dissolved polymer chains and the expected P3HT aggregation peaks at longer wavelengths. This presence of solvated chains in THF:MeOH (1:1) agrees with the smaller R_{hyd} of **P3HT-Dye** than P3HT-**3** and **P3HT-C_{60}**.

Photoluminescence spectroscopy provides further insight on the photophysical properties of these materials. The emission spectrum of P3HT-**3** in dilute THF solution shows a peak with two vibronic features centered at 600 nm (Figure S1-8). Compared to the fluorescence spectrum of P3HT-**3**, the emission of **P3HT-C_{60}** in dilute THF solution shows the same emission profile but is highly quenched (Figure S1-8a). The fullerene moiety quenches emission from the P3HT chain, as expected based on the literature.[139-143] The fluorescence spectrum of **P3HT-Dye** in dilute THF solution is not quenched in comparison with P3HT-**3** (Figure S1-8b), however it does not show any of P3HT-**3**'s vibronic structure. Sulforhodamine 101 dye is known to emit at 605 nm,[144] similar to P3HT-**3**. It is reasonable that emission from the dye moiety in addition to emission from P3HT-**3** contribute to the fluorescence spectrum of **P3HT-Dye**.

5. Thin Film Absorption Spectroscopy

Polymer thin films were prepared via drop-casting techniques. Solutions of P3HT-**3** and **P3HT-**$\mathbf{C_{60}}$ at 20 mg/mL in either THF or THF:MeOH (8:2) were drop-cast on pre-cleaned quartz substrates. Neither P3HT-**3** nor **P3HT-**$\mathbf{C_{60}}$ are sufficiently soluble in THF:MeOH (1:1) to enable drop-casting films. The absorption spectrum was measured immediately after drop-casting without thermal annealing. Representative absorption spectra are shown in Figure 1-3. The availability of commercially available azide-functionalized sulforhodamine 101 is insufficient for obtaining a sufficiently large quantity of **P3HT-Dye** adequate for film processing.

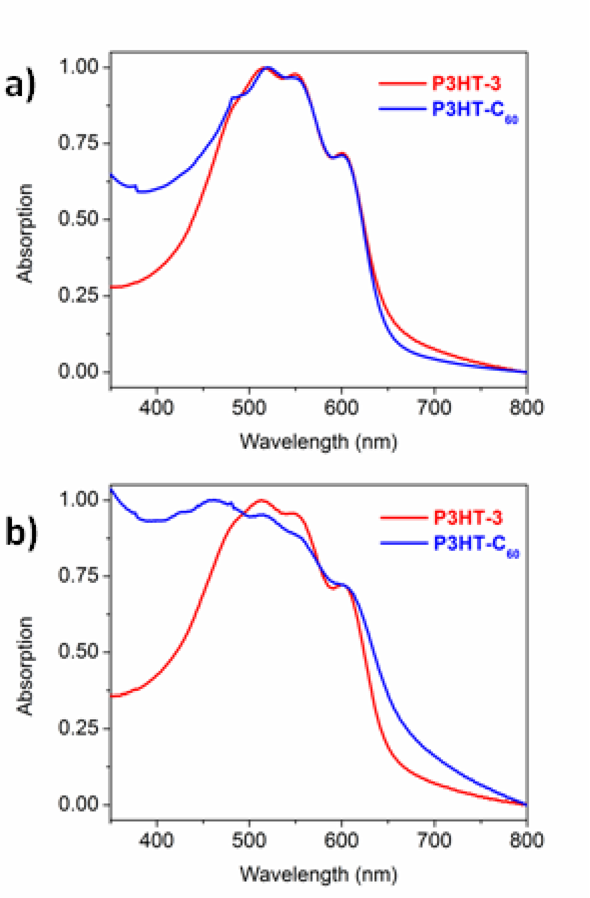

Figure 1-3. Thin film absorption comparison of P3HT-**3** and **P3HT-C$_{60}$** drop-cast from 20 mg/mL solutions in a) THF and b) THF:MeOH (8:2). Results have been normalized based on the absorption maximum.

P3HT-**3** films cast from THF and THF:MeOH (8:2) show similar absorption profiles. The absorption maximum (λ_{max} = 515 nm) is red-shifted compared to that of the solution spectrum (λ_{max} = 450 nm). Both films show vibronic structure with shoulder peaks at approximately 550 nm and 600 nm, as previously described in the literature for P3HT.[69] The red-shift in absorption indicates polymer chain aggregation in the solid state and an increase in the degree of π-stacking between P3HT chains.

In addition to the expected vibronic peaks, **P3HT-C$_{60}$** thin films deposited from THF show residual absorption at higher energies not present in P3HT-**3** films. This residual absorption exhibits a less ordered sample in comparison to P3HT-**3** films. **P3HT-C$_{60}$** films deposited from THF:MeOH (8:2) show broader absorption with a blue-shifted absorption maximum around 460 nm and the vibronic structure at longer wavelengths. The blue-shift in the maximum absorption peak indicates a further decrease in ordered polymer chains compared to films deposited from THF. The bulky fullerene group likely disrupts the packing of the P3HT chains leading to disordered regions in the thin film morphology. Even though **P3HT-C_{60}** induces a greater extent of association in solution, its films contain less interchain order compared to P3HT-**3**.

6. GIWAXS Analysis of Molecular Ordering in the Solid State

Grazing incidence wide-angle X-ray scattering, (GIWAXS), has been widely used to obtain information on molecular packing and orientation of conjugated polymers in the solid state.[145-148] Samples were obtained as thin films by drop-casting 5 mg/mL solutions of P3HT-**3** and **P3HT-C_{60}** in THF, THF:MeOH (8:2) (data found in the SI), or THF:MeOH (1:1) onto silicon wafers.

The one-dimensional GIWAXS profiles taken in the nominally in-plane and out-of-plane directions are shown in Figure 1-4. P3HT-**3** films cast from THF demonstrate mostly edge-on orientation with peaks typically attributed to alkyl stacking (100 and higher order) oriented preferentially perpendicular to the substrate. The peak normally assigned to π-stacking lies at approximately $q = 1.67$ Å^{-1} dominately in the in-plane direction, consistent with previous work.[84] **P3HT-C_{60}** films cast from THF also show a π-stacking peak at $q = 1.67$ Å^{-1} in the in-plane direction. Increasing the volume fraction of methanol for casting solutions of P3HT-**3** and **P3HT-C_{60}** results in a loss in preferential ordering with the emergence of the π-stacking peak in both in-plane and out-of-plane directions for these films. Films cast from THF:MeOH (1:1) exhibit polymer chains with no preferential orientation indicating a loss in anisotropy.

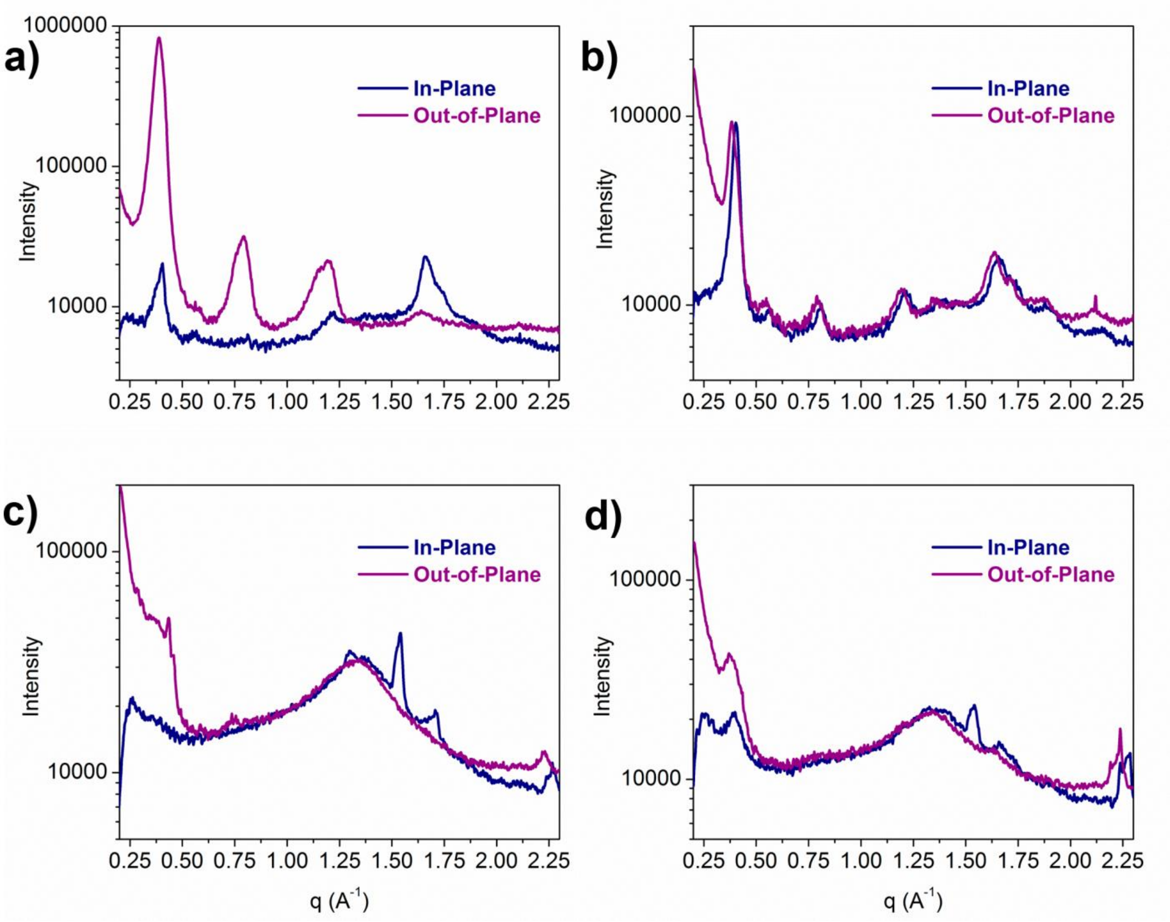

Figure 1-4. GIWAXS line scans containing both in-plane (blue) and out-of-plane (purple) scans for P3HT-**3** films drop-cast from 5 mg/mL solutions in a) THF and b) THF:MeOH (1:1) and **P3HT-C$_{60}$** films drop-cast from 5 mg/mL solutions in c) THF and d) THF:MeOH (1:1).

P3HT-C$_{60}$ films cast from each of the solvent systems do not exhibit clear alkyl stacking peaks compared to P3HT-**3** films, indicating substantially less internal order. The disordered **P3HT-C$_{60}$** films by GIWAXS correlate well with the disorder suggested by the thin film absorption spectra. All evidence is consistent with the fullerene end-group disrupting the interchain lattice formation.

7. Conclusion

Click chemistry based preparations of **P3HT-C_{60}** and **P3HT-Dye** are reported. A novel method was developed to synthesize **8** starting from $PC_{60}BM$ and the molecule was used for coupling with ethynyl-terminated P3HT-**4**. Coupling **8** with other ethynyl-terminated donor materials is a potential avenue for future study of charge transfer and molecular properties. The commercially available azide derivative of sulforhodamine 101 dye was also coupled with ethynyl-terminated P3HT.

The hydrodynamic radii and the absorption properties of **P3HT-C_{60}** and **P3HT-Dye** were measured using DLS and solution UV-Vis spectroscopy, respectively. As the solvent polarity is increased, **P3HT-C_{60}** is shown to form larger aggregates than P3HT-**3** whereas **P3HT-Dye** is shown to form smaller aggregates. Our studies demonstrate the degree to which functional end-groups, in total a small fraction of the overall macromolecular structure, can significantly impact the aggregation properties in solution. This end-group induced organization in solution is found to influence the molecular ordering in thin films based on thin film absorption spectroscopy and GIWAXS analysis of P3HT-**3** and **P3HT-C_{60}**. Pre-aggregation of **P3HT-C_{60}** in solution is found to produce less order in the thin film compared to P3HT-**3**. A plausible explanation for disorder in the **P3HT-C_{60}** films is disruption of polymer chain packing by the fullerene component upon transition from solution to thin film.

C. Triethoxysilane-Functionalized P3HT for Single-Molecule Microscopy

1. Introduction

The optoelectronic properties of conjugated polymers strongly depend on the conformation of individual polymer chains.[149] Studying the photophysics of conjugated polymers at the single chain level allows a deeper understanding of kinetic mechanism and the interactions of singlet and triplet excitons.[150-151] Conformations of individual polymers contribute to bulk characteristic; for example, light absorption and emission is influenced by individual chromaphores along the polymer chain.[150-151] The ability of the polymer chain to adopt different conformations with differing defects leads to excitation energy being transferred to the lowest energy chromaphore.[150-151] These observations provide insight into bulk absorption and emission measurements.[149]

Most spectroscopic techniques are only able to probe to the photophysical characteristics of polymer chains in the bulk.[21] Recently several groups have explored single-molecule microscopy methods.[150] These methods study single conjugated polymer chains within an inert matrix (Figure 1-5)[151-155] or in aqueous solutions (Figure 1-6).[117] However, these methods limit the number of potential chain conformations and do not correspond to the chemical environment from which these materials are solution-processed.[117] Switching to organic solvents allows for the study of a wide range of conformations along with exploring the dynamics of conformational changes.

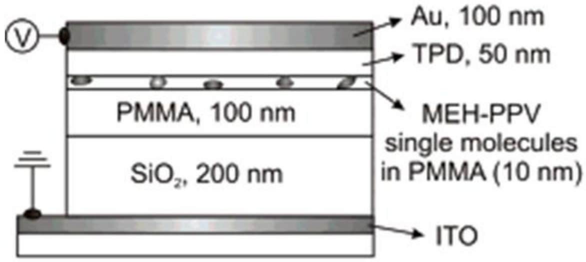

Figure 1-5. Example experimental set-up for single-molecule microscopy experiments performed with the conjugated polymer in an inert matrix of PMMA.[150]

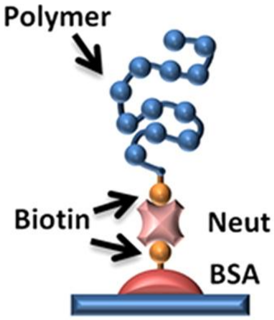

Figure 1-6. Attachment of a polymer chain to a substrate using biotin for imaging in aqueous solvents.[117]

In order to achieve single molecule microscopy in organic solvents, the development of a polymer with a single chain end functionalized for surface immobilization is needed. A common functional group used by self-assembled monolayers for surface attachment is triethoxysilane.[156-157] Incorporating a triethoxysilane group onto a single polymer chain end allows specific binding to a silicon dioxide substrate and is not removed in the presence of organic solvents.[158-160]

P3HT was chosen as the conjugated polymer for study based on the extensive literature background on its photophysical properties and its frequent use as a model system for semiconducting conjugated polymers.[45-48] As described above, P3HT has been well studied in polymer-based transistors and as the donor material in polymer-PCBM solar cells.[1-2,5-

[7,16,44-46] P3HT has been studied using a variety of spectroscopic techniques, from ultrafast to optical absorption spectroscopies in order to better understand the generation and migration of excitons in its well-dissolved, aggregated, and thin film configurations.[161-163] Improving our understanding of these photophysical processes contributes to understanding device performance.

In this contribution, P3HT containing a surface binding group on a single chain end is designed and synthesized. Through serial dilutions, this material is attached to a glass microscope slide with low surface coverage for the purposes of imaging single polymer chains. This method is compatible with almost any organic solvent. Here we provide the first successful study of single polymer chain conformations in organic solvents along with tracking conformational changes in real time.

2. Synthesis

Previous work utilizing single-molecule imaging to study surface-immobilized polymers required attachment of a biotin-functionalized poly(3-dodecylthiophene) (P3DDT) to a protein-coated surface.[69] In order to simplify the polymer deposition process and decrease the distance between the conjugated polymer and the substrate, a triethoxysilane group was chosen to replace the biotin-functionality based on its ability to bind to quartz and glass substrates.[158-159,164] Incorporation of this surface binding group provides conjugated polymers with the potential to bind directly to the substrate surface. If a similar polymerization and click chemistry procedure as demonstrated in the previous study[69] is used, only one chain end of the conjugated polymer contains a triethoxysilane group. Thus the polymer chain maintains the necessary conformational freedom to respond to changes in solvent environment.

Poly(3-hexylthiophene), P3HT, is considered a model system for conjugated polymers[45-48] and therefore a good candidate for single-molecule spectroscopic studies. Specifically, P3HT obtained via Kumada catalyst-transfer polycondensation methods exhibits well-defined, regioregular character with low dispersity.[51-53,64-65] The molecular weight of conjugated polymers produced using this method can be modulated by tuning the monomer-to-catalyst ratio and selection of the nickel catalyst determines the identity of the end-group incorporated onto a single chain end.[165] Using literature procedures, catalyst **2**, as depicted in Scheme S#, was synthesized in two steps from (dppe)$NiCl_2$.[69] **2** contains a triisopropylsilane(TIPS)-protected alkyne which allows post-polymerization functionalization via click chemistry. Controlled polymerization was carried out as shown in Scheme 1-4. 2,5-dibromo-3-hexylthiophene in THF was treated with 0.95 eq. of isopropylmagnesium chloride-lithium chloride complex to produce the reactive monomer. This solution was quickly added to a stirring solution of **2** at monomer-to-catalyst ratios of either 40:1 or 80:1. The polymerization was quenched with ethylmagnesium bromide to provide **P3HT-3** with a number average molecular weight, M_n, of 7.1 kDa and 11.8 kDa and a dispersity, *Đ*, of 1.3 and 1.4 for the 40:1 and 80:1 monomer-to-catalyst ratios respectively. The identity of the end-groups was confirmed by ^{1}HNMR spectroscopy and MALDI-TOF mass spectrometry using an analysis method described previously[77] and is reported in the Experimental and Supporting Information Section (SI).

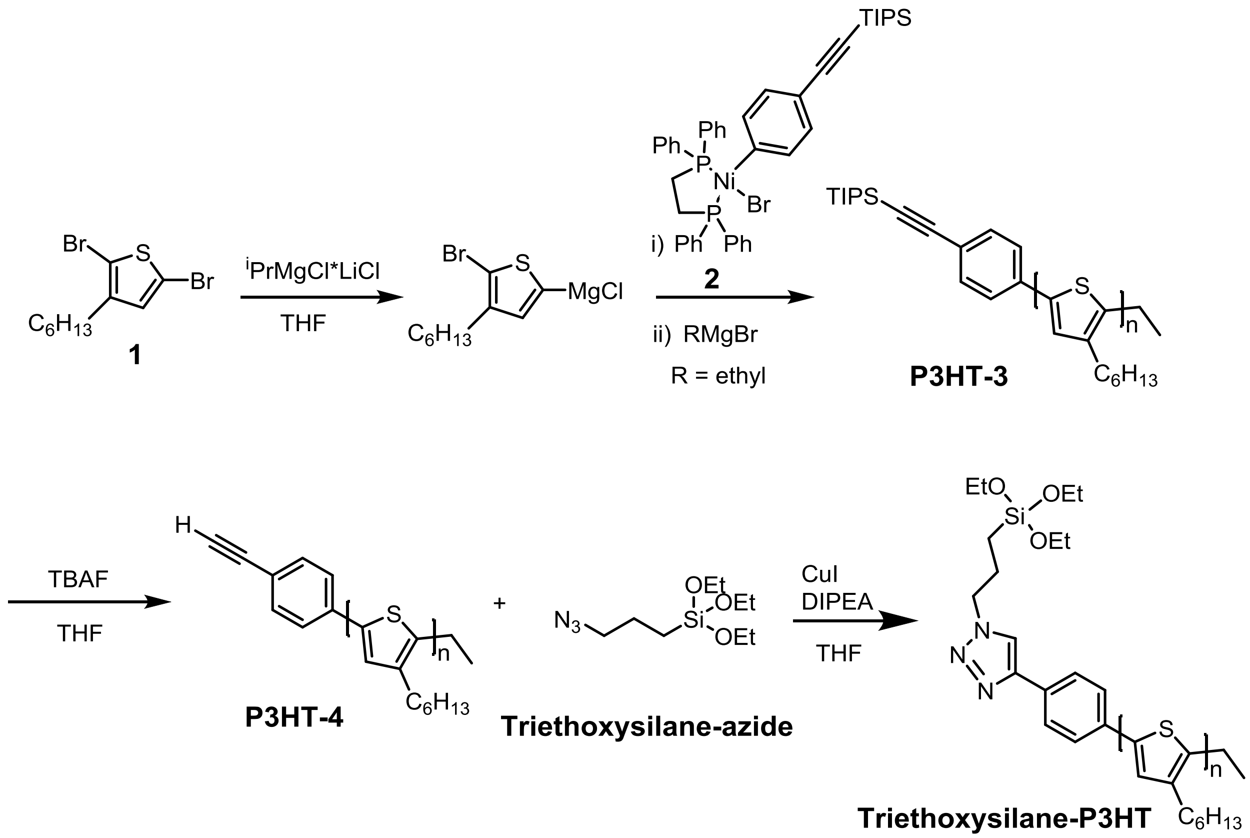

Scheme 1-4. Synthesis of **Triethoxysilane-P3HT**.

The TIPS-protecting group is removed under basic conditions using tetrabutylammonium fluoride (TBAF) in THF at room temperature to yield **P3HT-4** for both chain lengths. ^{1}HNMR spectroscopy confirms the removal of the TIPS-protecting group through the disappearance of the peak at 1.1 ppm and the appearance of the ethynyl peak at 3.1 ppm. **P3HT-4** was reacted with excess triethoxysilane-azide under click conditions comprising CuI and DIPEA with THF as the solvent.[103-104,107,113-114] The triethoxysilane-group was successfully incorporated onto one end of the polymer chain to produce **Triethoxysilane-P3HT** for both chain lengths as confirmed by ^{1}HNMR spectroscopy and MALDI-TOF. The presence of triethoxysilane at a single chain end activates **Triethoxysilane-P3HT** for surface attachment to a quartz or glass substrate.

3. **Triethoxysilane-P3HT** Surface Immobilization

Triethoxysilane groups are known to bind to silicon dioxide surfaces such as glass and quartz.[156-157,159] In order to determine whether or not **Triethoxysilane-P3HT** successfully binds to glass substrates, thin film UV-Vis absorption experiments were carried out using **Triethoxysilane-P3HT** and unfunctionalized **P3HT-4**. In the initial experiment proving selective surface attachment, glass substrates were immersed in either 0.1 mM **P3HT-4** or **Triethoxysilane-P3HT** solutions for several hours. The substrates were removed from the solutions, rinsed with chloroform, and sonicated in chloroform before being left in air to dry. Subsequent UV-Vis absorption measurements of both films are shown in Figure 1-7. **Triethoxysilane-P3HT** provides an absorption peak in the expected range whereas **P3HT-4** provides no significant absorption in this range. These results indicate only triethoxysilane-functionalized P3HT chains are able to bind to the glass surface and remain after repeated washing in a good solvent.

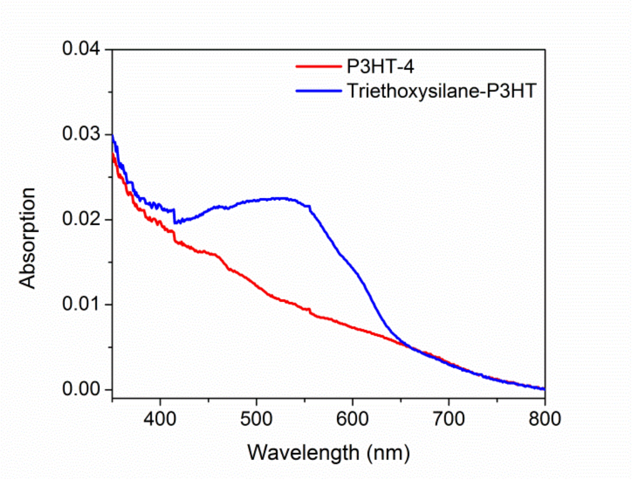

Figure 1-7. UV-Vis absorption spectra of **P3HT-4** (red) and **Triethoxysilane-P3HT** (blue) deposited on glass substrates.

4. Organic Solvent Based Single-Molecule Microscopy

Single-molecule microscopy has yet to be performed using organic solvents, required the development of new sample chamber. Previous sample chambers used materials compatible with aqueous but not organic solvents.[69] Brass was chosen for the chamber based on its solvent resistance (Figure 1-8) and the chamber joints were sealed with PTFE tape to prevent leaks. The set-up included a continuous flow of degassed solvent to prevent photodegradation and increase the signal-to-noise ratio. The microscope set-up is shown in Figure 1-9. Excitation was performed in epifluoresence mode with a 473 nm laser in continuous wave operation.

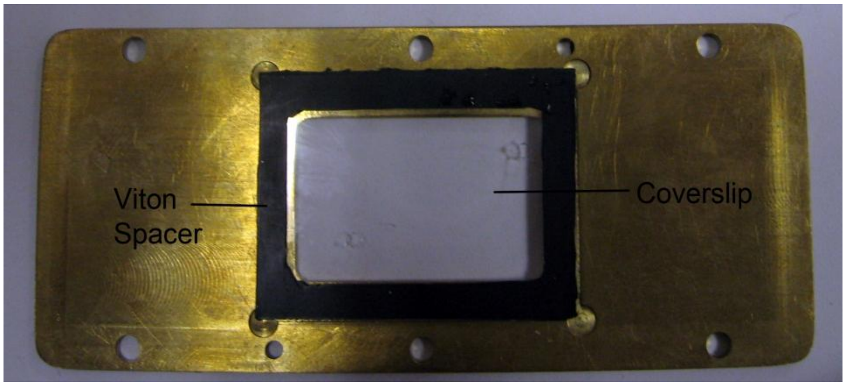

Figure 1-8. Example brass fitting with glass coverslip for single-molecule microscopy.

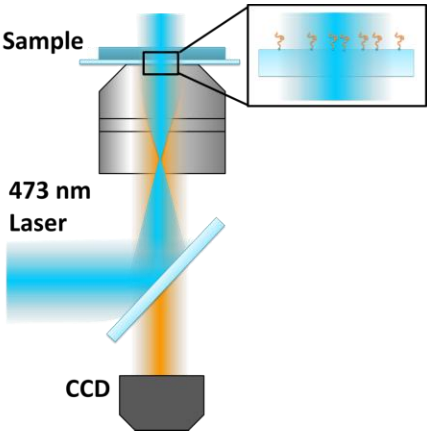

Figure 1-9. Example microscope set-up in epifluorescence mode utilizing a 473 nm laser.

To test the system and confirm selective binding of the polymer chains, initial single-molecule microscopy experiments were performed comparing **P3HT-4** and **Triethoxysilane-P3HT** with the same deposition conditions. Both materials were dissolved in anhydrous dichlorobenzene and diluted to pM concentrations in order to avoid the presence of aggregates. Hydrophilic glass substrates were incubated for thirty minutes in the solution. Substrates were washed thoroughly with fresh dichlorobenzene before imaging. The results are shown in Figure 1-10. **Triethoxysilane-P3HT** (left) shows distinct spots on the 2D map indicating the fluorescence of P3HT chains which are not present for **P3HT-4** (right). These results further confirm the specific binding of **Triethoxysilane-P3HT**.

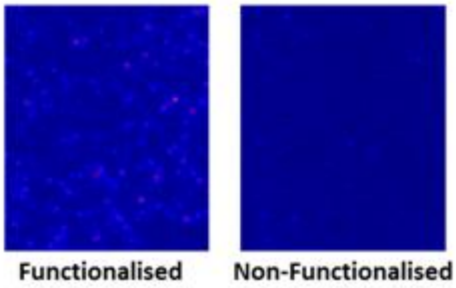

Figure 1-10. Single-molecule microscopy images of **Triethoxysilane-P3HT** (left) and **P3HT-4** (right).

5. Single-Molecule Microscopy in Two Different Organic Solvents

Using the set-up described above, single-molecule microscopy measurements were performed using two different organic solvents. Dichlorobenzene was chosen as the good solvent and dimethylsulfoxide (DMSO) as the poor solvent. The chain conformations are expected to be solvent-dependent based on bulk measurements.[77] These experiments provide a basis for understanding further studies utilizing solvent-switching techniques.

The following procedure was used to produce samples for single-molecule microscopy study. **Triethoxysilane-P3HT** was dissolved in THF and diluted to a 2 nM concentration. A solution containing 95% polymer in THF, 2.5% acetic acid, and 2.5% water (final concentration ~500 pM) was sonicated for five minutes. A plasma-etched silica substrate was introduced into the solution and sonicated for one hour. The substrate was then dried under vacuum for one hour, rinsed with dichlorobenzene, and dried with nitrogen. Samples were used immediately or stored for less than two days.

Single-molecule microscopy experiments indicate that **Triethoxysilane-P3HT** in dichlorobenzene exhibits the expected behavior of extended chains in solution. Single-molecule spectroscopy for a single polymer chain is shown in Figure 1-11. The decay trace indicates fast photobleaching due to inefficient energy transfer. The extended conformation results in a high number of active chromophore units (Figure 1-12). Multiple spots were measured in order to obtain statistically significant results. In dichlorobenzene, primarily decay behavior of extended chains was observed (Figure 1-13). Regular and irregular behavior is observed for a percentage of the measured spots. A possible explanation for the presence of traces corresponding to more collapsed conformations is the short length of the P3HT chains only having a limited number of chromophores.

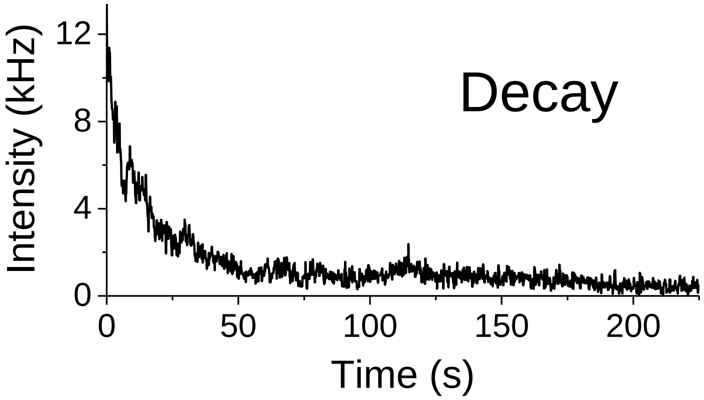

Figure 1-11. Single-molecule spectroscopy decay trace provided by a single **Triethoxysilane-P3HT** chain in dichlorobenzene.

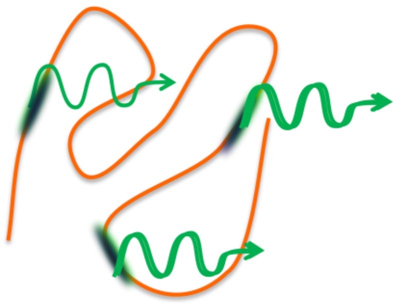

Figure 1-12. Depiction of inefficient energy transfer by extended **Triethoxysilane-P3HT** chains.

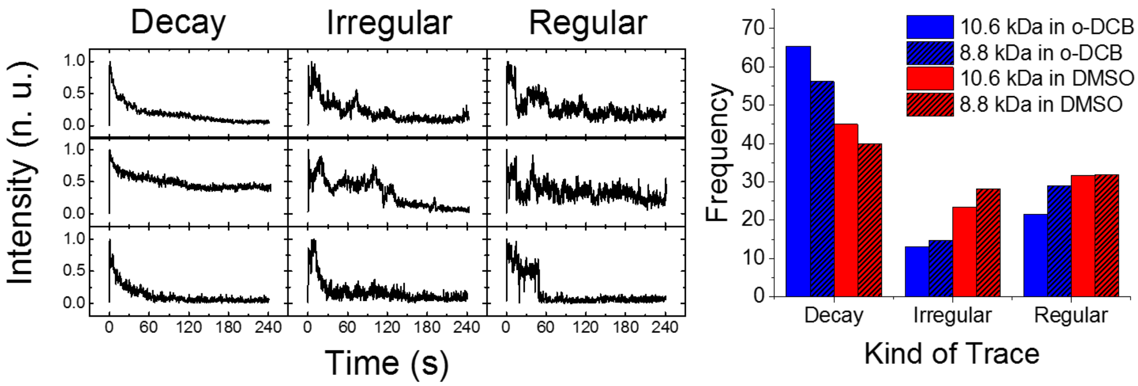

Figure 1-13. Single-molecule spectroscopy traces (left) and the distribution of these traces for different experimental conditions (left).

The three different traces observed in single-molecule spectroscopy experiments indicate different chain conformations. Decay traces likely correspond to chains existing in an extended conformation. Decay traces can also be associated with a disordered conformation, such as a random coil, which is unable to efficiently transfer energy along the chain. Regular traces indicate a stable photoluminescence (PL) intensity and sometimes blinking steps between two stable levels. These traces likely correspond to ordered, collapsed conformations, such as rod-like behavior. These conformations allow efficient energy transfer between different conjugated regions where absorbing chromophores feed into emitting ones. The blinking, or jumps in PL intensity, are associated with delocalized dark states which result in PL quenching. In contrast, irregular traces exhibit random fluctuations of PL intensity with no stable PL intensity levels or clear blinking events. These traces correspond to collapsed, disordered conformations, such as a molten globule, where some regions of the chain are quenched by localized dark states and others remain emissive. The explanation for these continuous changes in PL intensity is not fully understood but possibilities include dynamic conformational changes such that the number of emissive chromophores is constantly changing or different regions of the chain being randomly quenched at different times. Figure 1-14 provides a visual of the different potential chain conformations.

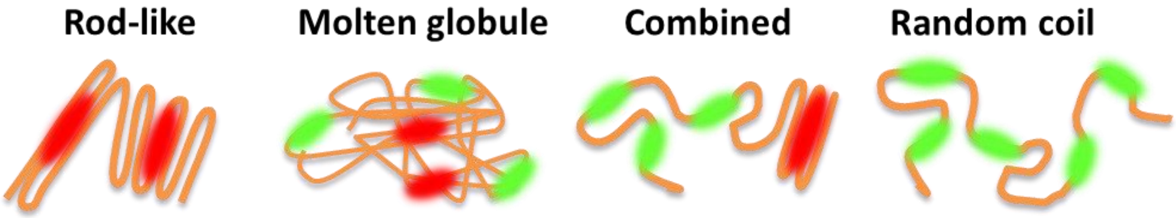

Figure 1-14. Possible chain conformations as observed by single-molecule spectroscopy.

Performing single-molecule microscopy experiments in DMSO suggests the presence of more collapsed chains. The regular (stable) trace from single-molecule spectroscopy shown in Figure # indicates efficient energy transfer to the lowest energy site until transitioning to dark states. The collapsed conformation gives rise to this type of signal due to a smaller number of active chromophore units (Figure 1-15). P3HT chains in DMSO exhibited a mixture of decay, regular, and irregular traces (Figure 1-16) based on measurements of multiple spots. The variety of traces observed for **Triethoxysilane-P3HT** in DMSO may be attributed to molten globule conformations where the disorder is too high to allow energy transfer to even nearby neighbors. Since most of the traces reach a steady-state above the noise, ordered regions surrounded by disordered regions may be the cause. The ordered regions are responsible for the initial decay whereas the disordered regions contribute to stable emission. The average PL intensity in DMSO is roughly half that in dichlorobenzene, likely indicating that the disordered portions of the chain are shorter. Comparing results using DMSO to dichlorobenzene, solvent is found to influence the distribution of conformation of single P3HT chains.

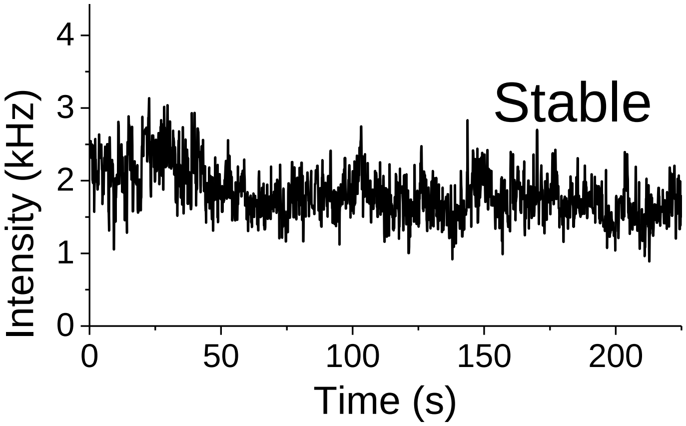

Figure 1-15. Single-molecule spectroscopy trace provided by a single **Triethoxysilane-P3HT** chain in DMSO.

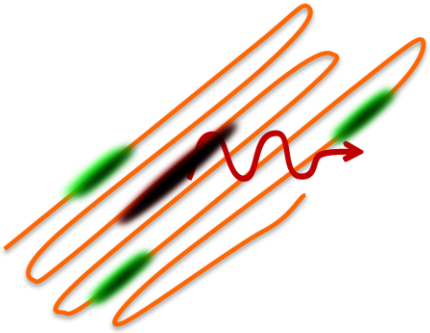

Figure 1-16. Depiction of collapsed conformation of **Triethoxysilane-P3HT** chains.

Triethoxysilane-P3HT (M_n = 8.8 kDa) was compared to **Triethoxysilane-P3HT-2** (M_n = 10.6 kDa). The same experimental procedure described above was applied to **Triethoxysilane-P3HT-2**. In dichlorobenzene, **Triethoxysilane-P3HT-2** provides decay traces from single-molecule spectroscopy, indicating the presence of extended chains. Compared to **Triethoxysilane-P3HT**, there are more instances of regular and irregular traces and the PL intensity if roughly doubled but the photobleaching rate (Figure 1-17 on left) remains similar for **Triethoxysilane-P3HT-2**. The higher molecular weight resulted in a greater number of emissive chromaphores but had inefficient energy transfer.

In DMSO, the distribution of traces remains the same along with the PL lifetimes for **Triethoxysilane-P3HT** and **Triethoxysilane-P3HT-2**. However, the average photobleaching rate is smaller (Figure 1-17 on right) for **Triethoxysilane-P3HT-2** compared to **Triethoxysilane-P3HT**. This data suggests the average number of active chromaphores remains similar with the increase in molecular weight. The longer photobleaching time indicates that there are a large number of chromaphores available which feed into the emissive ones.

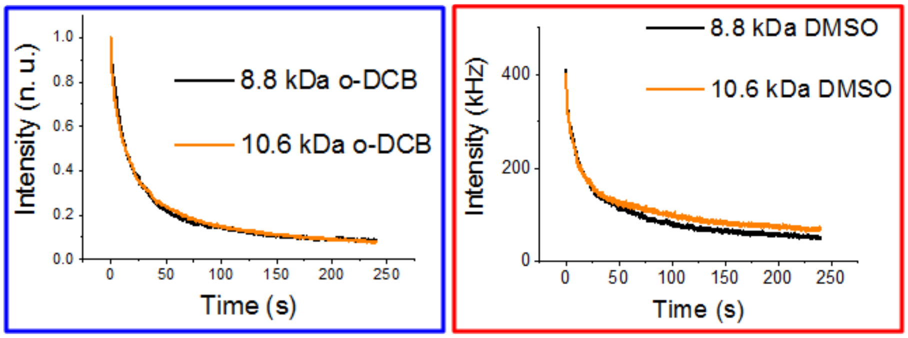

Figure 1-17. Intensity traces for single-molecule spectroscopy experiments comparing **Triethoxysilane-P3HT** and **Triethoxysilane-P3HT-2** in dichlorobenzene (left) and DSMO (right).

Dispersity provides further insight on the trends in the data. **Triethoxysilane-P3HT** (1.1) has a smaller dispersity compared to **Triethoxysilane-P3HT-2** (1.5). Using the measurements described above, the data taken in dichlorobenzene is plotted in a histogram comparing the number of spots with specific peak intensities (Figure 1-18). **Triethoxysilane-P3HT** (left) provides a smaller distribution of intensities for all three types of traces whereas **Triethoxysilane-P3HT-2** (right) reveals a larger distribution of intensities. These results suggest a larger dispersity enables a larger range of intensity values based on the availability of a wider range of polymer chain lengths in the extended conformation.

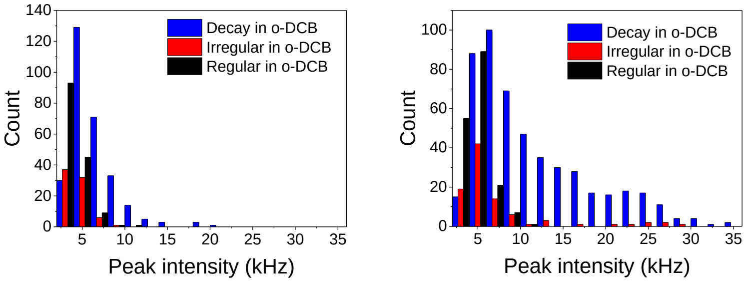

Figure 1-18. Distribution of intensities in dichlorobenzene for **Triethoxysilane-P3HT** (left) and **Triethoxysilane-P3HT-2** (right).

6. Solvent Switching

The experimental set-up developed above provides the possibility to study solvent switching in real time. The initial experiment sought to study changes in chain conformation switching from a poor solvent (DSMO) to a good solvent (dichlorobenzene) and the data are shown in Figure 1-19. The data indicates an increase in PL intensity upon switching from DMSO to dichlorobenzene for **Triethoxysilane-P3HT** (Figure 1-19b) before decaying back to the original level. When a conformational change occurs, it happens within about one second of switching solvents. These data provide direct evidence of conformational changes of single polymer chains and indicate how quickly changes in conformation can take place. Additionally, the return to the original PL intensity signifies the stochastic nature of the folding and unfolding processes of the single chains. In contrast, for **Triethoxysilane-P3HT-2**, fewer chains exhibit a change in behavior on switching solvents. The reduced ability of **Triethoxysilane-P3HT-2** to switch conformations can be explained by strong conformational stability of single chains due to higher self-aggregation.

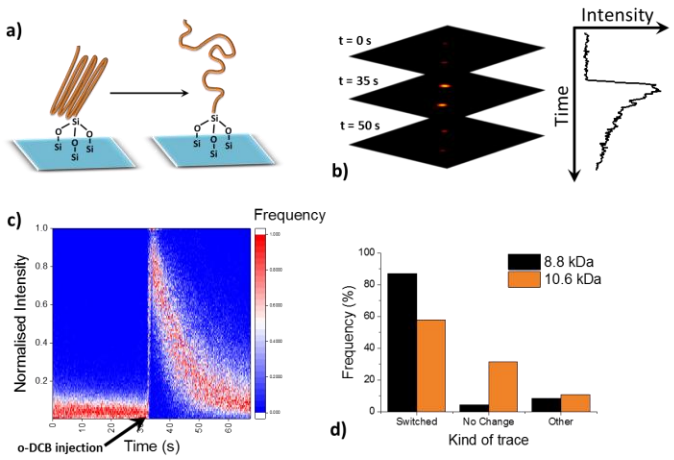

Figure 1-19. (a) Cartoon depicting changes in polymer chain conformation upon switching from DMSO to dichlorobenzene. (b) 2D intensity map of changes in intensity over time during solvent switching experiments. (c) Heat map of detected single-molecule traces. (d) Histogram indicating number of traces which changed PL behavior during solvent switching.

Considering a multistep process, experiments were performed starting in dichlorobenzene, switching to DMSO, and switching back to dichlorobenzene. The results are shown in Figure 1-20. The first step from dichlorobenzene to DMSO shows the expected decrease in signal intensity based on the results for a single solvent switching experiment. When the solvent was switched back to dichlorobenzene, only a partial recovery of the PL intensity was observed. For the opposite process (DMSO to dichlorobenzene to DMSO), the PL signal exhibits a sudden increase in intensity and then a sudden decrease. Results are similar for both molecular weights.

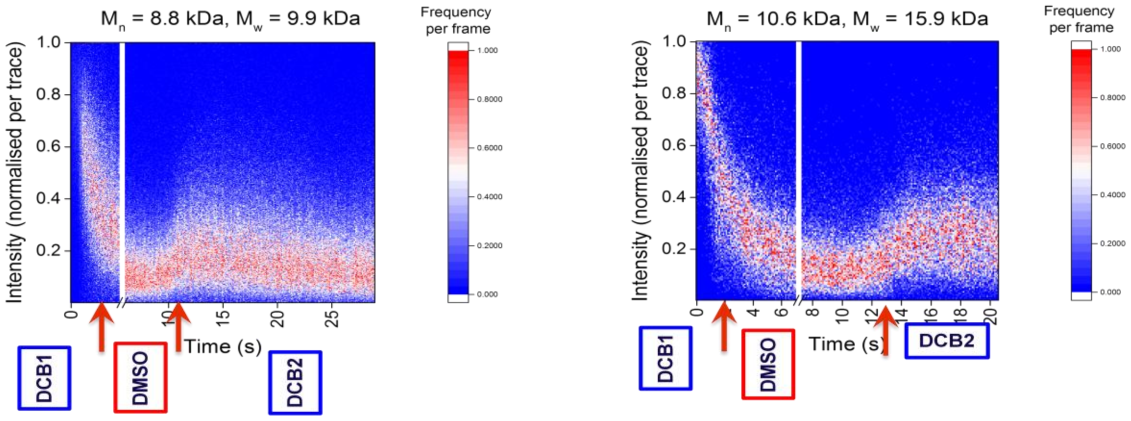

Figure 1-20. Heat maps of signal intensity as a function of time for **Triethoxysilane-P3HT** (left) and **Triethoxysilane-P3HT-2** (right) when the solvent changes from dichlorobenzene to DMSO to dichlorobenzene.

7. Conclusion

A conjugated polymer, **Triethoxysilane-P3HT**, was designed and synthesized for surface attachment. The triethoxysilane group was incorporated onto a single polymer chain end and allows specific binding of a single polymer chain end to a silicon dioxide surface. The development of this material made possible single-molecule spectroscopy and microscopy in organic solvents.

This is the first report of single-molecule spectroscopy and microscopy experiments in organic solvents. This technique enabled measurements in a variety of different organic solvents in order to explore the influence of solvent on chain conformation. **Triethoxysilane-P3HT** was studied at a low and high molecular weight in good (dichlorobenzene) and poor (DMSO) solvents. Both solvation and self-aggregation of single polymer chains were observed depending upon solvent conditions. These results contribute to our understanding of the photophysical properties of single polymer chains and how those properties relate to chain conformation.

Changes in chain conformation were observed in real time upon switching from one solvent to another. Switching from a poor to good solvent results in a sudden increase in PL intensity before it decays back to its original value. These data confirmed the stochastic nature of the folding and unfolding of single polymer chains. Developing this method opens up possibilities for future study. If the synthetic end-functionalization method can be applied to the synthesis of other conjugated polymer backbone structures, we could study the generalizability of these results. This technique is compatible with manipulation of single polymer chains and could lead to mechanical manipulation of polymer chains with magnetic or optical tweezers.

D. P3HT-b-PEG for Drug Delivery

1. Introduction

Poly(3-hexylthiophene)-*block*-polyethylene glycol is a rod-coil diblock copolymer consisting of two chemically incompatible blocks. It is known to microphase separate into different structures based on solvent and relative block lengths and to self-assemble into micelles.[166-168] P3HT tends to favor π-π stacking which is in opposition to the typical microphase separation.[167] Thus in the presence of a poor solvent or when the P3HT block is much greater than the PEG block, the π-π interactions dominate and a fibular morphology is observed (Figure 1-21 on left).[167] Solvent choice also influences the optical properties such as the absorption maximum and the presence of a shoulder peak, as highlighted by the different solution colors for different solvents (Figure 1-21 on right).[167] The influence of solvent on the microstructure of P3HT-*b*-PEG may provide structures suitable for drug delivery applications.

Figure 1-21. AFM images and suggested morphologies for P3HT-*b*-PEG (left). Optical properties of P3HT-*b*-PEG change with solvent (right).[167]

Polymer-based micelles have previously been studied for drug delivery applications.[169-173] Micelles are of interest in drug delivery as a method for drugs that have limited solubility in water.[174] The different solubilities, especially with respect to water, of the P3HT and PEG blocks open up potential to form micelles. Micelles form when the concentration is above the critical micelle concentration (CMC). At low concentrations, materials remain normally dissolved; however, as the concentration is increased above the critical micelle concentration, the hydrophobic ends are driven to form a cluster with the hydrophilic ends in greater contact with water.[175-176] Typically, a material is dissolved in a small amount of a favorable organic solvent and a greater amount of water is added. The solution is stirred and the organic solvent is allowed to evaporate, causing the polymer concentration to increase above the CMC and micelles to form.

PEG-based copolymers have previously been studied for drug delivery applications. PEG is often chosen as the hydrophilic block based on its high solubility in water, its chain mobility, and its low toxicity.[169-173] Block copolymers containing PEG and a poly(α,β-aspartic acid) was synthesized with a DOX drug incorporated onto the poly(α,β-aspartic acid) block and found to form stable micelles.[170] These micelles were found to target tumor cells and provide sustained release of the drug.[170] Poly(lactic acid) (PLA) derivatives are another common component due to being a biodegradable and biocompatible polyester along with being approved by the FDA for biomedical applications in humans.[173] PLA derivatives have potential to attach a reactive group which can stabilize the micelle or aid in targeting.[173]

Introducing P3HT as the second block with PEG provides the opportunity to image cells using fluorescence microscopy when P3HT-*b*-PEG micelles are taken up by cells. This approach has potential to further expand our understanding of micelle-based drug deliver. However; this strategy relies on P3HT fluorescence being sufficiently strong in the micellular structure. P3HT is known to fluoresce when dissolved in organic solvents but less is known about its fluorescence in micelles.[136,177] This study aims to explore the ability of P3HT-*b*-PEG to form micelles with sufficient fluorescence for imaging during drug delivery.

2. Synthesis

The P3HT was synthesized and deprotected as described in previous sections.[77] The deprotected ethynyl-terminated P3HT is active for copper-catalyzed azide-alkyne cycloaddition reactions. Ethynyl-terminated P3HT was reacted with azide-terminated PEG (M_n = 1000 g/mol) under click reaction conditions of CuI/DIPEA in THF as shown in Scheme 1-5. After allowing the reaction to proceed for 48 hours and purification by precipitation and washing in methanol, the diblock copolymer, P3HT-*b*-PEG, was achieved. Characterization by ^{1}HNMR showed a peak at 8.0 ppm which corresponds to the hydrogen on the triazole ring. GPC showed only one peak with a PDI of 1.2.

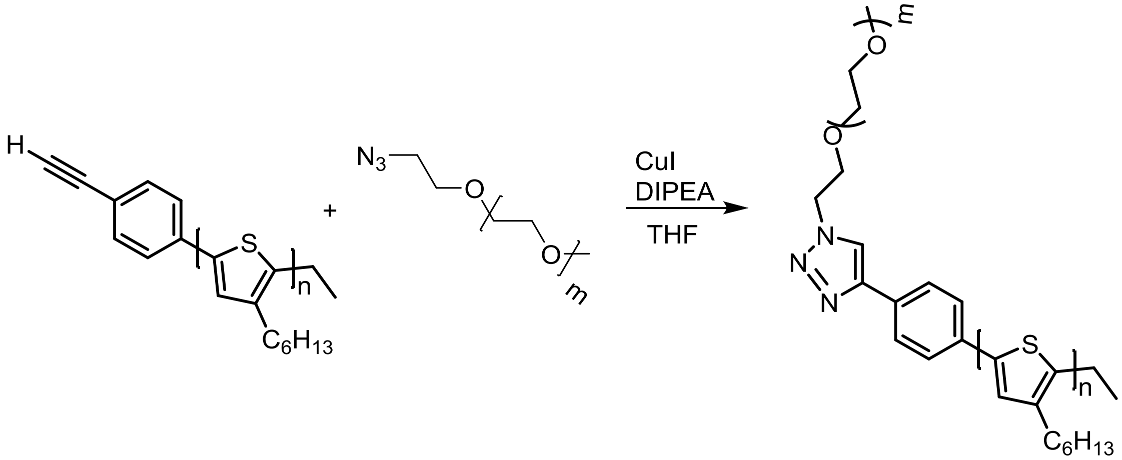

Scheme 1-5. Click coupling of ethynyl-terminated P3HT and azide-terminated PEG to produce P3HT-*b*-PEG.

MALDI analysis was used to confirm the incorporation of the PEG block onto the end of the P3HT by end-group analysis. The spacing between the peaks of P3HT-*b*-PEG in the

MALDI spectrum, shown in Figure 1-22, remains equal to the mass of the P3HT repeat unit. End-group analysis confirms the presence of the PEG moiety. The highest peak has a mass of 6177.993. After subtracting off the mass of the PEG ($M_n = 1000$) and the mass of the ethyl group, the P3HT block is found to have 31 repeating units. This is the same number of repeating units as the original P3HT material.

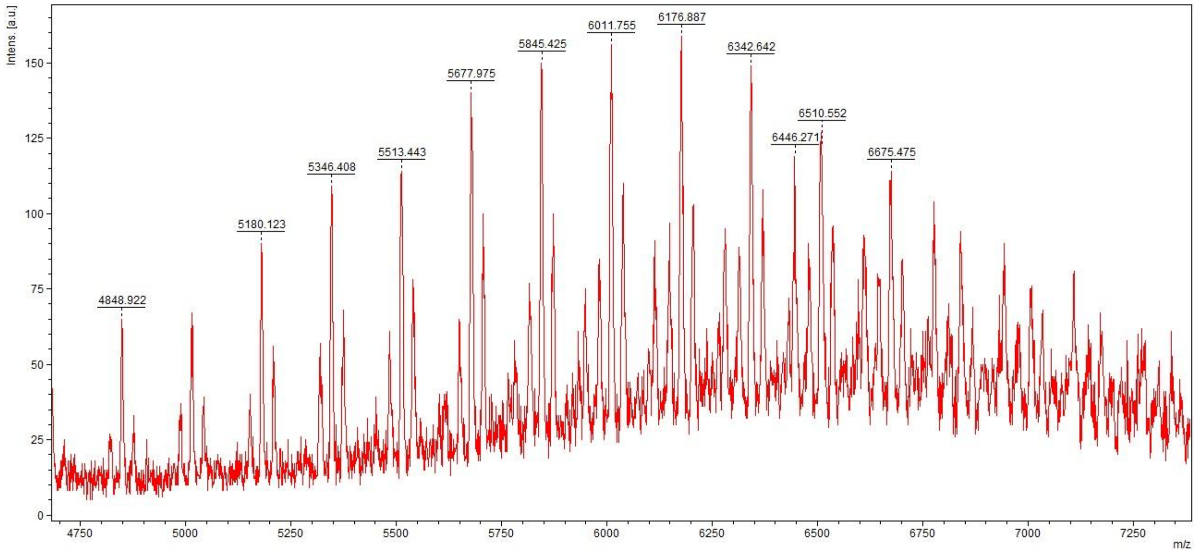

Figure 1-22. MALDI spectrum of P3HT-*b*-PEG.

3. Optical Properties of P3HT-*b*-PEG as Free Chains in Solution

The optical properties of P3HT-*b*-PEG depend on solvent. An example of this solvatochromism is shown in Figure 1-23 where the color of the solution changes from yellow-orange (THF) to transparent blue (dichloromethane). The different solubility properties of the P3HT block and the PEG block increase the potential solvents for this polymer.

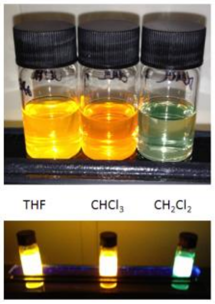

Figure 1-23. P3HT-*b*-PEG dissolved in THF (left), chloroform (center), and dichloromethane (right).

The optical absorption spectra of P3HT-*b*-PEG and P3HT in chloroform are shown on the left in Figure 1-24. The broad absorption peak of P3HT-*b*-PEG has a maximum around 450 nm as expected for P3HT in a good solvent whereas the absorption spectrum of P3HT has hit the detector limit. The spectra in dichloromethane are shown on the right in Figure 1-24. Both materials exhibit a red-shifted shoulder peak with an onset at about 650 nm such that P3HT-*b*-PEG provides a strong shoulder peak compared to P3HT. Emission spectra are shown in Figure 1-25 for chloroform (left) and dichloromethane (right) solutions. The emission maxima are very similar for all four solutions at about 575 nm.

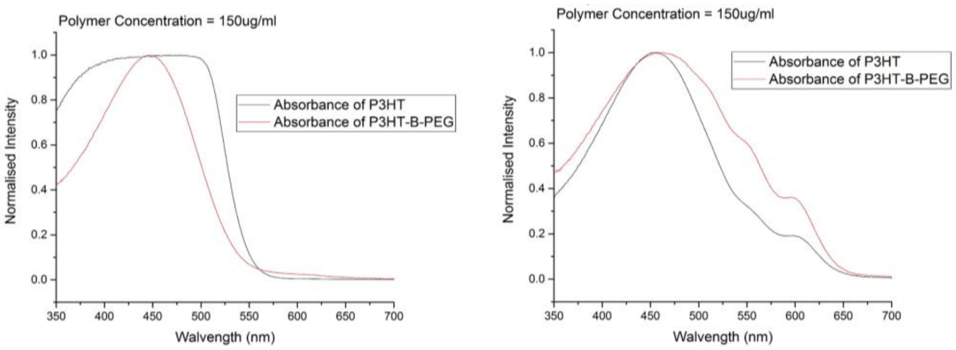

Figure 1-24. Optical absorption spectra of P3HT-*b*-PEG (red) and P3HT (blue) in chloroform (left) at 150 μg/mL and dichloromethane (right) at 150 μg/mL.

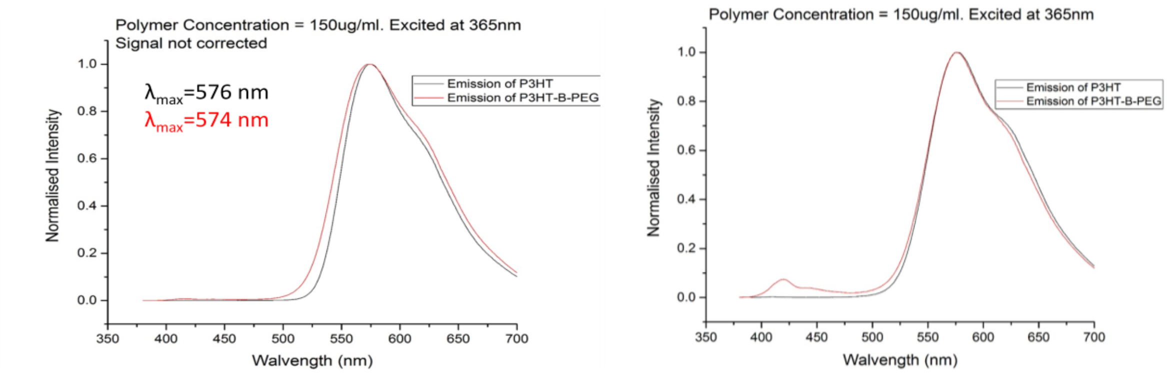

Figure 1-25. Emission spectra of P3HT (blue) and P3HT-*b*-PEG (red) in chloroform (left) and dichloromethane (right) at 150 μg/mL.

4. Photophysical Properties of P3HT-*b*-PEG Micelles

Micelles were formed using P3HT-*b*-PEG. The illustration below outlines the process used to form micelles with PEG surrounding a P3HT core. P3HT-*b*-PEG was dissolved in either chloroform or dichloromethane. Deionized water was slowly injected and the container was subjected to gentle agitation. The solvent was allowed to evaporate and the result was concentrated to about 50 μg/mL.

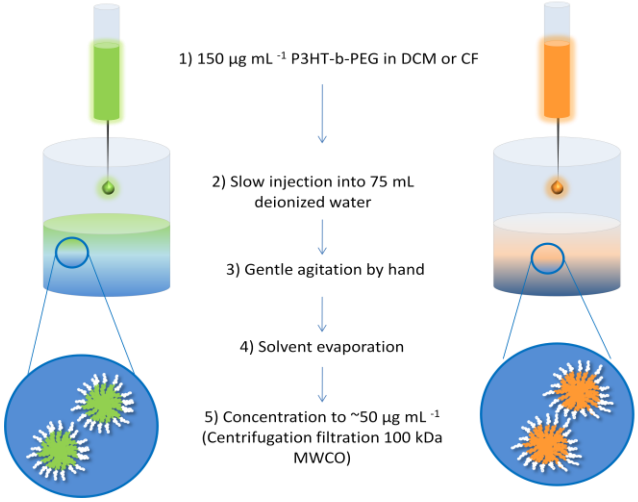

Figure 1-26. Process of micelle formation.

The optical properties of the resulting micelles were studied. The optical absorption maximum of the micelles is blue-shifted compared to the original polymer for both solvent conditions (Figure 1-27). The emission maximum also exhibits a small blue-shift. Before normalization, the emission intensity of the micelles is quenched by a factor of ten compared to the original polymer in solution. While the absorption and emission remain in an acceptable range, emission quenching is not desirable for fluorescence imaging applications. P3HT is known to self-quench when aggregated.[135] The formation of a micelle may simulate aggregation and provide a potential explanation for the lower emission intensity.

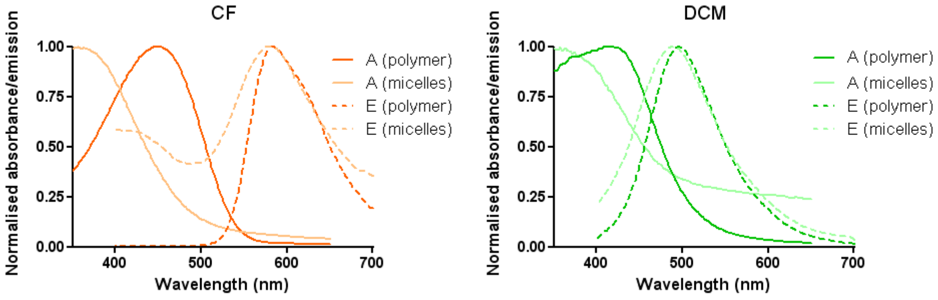

Figure 1-27. Absorption (solid) and emission (dashed) spectra of P3HT-*b*-PEG and P3HT-*b*-PEG micelles from chloroform (left) and dichloromethane (right).

To further characterize the micelles, nanoparticle tracking analysis was performed. The results are shown in Figure 1-28. Micelles formed from chloroform and dichloromethane provide similar size distribution profiles. The average hydrodynamic diameter is 125-130 nm and the distribution is narrow. TEM images shown in Figure 1-29 also show similarly sized particles. A narrow particle distribution provides potential for reproducibility.

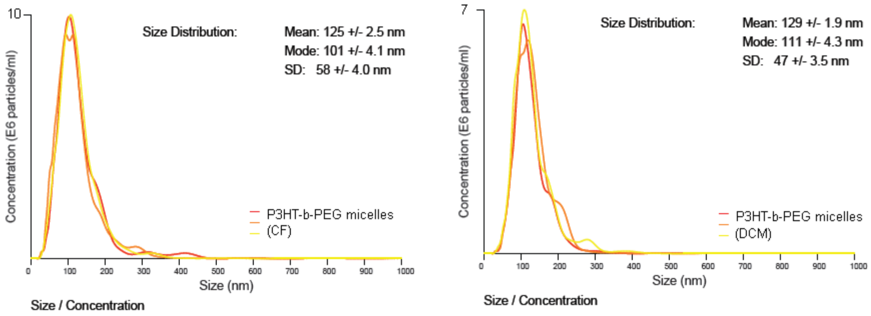

Figure 1-28. Nanoparticle tracking analysis results for P3HT-*b*-PEG micelles from chloroform (left) and dichloromethane (right).

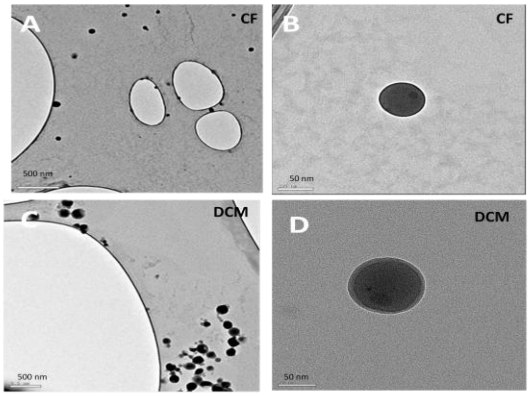

Figure 1-29. TEM images of P3HT-*b*-PEG micelles from chloroform (top) or dichloromethane (bottom).

P3HT-*b*-PEG micelles were introduced to cell cultures. Two different cell types were used: epithelial cells and J774 macrophages. The cells were incubated in a cell culture medium with P3HT-*b*-PEG micelles at a concentration of 150 μg/mL for 24 hours. For both cell types, the micelle fluorescence was too low to be detected above the autofluorescence.

5. Encapsulation of P3HT in PEG-PLGA Micelles

Due to the low fluorescence intensity of the P3HT-*b*-PEG micelles, encapsulation of P3HT in PEG-PLGA micelles was attempted. The general procedure is shown in Figure 1-30. P3HT was dissolved in either chloroform, dichloromethane, or THF at 150 μg/mL and PEG-PLGA at 3 mg/mL. Three PEG-PLGA lengths were investigated: PEG at 2 kDa with PLGA at 5 kDa, PEG at 2 kDa with PLGA at 15 kDa, and PEG at 5 kDa with PLGA at 45 kDa. The resulting solutions were sonicated for ten minutes. This solution was slowly injected into five mL of ice cold deionized water while under sonication. The solution was allowed to stir overnight at room temperature so that the organic solvent evaporated and the remaining concentration was 50 μg/mL. Experimental results found that neither chloroform nor dichloromethane were able to encapsulate P3HT; therefore, THF was chosen as the organic solvent.

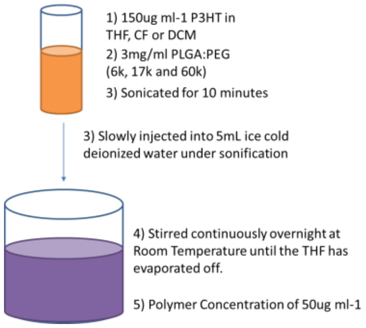

Figure 1-30. General procedure for obtaining PEG-PLGA micelles encapsulating P3HT.

The optical properties of the resulting micelles were investigated. The top row of Figure 1-31 shows the variations in color for the different molecular weights of PEG-PLGA with encapsulated P3HT. The highest molecular weight (PEG = 5 kDa and PLGA = 45 kDa) provides a more clear solution compared to the others. When a UV-lamp at 365 nm is used for excitation, no luminescence is visible which suggests all three systems have been quenched.

Figure 1-31. Solutions containing P3HT encapsulated by PEG-PLGA at three different molecular weights (top) and when excited by 365 nm light from a UV lamp (bottom).

Optical absorption (left) and emission (right) spectra are shown in Figure 1-32. The absorption spectra for all three materials are very similar to that of aggregated P3HT chains.[135] The highest molecular weight PEG-PLGA does exhibit a slight blue-shift in absorption. The emission spectra of the two lower molecular weight materials are similar and correspond to P3HT emission.[136] The higher molecular weight material displays a blue-shifted maximum and a blue-shifted shoulder peak. The differences in optical properties may explain the differences in solution color reported above.

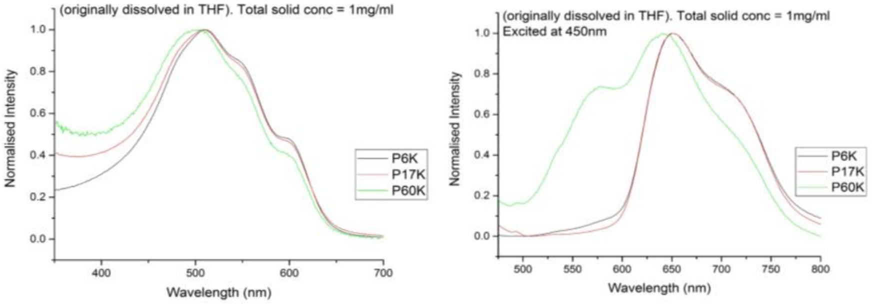

Figure 1-32. Absorption (left) and emission (right) of P3HT encapsulated by PEG-PLGA at three different molecular weights.

6. Conclusions

P3HT-*b*-PEG was successfully synthesized using controlled polymerization and copper-catalyzed click coupling. Its optically properties were studied using absorption and emission spectroscopy. The free polymer in a chloroform solution provides absorption and emission very similar to a solution solely containing P3HT. In dichloromethane, the emission is similar to chloroform but the absorption spectrum shows a shoulder peak.

P3HT-*b*-PEG was able to form micelles in water under minimal agitation. These particles were found to have diameters of about 125-130 nm with little difference observed between forming micelles from chloroform or dichloromethane. The micelles produced similar optical properties compared to their polymer counterparts; however, the emission intensity was quenched by a factor of ten. This decrease in emission intensity led to a failure in observing any fluorescence signal when the micelles were introduced into cell cultures. In order to move forward with drug delivery applications, the emission intensity of the micelle should be much higher.

E. Conclusions

The three studies in this chapter indicate the wide range of potential applications for functionalized P3HT derivatives. By employing a controlled polymerization method, the molecular weight and end-group can be modulated for the desired application. The synthesis of a tailored catalyst enabled the incorporation of a desired end-functional group. By choosing a protected alkyne group for catalyst transfer, the resulting P3HT chains were activated for copper-catalyzed azide-alkyne click chemistry. The potential P3HT derivatives are limited only by the ability to synthesize a suitable azide for coupling.

The three applications explored in this chapter range from expanding our basic understanding of P3HT aggregate formation to studying the photophysical properties of single polymer chains to micelles for drug delivery. As new applications for semiconducting polymers are developed, utilizing this synthetic method may provide a quick path to novel materials.

F. Experimental and Supplementary Information

1. Materials and Methods

All reagents and solvents were purchased from Sigma Aldrich, BDM, Fisher Scientific, Alfa Aesar, or Acros Organics and used without further purification unless specified. 1,2-Bis(diphenylphosphino)ethane nickel (II) chloride was purchased from Strem and used as received. PCBM was purchased from Solenne. 2,5-dibromo-3-hexylthiophene and 1-bromo-4-(triisopropylsilylethynyl)benzene were synthesized according to literature methods. 1,2-Bis(diphenylphosphino)ethane-bis(triphenylphosphine)nickel(0) was synthesized as previously reported. Deuterated solvents were purchased from Cambridge Isotopes

Laboratories, Inc. Solvents used for air and/or water sensitive reactions (THF, toluene, pentane, ether) were dried by passage through two columns of alumina and degassed by argon purge in a custom-built solvent purification system. ^{1}HNMR spectra were obtained on a Varian VNMRS 500 MHz or 600 MHz spectrometer. GPC chromatographs were obtained using a Waters 2690 Separation Module with two Agilent PLGEL 5µm, MIXED-D columns running $CHCl_3$/0.25% triethylamine as eluent. MALDI spectra were obtained on a Bruker Microflex series MALDI-TOF using a matrix of dithranol saturated chloroform.

2. Detailed Synthetic Procedures

Synthesis of (dppe)Ni(triisopropylsilylethynylbenzene)bromide, 2

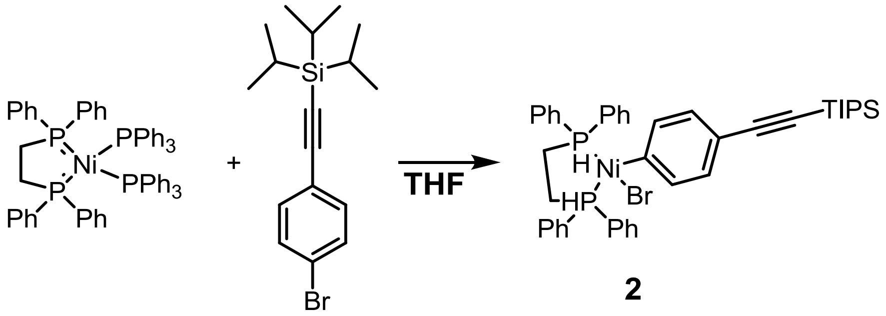

Scheme S1-1. Synthesis of (dppe)Ni(TIPS-ethynylbenzene)bromide.

In a nitrogen-filled glovebox, (dppe)Ni(PPh_3)$_2$ (0.200g, 0.204 mmol) was dissolved in dry THF (0.95 mL). 1-bromo-4-(triisopropylsilylethynyl)benzene (2.751g, 8.149 mmol) was added slowly via syringe to the stirring solution. The reaction mixture was allowed to stir for 48 hours. Then the solvent was evaporated off under reduced pressure. The resulting solid was fully precipitated with pentane (~25mL), filtered, and dried under vacuum. For purification, the solid was dissolved in a minimum amount of toluene (~250µL) and reprecipitated with pentane (~25mL). The solid was recovered by filtration and dried under vacuum. The resulting orange solid, **2** (0.0994g, 61%) was stored at -35°C.

^{1}HNMR (600 MHz, C_6D_6) δ (ppm): 8.00 (t, 3H), 7.40 (t, 2H), 7.25 (dd, 4H), 7.10 (m, 6H), 7.00 (m, 1H), 6.95 (t, 2H), 6.85 (t, 3H), 1.70 (ddd, 2H), 1.20 (d, 14H), 1.15 (m, 3H).

Polymerization of 2,5-dibromo-3-hexylthiophene

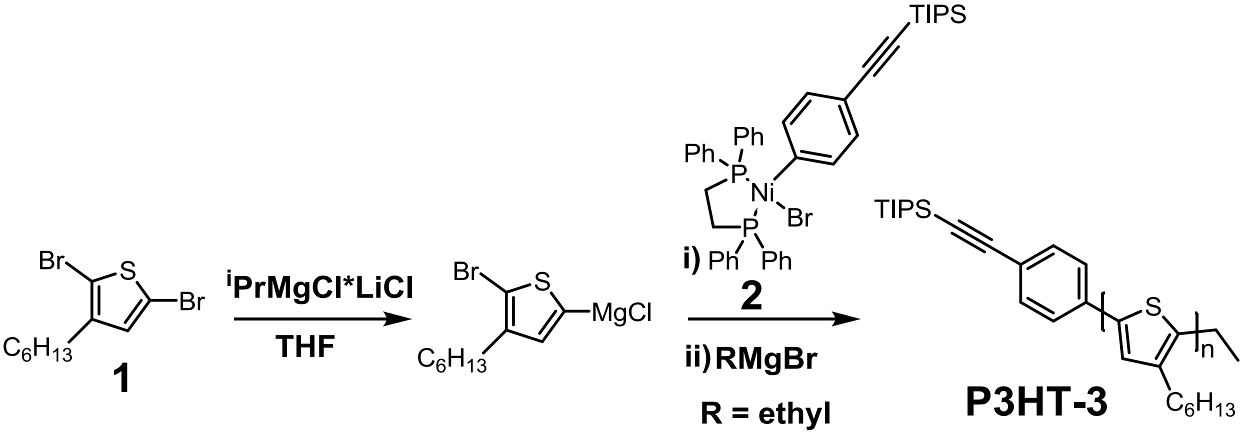

Scheme S1-2. Polymerization of 2,5-dibromo-3-hexylthiophene.

In a nitrogren-filled glovebox, 2,5-dibromo-3-hexylthiophene (0.473g, 1.45mmol) was dissolved in THF (3mL). Isopropyl magnesium chloride-lithium chloride complex (1.08mL, 1.3M in THF) was slowly added via syringe to the stirring solution. After 45 minutes, the reaction mixture was added to a stirring solution of **2** (0.046g, 0.0.058mmol, 10mL of THF) in one shot. The polymerization was allowed to proceed for 3 minutes before being quenched by ethyl magnesium bromide (0.58mL, 1M in THF). The reaction mixture was allowed to stir for 2 hours in the glovebox before being removed and quenched with methanol. The polymer was precipitated with ~50mL of methanol and centrifuged. The supernant was discarded and the polymer was washed twice with methanol (~50mL). The resulting polymer was dried under vacuum to give a black solid, P3HT-**3** (0.190g, 79%) GPC: M_n = 6400, M_w = 8700, $Đ$ = 1.37. ^{1}HNMR (600MHz, $CDCl_3$) δ (ppm): 7.5 (d, 0.06H), 7.45 (d, 0.06H), 6.95 (s, 1H), 2.8 (t, 2H), 1.7 (t, 2H), 1.4 (t, 2H), 1.3 (t, 4H), 1.15 (s, 0.58H), 0.9 (t, 3H). ^{13}CNMR (600 MHz, $CDCl_3$) δ (ppm): 140.5, 134.5, 131.0, 128.5, 31.5, 30.5, 29.5, 29.3, 22.5, 14.0.

Removal of triisopropylsilyl-protecting group from terminal alkyne of P3HT-3

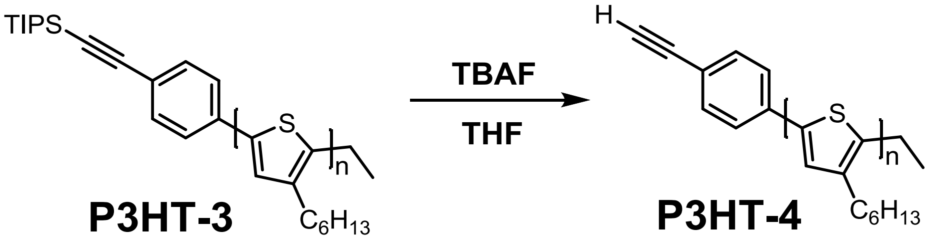

Scheme S1-3. Deprotection of P3HT-3.

P3HT-**3** (0.050g, 0.0061mmol) was dissolved in THF (1.0mL) under an argon atmosphere. TBAF (0.07mL, 1M in THF) was added slowly via syringe. The reaction was allowed to proceed for about 15 hours. The polymer was precipitated in methanol (~50mL) and centrifuged. The supernant was discarded and the polymer was washed twice with methanol (~50mL). The resulting polymer was dried under vacuum to give a black solid, P3HT-**4** (0.041g, 84%, quantitative deprotection). $M_n = 6200$, $M_w = 8300$, Đ = 1.34. ^{1}HNMR (600MHz, $CDCl_3$) δ (ppm): 7.5 (d, 0.08H), 7.45 (d, 0.08H), 6.95 (s, 1H), 3.1 (s, 0.04H), 2.8 (t, 2H), 1.7 (t, 2H), 1.4 (t, 2H), 1.3 (t, 4H), 0.9 (t, 3H). ^{13}CNMR (600 MHz, $CDCl_3$) δ (ppm): 140.5, 134.5, 131.0, 128.5, 31.5, 30.5, 29.5, 29.3, 22.5, 14.0.

PCBM reduction to compound **6**

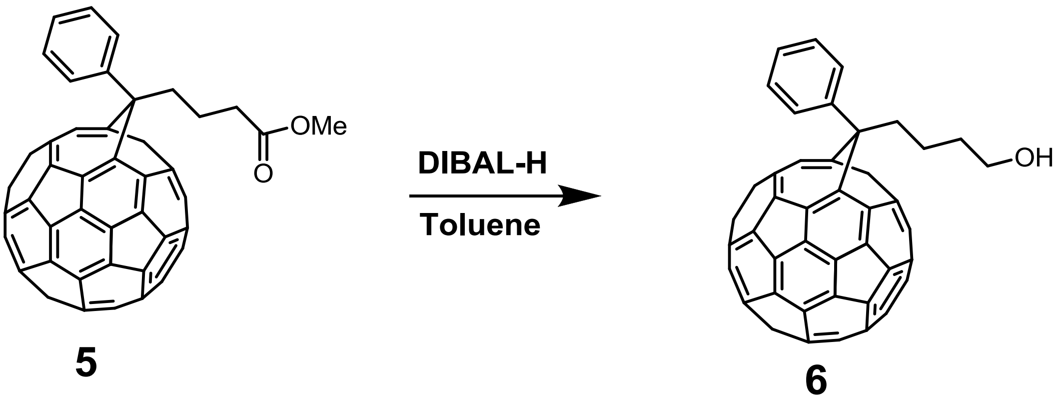

Scheme S1-4. PCBM reduction to compound **6**.

6 was synthesized according to literature methods.[120] Under a nitrogen atmosphere, PCBM, **5** (0.325 mmol, 1 eq) was dissolved in dry toluene (100 mL). The reaction flask was cooled to 0°C. DIBAL-H (1 M in hexanes, 0.71 mmol, 3 eq.) was added slowly via syringe. The reaction was allowed to warm to room temperature and stirred for 24 hours. The reaction was quenched with a saturated solution of NH_4Cl (10 mL). The organic layer was washed three times with brine, dried over sodium sulfate and the solvent removed under reduced pressure. The product was purified using column chromatography on silica gel with 9:1 toluene to ethyl acetate as the eluent. **6** was produced with a yield of 70%. ^{1}HNMR (500 MHz, $CDCl_3$) δ (ppm): 7.93 (m, 2H), 7.55 (m, 2H), 7.48 (m, 1H), 3.74 (q, 2H), 2.90 (m, 2H), 1.92-1.98 (m, 2H), 1.78 (m, 2H). Calculated mass: 882.104, Found (MALDI): 883.848.

Synthesis of compound **7**

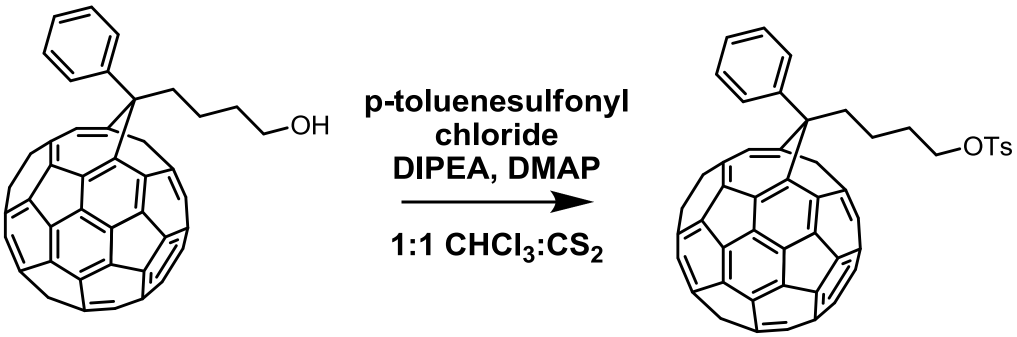

6

7

Scheme S1-5. Synthesis of compound **7**.

Under argon atmosphere, compound **6** (0.068 mmol, 1 eq.), p-toluenesulfonyl chloride (0.272 mmol, 4 eq.), and DMAP (0.068 mmol, 1 eq.) were dissolved in chloroform (1.50 mL) and carbon disulfide (1.50 mL). DIPEA (0.08 mL, 7 eq.) was added via syringe. The reaction was allowed to stir for 15 hours. The reaction mixture was diluted with dichloromethane and washed three times with water. The organic layer was dried over sodium sulfate and the solvent removed under reduced pressure. The product was purified using column chromatography on silica gel starting with an eluent mixture of 2:1 hexane to chloroform and ending with a mixture of 1:2 hexane to chloroform. **7** was produced with a yield of 60.%. ^{1}HNMR (500 MHz, $CDCl_3$) δ (ppm): 7.87 (m, 2H), 7.78 (d, 2H), 7.55 (m, 2H), 7.48 (m, 1H), 7.34 (d, 2H), 4.12 (m, 2H), 2.83 (m, 2H), 2.45 (s, 3H), 1.85 (m, 4H). Calculated mass: 1036.113, Found (MALDI): 1036.286.

Synthesis of compound **8**

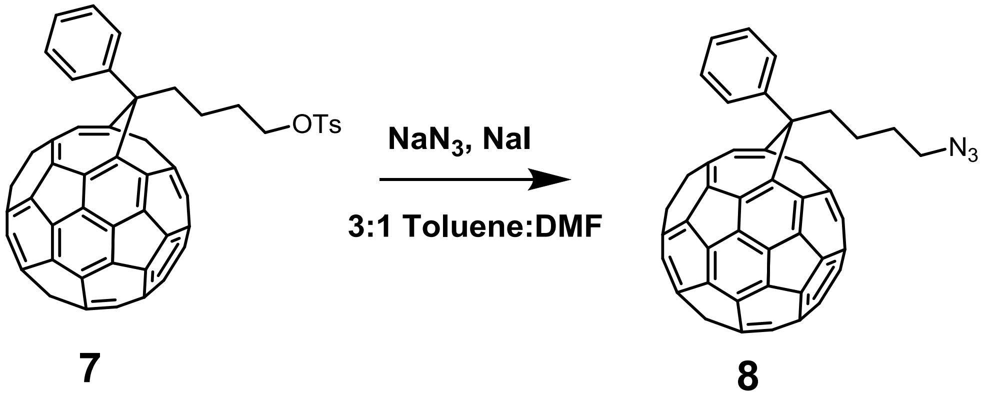

Scheme S1-6. Synthesis of compound **8**.

In a nitrogen-filled glovebox, **7** (0.0282 mmol, 1 eq.), sodium azide (0.282 mmol, 10 eq.), and sodium iodide (0.0563 mmol, 2 eq.) were dissolved in 3:1 toluene:DMF (2.2mL:0.7mL). The reaction mixture was removed from the nitrogen glovebox, heated to 50°C, and allowed to stir for 15 hours. The reaction was cooled to room temperature and diluted with carbon disulfide. The organic layer was washed three times with water and dried over sodium sulfate. The solvent was removed under reduced pressure to provide **8**. The instability of the product prevented further purification before use in the next step. ^{1}HNMR (500 MHz, $CDCl_3$) δ (ppm): 7.93 (d, 2H), 7.55 (t, 2H), 7.48 (t, 1H), 3.39 (m, 2H), 2.90 (m, 2H), 1.91 (m, 2H), 1.80 (m, 2H).

Click coupling of P3HT-4 and compound **8**

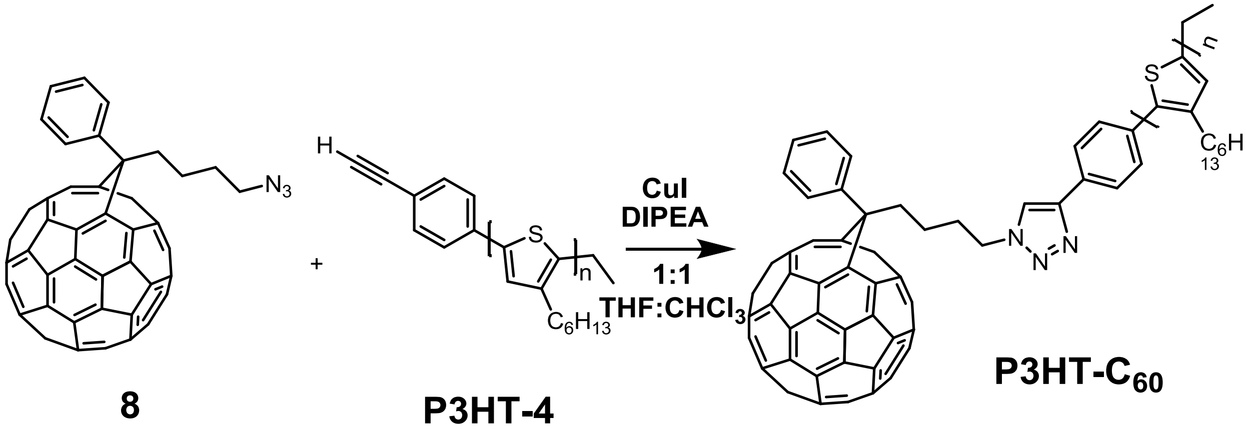

Scheme S1-7. Click coupling of P3HT-4 and compound **8**.

Under an argon atmosphere, P3HT-**4** (0.00563 mmol, 1 eq.), **8** (0.0282 mmol, 5 eq.), and copper iodide (0.113 mmol, 20 eq.) were dissolved in 1:1 THF:$CHCl_3$ (1mL:1mL). DIPEA (0.563 mmol, 100 eq.) was added via syringe. The reaction mixture was heated to 60°C and allowed to stir for 48 hours. The reaction mixture was cooled to room temperature. The product was precipitated with methanol and centrifuged. The supernant was discarded and the product was washed twice with methanol. The product was purified using column chromatography on silica gel with carbon disulfide as the eluent. The product stuck to the silica gel and was recovered by soxhlet extraction with chloroform. **P3HT-C_{60}** was produced as a black solid with a yield of 61%. ^{1}HNMR (600 MHz, $CDCl_3$) δ (ppm): 7.88 (d, 0.07H), 7.80 (d, 0.06H), 7.70 (s, 0.06H), 7.65 (d, 0.06H), 7.53 (d, 0.11H), 6.97 (s, 1H), 2.80 (t, 2H), 1.7 (t, 2H), 1.4 (t, 2H), 1.3 (t, 4H), 0.9 (t, 3H). GPC: M_n = 7700, M_w = 10,100, $Đ$ = 1.31.

Click coupling of P3HT-4 and Sulforhodamine 101 Azide

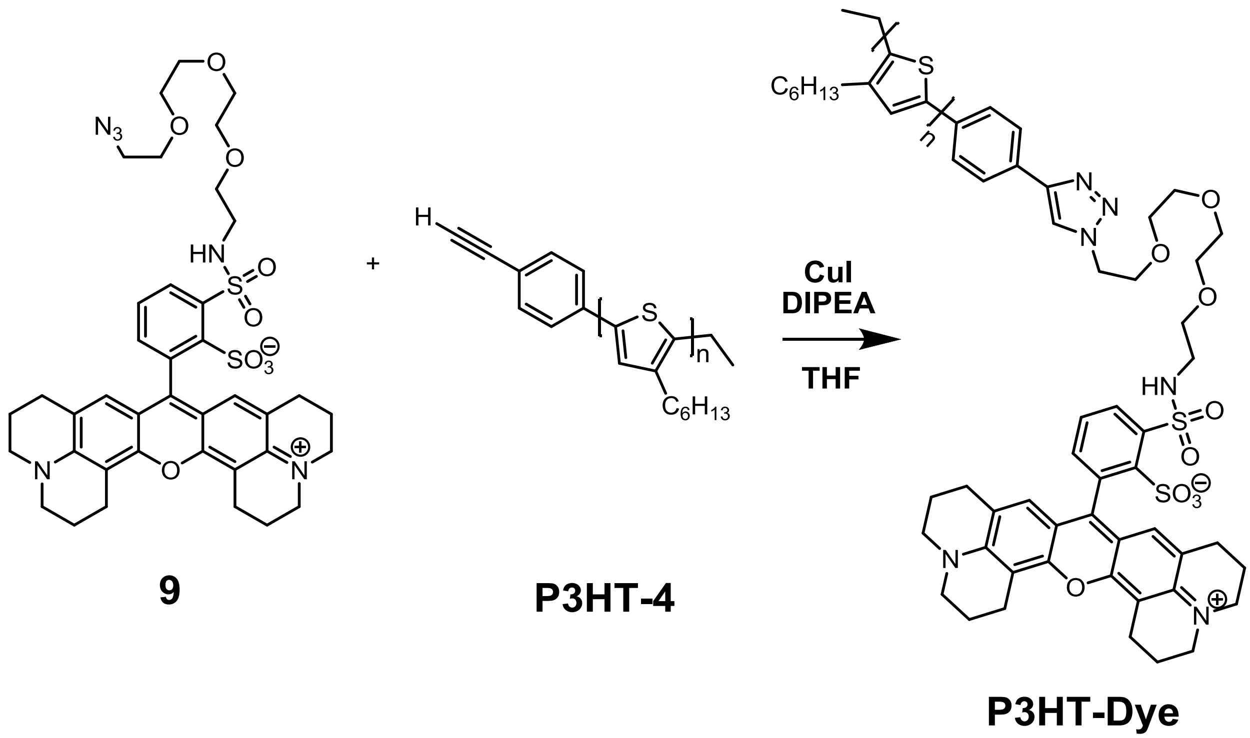

Scheme S1-8. Click coupling of P3HT-4 and Sulforhodamine 101 azide.

Under an argon atmosphere, P3HT-**4** (3.72×10^{-4} mmol, 1 eq.), azido-PEG3-sulforhodamine 101 conjugate (0.0019 mmol, 5 eq.), and copper iodide (0.0074 mmol, 20 eq.) were dissolved in THF. DIPEA (0.037 mmol, 100 eq.) was added via syringe. The reaction mixture was heated to 40°C and allowed to stir for 2.5 days. The reaction mixture was cooled to room temperature. The product was precipitated out with methanol and centrifuged. The supernant was discarded and the product was washed with methanol. **P3HT-Dye** was produced as a black solid with a yield of 69%. ^{1}HNMR (600 MHz, $CDCl_3$): 7.70 (s, 0.06H), 7.65 (d, 0.06H), 6.97 (s, 1H), 3.6 (t, 0.3H), 2.80 (t, 2H), 2.7 (dd, 0.24H), 1.9 (m, 0.24H), 1.7 (t, 2H), 1.6-1.5 (m, 0.24H) 1.4 (t, 2H), 1.3 (t, 4H), 0.9 (t, 3H).* MALDI spectrum reported in Figure S4b. Spectrum shows fragmentation with loss of SO_3^- group. GPC: $M_n = 7200$, $M_w = 9400$, $Đ = 1.30$. Peaks from single protons on the dye moiety were impossible to resolve due to limited quantity of material.

Click coupling of P3HT-4 and triethoxysilane-azide

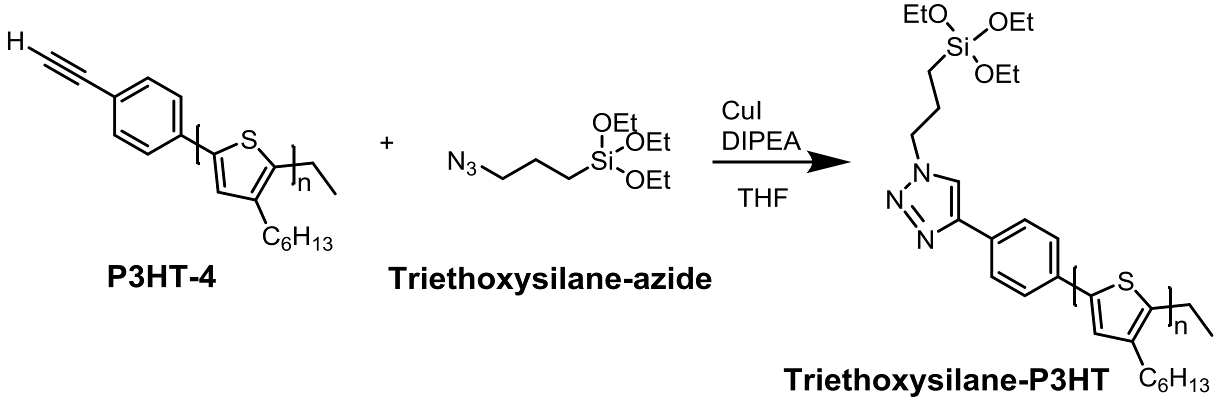

Scheme S1-9. Click coupling of P3HT-4 and triethoxysilane-azide.

Under an argon atmosphere, P3HT-**4** (0.019 mmol, 1 eq.), triethoxysilane-azide (0.093 mmol, 5 eq.), and copper iodide (0.056 mmol, 3 eq.) were dissolved in THF. DIPEA (0.56 mmol, 30 eq.) was added via syringe. The reaction mixture was heated to 40°C and allowed to stir for 2 days. The reaction mixture was cooled to room temperature. The product was precipitated out with ethyl acetate and centrifuged. The supernant was discarded and the product was washed with ethyl acetate. **Triethoxysilane-P3HT** was produced as a black solid with a yield of 81%. GPC: M_n = 8800, M_w = 9900, $Đ$ = 1.1. ^{1}HNMR (600MHz, $CDCl_3$) δ (ppm): 7.83 (d, 0.03H), 7.79 (s, 0.01H), 7.64 (d, 0.03H), 6.97 (s, 1H), 4.41 (t, 0.02), 3.82 (m, 0.07H), 2.8 (t, 2H), 1.7 (t, 2H), 1.4 (t, 2H), 1.3 (t, 4H), 0.9 (t, 3H), 0.64 (t, 0.05H).

Triethoxysilane-P3HT with a longer chain length

A procedure analogous to the one described above was followed to produce **Triethoxysilane-P3HT-2**. **Triethoxysilane-P3HT-2** was obtained at a longer chain length than **Triethoxysilane-P3HT** by increasing the monomer-to-catalyst ratio during the initial polymerization step from 40:1 to 80:1.

P3HT-3-2: M_n = 11,800, M_w = 16,500, $Đ$ = 1.4.

P3HT-4-2: M_n = 11,200, M_w = 15,800, $Đ$ = 1.4.

Triethoxysilane-P3HT-2: M_n = 10,600, M_w = 15,900, $Đ$ = 1.5.

Click Coupling of P3HT-4 and azide-terminated PEG

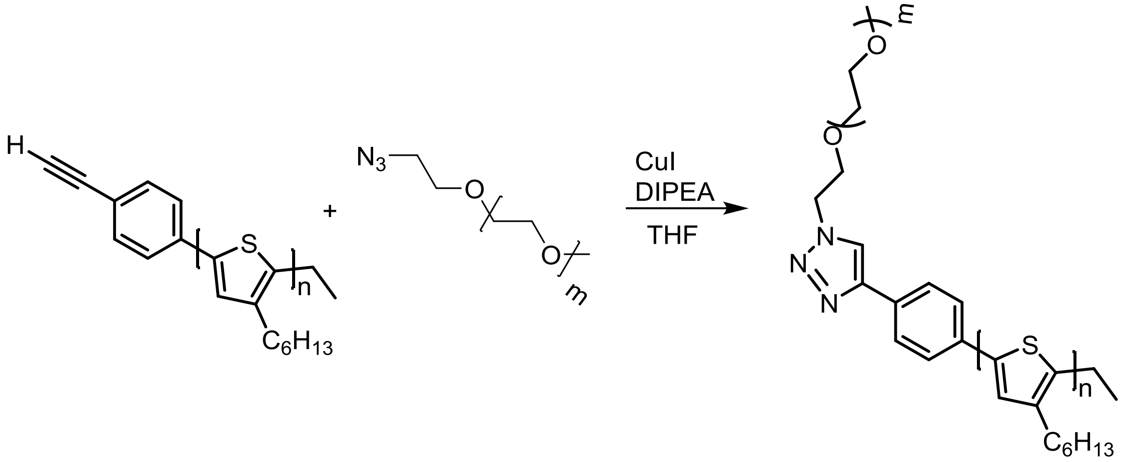

Scheme S1-10. Click coupling of P3HT-4 and azide-terminated PEG.

Polymer **3** (0.065g, 0.0102mmol), PEG-azide (0.102g, 0.102mmol), and copper iodide (0.0059g, 0.0309mmol) were dissolved in THF (4.5mL) under an argon atmosphere. DIPEA (0.054mL, 0.309mmol) was added via syringe. The reaction mixture was heated to 40°C and allowed to stir for 48 hours. After cooling to room temperature, the polymer was precipitated with methanol (~50mL) and centrifuged. The supernant was discarded and the polymer was washed twice with methanol (~50 mL). The polymer was dried under vacuum to yield a black solid, **4** (0.055g, 83%) M_n = 8300, M_w = 10k, PDI = 1.22. ^{1}HNMR (600MHz, $CDCl_3$) δ (ppm): 8.0 (s, 0.02H), 7.85 (d, 0.04H), 7.6 (d, 0.04H), 6.95 (s, 1H), 4.6 (t, 0.04H), 3.9 (t, 0.04H), 3.7-3.6 (t, 4H), 3.35 (s, 0.12H), 2.8 (t, 2H), 1.7 (t, 2H), 1.4 (t, 2H), 1.3 (t, 4H), 0.9 (t,3H). ^{13}CNMR (600 MHz, $CDCl_3$) δ (ppm): 140.5, 134.5, 131.0, 128.5, 70.5, 70.5, 31.5, 30.5, 29.5, 29.3, 22.5, 14.0.

3. Additional Spectra and Graphs

^{1}HNMR Spectra

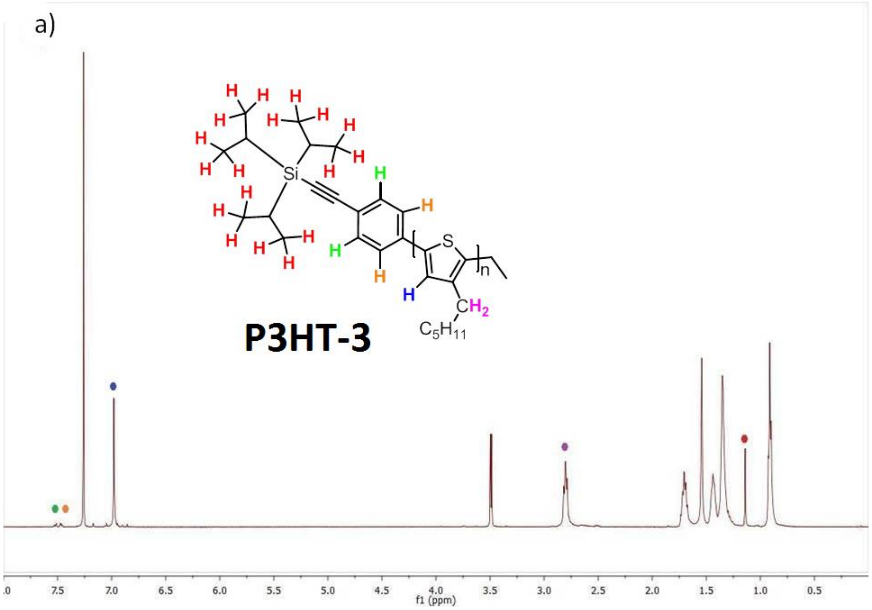

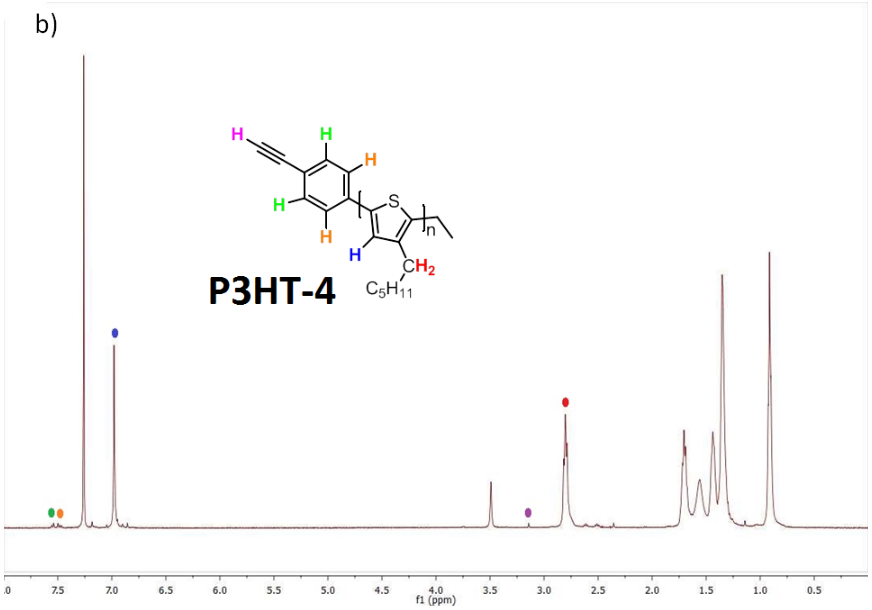

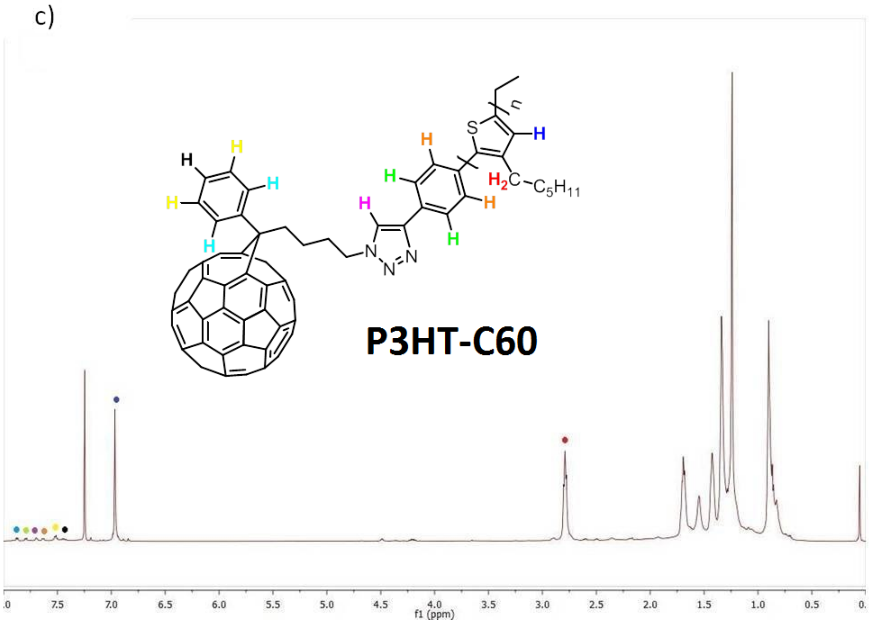

Figure S1-1. ^{1}HNMR spectra of a) P3HT-3, b) P3HT-4, and c) P3HT-C_{60}.

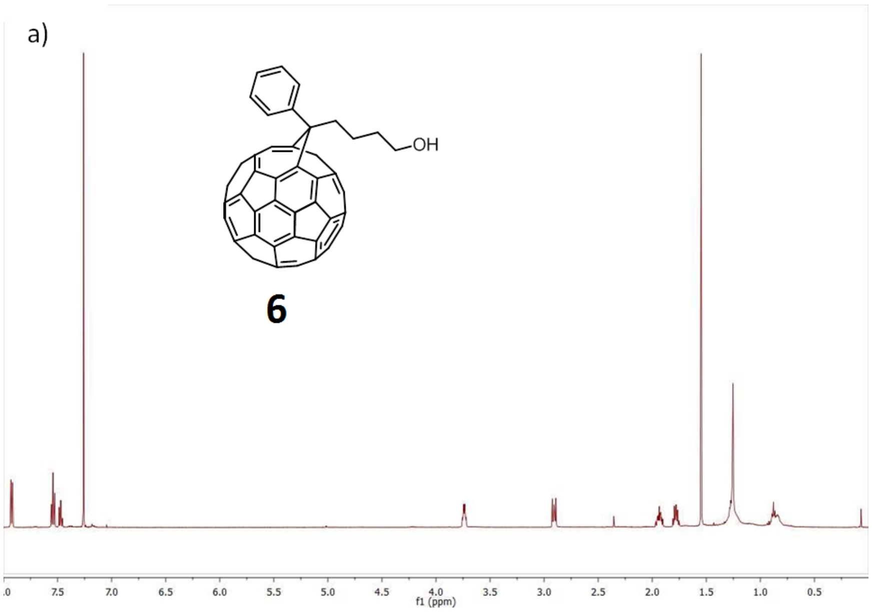

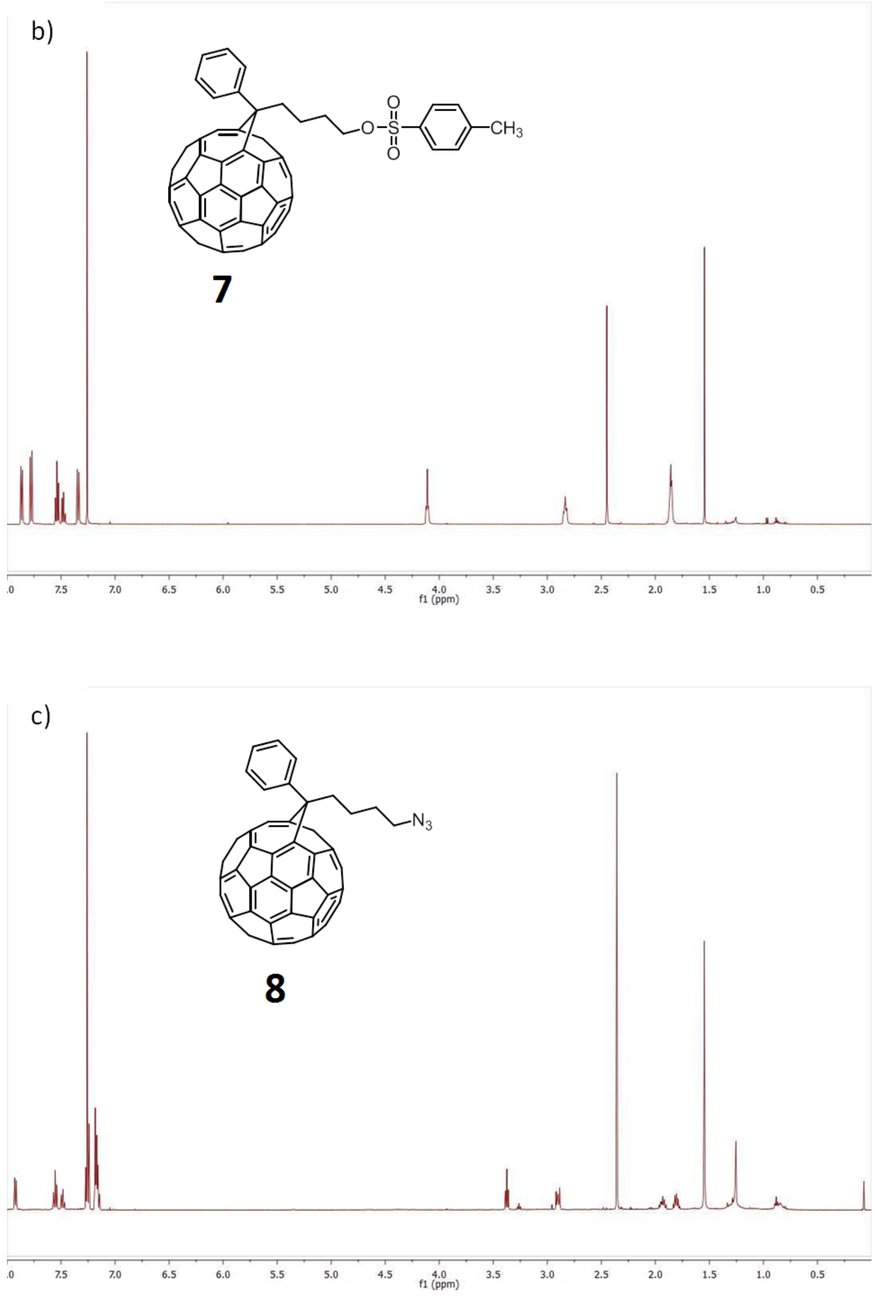

Figure S1-2. ^{1}HNMR spectra of PCBM derivatives.

MALDI Spectra

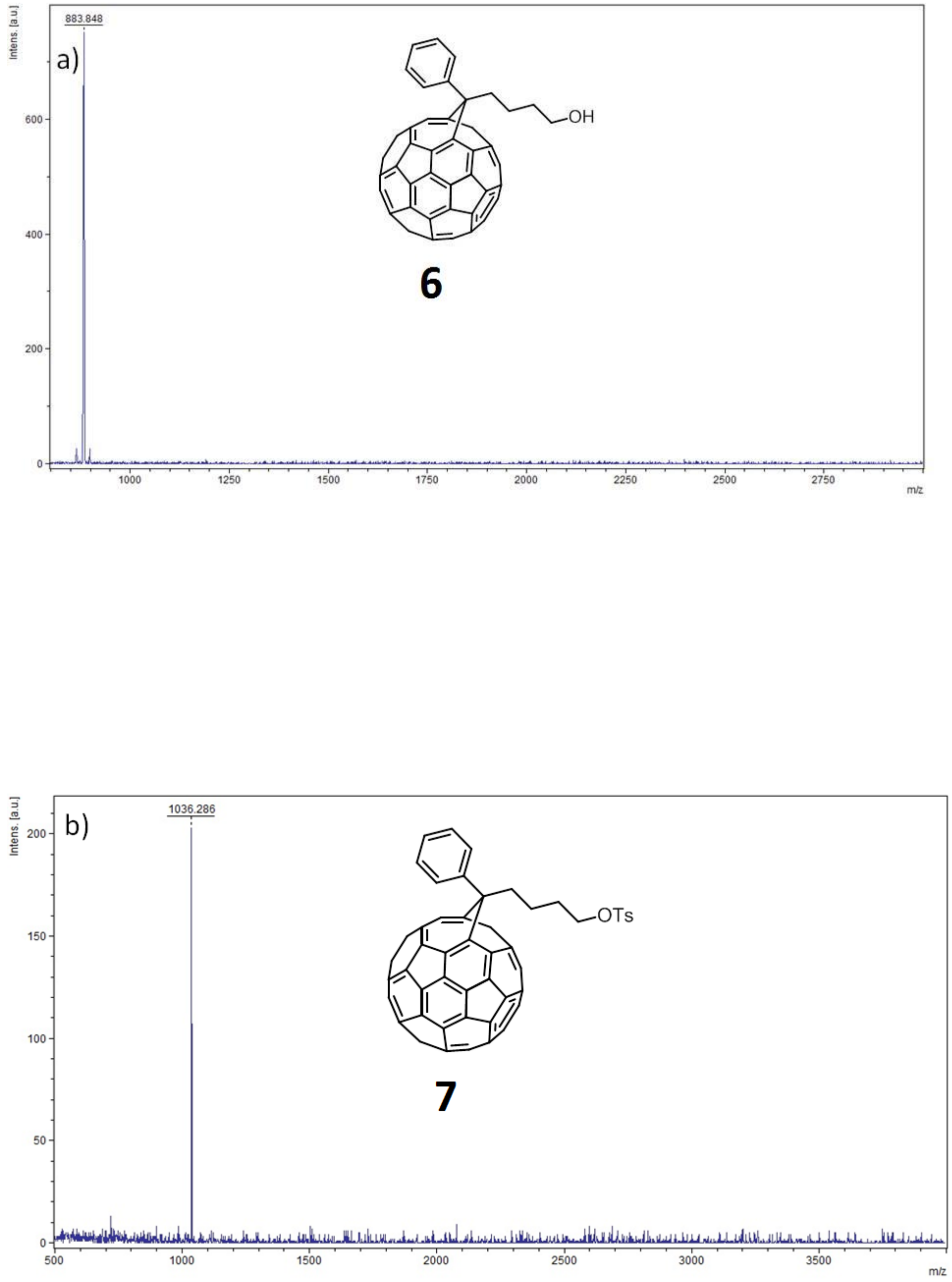

Figure S1-3. MALDI spectra of PCBM derivatives.

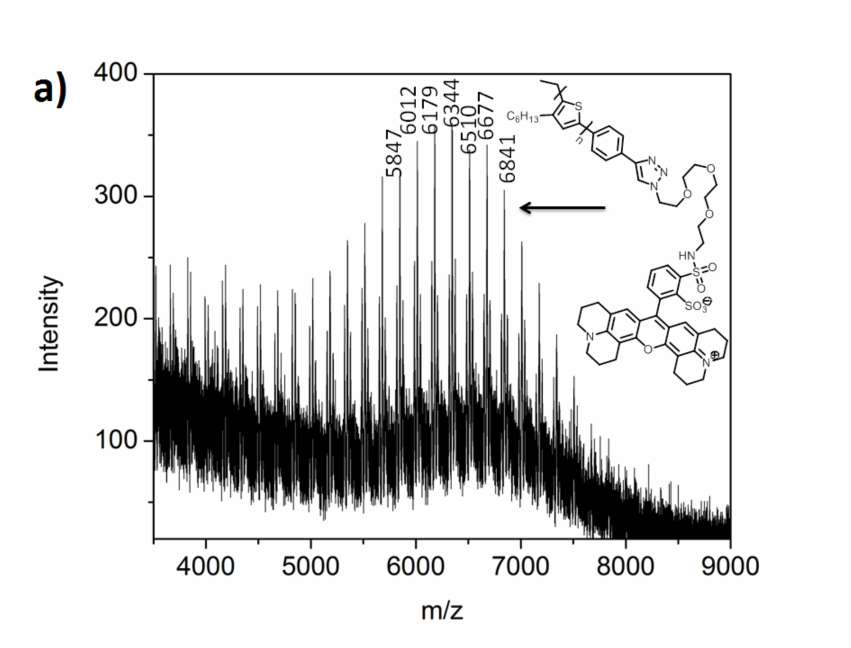

Figure S1-4. MALDI spectrum of P3HT-Dye.

UV-Vis Absorption Spectra

Absorption spectra were measured using a Perkin Elmer Lambda 750 UV/Vis Spectrometer containing a STD detection module. Solvents for solution spectra were used without further purification. Solutions were measured in 10 nm path length quartz cuvettes. Solutions were prepared in THF, THF:MeOH (8:2), and THF:MeOH (1:1) at a concentration of 0.75μM, unless otherwise specified. Thin films were fabricated using spin-coating in air at room temperature by depositing 30 μL of solution on a clean quartz substrate and spinning for 60 seconds at 2500 rpm.

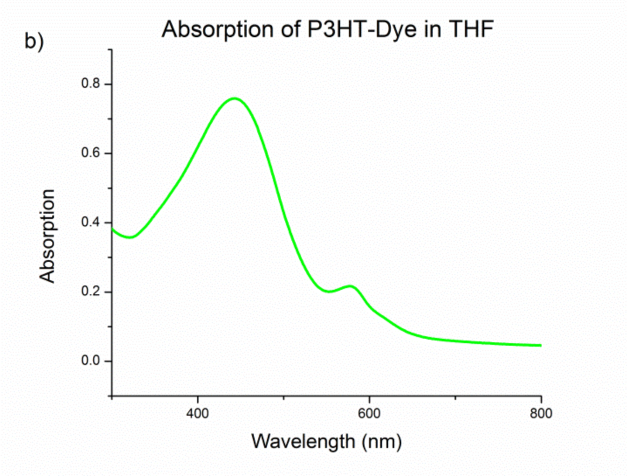

Figure S1-5. Optical absorption spectrum of P3HT-Dye in THF.

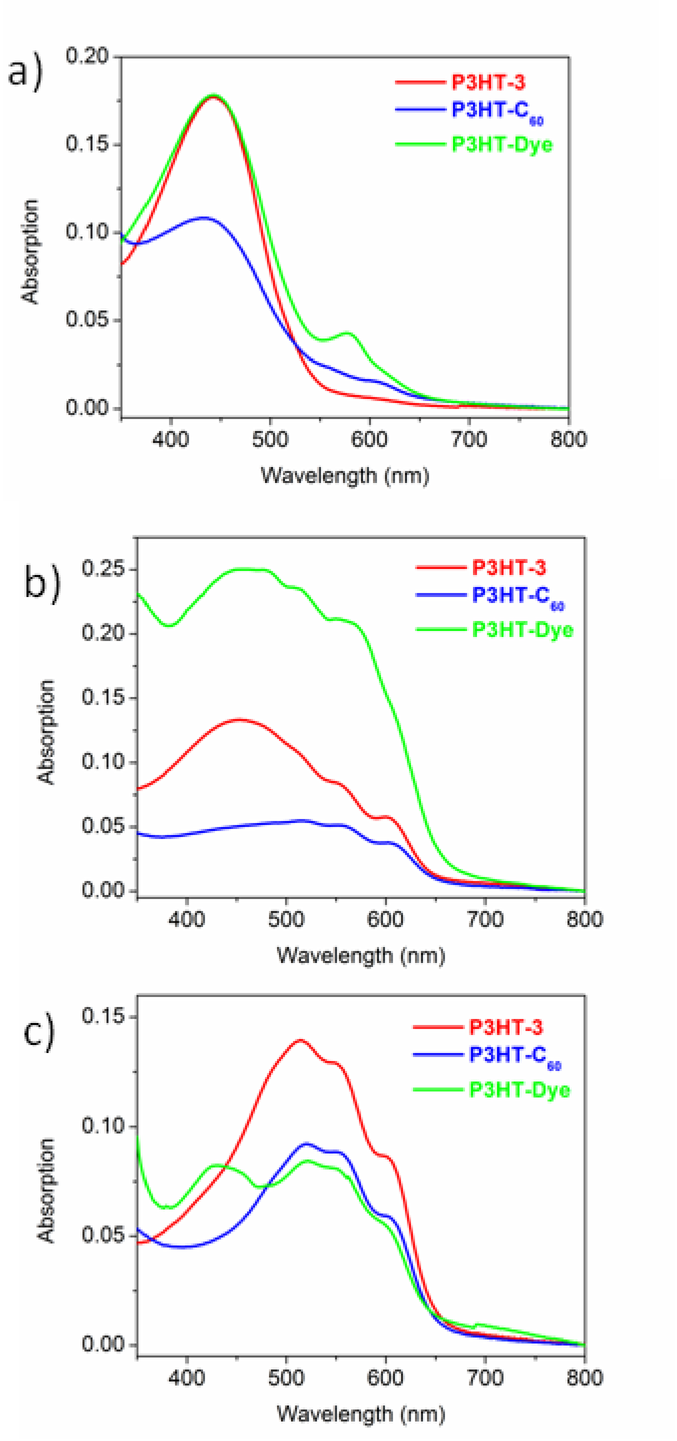

Figure S1-6. Absorption spectra of P3HT-**3**, **P3HT-C$_{60}$**, and **P3HT-Dye** in a) THF, b) THF:MeOH (8:2), and c) THF:MeOH (1:1). All measurements were taken with a concentration of 0.75 μM at room temperature.

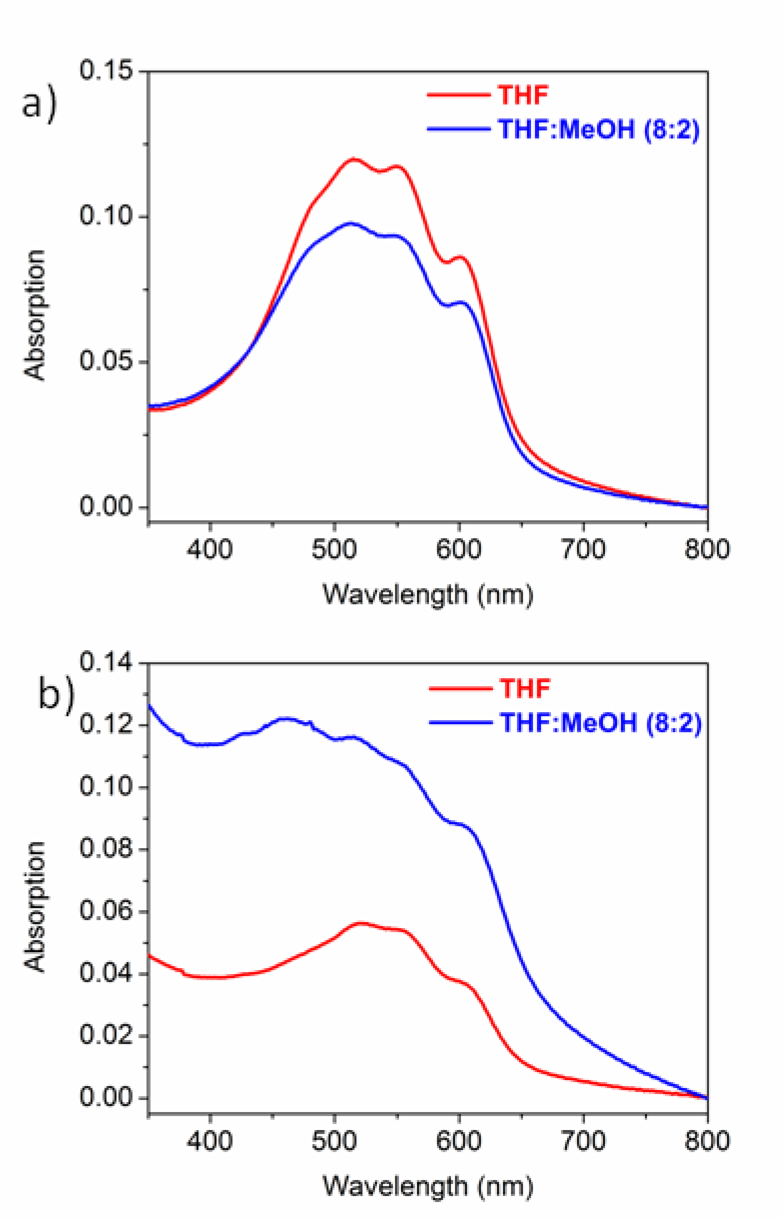

Figure S1-7. Absorption spectra of thin films of a) P3HT-**3** and b) **P3HT-C$_{60}$** drop-cast from 20 mg/mL solutions in THF (red) and THF:MeOH (8:2) (blue).

Photoluminescence Spectroscopy

Photoluminescence spectra were recorded on a PTI fluorimeter equipped with a Xenon lamp excitation source. Solvents were used without further purification. Solutions were measured in 10 nm path length quartz cuvettes. Solutions were prepared in THF at a concentration of 0.75μM. The excitation wavelength used was 450 nm for each spectrum.

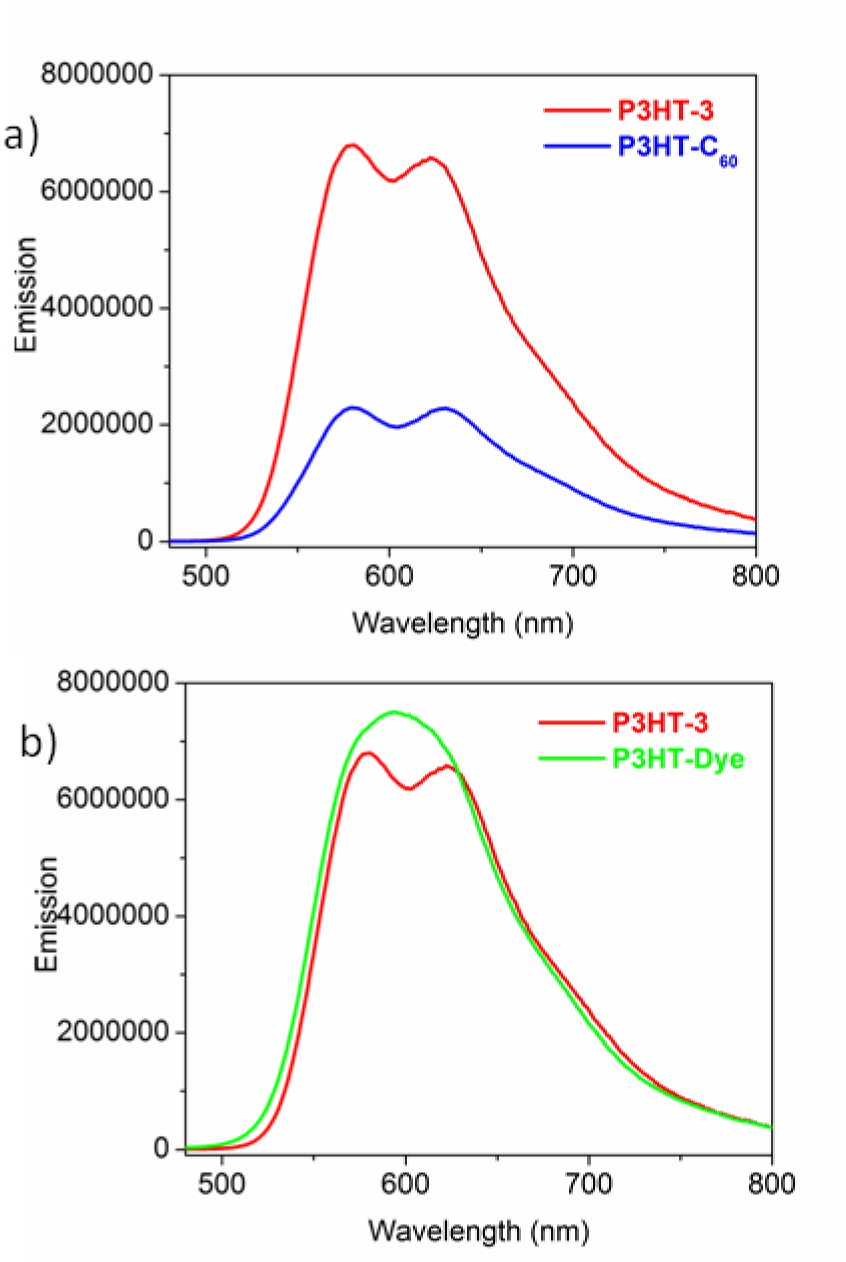

Figure S1-8. Emission spectra of THF solutions of a) P3HT-**3** compared to **P3HT-C$_{60}$** and b) P3HT-**3** compared to **P3HT-Dye**. All solutions were measured at a concentration of 0.75μM. The excitation wavelength was 450 nm for each emission spectrum.

Dynamic Light Scattering (DLS)

Dynamic light scattering measurements were taken using a DynaPro NanoStar with Dynamics software for data collection and analysis from Wyatt Technology. Measurements were carried out using a He-Ne laser at a wavelength of 658 nm at room temperature. The concentration used for each sample was 0.1 mg/mL. An autocorrelation function is determined using the provided software to fit the data. The diffusion coefficient is extracted from the autocorrelation function such that the hydrodynamic radius is calculated using the Stokes-Einstein equation.

Grazing Incidence Wide Angle X-ray Scattering (GIWAXS)

GIWAXS experiments were performed at the Stanford Synchrotron Radiation Lightsource (SSRL) at beamline 11-3. Samples were prepared by spin coating solutions onto Si substrates. A MAR 2300 area detector was used for 2D diffraction pattern collection. The energy of the incident beam is 12.7 keV. The angle of incidence used was 0.12° and the sample-to-detector distance was 40 cm. Samples were kept in a helium atmosphere to minimize X-ray damage and background scattering.

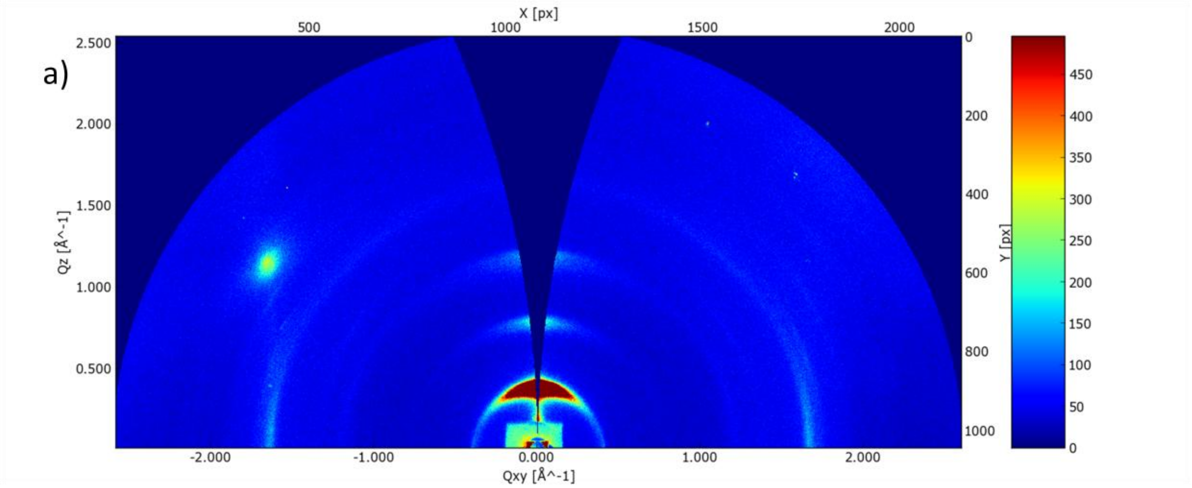

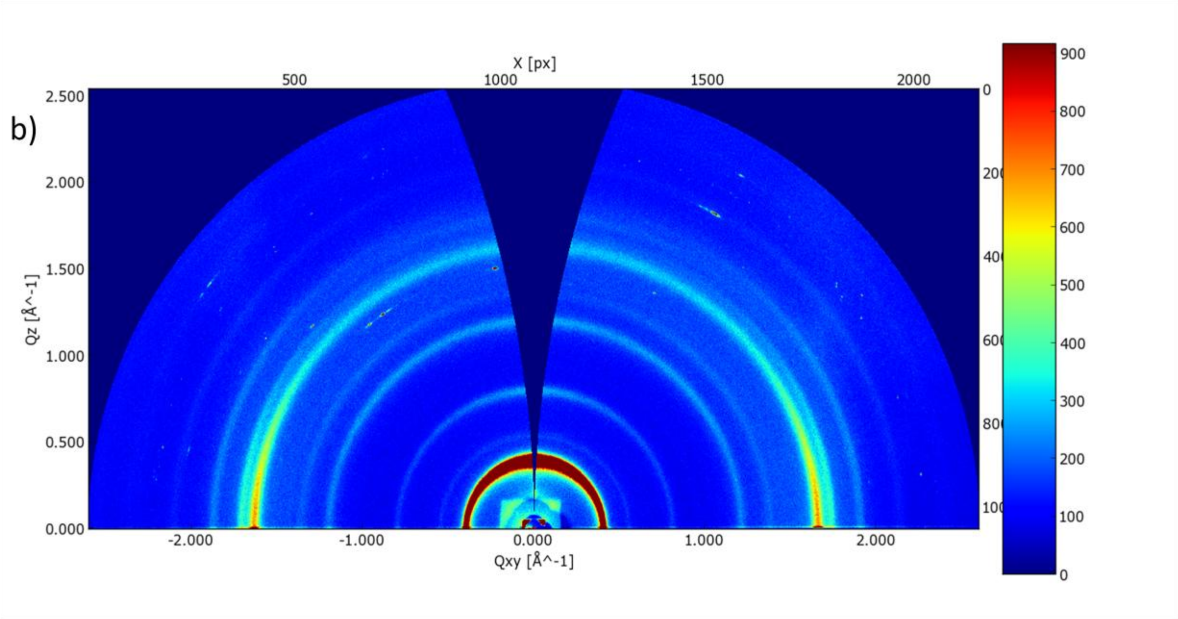
b)
X [px]
500
1000
1500
2000
Qz [Å^-1]
2.500
2.000
1.500
1.000
0.500
0.000
Qxy [Å^-1]
-2.000
-1.000
0.000
1.000
2.000
900
800
700
600
500
400
300
200
100
0

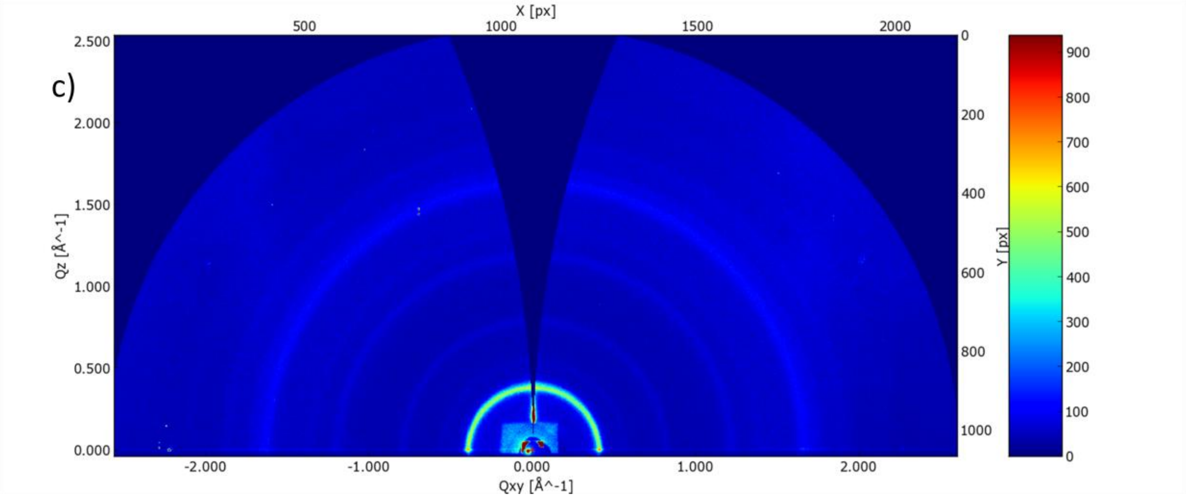
c)
X [px]
500
1000
1500
2000
Y [px]
0
200
400
600
800
1000
Qz [Å^-1]
2.500
2.000
1.500
1.000
0.500
0.000
Qxy [Å^-1]
-2.000
-1.000
0.000
1.000
2.000
900
800
700
600
500
400
300
200
100
0

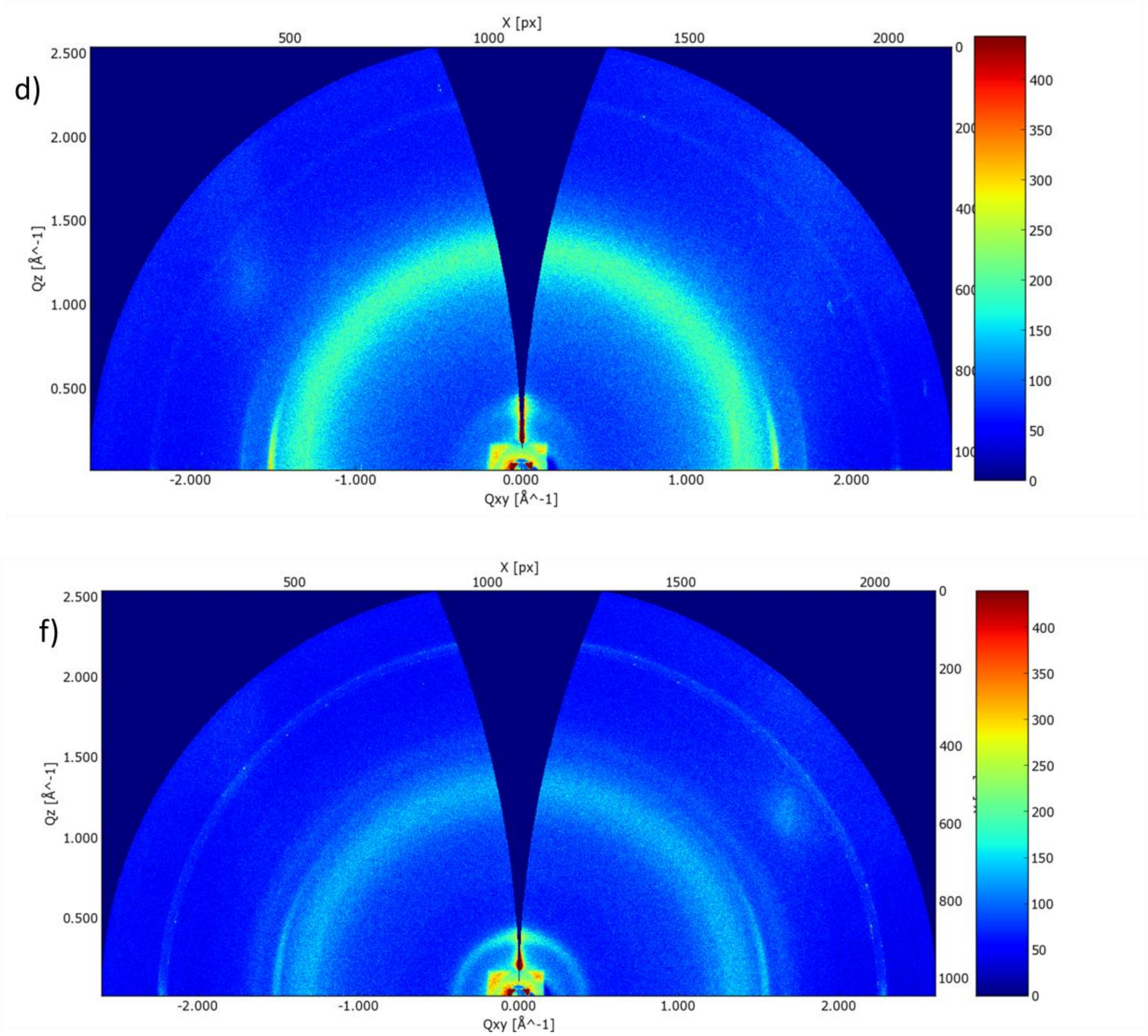

Figure S1-9. GIWAXS patterns for P3HT-**3** films drop-cast from 5 mg/mL solutions in a) THF, b) THF:MeOH (8:2), c) THF:MeOH (1:1) and **P3HT-C$_{60}$** films drop-cast from 5 mg/mL solutions in d) THF, e) THF:MeOH (8:2), and f) THF:MeOH (1:1).

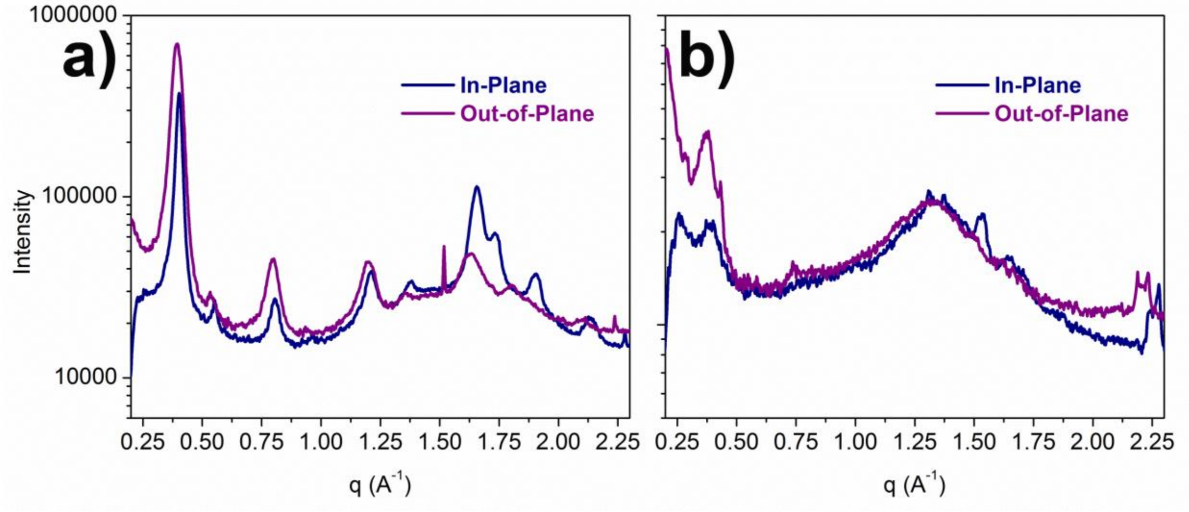

Figure S1-10. GIWAXS profiles for a) P3HT-**3** films drop-cast from 5 mg/mL solutions in THF:MeOH (8:2) and b) **P3HT-C$_{60}$** films drop-cast from 5 mg/mL solutions in THF:MeOH (8:2).

G. References

1. Reese, C., Roberts, M., Ling, M.-M., Bao, Z. Organic Thin Film Transistors. *Materials Today*, **2004**, 20-27.

2. Klauk, H. Organic Thin Film Transistors. *Chem. Soc. Rev.* **2010**, *39*, 2643-2666.

3. Yi, Z., Wang, S., Liu, Y. Design of High Mobility Diketopyrrolopyrrole-Based π-Conjugated Copolymers for Organic Thin Film Transistors. *Adv. Mater.* **2015**, *27*, 3589-3606.

4. Newman, C. R., Frisbie, C. D., Filho, D. A. S., Bredas, J.-L., Ewbank, P. C., Mann, K. R. Introduction to Organic Thin Film Transistors and Design of n-Channel Organic Semiconductors. *Chem. Mater.* **2004**, *16*, 4436-4451.

5. Holliday, S., Donaghey, J. E., McCulloch, I. Advances in Charge Carrier Mobilities of Semiconducting Polymers Used in Organic Transistors. *Chem. Mater.* **2004**, *26*, 647-663.

6. Dong, H., Fu, X., Liu, J., Wang, Z., Hu, W. 25th Anniversary Article: Key Points for High-Mobility Field-Effect Transistors. *Adv. Mater.* **2013**, *25*, 6158-6183.

7. Sirringhaus, H. 25th Anniversary Article: Field-Effect Transistors: The Path Beyond Amorphous Silicon. *Adv. Mater.* **2014**, *26*, 1319-1335.

8. Xu, R.-P., Li, Y.-Q., Tang, J.-X. Recent Advances in Flexible Organic Light-Emitting Diodes. *J. Mater. Chem. C*, **2016**, *4*, 9116-9142.

9. Wong, M. Y., Zysman-Colman, E. Purely Organic Thermally Activated Delayed Fluorescence Materials for Organic Light-Emitting Diodes. *Adv. Mater.* **2017**, DOI: 10.1002/adma.201605444.

10. Thejokalyani, N., Dhoble, S. J. Novel Approaches for Energy Efficient Solid State Lighting by RGB Organic Light-Emitting Diodes – A Review. *Renew.Sust. Energ. Rev.* **2014**, *32*, 448-467.

11. Wang, J., Zhang, F., Zhang, J., Tang, W., Tang, A., Pang, H., Xu, Z., Teng, F., Wang, Y. Key Issues and Recent Progress of High Efficient Organic Light-Emitting Diodes. *J. Photoch. Photobio. C*, **2013**, *17*, 69-104.

12. Im, Y., Kim, M., Cho, Y. J., Seo, J.-A., Yook, K. S., Lee, J. Y. Molecular Design Strategy of Thermally Activated Delayed Fluorescence Emitters. *Chem. Mater.* **2017**, *29*, 1946-1963.

13. Burroughes, J. H., Bradley, D. D. C., Brown, A. R., Marks, R. N., Mackay, K., Friend, R. H., Burns, P. L., Holmes, A. B. Light-Emitting Diodes Based on Conjugated Polymers. *Nature*, **1990**, *347*, 539-541.

14. Gunes, S., Neugebauer, H., Sariciftci, N. S. Conjugated Polymer-Based Organic Solar Cells. **2007**, *107*, 1324-1338.

15. Dou, L., You, J., Hong, Z., Xu, Z., Li, G., Steet, R. A., Yang, Y. 25th Anniversary Article: A Decade of Organic/Polymeric Photovoltaic Research. *Adv. Mater.* **2013**, *25*, 6642-6671.

16. Li, G., Zhu, R., Yang, Y. Polymer Solar Cells. *Nat. Photonics*, **2012**, *6*, 153-161.

17. Lu, L., Zheng, T., Wu, Q., Schneider, A. M., Zhao, D., Yu, L. Recent Advances in Bulk Heterojunction Polymer Solar Cells. *Chem. Rev.* **2015**, *115*, 12666-12731.

18. Leclerc, M., Morin, J.-F. (Eds.) *Design and Synthesis of Conjugated Polymers*. Wiley-VCH: Weinheim, Germany (**2010**).

19. Skotheim, T. A., Reynolds, J. R. (Eds.) *Conjugated Polymers: Theory, Synthesis, Properties, and Characterization*. CRC Press: Boca Raton (**2006**).

20. Li, Y. Molecular Design of Photovoltaic Materials for Polymer Solar Cells: Toward Suitable Electronic Energy Levels and Broad Absorption. *Accounts Chem. Res.* **2012**, *45*, 723-733.

21. Barford, W. (Eds.) *Electronic and Optical Properties of Conjugated Polymers, 2nd Edition*. Oxford University Press: Oxford, UK (**2013**).

22. Zhou, H., Yang, L., You, W. Rational Design of High Performance Conjugated Polymers for Organic Solar Cells. *Macromolecules,* **2012**, *45*, 607-632.

23. Heremans, P., Cheyns, D., Rand, B. P. Strategies for Increasing the Efficiency of Heterojunction Organic Solar Cells: Material Selection and Device Architecture. *Accounts Chem. Res.* **2009**, *42*, 1740-1747.

24. Bredas, J.-L., Norton, J. E., Cornil, J., Coropceanu, V. Molecular Understanding of Organic Solar Cells: The Challenges. *Accounts Chem. Res.* **2009**, *42*, 1691-1699.

25. Clarke, T. M., Durrant, J. R. Charge Photogeneration in Organic Solar Cells. *Chem. Rev.* **2010**, *110*, 6736-6767.

26. Hoppe, H., Sariciftci, N. S. Organic Solar Cells: An Overview. *J. Mater. Res.* **2004**, *19*, 1924-1945.

27. Brabec, C. J., Sariciftci, N. S., Hummelen, J. C. Plastic Solar Cells. *Adv. Funct. Mater.* **2001**, *11*, 15-26.

28. Yao, Y., Dong, H., Hu, W. Charge Transport in Organic and Polymeric Semiconductors for Flexible and Stretchable Devices. *Adv. Mater.* **2016**, *28*, 4513-4523.

29. Coropceanu, V., Cornil, J., Filho, D. A. S., Olivier, Y., Silbey, R., Bredas, J.-L. Charge Transport in Organic Semiconductors. *Chem. Rev.* **2007**, *107*, 926-952.

30. Movaghar, B., Grunewald, M., Ries, B., Bassler, H., Wurtz, D. Diffusion and Relaxation of Energy in Disordered Organic and Inorganic Materials. *Phys. Rev. B,* **1986**, *33*, 5545-5554.

31. Zaumseil, J., Sirringhaus, H. Electron and Ambipolar Transport in Organic Field-Effect Transistors. *Chem. Rev.* **2007**, *107*, 1296-1323.

32. Fishchuk, I. I., Kadashchuk, A., Hoffmann, S. T., Athanasopoulos, S., Genoe, J., Bassler, H., Kohler, A. Unified Description for Hopping Transport in Organic Semiconductors Including Both Energetic Disorder and Polaronic Contributions. *Phys. Rev. B*, **2013**, *88*, 125202.

33. Zhang, K., Hu, Z., Sun, C., Wu, Z., Huang, F., Cao, Y. Toward Solution-Processed High-Performance Polymer Solar Cells: from Materials Design to Device Engineering. *Chem. Mater.* **2017**, *29*, 141-148.

34. Etxebarria, I.; Ajuria, J.; Pacios, R. Solution-Processable Polymeric Solar Cells: A Review on Materials, Strategies, and Cell Architectures to Overcome 10%. *Org. Electron.* **2015**, *19*, 34–60.

35. Kippelen, B.; Brédas, J.-L. Organic Photovoltaics. *Energy Environ. Sci.* **2009**, *2*, 251-261.

36. Xiao, S., Zhang, Q., You, W. Molecular Engineering of Conjugated Polymers for Solar Cells: An Updated Report. *Adv. Mater.* **2017**, DOI: 10.1002/adma.201601391.

37. Beaujuge, P. M., Frechet, J. M. J. Molecular Design and Ordering Effects in π-Functional Materials for Transistor and Solar Cell Applications. *J. Am. Chem. Soc.* **2011**, *133*, 20009-20029.

38. Mei, J., Bao, Z. Side Chain Engineering in Solution-Processable Conjugated Polymers. *Chem. Mater.* **2014**, *26*, 604-615.

39. Lei, T., Wang, J.-Y., Pei, J. Roles of Flexible Chains in Organic Semiconducting Materials. *Chem. Mater.* **2014**, *26*, 594-604.

40. Schwartz, B. J. Conjugated Polymers as Molecular Materials: How Chain Conformation and Film Morphology Influence Energy Transfer and Interchain Interactions. *Annu. Rev. Phys. Chem.* **2003**, *54*, 141-172.

41. Duan, C., Willems, R. E. M., van Franeker, J. J., Bruijnaers, B. J., Wienk, M. M., Janssen, R. A. J. Effect of Side Chain Length on Charge Transport, Morphology, and Photovoltaic Performance of Conjugated Polymers in Bulk Heterojunction Solar Cells. *J. Mater. Chem. A*, **2016**, *4*, 1855-1866.

42. Fall, S., Biniek, L., Odarchenko, Y., Anokhin, D. V., de Tournadre, G., Leveque, P., Leclerc, N., Ivanov, D. A., Simonetti, O., Giraudet, Heiser, T. Tailoring the Microstructure and Charge Transport in Conjugated Polymers by Alkyl Side-Chain Engineering. *J. Mater. Chem. C*, **2016**, *4*, 286-294.

43. Wang, X., Deng, W., Chen, Y., Wang, X., Ye, P., Wu, X., Yan, C., Zhan, X., Liu, F., Huang, H. Fine-Tuning Solid State Packing and Significantly Improving Photovoltaic Performance of Conjugated Polymers Through Side Chain Engineering via Random Polymerization. *J. Mater. Chem. A*, **2017**, *5*, 5585-5593.

44. Dang, M. T., Hirsch, L., Wantz, G. P3HT:PCBM, Best Seller in Polymer Photovoltaic Research. *Adv. Mater.* **2011**, *23*, 3597-3602.

45. Dennler, G., Scharber, M. C., Brabec, C. J. Polymer-Fullerene Bulk Heterojunction Solar Cells. *Adv. Mater.* **2009**, *21*, 1323-1338.

46. Dang, M. T., Hirsch, L., Wantz, G., Wuest, J. D. Controlling the Morphology and Performance of Bulk Heterojunctions in Solar Cells. Lessons Learned from the Benchmark Poly(3-hexylthiophene):[6,6]-Phenyl-C_{60}-butyric Acid Methyl Ester System. *Chem. Rev.* **2013**, *113*, 3734-3765.

47. Li, G., Shrotriya, V., Yao, Y., Huang, J., Yang, Y. Manipulating Regioregular Poly(3-hexylthiophene):[6,6]-Phenyl-C_{60}-butyric Acid Methyl Ester Blends – Route Toward Higher Efficiency Solar Cells. *J. Mater. Chem.* **2007**, *17*, 3126-3140.

48. Kleinschmidt, A. T., Root, S. E., Lipomi, D. J. Poly(3-hexylthiophene) (P3HT): Fruit Fly or Outlier in Organic Solar Cell Research? *J. Mater. Chem. A*, **2017**, DOI: 10.1039/C6TA08317J.

49. Schilinsky, P., Wauldauf, C., Brabec, C. J. Performance Analysis of Printed Bulk Heterojunction Solar Cells. *Adv. Funct. Mater.* **2006**, *16*, 1669-1672.

50. Hoth, C. N., Choulis, S. A., Schilinsky, P., Brabec, C. J. High Photovoltaic Performance of Inkjet Printed Polymer:Fullerene Blends. *Adv. Mater.* **2007**, *19*, 3973-3978.

51. McCullough, R. D., Williams, S. P., Tristram-Nagle, S., Jayaraman, M., Ewbank, P. C., Miller, L. The First Synthesis and New Properties of Regioregular, Head-to-Tail Coupled Polythiophenes. *Synth. Met.* **1995**, *69*, 279-282.

52. Loewe, R. S., Ewbank, P. C., Liu, J., Zhai, L., McCullough, R. D. Regioregular, Head-to-Tail Coupled Poly(3-alkylthiophenes) Made Easy by the GRIM Method: Investigation of the Reaction and the Origin of Regioselectivity. *Macromolecules*, **2001**, *34*, 4324-4333.

53. Kang, S., Ono, R. J., Bielawski, C. W. Synthesis of Poly(3-hexylthiophene)-*block*-Poly(ethylene)-*block*-Poly(3-hexylthiophene) via a Combination of Ring Opening Olefin Metathesis Polymerization and Gringard Metathesis Polymerization. *J. Polym. Sci. A1*, **2013**, *51*, 3810-3817.

54. Iraqi, A., Barker, G. W. Synthesis and Characterisation of Telechelic Regioregular Head-to-Tail Poly(3-alkylthiophenes). *J. Mater. Chem.* **1998**, *8*, 25-29.

55. Liversedge, I. A., Higgins, S. J., Giles, M., Heeney, M., McCulloch, I. Suzuki Route to Regioregular Polyalkylthiophenes Using Ir-Catalyzed Borylation to Make the Monomer and Pd Complexes of Bulky Phosphanes as Coupling Catalysts for Polymerization. *Tetrahedron Lett.* **2006**, *47*, 5143-5146.

56. Li, W., Han, Y., Li, B., Liu, C., Bo, Z. Tris[tri(2-thienyl)phosphine]palladium as the Catalyst Precursor for Thiophene-Based Suzuki-Miyaura Crosscoupling and Polycondensation. *J. Polym. Sci. Part A: Polym. Chem.* **2008**, *46*, 4556-4563.

57. Wang, Q., Takita, R., Kikusaki, Y., Ozawa, F. Palladium-Catalyzed Dehydrohalogenative Polycondensation of 2-Bromo-3-Hexylthiophene: An Efficient Approach to Head-to-Tail Poly(3-hexylthiophene). *J. Am. Chem. Soc.* **2010**, *132*, 11420-11421.

58. Amou, S., Haba, O., Shirato, K., Hayakawa, T., Ueda, M., Takeuchi, K., Asai, M. Head-to-Tail Regioregularity of Poly(3-hexylthiophene) in Oxidative Coupling Polymerization with $FeCl_3$. *J. Polym. Sci. Part A: Polym. Chem.* **1999**, *37*, 1943-1948.

59. Yu, S., Hayakawa, T., Ueda, M. Synthesis of Poly(3-hexylthiophene) by Using the $VO(acac)_2$-$FeCl_3$-O_2 Catalytic System. *Chem. Lett.* **1999**, 559-560.

60. Marrocchi, A., Lanari, D., Facchetti, A., Vaccaro, L. Poly(3-hexylthiophene): Synthetic Methodologies and Properties in Bulk Heterojunction Solar Cells. *Energy Environ. Sci.* **2012**, *5*, 8457-8474.

61. Mauer, R., Kastler, M., Laquai, F. The Impact of Polymer Regioregularity on Charge Transport and Efficiency of P3HT:PCBM Photovoltaic Devices. *Adv. Funct. Mater.* **2010**, *20*, 2085-2092.

62. Tsoi, W. C., Spencer, S. J., Yang, L., Ballantyne, A. M., Nicholson, P. G., Turnbull, A., Shard, A. G., Murphy, C. E., Bradley, D. D. C., Nelson, J., Kim, J.-S. Effect of Crystallization on Electronic Energy Levels and Thin Film Morphology of P3HT:PCBM Blends. *Macromolecules*, **2011**, *44*, 2944-2952.

63. Zhou, K., Liu, J., Zhang, R., Zhao, Q., Cao, X., Yu, X., Xing, R., Han, Y. The Molecular Regioregularity Induced Morphological Evolution of Polymer Blend Thin Films. *Polymer,* **2016**, *86*, 105-112.

64. Kiriy, A., Senkovskyy, V., Sommer, M. Kumada Catalyst-Transfer Polycondensation: Mechanism, Opportunities, and Challenges. *Macromol. Rapid Commun.* **2011**, *32*, 1503-1517.

65. Bronstein, H. A., Luscombe, C. K. Externally Initiated Regioregular P3HT with Controlled Molecular Weight and Narrow Polydispersity. *J. Am. Chem. Soc.* **2009**, *131*, 12894-12895.

66. Ono, R. J., Kang, S., Bielawski, C. W. Controlled Chain Growth Kumada Catalyst Transfer Polycondensation of Conjugated Alternating Copolymer. *Macromolecules*, **2012**, *45*, 2321-2326.

67. Verploegen, E., Mondal, R., Bettinger, C. J., Sok, S., Toney, M. F., Bao, Z. Effects of Thermal Annealing Upon the Morphology of Polymer-Fullerene Blends. *Adv. Funct. Mater.* **2010**, *20*, 3519-3529.

68. Thompson, B. C., Frechet, J. M. J. Polymer-Fullerene Composite Solar Cells. *Angew. Chem. Int. Ed.* **2008**, *47*, 58-77.

69. Scharsich, C., Lohwasser, R. H., Sommer, M., Asawapirom, U., Scherf, U., Thelakkat, M., Neher, D., Kohler, A. Control of Aggregate Formation in Poly(3-hexylthiophene) by Solvent, Molecular Weight, and Synthetic Method. *J. Polym. Sci. Part B: Polym. Phys.* **2012**, *50*, 442-453.

70. Li, L., Lu, G., Yang, X. Improving Performance of Polymer Photovoltaic Devices Using an Annealing-Free Approach via Construction of Ordered Aggregates in Solution. *J. Mater. Chem.* **2008**, *18*, 1984-1990.

71. Mihailetchi, V. D., Koster, L. J. A., Hummelen, J. C., Blom, P. W. M. *Phys. Rev. Lett.* **2004**, *93*, 216601.

72. Liu, X., Ding, K., Panda, A., Forrest, S. R. Charge Transfer States in Dilute Donor-Acceptor Blend Organic Heterojunctions. *ACS Nano*, **2016**, *10*, 7619-7626.

73. Hwang, I.-W., Moses, D., Heeger, A. J. Photoinduced Carrier Generation in P3HT/PCBM Bulk Heterojunction Materials. *J. Phys. Chem. C*, **2008**, *112*, 4350-4354.

74. Bakulin, A. A., Rao, A., Pavelyev, V. G., van Loosdrecht, P. H. M., Pshenichnivok, M. S., Niedzialek, D., Cornil, J., Beljonne, D., Friend, R. H. The Role of Driving Energy and Delocalized States for Charge Separation in Organic Semiconductors. *Science*, **2012**, *335*, 1340-1344.

75. Gaudiana, R. Organic Photovoltaics: Challenges and Opportunities. *J. Polym. Sci. Part B: Polym. Phys.* **2012**, *50*, 1014-1017.

76. Shaheen, S. E., Ginley, D. S., Jabbour, G. E. Organic-Based Photovoltaics: Toward Lower Cost Power Generation. *MRS Bulletin*, **2005**, *30*, 10-19.

77. Fronk, S. L., Mai, C.-K., Ford, M., Noland, R. P., Bazan, G. C. End-Group-Mediated Aggregation of Poly(3-hexylthiophene). *Macromolecules*, **2015**, *48*, 6224-6232.

78. Diao, Y.; Shaw, L.; Mannsfeld, S. C. B. Morphology Control Strategies for Solution-Processed Organic Semiconductor Films. *Energy Environ. Sci.* **2014**, *7*, 2145–2159.

79. Yang, X.; Loos, J. Toward High-Performance Polymer Solar Cells: The Importance of Morphology Control. *Macromolecules* **2007**, *40*, 1353–1362.

80. van Bavel, S.; Veenstra, S.; Loos, J. On the Importance of Morphology Control in Polymer Solar Cells. *Macromol. Rapid Commun.* **2010**, *31*, 1835–1845.

81. Jackson, N. E.; Savoie, B. M.; Marks, T. J.; Chen, L. X.; Ratner, M. A. The Next Breakthrough for Organic Photovoltaics? *J. Phys. Chem. Lett.* **2015**, *6*, 77-84.

82. Rivnay, J.; Mannsfeld, S. C. B.; Miller, C. E.; Salleo, A.; Toney, M. F. Quantitative Determination of Organic Semiconductor Microstructure from the Molecular to Device Scale. *Chem. Rev.* **2012**, *112*, 5488–5519.

83. Peet, J.; Senatore, M. L.; Heeger, A. J.; Bazan, G. C. The Role of Processing in the Fabrication and Optimization of Plastic Solar Cells. *Adv. Mater.* **2009**, *21*, 1521–1527.

84. Yang, H.; Shin, T. J.; Yang, L.; Cho, K.; Ryu, C. Y.; Bao, Z. Effect of Mesoscale Crystalline Structure on the Field-Effect Mobility of Regioregular Poly(3-hexylthiophene) in Thin Film Transistors. *Adv. Funct. Mater.* **2005**, *15*, 671–676.

85. Nguyen, T.; Martini, I. B.; Liu, J.; Schwartz, B. J. Controlling Interchain Interactions in Conjugated Polymers: The Effect of Chain Morphology on Exciton-Exciton Annihilation and Aggregation in MEH-PPV Films. *J. Phys. Chem. B,* **2000**, *104*, 237–255.

86. Park, Y. D.; Lee, H. S.; Choi, Y. J.; Kwak, D.; Cho, J. H.; Lee, S.; Cho, K. Solubility-Induced Ordered Polythiophene Precursors for High-Performance Organic Thin Film Transistors. *Adv. Funct. Mater.* **2009**, *19*, 1200–1206.

87. Yang, C.; Lee, J. K.; Heeger, A. J.; Wudl, F. Well-Defined Donor-Acceptor Rod-Coil Diblock Copolymers Based on P3HT Containing C_{60}: the Morphology and Role as a Surfactant in Bulk Heterojunction Solar Cells. *J. Mater. Chem.* **2009**, *19*, 5416.

88. Smeets, A.; Willot, P.; Winter, J. De; Gerbaux, P.; Verbiest, T.; Koeckelberghs, G. End-Group Functionalization and Synthesis of Block-Copolythiophenes by Modified Nickel Initiators. *Macromolecules,* **2011**, *44*, 6017–6025.

89. Liu, J.; McCullough, R. D. End Group Modification of Regioregular Polythiophene through Postpolymerization Functionalization. *Macromolecules. 35*, 9882-9889.

90. Langeveld-Voss, B. M. W.; Janssen, R. A. J.; Spiering, A. J. H.; van Dongen, J. L. J.; Vonk, E. C.; Claessens, H. A. End-Group Modification of Regioregular Poly(3-alkylthiophene)s. *Chem. Commun.* **2000**, 81-82.

91. Liu, J.; Tanaka, T.; Sivula, K.; Alivisatos, A. P.; Frchet, J. M. J. Employing End-Functional Polythiophene To Control the Morphology of Nanocrystal-Polymer Composites in Hybrid Solar Cells. *J. Am. Chem. Soc.* **2004**, *126*, 6550-6551.

92. Ihn, K. J.; Moulton, J.; Smith, P. Whiskers of Poly(3-alkylthiophenes). *J. Polym. Sci. Part B Polym. Phys.* **1993**, *31*, 735–742.

93. Keum, J. K.; Xiao, K.; Ivanov, I. N.; Hong, K.; Browning, J. F.; Smith, G. S.; Shao, M.; Littrell, K. C.; Rondinone, A. J.; Andrew Payzant, E.; Chen, J.; Hensley, D. K.

Solvent Quality-Induced Nucleation and Growth of Parallelpiped Nanorods in Dilute Poly(3-hexylthiophene) (P3HT) Solution and the Impact on the Crystalline Morphology of Solution-Cast Thin Film. *CrystEngComm* **2013**, *15*, 1114-1124.

94. Kline, R. J.; McGehee, M. D.; Kadnikova, E. N.; Liu, J.; Frechet, J. M. J.; Toney, M. F. Dependence of Regioregular Poly(3-hexylthiophene) Film Morphology and Field Effect Mobility on Molecular Weight. *Macromolecules*, **2005**, *38*, 3312–3319.

95. Yang, X.; Loos, J.; Veenstra, S. C.; Verhees, W. J. H.; Wienk, M. M.; Kroon, J. M.; Michels, M. A. J.; Janssen, R. A. J. Nanoscale Morphology of High-Performance Polymer Solar Cells. *Nano Lett.* **2005**, *5*, 579–583.

96. Peet, J.; Kim, J. Y.; Coates, N. E.; Ma, W. L.; Moses, D.; Heeger, a J.; Bazan, G. C. Efficiency Enhancement in Low-Bandgap Polymer Solar Cells by Processing with Alkane Dithiols. *Nat. Mater.* **2007**, *6*, 497–500.

97. Ho, V.; Boudouris, B. W.; McCulloch, B. L.; Shuttle, C. G.; Burkhardt, M.; Chabinyc, M. L.; Segalman, R. A. Poly(3-alkylthiophene) Diblock Copolymers with Ordered Microstructures and Continuous Semiconducting Pathways. *J. Am. Chem. Soc.* **2011**, *133*, 9270-9273.

98. Lee, J.; Kim, M.; Kang, B.; Jo, S. B.; Kim, H. G.; Shin, J.; Cho, K. Side-Chain Engineering for Fine-Tuning of Energy Levels and Nanoscale Morphology in Polymers Solar Cells. *Adv. Energy Mater.* **2014**, *4*, 1400087.

99. Kline, R. J.; Delongchamp, D. M.; Fischer, D. A.; Lin, E. K.; Richter, L. J.; Chabinyc, M. L.; Toney, M. F.; Heeney, M., McCulloch. Critical Role of Side-Chain Attachment Density on the Order and Device Performance of Polythiophenes. *Macromolecules.* **2007**, *40*, 7960–7965.

100. Akkerman, H. B.; Mannsfeld, S. C. B.; Kaushik, A. P.; Verploegen, E.; Burnier, L.; Zoombelt, A. P.; Saatho, J. D.; Hong, S.; Atahan-evrenk, S.; Liu, X., Aspuru-Guzik, A., Toney, M. F., Clancy, P., Bao, Z. Effects of Odd-Even Side Chain Length of Alkyl-Substituted Diphenylbithiophenes on First Monolayer Thin Film Packing Structure. *J. Am. Chem. Soc.* **2013**, *135*, 11006-11014.

101. Kim, J. S.; Lee, Y.; Lee, J. H.; Park, J. H.; Kim, J. K.; Cho, K. High-Efficiency Organic Solar Cells Based on End-Functional-Group Modified Poly(3-hexylthiophene). *Adv. Mater.* **2010**, *22*, 1355-1360.

102. Mao, Z.; Vakhshouri, K.; Jaye, C.; Fischer, D. A.; Fernando, R.; DeLongchamp, D. M.; Gomez, E. D.; Sauve, G. Synthesis of Perfluoroalkyl End-Functionalized Poly(3-hexylthiophene) and the Effect of Fluorinated Groups on Solar Cell Performance. *Macromolecules.* **2013**, *46*, 103-112.

103. Gauthier, M. A.; Gibson, M. I.; Klok, H-A. Synthesis of Functional Polymers by Post-Polymerization Modification. *Angew. Chem. Int. Ed.* **2009**, *48*, 48-58.

104. Golas, P. L.; Matyjaszewski, K. Marrying Click Chemistry with Polymerization: Expanding the Scope of Polymeric Materials. *Chem. Soc. Rev.* **2010**, *39*, 1338-1354.

105. Lee, J. U.; Jung, J. W.; Emrick, T.; Russell, T. P.; Jo, W. H. Synthesis of End-Capped P3HT and its Application for High-Performance of P3HT/PCBM Bulk Heterojunction Solar Cells. *J. Mater. Chem.* **2010**, *20*, 3287-3294.

106. Ahn, S.; Pickel, D. L.; Kochemba, W. M.; Chen, J.; Uhrig, D.; Hinestrosa, J. P.; Carrillo, J-M.; Shao, M.; Do, C.; Messman, J. M.; Brown, W. M.; Sumpter, B. G.; Kilbey, S. M. Poly(3-hexylthiophene) Molecular Bottlebrushes via Ring-Opening Metathesis Polymerization: Macromolecular Architecture Enhanced Aggregation. *ACS Macro Lett.* **2013**, *2*, 761-765.

107. Kolb, H. C.; Finn, M. G.; Sharpless, K. B. Click Chemistry: Diverse Chemical Function from a Few Good Reactions. *Angew. Chem. Int. Ed.* **2001**, *40*, 2004–2021.

108. Javier, A. E.; Patel, S. N.; Hallinan, D. T.; Srinivasan, V.; Balsara, N. P. Simultaneous Electronic and Ionic Conduction in a Block Copolymer: Application in Lithium Battery Electrodes. *Angew. Chem. Int. Ed. Engl.* **2011**, *50*, 9848–9851.

109. Hufnagel, M.; Fischer, M.; Thurn-Albrecht, T.; Thelakkat, M. Donor-Acceptor Block Copolymers Carrying Pendant $PC_{71}BM$ Fullerenes with Ordered Nanoscale Morphology. *Polym. Chem.* **2015**, *6*, 813-826.

110. Gwyther, J.; Gilroy, J. B.; Rupar, P. A.; Lunn, D. J.; Kynaston, E.; Patra, S. K.; Whittell, G. R.; Winnik, M. A.; Manners, I. Dimensional Control of Block Copolymer Nanofibers with a π-Conjugated Core: Crystallization-Driven Solution Self-Assembly of Amphiphilic Poly(3-hexylthiophene)-*block*-Poly(2-vinylpyridine). *Chem. Eur. J.* **2013**, *19*, 9186-9197.

111. Li, J.; Benicewicz, B. C. Synthesis of Well-Defined Side Chain Fullerene Polymers and Study of Their Self-Aggregation Behaviors. *J. Polym. Sci. Part A Polym. Chem.* **2013**, *51*, 3572–3582.

112. Fujita, H.; Michinobu, T.; Tokita, M.; Ueda, M.; Higashihara, T. Synthesis and Postfunctionalization of Rod-Coil Diblock and Coil-Rod-Coil Triblock Copolymers Composed of Poly(3-hexylthiophene) and Poly(4-(4'-N,N-dihexylaminophenylethynyl)styrene) Segments. *Macromolecules*. **2012**, *45*, 9643-9656.

113. Lee, J. K.; Ko, S.; Bao, Z. In Situ Hetero End-Functionalized Polythiophene and Subsequent “Click” Chemistry with DNA. *Macromol. Rapid Commun.* **2012**, *33*, 938–942.

114. Handa, N. V.; Serrano, A. V.; Robb, M. J.; Hawker, C. J. Exploring the Synthesis and Impact of End-Functional Poly(3-hexylthiopene). *J. Polym. Sci. Part A Polym. Chem.* **2015**, *53*, 831-841.

115. Loewe, R. S.; Khersonsky, S. M.; McCullough, R. D. A Simple Method to Prepare Head-to-Tail Coupled, Regioregular Poly(3-alkylthiophenes) Using Gringard Metathesis. *Adv. Mater.* **1999**, *11*, 250–253.

116. Monnaie, F.; Brullot, W.; Verbiest, T.; De Winter, J.; Gerbaux, P.; Smeets, A.; Koeckelberghs, G. Synthesis of End-Group Functionalized P3HT: General Protocol for P3HT/Nanoparticle Hybrids. *Macromolecules* **2013**, *46*, 8500–8508.

117. Dalgarno, P. A; Traina, C. A; Penedo, J. C.; Bazan, G. C.; Samuel, I. D. W. Solution-Based Single Molecule Imaging of Surface-Immobilized Conjugated Polymers. *J. Am. Chem. Soc.* **2013**, *135*, 7187–7193.

118. Arnould, M. A.; Polce, M. J.; Quirk, R. P.; Wesdemiotis, C. Probing Chain-End Functionalization Reactions in Living Anionic Polymerization via Matrix-Assisted Laser Desorption Ionization Time-of-Flight Mass Spectrometry. *Int. J. Mass Spectrom.* **2004**, *238*, 245-255.

119. Diacon, A.; Derue, L.; Lecourtier, C.; Dautel, O.; Wantz, G.; Hudhomme, P. Cross-linkable Azido C_{60} Fullerene Derivatives for Efficient Thermal Stabilization of Bulk Heterojunction Solar Cells. *J. Mater. Chem. C* **2014**, *2*, 7163-7167.

120. Ko, Y.-G.; Hahm, S. G.; Murata, K.; Kim, Y. Y.; Ree, B. J.; Song, S.; Michinobu, T.; Ree, M. New Fullerene-Based Polymers and Their Electrical Memory Characteristics. *Macromolecules* **2014**, *47*, 8154–8163.

121. Yue, S.; Berry, G. C.; McCullough, R. D. Intermolecular Association and Supramolecular Oranization in Dilute Solution. *Macromolecules* **1996**, *29*, 933-939.

122. Li, Y.-C.; Chen, C.-Y.; Chang, Y.-X.; Chuang, P.-Y.; Chen, J.-H.; Chen, H.-L.; Hsu, C.-S.; Ivanov, V. A.; Khalatur, P. G.; Chen, S.-A. Scattering Study of the Conformational Structure and Aggregation Behavior of a Conjugated Polymer Solution. *Langmuir* **2009**, *25*, 4668–4677.

123. Parashchuk, O. D.; Laptinskaya, T. V; Paraschuk, D. Y. Macromolecular Dynamics of Conjugated Polymer in Donor-Acceptor Blends with Charge Transfer Complex. *Phys. Chem. Chem. Phys.* **2011**, *13*, 3775–3781.

124. Huang, Y.; Cheng, H.; Han, C. C. Morphology Evolution and Structural Transformation of Solution-Processed of Methanolfullerene Thin Film under Thermal Annealing. *Macromolecules.* **2011**, *44*, 5020–5026.

125. Huang, Y.; Cheng, H.; Han, C. C. Temperature Induced Structure Evolution of Regioregular Poly(3-hexylthiophene) in Dilute Solutions and its Influence on Thin Film Morphology. *Macromolecules* **2010**, *43*, 10031–10037.

126. Chu, B. *Laser Light Scattering*; Academic Press: New York, 1974.

127. Burn, B. J.; Pecora, R. *Dynamic Light Scattering*; Plenum Press: New York, 1976.

128. MacHui, F.; Abbott, S.; Waller, D.; Koppe, M.; Brabec, C. J. Determination of Solubility Parameters for Organic Semiconductor Formulations. *Macromol. Chem. Phys.* **2011**, *212*, 2159–2165.

129. Machui, F.; Langner, S.; Zhu, X.; Abbott, S.; Brabec, C. J. Determination of the P3HT:PCBM Solubility Parameters via a Binary Solvent Gradient Method: Impact of Solubility on the Photovoltaic Performance. *Sol. Energy Mater. Sol. Cells* **2012**, *100*, 138–146.

130. Duong, D. T.; Walker, B.; Lin, J.; Kim, C.; Love, J.; Purushothaman, B.; Anthony, J. E.; Nguyen, T. Q. Molecular Solubility and Hansen Solubility Parameters for the Analysis of Phase Separation in Bulk Heterojunctions. *J. Polym. Sci. Part B Polym. Phys.* **2012**, *50*, 1405–1413.

131. Chang, M.; Choi, D.; Fu, B.; Reichmanis, E. Solvent-Based Hydrogen Bonding: Impact on Poly(3-hexylthiophene) Nanoscale Morphology and Charge Transport Characteristics. *ACS Nano.* **2013**, *7,* 5402–5413.

132. Yamamoto, T.; Komarudin, D.; Arai, M.; Lee, B.; Suganuma, H.; Asakawa, N.; Inoue, Y.; Kubota, K.; Sasaki, S.; Fukuda, T.; Matsuda, H. Extensive Studies on π-Stacking of Poly(3-alkylthiophene-2,5-diyl)s and Poly(4-alkylthiazole-2,5-diyl)s by Optical Spectroscopy, NMR Analysis, Light-Scattering Analysis, and X-Ray Crystallography. *J. Am. Chem. Soc.* **1998**, *7863*, 2047–2058.

133. Nath, S.; Pal, H.; Sapre, A. V. Effect of Solvent Polarity on the Aggregation of C_{60}. *Chemical Physical Letters,* **2000**, *327*, 143–148.

134. Theander, M.; Svensson, M.; Ruseckas, A.; Zigmantas, D.; Andersson, M. R.; Ingan, O. High Luminescence from a Substituted Polythiophene in a Solvent with Low Solubility. *Chemical Physical Letters.* **2001**, *337*, 277–283.

135. Clark, J.; Silva, C.; Friend, R.; Spano, F. Role of Intermolecular Coupling in the Photophysics of Disordered Organic Semiconductors: Aggregate Emission in Regioregular Polythiophene. *Phys. Rev. Lett.* **2007**, *98*, 206406.

136. Rumbles, G.; Samuel, I. D. W.; Magnani, L.; Murray, K. A.; Demello, A. J.; Crystal, B.; Moratti, S. C.; Stone, B. M.; Holmes, A. B.; Friend, R. H. Chromism and Luminescence in Regioregular Poly(3-hexylthiophene). *Synthetic Metals*. **1996**, *76*, 47–51.

137. Brown, P. J.; Thomas, D. S.; Köhler, A.; Wilson, J. S.; Kim, J-S.; Ramsdale, C. M.; Sirringhaus, H.; Friend, R. H. Effect of Interchain Interactions on the Absorption and Emission of Poly(3-hexylthiophene). *Phys. Rev. B.* **2003**, *67*, 064203.

138. Wang, G.; Swensen, J.; Moses, D.; Heeger, A. J. Increased Mobility from Regioregular Poly(3-hexylthiophene) Field Effect Transistors. *J. Appl. Phys.* **2003**, *93* (10), 6137-6141.

139. Healy, A. T.; Boudouris, B. W.; Frisbie, C. D.; Hillmyer, M. A.; Blank, D. A. Intramolecular Exciton Diffusion in Poly(3-hexylthiophene). *J. Phys. Chem. Lett.* **2013**, *4*, 3445-3449.

140. Johnson, K.; Huang, Y-S.; Huettner, S.; Sommer, M.; Brinkmann, M.; Mulherin, R.; Niedzialek, D.; Beljonne, D.; Clark, J.; Huck, W. T. S.; Friend, R. H. Control of Intrachain Charge Transfer in Model Systems for Block Copolymer Photovoltaic Materials. *J. Am. Chem. Soc.* **2013**, *135*, 5074-5083.

141. Chen, M.; Li, M.; Wang, H.; Qu, S.; Zhao, X.; Xie, L.; Yang, S. Side-Chain Substitution of Poly(3-hexylthiophene) (P3HT) by PCBM via Postpolymerization: An Intramolecular Hybrid of Donor and Acceptor. *Polym. Chem.* **2013**, *4*, 550-557.

142. Lee, J. U.; Cirpan, A.; Emrick, T.; Russell, T. P.; Jo, W. H. Synthesis and Photophysical Property of Well-Defined Donor-Acceptor Diblock Copolymer Based on Regioregular Poly(3-hexylthiophene) and Fullerene. *J. Mater. Chem.* **2009**, *19*, 1483-1489.

143. van Hal, P. A.; Knol, J.; Langeveld-Voss, B. M. W.; Meskers, S. C. J.; Hummelen, J. C.; Janssen, R. A. J. Photoinduced Energy and Electron Transfer in Fullerene-Oligothiophene-Fullerene Triads. *J. Phys. Chem. A* **2000**, *104*, 5974-5988.

144. Velapoldi, R. A.; Tonneson, H. H. Corrected Emission Spectra and Quantum Yields for a Series of Fluorescent Compounds in the Visible Spectral Region. *Journal of Fluorescence*. **2004**, *14* (4), 465-472.

145. Rogers, J. T.; Schmidt, K.; Toney, M. F.; Kramer, E. J.; Bazan, G. C. Structural Order in Bulk Heterojunction Films Prepared with Solvent Additives. *Adv. Mater.* **2011**, *23*, 2284–2288.

146. Verploegen, E.; Miller, C. E.; Schmidt, K.; Bao, Z.; Toney, M. F. Manipulating the Morphology of P3HT-PCBM Bulk Heterojunction Blends with Solvent Vapor Annealing. *Chem. Mater.* **2012**, *24*, 3923–3931.

147. Perez, L. A.; Zalar, P.; Ying, L.; Schmidt, K.; Toney, M. F.; Nguyen, T.; Bazan, G. C.; Kramer, E. J. Effect of Backbone Regioregularity on the Structure and Orientation of a Donor-Acceptor Semiconducting Polymer. *Macromolecules.* **2014**, *47*, 1403-1410.

148. Gargi, D.; Kline, R. J.; Delongchamp, D. M.; Fischer, D. A.; Toney, M. F.; Connor, B. T. O. Charge Transport in Highly Face-On Poly(3-hexylthiophene) Films. *J. Phys. Chem. C.* **2013**. *117*, 17421-17428.

149. Kobayashi, H., Onda, S., Furumaki, S., Habuchi, S., Vacha, M. A Single-Molecule Approach to Conformation and Photophysics of Conjugated Polymers. *Chem. Phys. Lett.* **2012**, *528*, 1-6.

150. Barbara, P. F., Gesquiere, A. J., Park, S.-J., Lee, Y. J. Single-Molecule Spectroscopy of Conjugated Polymers. *Acc. Chem. Res.* **2005**, *38*, 602-610.

151. Lupton, J. M. Single-Molecule Spectroscopy for Plastic Electronics: Materials Analysis from the Bottom Up. *Adv. Mater.* **2010**, *22*, 1689-1621.

152. Adachi, T., Lakhwani, G., Traub, M. C., Ono, R. J., Bielawski, C. W., Barbara, P. F., Bout, D. A. V. Conformational Effect on Energy Transfer in Single Polythiophene Chains. *J. Phys. Chem. B*, **2012**, *116*, 9866-9872.

153. Lin, H., Hania, R. P., Bloem, R., Mirzov, O., Thomsson, D., Scheblykin, I. G. Single Chain *versus* Single Aggregate Spectroscopy of Conjugated Polymers. Where is the Border? *Phys. Chem. Chem. Phys.* **2010**, *12*, 11770-11777.

154. Adachi, T., Vogelsang, J., Lupton. J. M. Chromophore Bending Controls Fluorescence Lifetime in Single Conjugated Polymer Chains. *J. Phys. Chem. Lett.* **2014**, *5*, 2165-2170.

155. Sahoo, D., Tian, Y., Sforazzini, G., Anderson, H. L., Scheblykin, I. G. Photoinduced Fluorescence Quenching in Conjugated Polymers Dispersed in Solid Matrices at Low Concentration. *J. Mater. Chem. C*, **2014**, *2*, 6601-6608.

156. Ito, Y., Virkar, A. A., Mannsfeld, S., Oh, J. H., Toney, M., Locklin, J., Bao, Z. Crystalline Ultrasmooth Self-Assembled Monolayers of Alkylsilanes for Organic Field Effect Transistors. *J. Am. Chem. Soc.* **2009**, *131*, 9396-9404.

157. Tulevski, G. S., Miao, Q., Fukuto, M., Abram, R., Ocko, B., Pindak, R., Steigerwald, M. L., Kagan, C. R., Nuckolls, C. Attaching Organic Semiconductors to Gate Oxides: In Situ Assembly of Monolayer Field Effect Transistors. *J. Am. Chem. Soc.* **2004**, *126*, 15048-15050.

158. Guo, Z., Lei, A., Liang, X., Xu, Q. Click Chemistry: A New Facile and Efficient Strategy for Preparation of Functionalized HPLC Packings. *Chem. Commun.* **2006**, 4512-4514.

159. Subramanian, N., Schmidt, R., Wood-Adams, P. M., DeWolf, C. E. Space-Filling Triethoxysilane: Synthesis and Self-Assembly into Low-Density Monolayers. *Langmuir*, **2010**, *26*, 18628-18630.

160. Nakazawa, J., Smith, B. J., Stack, T. D. P. Discrete Complexes Immobilized Onto Click-SBA-15 Silica: Controllable Loadings and the Impact of Surface Coverage on Catalysis. *J. Am. Chem. Soc.* **2012**, *134*, 2750-2759.

161. Cunningham, P. D., Hayden, L. M. Carrier Dynamics Resulting from Above and Below Gap Excitation of P3HT and P3HT/PCBM Investigated by Optical-Pump Terahertz-Probe Spectroscopy. *J. Phys. Chem. C*, **2008**, *112*, 7928-7935.

162. Marsh, R. A., Hodgkiss, J. M., Albert-Siefried, S., Friend, R. H. Effect of Annealing on P3HT:PCBM Charge Transfer and Nanoscale Morphology Probed by Ultrafast Spectroscopy. *Nano Lett.* **2010**, *10*, 923-930.

163. Piris, J., Dykstra, T. E., Bakulin, A. A., van Loosdrecht, P. H. M., Knulst, W., Trinh, M. T., Schins, J. M., Siebbeles, L. D. A. Photogeneration and Ultrafast Dynamics of Excitons and Charges in P3HT/PCBM Blends. *J. Phys. Chem. C*, **2009**, *113*, 14500-14506.

164. Demirel, G. B.; Dilsiz, N.; Cakmak, M.; Caykara, T. Molecular Design of Photoswitchable Surfaces with Controlled Wettability. *J. Mater. Chem.* **2011**, *21*, 3189-3196.

165. Traina, C. A.; Bakus, R. C.; Bazan, G. C. Design and Synthesis of Monofunctionalized, Water-Soluble Conjugated Polymers for Biosensing and Imaging Applications. *J. Am. Chem. Soc.* **2011**, *133*, 12600-12607.

166. Kamps, A. C.; Fryd, M.; Park, S. Hierarchically Self-Assembly of Amphiphilic Semiconducting Polymers into Isolated, Bundled, and Branched Nanofibers. *ACS Nano*. **2012**, *6 (3)*, 2844-2852.

167. Yang, H.; Xia, H.; Wang, G.; Peng, J.; Qui, F. Insights Into Poly(3-hexylthiophene)-*b*-Poly(ethylene oxide) Block Copolymer: Synthesis and Solvent-Induced Structure Formation in Thin Films. *J. Polym. Sci. A1*. **2012**, *50*, 5060-5067.

168. Kempf, C. N.; Smith, K. A.; Pesek, S. L.; Li, X.; Verduzco, R. Amphiphilic Poly(alkylthiophene) Block Copolymers Prepared via Externally Initiated GRIM and Click Coupling. *Polym. Chem.* **2013**, *4*, 2158-2163.

169. Rosler, A., Vandermeulen, G. W. M., Klok, H.-A. Advanced Drug Delivery Devices via Self-Assembly of Amphiphilic Block Copolymers. *Adv. Drug Deliver. Rev.* **2012**, *64*, 270-279.

170. Kataoka, K, Harada, A., Nagasaki, Y. Block Copolymer Micelles for Drug Delivery: Design, Characterization, and Biological Significance. *Adv. Drug Deliver. Rev.* **2001**, *47*, 113-131.

171. Jones, M.-C., Leroux, J.-C. Polymeric Micelles – A New Generation of Colloidal Drug Carriers. *Eur. J. Pharm. Biopharm.* **1999**, *48*, 101-111.

172. Kim, S., Kim, J.-H., Jeon, O., Kwon, I. C., Park, K. Engineering Polymers for Advanced Drug Delivery. *Eur. J. Pharm. Biopharm.* **2009**, *71*, 420-430.

173. Gaucher, G., Dufresne, M.-H., Sant, V. P., Kang, N., Maysinger, D., Leroux, J.-C. Block Copolymer Micelles: Preparation, Characterization, and Application in Drug Delivery. *J. Control. Release*, **2005**, *109*, 169-188.

174. Xu, W., Ling, P., Zhang, T. Polymeric Micelles, a Promising Drug Delivery System to Enhance Bioavailability of Poorly Water-Soluble Drugs. *J. Drug Deliv.* **2013**, 1-15.

175. Cui, X., Mao, S., Liu, M., Yuan, H., Du, Y. Mechanism of Surfactant Micelle Formation. *Langmuir*, **2008**, *24*, 10771-10775.

176. Gohy, J.-F. Block Copolymer Micelles. *Adv. Polym. Sci.* **2005**, *190*, 65-136.

177. Ouhib, F., Desbief, S., Lazzaroni, R., Melinte, S., Dutu, C. A., Jerome, C., Detrembleur, C. Electrografting Onto ITO Substrates of Poly(thiophene)-Based Micelles Decorated by Acrylate Groups. *Polym. Chem.* **2013**, *4*, 4151-4161.

II. Introduction of Chiral Side Chains to Explore Structure-Property Relationships of Donor-Acceptor Copolymers

A. Background

Conjugated polymers containing alternating electron rich (donor, D) and electron poor (acceptor, A) monomer units have attracted substantial attention as high-performing semiconducting materials for applications in organic solar cells[1-5] and organic field effect transistors.[6-8] D-A copolymers have certain advantages over conjugated homopolymers. Specifically, the choice of donor and acceptor units can be used to tune the HOMO and LUMO energy levels as the HOMO level primarily depends on the donor unit and the LUMO level primarily depends on the acceptor unit.[9-12] Internal charge transfer between the donor and acceptor units can result in a narrow bandgap material with a low lying HOMO level.[9-13] The absorption of D-A copolymers differs from that of homopolymers due to the presence of an intramolecular charge transfer absorption band present at longer wavelengths.[10] This broadening of the absorption band benefits D-A copolymers used in photovoltaic applications by allowing more photons in the visible wavelength range to be absorbed.[14] Typically, in polymer solar cells, absorbing more photons results in a higher short circuit current.[14] Another parameter, the open-circuit voltage (V_{oc}), is influenced by the difference in the HOMO level of the donor and the LUMO of the acceptor.[15] Thus decreasing the HOMO level of the donor has potential to increase the V_{oc}.

In order to retain regioregularity, symmetric donor and acceptor units are often preferred.[2,16] Donor units are often scaled from strong to weak based on their electron donating ability such that stronger donor units tend to produce polymers with narrower bandgaps.[2,16] For example, thiophene-based units tend to possess a stronger electron-donating ability compared to benzene-based units.[17] Thus cyclopentadithiophene-based polymers tend to have smaller bandgaps compared to fluorene-based polymers.[17] Ideal donor units should minimize steric hindrance to promote a more planar backbone structure.[18] A planar conjugated backbone promotes charge transport along the polymer chain in addition to potential for promoting interchain π-π stacking.[19-20] Acceptor units can also be scaled from strong to weak based on their electron accepting ability.[2,16] Common acceptor units include benzothiadiazole, isoindigo, and diketopyrrolopyrrole.[2] Steric hindrance from interactions between atoms or side chains of the donor and acceptor units can be further minimized through the introduction of spacer units such as unsubstituted thiophenes.[16]

Interchain interactions that promote effective electronic coupling are often achieved when ordered polymer domains are present in the thin film.[21-23] Interchain interactions are influenced by the planarity of the conjugated backbone and the length and structure of the side chains.[24-25] Short π-π stacking distances promote electronic coupling between polymer chains and are often measured using x-ray scattering techniques.[26-27] Effective electronic coupling leads to higher charge carrier mobilities, an essential parameter that mediates charge extraction in solar cells and the velocity of charge carriers in transistor channels.[28-30] Additionally, interchain interactions between the backbones of conjugated polymers often result in the formation of aggregates in solution.[31-32] The ability of the polymer chains to aggregate depends on the solvent and concentration.[33-35] Addition of a small amount of poor solvent can induce aggregation,[35] however, certain conjugated polymers aggregate even in “good” solvents.[36] Work by Koynov and coworkers found that in larger aggregates of

MEH-PPV, polymer chains tend to adopt an extended chain conformation and thus exhibit a redshift in absorption maximum.[37]

The transition from solution to solid state influences the resulting film properties.[29,35] Understanding and controlling polymer organization during this process provides a handle on improving thin film device performance.[38-40] Current extrinsic methods to influence this transition include solvent choice,[34] solvent additives,[35,40] solution temperature, and pre-aggregation in solution.[33] Solvent additives and solvent choice have an effect on the drying kinetics in order to promote crystallization or a desirable degree of phase separation in a multicomponent system.[41-43] Studies of polymer pre-aggregation in solution have found that ordered chains in solution translate to ordered chains in the solid state.[33,44] Intrinsic methods such as the molecular design of the conjugated backbone and solubilizing side chains, as discussed below, also play a role during this transition.

The choice of side-chain impacts the polymer solubility, the solid state packing, interchain interactions, and polymer aggregation which in turn influence device properties such as charge carrier mobility and power conversion efficiency (PCE) in organic solar cells.[24-25,45-47] The goal of many organic thin film electronic devices is solution processability and thus the side chain is an essential component of the molecular design.[16] Many options for side chains have been studied including alkyl and branched alkyl chains, alkyoxy chains, electron-withdrawing side chains which often include fluoro-groups, conjugated side chains, pendant ionic side chains, terminally functionalized side chains, and oligoether side chains.[24-25,48-55] Alkyl and branched alkyl side chains are common due to their ability to impart solubility in organic solvents with longer side chains often increasing polymer solubility.[24-25] However longer side chains may increase the π-π stacking distance which can have a negative impact on charge carrier mobility in transistors and short circuit current in solar cells but a positive impact on open circuit voltage.[53,56] Similarly, branched side chains tend to promote steric hindrance between polymer chains, preventing the interdigitation often observed for linear side chains.[47,50] For some conjugated backbones, side chain position influences the material properties.[56-57] P3HT provides the most obvious example as regioregular P3HT exhibits less steric hindrance compared to regiorandom P3HT.[56] Electron-withdrawing side chains and conjugated side chains have an effect on the energy levels of the conjugated polymer in addition to improving solubility.[58-59] Ionic side chains and oligoether chains are often used to impart solubility in more polar solvents.[60-63] Processing from solvents of orthogonal polarities can be beneficial when constructing multilayer solution-processable devices.[61-63]

Chiral side chains offer a method of introducing asymmetry to a conjugated polymer structure.[64-66] Assuming the asymmetry of the side chain translates to the conjugated polymer backbone, introducing a chiral center offers a handle to study the polymer secondary structure using circular dichoism spectroscopy.[67-68] CD spectroscopy is based on the interaction of a material with left vs. right circularly polarized light.[67-68] Asymmetric materials will preferentially absorb one orientation based on the handedness of the helical structure, resulting in a Cotton effect in the CD spectrum.[69] These Cotton effects are only present at wavelengths where linear optical absorption is observed.[69] Typical CD spectrometers produce a left axis, Θ, with units in millidegrees which can be converted to units of absorption using the following equation:

$\Delta A = A_L - A_R = \Theta / 32{,}982.$[69]

The conjugated polymers that contain chiral side chains are said to exhibit "induced circular dichroism" in contrast to molecules where the chromophore itself is chiral.[69] In this case, the asymmetry of the side chain is translated to the chromophoric backbone.[69] When absorption by an aggregated species is observed, the interaction of multiple polymer chains is responsible for the resulting CD signal. In this case, exciton coupling results in Davydov splitting of the excited states such that bisignate Cotton effects are observed.[69] The degree of circular polarization in absorption can be calculated for a specific wavelength using the anisotropy factor:

$g_{abs} = \Delta A / A$, where A is the linear optical absorption.[69]

Recent interest in conjugated polymers containing chiral side chains stems from their ability to self-assemble into novel helical nanostructures.[70-73] Recent work has focused on developing materials for chiral sensing applications,[74] synthesizing pH- and thermoresponsive polyallene-polythiophene-polyallene triblock copolymers,[75] designing of liquid crystalline block copolymers with potential applications in drug delivery and as biological mimics,[76] and constructing helix-to-tube nanostructures.[71] In addition to the novel nanostructures and applications, introduction of a chiral side chain provides a handle to investigate the secondary structure and aggregate properties of conjugated polymers.[77-80] Early work by Meijer and coworkers explored the chiroptical properties of polythiophenes containing chiral substituents.[77] Using a combination of solution and thin film spectroscopic and x-ray techniques, they found chirally-substituted polythiophenes exhibit a CD response in the form of bisignate Cotton effects when polymer chains exist as highly ordered chiral aggregates but not as well-dissolved single chains.[77] This paper in combination with exciton chirality theory laid the foundation for future work studying conjugated polymer secondary structure via chiroptical methods including work further work on polythiophenes,[81] polyfluorenes,[82] polyactetylenes,[73] and poly(phenylenevinylene)s.[74,83]

B. Comparison of Chiroptical Properties of PCPDTBT and PCDTPT**

1. Introduction

PCPDTBT and PCDTPT are two narrow bandgap D-A conjugated polymers known to perform well in solar cell[84-87] and transistor applications[88-90] respectively. The synthesis and characterization of PCPDTBT has been widely studied in the literature for applications in polymer solar cells and transistors.[84,91] Microwave-assisted Stille coupling polymerization was found to provide high molecular weight and control over the end-groups.[84] The use of solvent additives and thermal treatment when preparing PCPDTBT/PCBM solar cells has resulted in improved PCEs.[42,92] The synthesis of regioregular PCDTPT is similar to that of PCPDTBT with similar potential for high molecular weight and controlled end-groups.[88] At the same channel length, hole mobilities for PCDTPT and PCPDTBT were measured to be 25.4 and 22.2 cm^2/Vs, respectively.[90] The single structural difference between the two conjugated polymer backbones is the replacement of a –CH group on the benzothiadiazole ring of PCPDTBT with a pyridal N group for PCDTPT (Figure 2-1). This single functional group substitution results in differences in the optoelectronic properties and device performance of the two polymers.[84,88] A potential explanation for these observations is differences in polymer secondary structure.

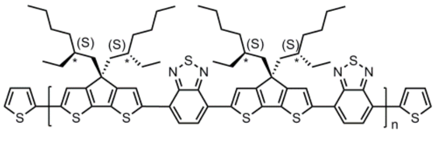

PCDTBT*

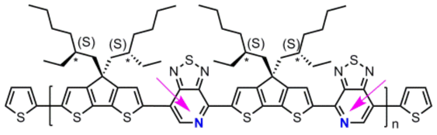

PCDTPT*

Figure 2-1. Molecular structures of PCPDTBT* and PCDTPT*. The arrows are meant to guide the eye and highlight the regioregularity of the PT units relative to the backbone direction.

Here, 2-(S)-ethylhexyl side chains are introduced to the CDT unit of both PCPDTBT and PCDTPT to produce PCPDTBT* and PCDTPT* respectively. Limited emphasis has previously been placed on understanding of the preferred secondary structure as a function of backbone composition.[22-23,93] A more thorough knowledge of the organization of the polymer chains in solution and during the transition from solution to the solid state may be helpful in better predicting the optimal processing conditions necessary to achieve desirable device characteristics.[20,33,38,40,94] This structure substitution of chiral for racemic side chains introduces the possibility of studying the polymer secondary structure by examining their chiroptical response, assuming the asymmetry of the side chain translates to the conjugated polymer backbone. Using optical absorption and circular dichroism spectroscopies, we can explore the different coil conformations and geometries of multichain aggregates formed in solutions of varying polarity and in the solid state.[95] As a follow-up effort, PCDTFBT*, with a substitution of the –CH group for a –CF group on the benzothiadiazole ring, and PIPCP* were synthesized and characterized for further comparison.

2. Synthesis

As shown in Scheme 2-1, (S)-2-ethylhexan-1-ol was synthesized according to literature procedures.[96] Reduction of the α,β-unsaturated aldehyde to the chiral alcohol is accomplished using Baker's yeast as a biocatalyst. High chiral purity was deemed necessary to accentuate any changes in polymer structural characteristics. The optical purity of (S)-2-ethylhexan-1-ol was confirmed using polarimetry and through the use of a chiral derivatizing agent (CDA). The optical rotation was found to be +2.95 when measured at a concentration of 1.2 g/100 mL in acetone and the enantiomeric excess was determined to be 95% based upon comparison with the known optical rotation.[97] CDAs are used to determine stereochemistry and chiral purity using Mosher's method.[98-100] Diastereomers have different ^{1}H NMR chemical shifts, whereas enantiomers do not; thus a reaction to form a diastereomer allows for determination of enantiomeric purity.[101-102] Accordingly, (S)-2-ethylhexan-1-ol was reacted with (S)-(+)-10-camphorsulfonyl chloride (Scheme S2-2) to produce an adduct with a distinct doublet peak with at 4.16 ppm (Figure S2-1a). In contrast, the corresponding analogous adduct resulting from the reaction with racemic 2-ethylhexan-1-ol (Scheme S2-3) gave rise to a multiplet of peaks at 4.2-4.1 ppm (Figure S2-1b). These CDA results confirm the high chiral purity of the 2-ethylhexyl framework subsequently used to solubilize the polymer chains.

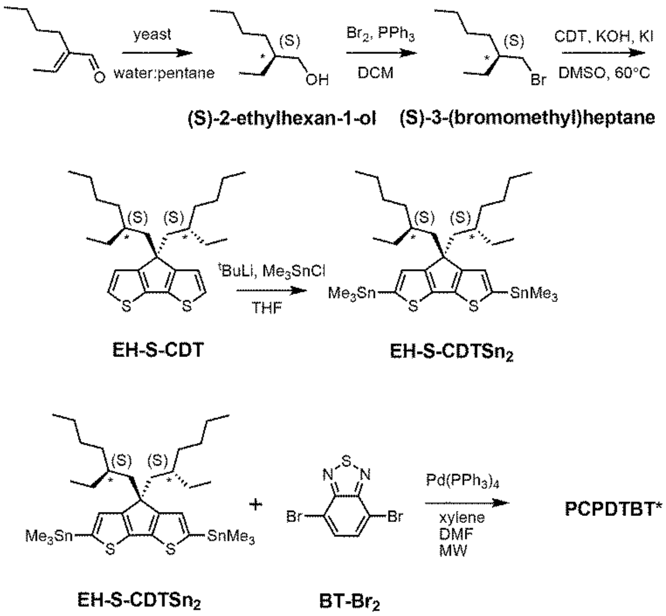

Scheme 2-1. Synthesis of PCPDTBT*.

The remaining sequence of steps required for the preparation of the target PCPDTBT* is outlined in Scheme 2-1. (S)-2-ethylhexan-1-ol was converted to (S)-3-(bromomethyl)heptane via reaction with 2.7 eq. Br_2 and 1.4 eq. PPh_3 in dichloromethane. Attachment of the chiral sidegroups to the CDT framework to yield EH-S-CDT was accomplished by employing previously described alkylation protocols.[103] Reaction of EH-S-CDT with 2.5 eq. ^{t}BuLi and 3 eq. Me_3SnCl provided the bisstannylated intermediate EH-S-CDTSn$_2$. The polymerization between EH-S-CDTSn$_2$ (1.05 eq.) and 4,7-dibromo-2,1,3-benzothiadiazole (BT-Br$_2$) (1 eq.) was carried out by using microwave-assisted Stille-coupling polymerization conditions in a xylene:DMF solvent system with 0.052 eq. $Pd(PPh_3)_4$ as the catalyst.[84] After purification using Soxhlet extraction, the resulting polymer, PCPDTBT*, was obtained with a number average molecular weight (M_n) of 23K and a dispersity ($Đ$) of 1.6. The analogous polymer with racemic 2-ethylhexyl side chains (PCPDTBT) was also prepared in order to have a reference material. This procedure follows literature precedent and can be found in the Supporting Information (Scheme S2-

10). PCPDTBT was obtained with M_n = 32K and $Đ$ = 2.3. Characterization by differential scanning calorimetry (DSC) reveals no phase transitions between 20°C and 300°C for either material (Figure S2-2), in agreement with previous studies on PCPDTBT.[84]

PCDTPT* was synthesized as shown in Scheme 2-2.[88] A regiospecific Stille coupling reaction between EH-S-CDTSn$_2$ and two equivalents of PT-Br$_2$ was used to provide PT-EH-S-CDT-PT. The target polymer was attained through the reaction of 1 eq. PT-EH-S-CDT-PT and 1.05 eq. EH-S-CDTSn$_2$ and subsequent purification via Soxhlet extraction. PCDTPT* obtained in this manner had M_n = 17K and $Đ$ = 1.7. The analogous reference polymer with racemic 2-ethylhexyl side chains (PCDTPT, M_n = 23K and $Đ$ = 2.0) was synthesized using the same procedure (Scheme S2-11). Characterization by DSC shows no phase transitions between 20°C and 300°C for either material (Figure S2-3).

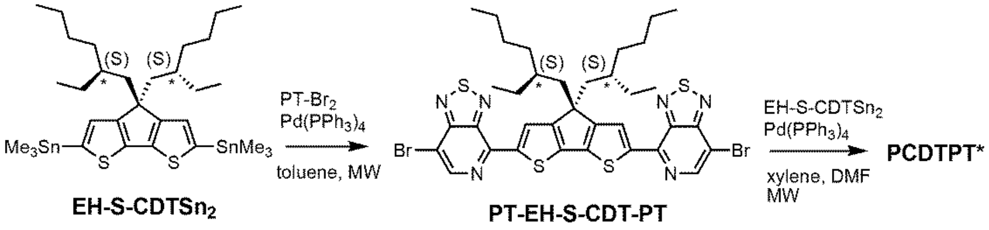

Scheme 2-2. Synthesis of PCDTPT*.

3. Absorption & CD Spectroscopies of PCPDTBT* in Solution

Optical absorption and circular dichroism (CD) spectroscopy were measured for PCPDTBT* and PCPDTBT in dilute chlorobenzene (CB) and in a 1:1 CB:diiodoctane (DIO) solvent mixture. DIO is known to be a poor solvent for PCPDTBT and has been used as a solvent additive for modifying bulk heterojunction PCPDTBT/fullerene blend morphologies during the spin-coating deposition step.[42] A solvent ratio of 1:1 CB:DIO was chosen for this study as aggregation of polymer chains is favored for PCPDTBT* and

PCPDTBT without causing either material to obviously precipitate out of solution. Specifically, PCPDTBT is known to form aggregates as the volume of DIO is increased relative to CB.[35]

The optical absorption spectrum of PCPDTBT* in dilute CB shown in Figure 2-2 is consistent with a solvated polymer in a good solvent with minimal interchain interactions.[84] Evidence for aggregate formation is observed for PCPDTBT* in CB:DIO. Specifically, PCPDTBT* shows a distinct shoulder peak at longer wavelengths (795-810 nm). This feature has been previously implicated to arise from aggregated chains in solution[35] and is more prominent for PCPDTBT* than PCPDTBT. Note also that the M_n of PCPDTBT* is lower than that of PCPDTBT, which should discourage aggregation. Instead, the presence of the chiral side chain induces a greater degree of order within the aggregates of PCPDTBT* compared to PCPDTBT. Further evidence is provided by the high degree of order in PCPDTBT* films as discussed in the next section. Altogether, these observations indicate preferential aggregation of PCPDTBT* as a result of the greater structural precision of the solubilizing side chains.

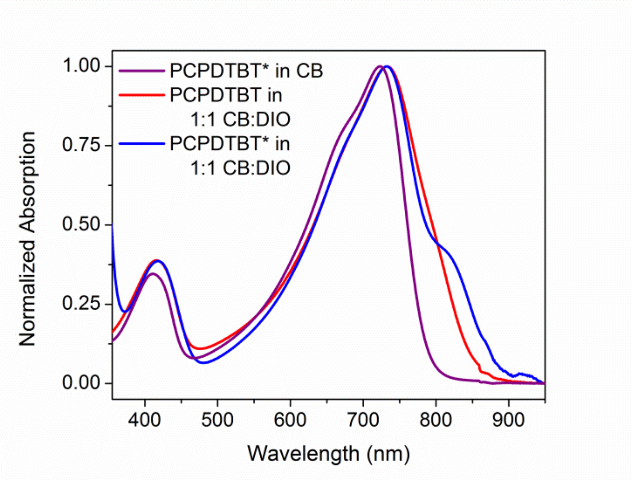

Figure 2-2. Normalized optical absorption spectra of PCPDTBT* in CB (purple), PCPDTBT in CB:DIO (red), and PCPDTBT* in CB:DIO (blue).

Figure 2-3 provides the CD spectra for PCPDTBT* and PCPDTBT as a function of solvent conditions. These data reveal that CD signals are present for PCPDTBT* in CB:DIO, but not for PCPDTBT* in CB or for PCPDTBT in CB:DIO. A bisignate Cotton effect is observed for PCPDTBT* at the higher energy π→π* transition. There is also a CD signal at longer wavelengths (centered at 870 nm), primarily located within the absorption profile of the aggregate. This result, combined with the absence of a CD signal in CB solution, supports the hypothesis that PCPDTBT* is chiroptically active only when the chains are incorporated within a multichain aggregate.[104] It should be noted that the CD signal at 950 nm, where no CD signal is expected based on the absence of any linear absorption, likely results from scattering due to the crystalline nature of PCPDTBT* (to be discussed further in the following section).

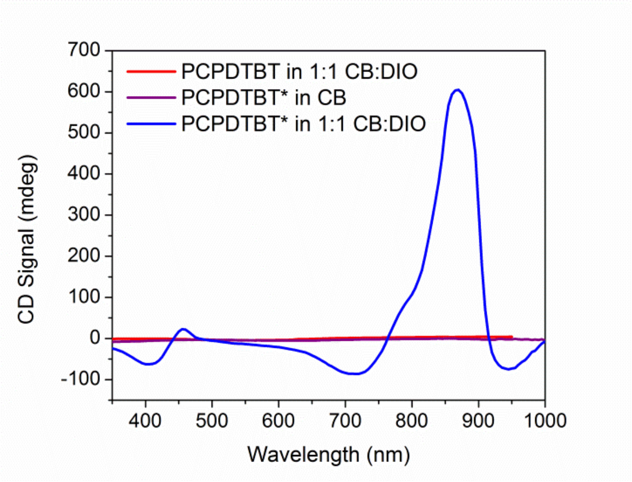

Figure 2-3. CD spectra of PCPDTBT* in CB (purple), PCPDTBT in CB:DIO (red), and PCPDTBT* in CB:DIO (blue).

Temperature dependent spectra of PCPDTBT* were measured in dilute CB:DIO solutions, and the results are shown in Figure 2-4. In these experiments, solutions were heated from 25°C to 90°C and absorption/CD measurements were taken every 10°C. Absorption measurements show a progressive decrease in the shoulder peak attributed to aggregates with increasing temperature. Such a process is reasonable; the solubility of the chains improves thereby increasing the fraction of the sample present as well-solvated chains with less pronounced interchain contacts. Once 80°C is reached, the shoulder peak disappears and the polymer chains are well-dissolved. This spectrum mirrors that of PCPDTBT* dissolved in CB, confirming the presence of individual chains in solution. Temperature-dependent absorption of PCPDTBT was also measured and shows a similar decrease in shoulder peak with increasing temperature (Figure S2-7). The CD signal also decreases with increasing temperature. By 90°C, no CD signal was observed. This correspondence between thermochromic behavior and CD signatures further confirms that chiroptical properties depend upon interchain interactions.

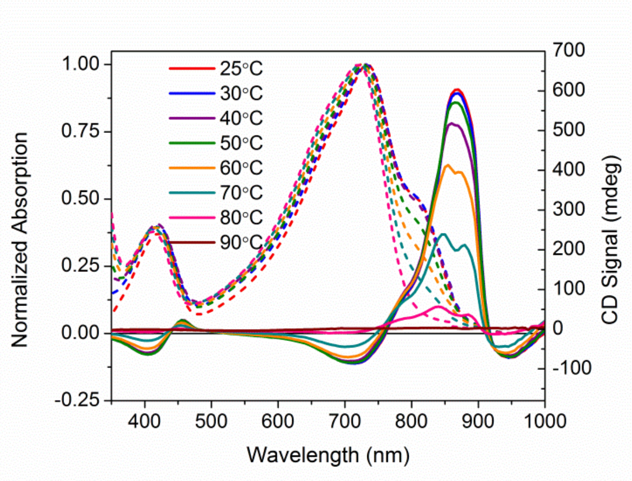

Figure 2-4. Normalized optical absorption (dashed) and CD (solid) spectra of PCPDTBT* in CB:DIO as a function of temperature, from 25-90°C.

Solutions of PCPDTBT* in CB:DIO were heated to 90°C, held at 90°C for 15 minutes, and cooled back to 25°C at cooling rates of 1°C/minute and 5°C/minute. One week after performing these controlled cooling measurements, the CD response was again measured (Figure 2-5a). The solution cooled at 1°C/minute displayed a stronger CD signal at the aggregate absorption peak (centered at 870 nm), compared to the solution cooled at

5°C/minute. However, the absorption profile of the two solutions remains the same (Figure 2-5b). Varying the cooling rate therefore does not change the aggregate absorption peak. This suggests the difference in CD signal stems from different order within the aggregate rather than a different ratio of aggregated and solvated chains. Cooling at a slower rate allows the polymer chains to reach a more thermodynamically-preferred structure, whereas cooling at a faster rate leaves the polymer chains kinetically trapped in a less well-ordered state.

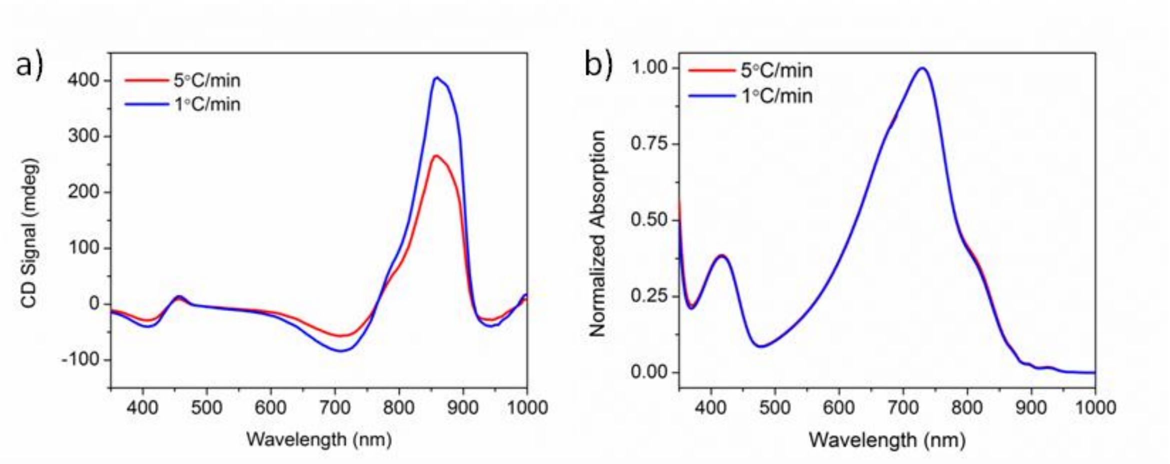

Figure 2-5. (a) CD and (b) normalized absorption spectra of PCPDTBT* in CB:DIO measured 1 week after cooling at 5°C min^{-1} (red) and 1°C min^{-1} (blue).

The degree of circular polarization in absorption can be estimated using the anisotropy factor, g_{abs}, which compares the difference in left (A_L) and right (A_R) circularly polarized light with the linear optical absorption (A) ($g_{abs} = (A_L - A_R)/A$).[69] The average g_{abs} calculated for the aggregate absorption peak in CB:DIO (825 nm) of PCPDTBT* is 0.013.

4. Solid State Characterization of PCPDTBT*

Thin films of PCPDTBT* and PCPDTBT were obtained by spin-coating 8 mg/mL CB solutions onto clean glass substrates and were examined using optical absorption spectroscopy, CD spectroscopy, atomic force microscopy (AFM), and grazing incident wide-angle x-ray scattering (GIWAXS). Optical absorption spectroscopy of both materials shows a red shift in absorption toward the low energy shoulder peak observed in solution (Figure 2-6). The PCPDTBT absorption spectra agree with the literature.[84] However, PCPDTBT* shows a small redshift in absorption maximum (21 nm) compared to PCPDTBT.

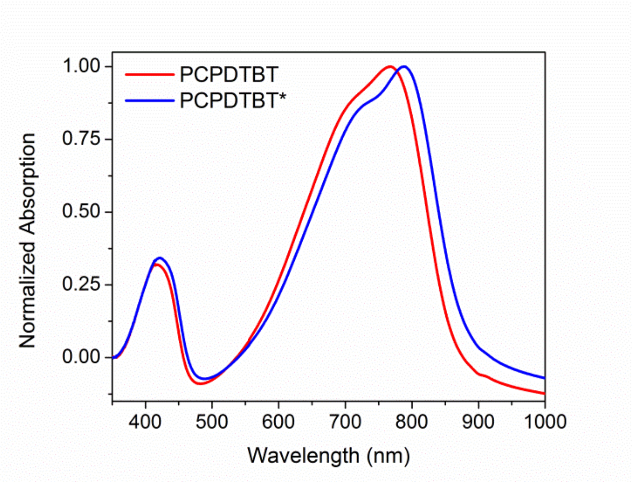

Figure 2-6. Normalized thin film absorption spectra of PCPDTBT (red) and PCPDTBT* (blue).

Thin film CD spectra are shown in Figure 2-7. PCPDTBT thin films show no chiral response, as expected. PCPDTBT* thin films show two CD signatures similar to those observed in solution. A clear bisignate Cotton effect is observed at the high-energy π→π* transition. This CD peak is more prominent in the thin film compared to solution. A bisignate Cotton effect is also observed at the absorption aggregate peak (centered at 825 nm). No significant change in absorption or CD signal is observed when films are thermally annealed (Figure S2-8 and S2-17).

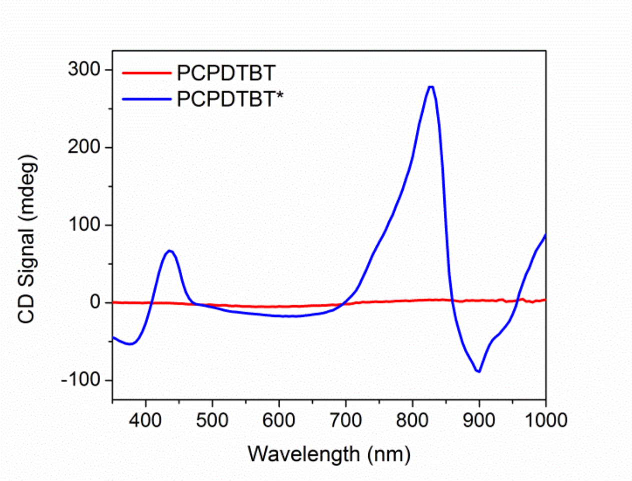

Figure 2-7. Thin film CD spectra of PCPDTBT (red) and PCPDTBT* (blue).

The anisotropy factor can also be calculated for thin films. The average g_{abs} calculated for the aggregate absorption peak (830 nm) of PCPDTBT* is 0.037. Therefore, the g_{abs} value increases for the thin film compared to solution.

Possible changes in surface features were studied using AFM. Surface topography images are shown in Figure 2-8. PCPDTBT shows a smooth film, whereas PCPDTBT* shows fiber-like structure. The surface roughness of PCPDTBT* (8.5 nm) is also greater than that of PCPDTBT (2.8 nm). These results provide the first indication of a difference in solid state ordering induced by chiral vs. racemic side chains.

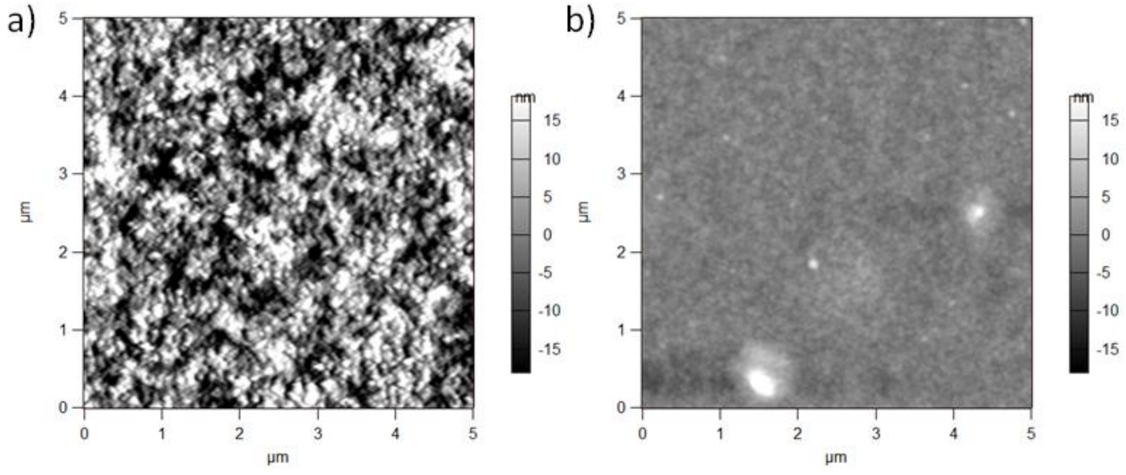

Figure 2-8. AFM topography images (5 X 5 μm^2) of a) PCPDTBT* and b) PCPDTBT thin films.

Crystalline domains in the thin films of PCPDTBT* and PCPDTBT were studied using GIWAXS.[27] The 2-D GIWAXS images are shown in Figure 2-9 and line cut profiles are shown in Figure S2-24. The π-π stacking peaks are observed at 16.7 nm^{-1} (d = 0.38 nm) and 15.8 nm^{-1} (d = 0.40 nm) for PCPDTBT* (Figure 2-9b) and PCPDTBT (Figure 2-9a), respectively. The alkyl chain stacking peaks are observed at 5.87 nm^{-1} (d = 1.07 nm) and 5.51 nm^{-1} (d = 1.14 nm) for PCPDTBT* and PCPDTBT respectively, which is in agreement with the literature for PCPDTBT.[28] The increase in d-spacing with the presence of the racemic groups suggests that PCPDTBT* exhibits tighter packing compared to PCPDTBT. Crystalline correlation lengths (CCL) were calculated for both films using the Scherrer equation.[29] The CCL for the alkyl chain stacking peak of PCPDTBT is 2.05 nm. The CCL value for PCPDTBT* is 3.78 nm, almost double that of PCPDTBT. The CCLs for the π-π stacking are 8.10 nm for PCPDTBT* and 6.24 nm for PCPDTBT. The increase in the CCL for the chiral polymer indicates larger or more perfect crystallites with increasing homogeneity of molecular structure.

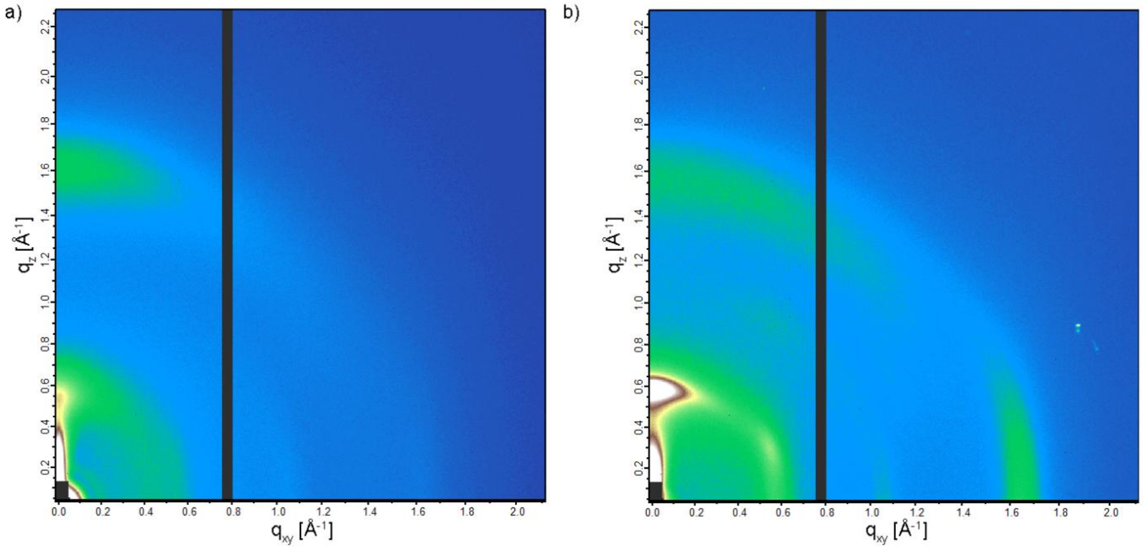

Figure 2-9. 2-D GIWAXS images of a) PCPDTBT and b) PCPDTBT*.

For equally thick films with isostructural materials, the GIWAXS diffraction intensity can be related to the amount of crystalline component in the film.[27] The 2-D GIWAXS image of PCPDTBT* displays an intense peak at 16.5 nm^{-1} in the in-plane direction which is almost absent in PCPDTBT. Similarly, the scattering peak intensity of the alkyl chain stacking peak in the out-of-plane direction is much stronger for PCPDTBT* than PCPDTBT. The greater scattering intensity of PCPDTBT* films compared to PCPDTBT suggests a larger fraction of crystalline material in PCPDTBT* films. Combining the CCL and scattering intensity data, we find that PCPDTBT* films are substantially more ordered than PCPDTBT films.

There exist several possible intramolecular conformations and intermolecular ensemble arrangements for polymers with chiral side chains that can give rise to CD signals.[77,105-106] Single polymer chains may form helical secondary structures while remaining well-dissolved in solution or when introduced into confined environments. Alternatively, asymmetric supramolecular structures may form, analogous to cholersteric liquid crystals, in which there is no requirement for a non-planar polymer backbone. Fully solvated PCPDTBT* is unlikely to form a stable helical structure based on the absence of a CD signal in a good solvent. Differentiating between a helical backbone structure within the aggregates and a supramolecular chiral packing motif is more difficult. Moreover, there is no reason why chiral helical chains cannot pack in non-centrosymmetric units.

5. Chiroptical Solution Characterization of PCDTPT*

The chiroptical properties of PCPDTBT* provoke the question of generality in structurally related conjugated polymers. PCDTPT* was therefore synthesized and characterized for comparison. The mixed solvent system tested with PCPDTBT* (1:1 CB:DIO), did not induce aggregation of PCDTPT chains. Therefore, multiple solvent systems were screened and 8:2 CB:dimethyl sulfoxide (DMSO) showed the optimal balance of inducing aggregation without causing the polymer chains to precipitate out of solution.

As shown in Figure 2-10, dilute CB:DMSO solutions of PCDTPT* and PCDTPT show very similar absorption profiles, with shoulder peaks at ~875 nm. The spectra obtained in the poor solvent mixture is substantially red-shifted from what is observed for PCDPTP* in the good solvent CB. As the temperature is increased, the absorption shoulder of PCDTPT* in CB:DMSO progressively disappears (Figure 2-11). These features qualitatively resemble the temperature dependence of PCPDTBT* absorption.

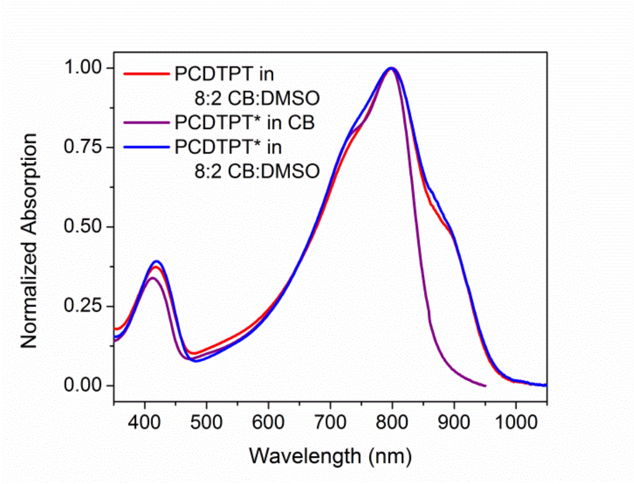

Figure 2-10. Normalized optical absorption spectra of PCDTPT in CB:DMSO (red), PCDTPT* in CB (purple), and PCDTPT* in CB:DMSO (blue).

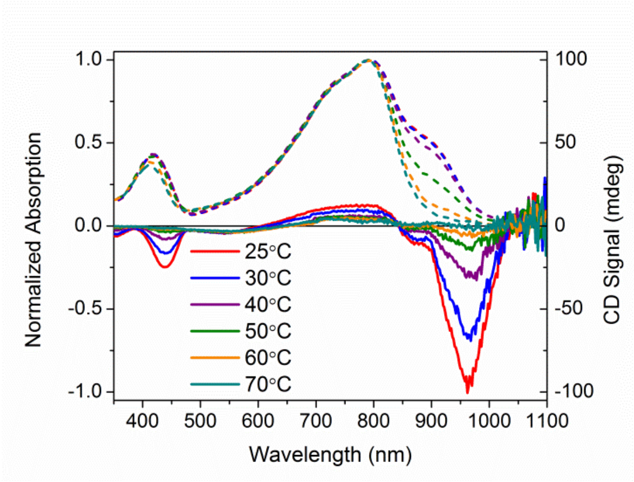

Figure 2-11. Normalized optical absorption (dashed) and CD (solid) spectra of PCDTPT* in CB:DMSO as a function of temperature, from 25-70°C.

CD signals are present for PCDTPT* in CB:DMSO solutions but not for PCDTPT in CB:DMSO or PCDTPT* in CB solutions (Figure 2-12). Similar to PCPDTBT*, a bisignate Cotton effect is observed at the high energy π→π* transition. A second bisignate Cotton effect is centered near the absorption shoulder peak (960 nm). The CD spectrum of PCDTPT* as an aggregate in solution is opposite in sign compared to that of PCPDTBT* despite containing the same chiral substituent. A plausible explanation for this phenomenon is the different solvent system used. Previous work has highlighted how a change in solvent polarity can induce an inversion of the CD spectrum for a single material.[107-110] DMSO is a more polar solvent than DIO, potentially giving rise to a similar effect in this study. As solutions of PCDTPT* in CB:DMSO are heated, the CD signal essentially disappears (Figure 2-11). These data further confirm the necessity of a multichain aggregate to achieve chiroptical response. For PCDTPT* in CB:DMSO, the average g_{abs} calculated for the aggregate absorption peak (920 nm) is -0.0016, much smaller in magnitude relative to PCPDTBT* in CB:DIO (0.013).

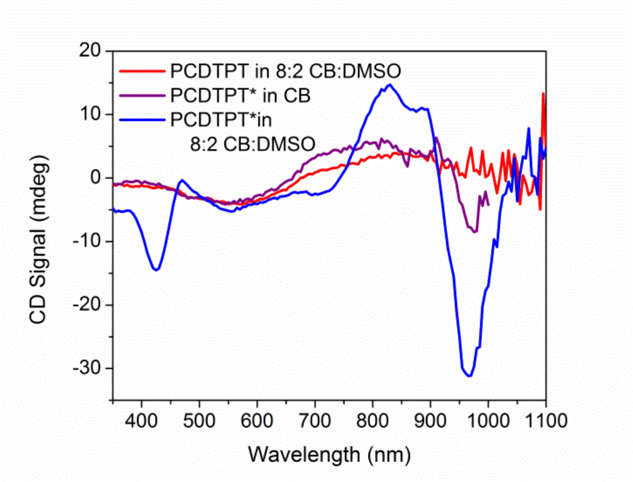

Figure 2-12. CD spectra of PCDTPT in CB:DMSO (red), PCDTPT* in CB (purple), and PCDTPT* in CB:DMSO (blue).

6. Solid State Characterization of PCDTPT*

Thin films spun-cast from 8 mg/mL solutions of PCDTPT* and PCDTPT in CB onto clean glass substrates exhibit absorption characteristics similar to each other and both are red shifted relative to what is observed in solution (Figure 2-13). Thermal annealing does not significantly change the absorption profile (Figure S2-12). Surprisingly, CD spectroscopy shows no measurable signal for either PCDTPT or PCDTPT* films (Figure 2-14). The absence of a CD signal indicates the failure of PCDTPT* to achieve chiral organization in the thin film. AFM topography images (Figure S2-23) show little difference between PCDTPT and PCDTPT* films, further emphasizing the absence of obvious morphological differences.

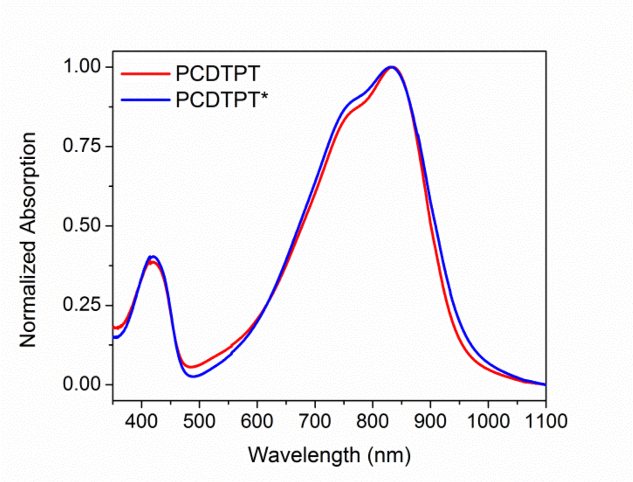

Figure 2-13. Normalized thin film absorption spectra of PCDTPT (red) and PCDTPT* (blue).

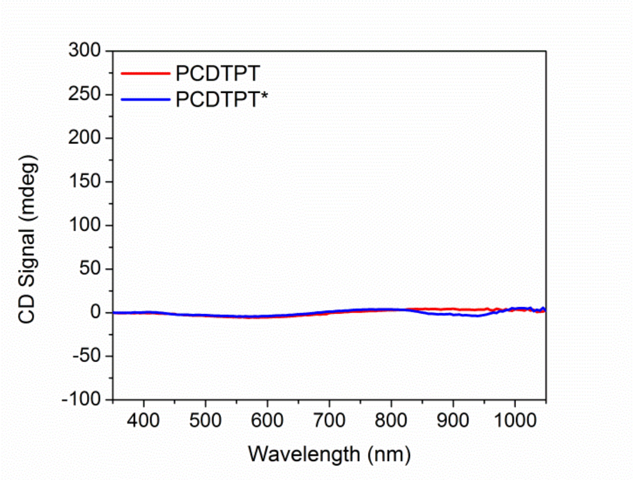

Figure 2-14. CD spectra of thin film controls: PCDTPT (red) and PCDTPT* (blue).

7. Comparison of PCPDTBT* and PCDTPT*

Both PCPDTBT* and PCDTPT* form aggregated domains with chiral response in poor solvents. However, PCDTPT* assembles with a weaker degree of chiral order. Specifically, PCPDTBT* provides an average g_{abs} value one order of magnitude greater than PCDTPT* in solution within the absorption range attributed to aggregated chains. Even more revealing, PCPDTBT* exhibits a chiral response in the thin film whereas PCDTPT* does not. This suggests that the substitution of one –CH group for a –N group on the benzothiadiazole unit results in substantially different secondary structures for PCPDTBT* and PCDTPT*.

It seemed reasonable to explore whether the higher degree of chiral order in PCPDTBT* compared to PCDTPT* may result from differences in the ability to form helical conformations and therefore on the rotational barriers between structural units in the backbone. A polymer coil with more conformational freedom would reasonably more readily achieve twisted conformations required in the helical secondary structure. Therefore, density functional theory (DFT), using the CAM-B3LYP functional and the 6-31G basis set was employed to estimate the rotational barrier of CDT-BT and CDT-pPT (pyridyl nitrogen) monomer units, see Figure 2-15 for molecular substructures.[111] The results using a dielectric function similar to chlorobenzene are provided in Figure 2-15, while results calculated in vacuum are given in Figure S2-25. The calculated rotational barrier of CDT-pPT (~9 kcal/mol) is greater than CDT-BT (~4 kcal/mol). By extension, the rotational barriers of structural units in PCDTPT* are likely higher than those in PCPDTBT* based on the presence of the CDT-pPT structural units in the conjugated backbone.[89,112] As a result, the lower rotational barrier of PCPDTBT*, relative to the stiffer PCDTPT*, would lower the energy requirements to acquire a helical conformation, providing a greater g_{abs} value.

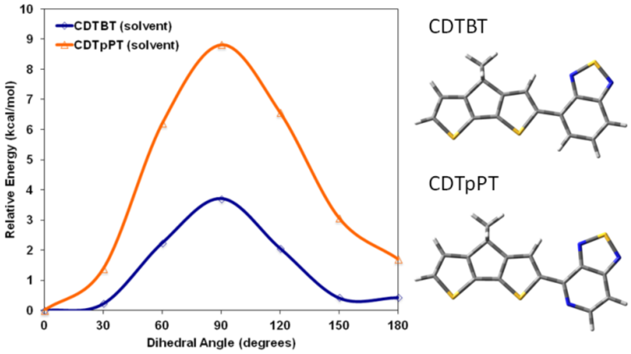

Figure 2-15. Calculated rotational barriers for CDT-BT (blue) and CDT-pPT (orange) in chlorobenzene.

8. Chiroptical Solution Studies of Mixtures of PCPDTBT and PCPDTBT*

In order to probe for potential intrachain helical structures, a mixture of PCPDTBT and PCPDTBT* at a ratio of 9:1 in CB:DIO was studied. The CD signal disappeared upon heating to 60°C. The solution was allowed to heat at 60°C overnight after degassing with argon. After allowing the solution to cool back down to 25°C, the CD signal was re-measured and the results are shown in Figure 2-16. The initial CD signal is roughly one-tenth of the CD signal using just PCPDTBT* in CB:DIO; corresponding to the solution containing only one-tenth PCPDTBT*. After heating overnight, the CD signal is still present and larger than the original signal.

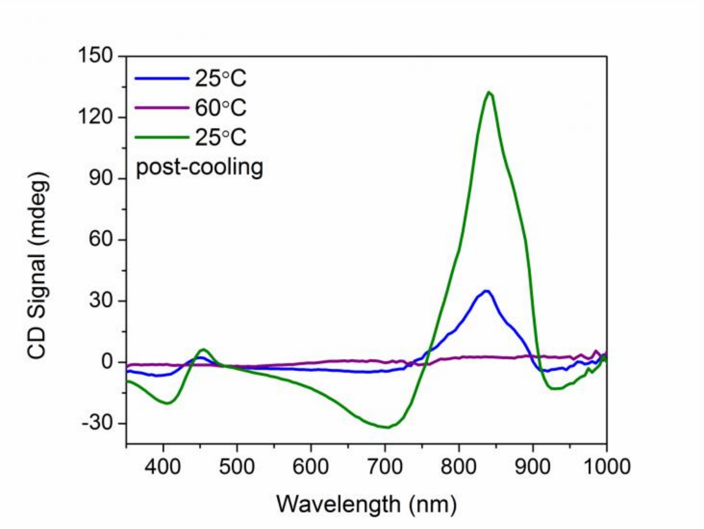

Figure 2-16. CD spectra of 9:1 PCPDTBT:PCPDTBT* in CB:DIO at 25°C (blue), at 60°C (purple), and at 25°C after heating overnight (green).

9. Conclusions

In conclusion, we provide the synthesis of two narrow bandgap conjugated polymers containing chiral 2-ethylhexyl side chains and backbone structures that have found widespread utility in the fabrication of organic (opto)electronic devices. The absorption and CD spectra of PCPDTBT* and PCDTPT* and comparison versus their non-chiral counterparts are consistent with helical aggregates in solution. That one can achieve a similar fraction of aggregated chains for PCPDTBT* and obtain different g_{abs} values (Figure 2-5) indicates that there is complexity in the internal structure of the aggregates. It appears that the degree of aggregation is temperature dependent and thermodynamically determined, whereas the fraction of more ordered chiral, and most likely helical, domains reflect the kinetics of the assembly process. As determined by GIWAXS examination, in the case of PCPDTBT*, the more homogenous molecular structure relative to PCPDTBT translates to a more ordered thin film upon solution deposition. The greater degree of order in the thin films of PCPDTBT* compared to PCPDTBT provides potential for higher charge-carrier mobilities. Thus future work to determine the performance of these materials in OFETs and OPV devices is warranted.

Despite their close structural similarities at the molecular level, PCDTPT* shows a smaller tendency to form chiral aggregates based on its smaller solution g_{abs} compared to PCPDTBT* and on the fact that it fails to provide a chiral response in the thin film. This difference may be rationalized by the calculated higher barrier to rotation within the CDT-pPT unit, compared to the CDT-BT unit. The higher rotational barrier contributes to a planar structure of PCDTPT*. The tendency toward a more planar structure for PCDTPT* is worth highlighting, since it may contribute to the polymer's high carrier mobility previously observed in aligned fiber OFETs, where charge transport occurs predominantly along the backbone direction. One should also consider that helical backbone arrangements may be present in solid-state organizations of other common narrow bandgap conjugated polymers with racemic side chains. Such a situation would lead to an equal number of helical subunits of opposite chirality. If so, our understanding of long range packing preferences that determine electronic coupling and the vast amount of detailed structural characterization of narrow bandgap conjugated polymers in the literature would need to be further refined.

C. Chiroptical Properties of PCDTFBT as a Function of Molecular Weight*

1. Introduction

The hypothesized relationship between calculated rotational barrier and the ability of a conjugated polymer containing a chiral side chain to form a helical structure posed by the previous work prompted the study of another analogous conjugated polymer backbone structure, PCDTFBT (Figure 2-17). The rotational barrier of CDT-FBT was determined to be similar to CDT-BT.[113] The monomer unit of PCDTFBT differs from PCPDTBT by the replacement of the benzothiadiazole acceptor unit with a fluorobenzothiadiazole (FBT) such that a single –CH is replaced by –CF. Replacing a hydrogen atom with a fluorine atom increases the electron poor character of the acceptor unit and lowers the HOMO level of the resulting D-A conjugated polymer.[113] Thus, like PCPDTBT and PCDTPT, PCDTFBT has also been tested in organic solar cell applications as the donor material in combination with PCBM.[114] For solar cell applications with PEDOT-PSS as the hole-transport layer, unlike the PT unit, the FBT unit does not contain a basic nitrogen atom which can be protonated by the acidic PEDOT-PSS.[115]

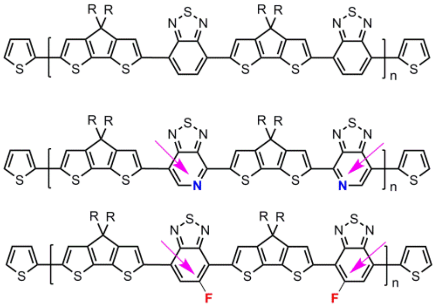

Figure 3-17. Chemical structures of PCPDTBT (top), PCDTPT (middle), and PCDTFBT (bottom).

The previous work hypothesized the formation of a helical aggregate structure rather than helical single polymer chains. This raised the question concerning the effect of molecular weight on the helical aggregate formation. A chiral response from a polymer chain containing only a few repeat units would provide support for the idea of a helical aggregate structure. With only a few repeat units, the polymer chain is unlikely to be able to form a single chain helix with a measurable CD signal. PCDTFBT*, containing chiral 2-(S)-ethylhexyl side chains, was synthesized at three different molecular weight values along with its racemic analog. The three different molecular weights were obtained by saving three different fractions during the Soxhlet extraction. This method allows comparison of different molecular weights from the same batch of polymer, removing uncertainty concerning differing purity of the starting monomer units. The results are reported below.

2. Synthesis

The target polymer, PCDTFBT*, is regiorandom rather than regioregular, with respect to the fluorine orientation toward the CDT, as opposed to PCDTPT*. Previous work has shown while regioregular PCDTFBT provides higher charge carrier mobilities, there is little difference in the absorption and x-ray scattering characteristics[114]. The synthesis of EH-S-$CDTSn_2$ was carried out exactly as described in the previous section.[95] The polymerization of EH-S-$CDTSn_2$ and FBT-Br_2 was carried out by using microwave-assisted Stille-coupling polymerization conditions in a xylene:DMF solvent system with 0.052 eq. $Pd(PPh_3)_4$ as the catalyst as shown in Scheme 2-3.[114] The resulting polymer was purified via Soxhlet extraction and each solvent fraction (hexane, chloroform, and the remaining insoluble material) was saved. Thus PCDTFBT* at three different molecular weights was obtained. The molecular weight was determined using GPC running chloroform as the eluent relative to PS standards. The hexane fraction of PCDTFBT* (H-PCDTFBT*) produced M_n = 2.9k and $Đ$ = 1.2 and the chloroform fraction (C-PCDTFBT*) produced M_n = 14k and $Đ$ = 1.7. The highest molecular weight fraction (I-PCDTFBT*) was insoluble in chloroform and therefore no molecular weight data is available. PCDTFBT, containing racemic 2-ethylhexyl side chains, was synthesized using the same procedure (Scheme S2-13). The hexane fraction of PCDTFBT (H-PCDTFBT) produced M_n = 3.2k and $Đ$ = 1.2 and the chloroform fraction (C-PCDTFBT) produced M_n = 13k and $Đ$ = 1.5. The highest molecular weight fraction of PCDTFBT (I-PCDTFBT) was also insoluble in chloroform and lacking in molecular weight data. Molecular weight data is summarized in Table 2-1.

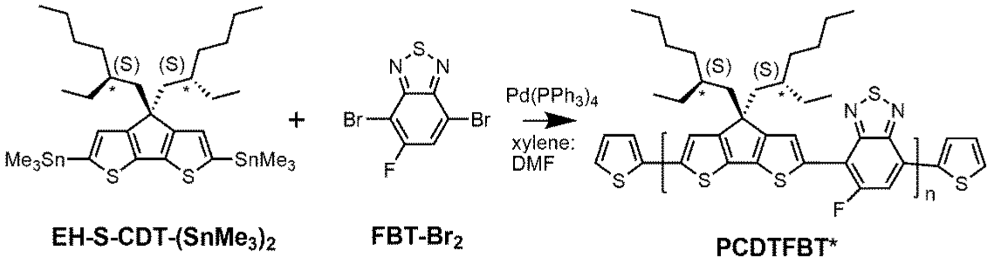

Scheme 2-3. Synthesis of PCDTFBT*.

Table 2-1. Molecular Weight Data for PCDTFBT

	M_n (Da)	$Đ$
H-PCDTFBT*	2.9k	1.2
C-PCDTFBT*	14k	1.7
I-PCDTFBT*	n/a	n/a
H-PCDTFBT	3.2k	1.2
C-PCDTFBT	13k	1.5
I-PCDTFBT	n/a	n/a

3. Chiroptical Properties of PCDTFBT* in Solution

The solvent system chosen to induce aggregation without causing the polymer chains to precipitate out of solution for PCDTFBT* was dependent on molecular weight. The appropriate balance was achieved using the following solvent systems: 2:8 CB:DMSO for H-PCDTFBT*, 8:2 CB:DMSO for C-PCDTFBT*, and CB for I-PCDTFBT*. The same solvent systems were used for the racemic analogs. Dilute solutions were used for all spectroscopic work.

Optical absorption spectra of C-PCDTFBT* and C-PCDTFBT were measured in both CB and 8:2 CB:DMSO at 0.03 mg/mL. No obvious difference is observed in the two spectra as shown in Figure 2-18a. Optical absorption spectra of PCDTFBT* were measured as a function of molecular weight in CB and the results are shown in Figure 2-18b. The onset of absorption and the absorption maximum show a redshift as the molecular weight increases. Previous work studying conjugated polymer optical properties as a function of molecular weight has shown similar results.[116-118] The increased number of repeat units on the conjugated backbone allows electron delocalization over a larger area – more electron delocalization typically leads to a narrower bandgap – or due to increased, ordered aggregates.[116-118]

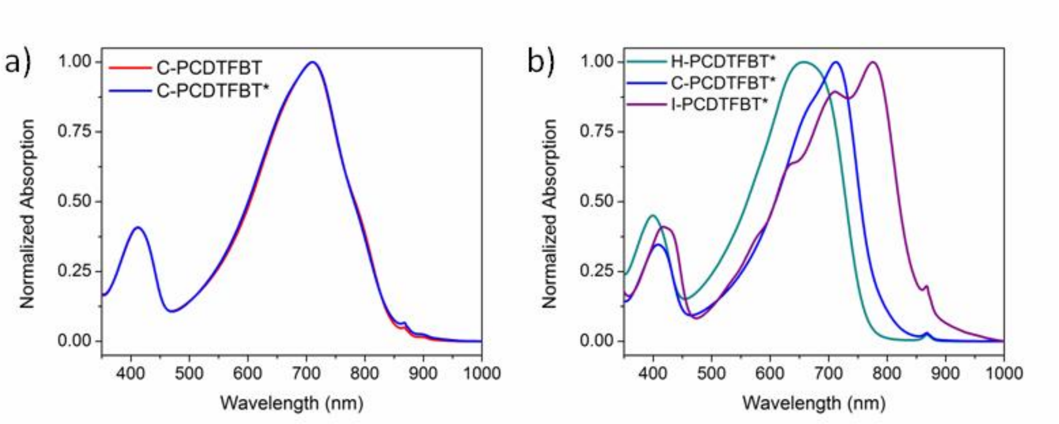

Figure 3-18. Normalized optical absorption spectra of a) C-PCDTFBT (red) and C-PCDTFBT* (blue) in 8:2 CB:DMSO and b) H-PCDTFBT* (cyan), C-PCDTFBT* (blue), and I-PCDTFBT* (purple) in CB.

H-PCDTFBT* in 2:8 CB:DMSO and C-PCDTFBT* in 8:2 CB:DMSO exhibit small, red-shifted shoulder peaks compared to solutions in CB (Figure S2-12, S2-13). This feature has been previously implicated to arise from aggregated chains in solution[25] as mentioned in the previous section. I-PCDTFBT* showed evidence of polymer chain precipitation when even a small amount of poor solvent was added to solutions in CB. Therefore, this observation combined with the absorption spectrum indicated aggregation of I-PCDTFBT* in CB. This result is unsurprising considering higher molecular weight conjugated polymers tend to be less soluble.

Bisignate Cotton effects are observed for H-PCDTFBT* (Figure 2-19b), C-PCDTFBT* (Figure 2-19), and I-PCDTFBT* (Figure 2-19b) in solutions containing aggregated chains but no signal is observed for their racemic counterparts. Similar to PCPDTBT* and

PCDTPT*, all three molecular weights of PCDTFBT* provide bisignate Cotton effects at the π→π* transition and in the aggregate absorption wavelength region. These results suggest a helical aggregate structure rather than single-chain helices.[77] As the molecular weight increases, the CD maximum at the aggregate absorption shifts to longer wavelengths. This red-shift agrees with the red-shift observed in the optical absorption spectra. H-PCDTFBT* provides the lowest intensity CD response. Two possible explanations include one, the presence of more well-dissolved chains or two, a smaller ratio of chiral aggregation. It is not possible to reach a conclusion from the data provided.

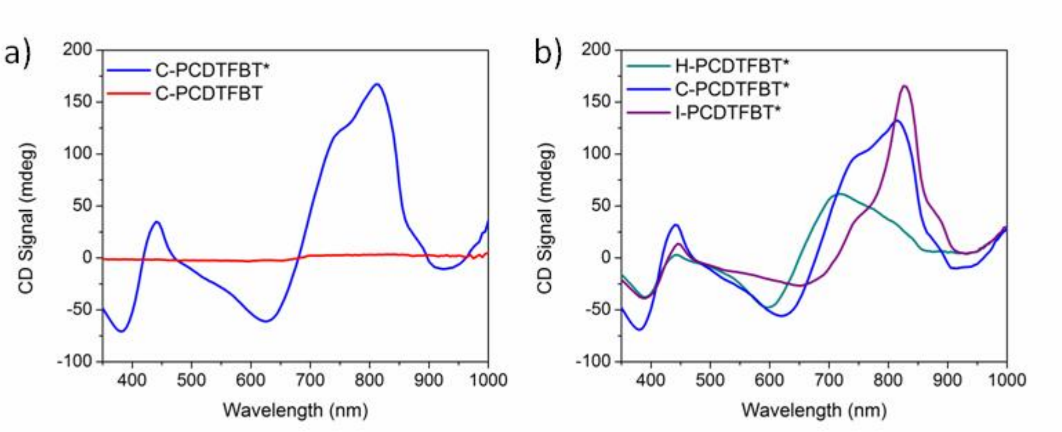

Figure 2-19. CD spectra of a) C-PCDTFBT (red) and C-PCDTFBT* (blue) in 8:2 CB:DMSO and b) H-PCDTFBT* in 2:8 CB:DMSO (cyan), C-PCDTFBT* in 8:2 CB:DMSO (blue), and I-PCDTFBT* in CB (purple).

Temperature dependent spectra of C-PCDTFBT* were measured in dilute 8:2 CB:DMSO solutions, and the results are shown in Figure 2-20. In these experiments, solutions were heated from 25°C to 90°C and absorption/CD measurements were taken every 10°C. C-PCDTFBT* was chosen as a representative example of the three molecular weights. Optical absorption spectra for H-PCDTFBT* and I-PCDTFBT* can be found in the SI of this section. As the temperature increases, the absorption shoulder peak decreases such that the spectrum at 90°C resembles that of C-PCDTFBT* in CB. This suggests the break-up of aggregates into single chains with increasing temperature.

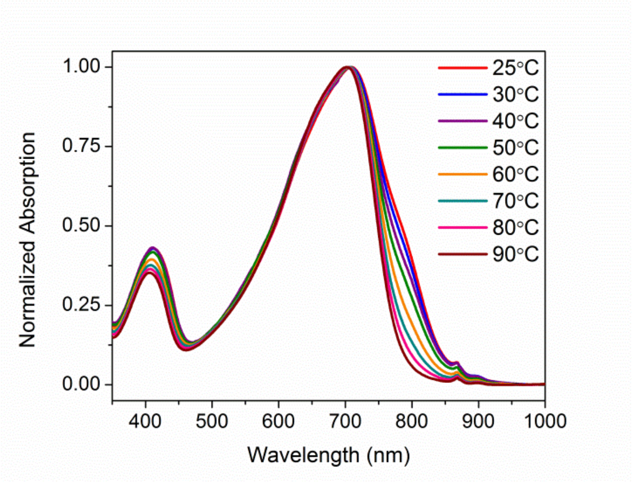

Figure 3-20. Normalized optical absorption spectra of C-PCDTFBT* in 8:2 CB:DMSO as a function of temperature, from 25-90°C.

Temperature dependent CD spectra of C-PCDTFBT* show a decrease in signal strength with increasing temperature (Figure 2-21). The CD response disappears by 90°C. The thermochromic behavior of C-PCDTFBT* as measured by both optical absorption and CD spectroscopies supports the hypothesis that interchain interactions are necessary to obtain a chiroptical response. This is in agreement with the observed behavior of PCPDTBT* and PCDTPT* in solution.

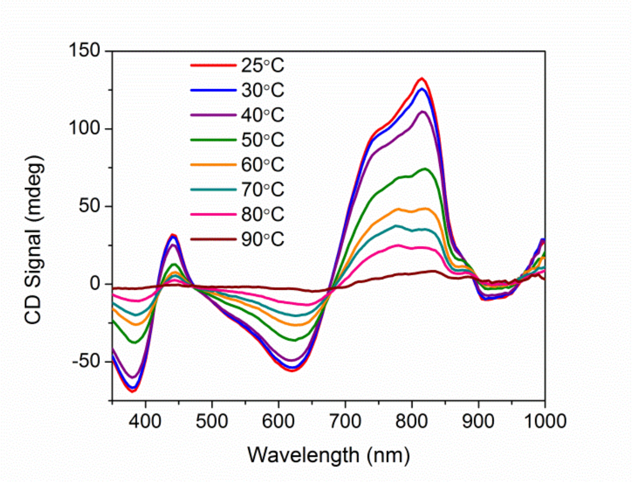

Figure 2-21. CD spectra of C-PCDTFBT* in 8:2 CB:DMSO as a function of temperature, from 25-90°C.

The average g_{abs} was calculated for the aggregate absorption peak for each molecular weight of PCDTFBT* and summarized in Table 2-2. The g_{abs} of H-PCDTFBT* is one order of magnitude lower than C-PCDTFBT* and I-PCDTFBT*. This further suggests a lesser degree of chiral organization in H-PCDTFBT* compared to C-PCDTFBT* and I-PCDTFBT*. The g_{abs} values of C-PCDTFBT* and I-PCDTFBT* in solution are on the same order of magnitude as PCPDTBT* (0.013).

Table 2-2. Average g_{abs} Values at the Aggregate Absorption Peak

	G_{abs}	Wavelength (nm)
H-PCDTFBT*	0.0022	720
C-PCDTFBT*	0.014	815
I-PCDTFBT*	0.019	825

4. Chiroptical Properties of PCDTFBT* in the Solid State

Thin films of C-PCDTFBT*, H-PCDTFBT*, C-PCDTFBT, and H-PCDTFBT were obtained by spin-coating or drop-casting 5 mg/mL CB solutions onto clean glass substrates and characterized using optical absorption and CD spectroscopies. Analogous films of I-PCDTFBT* and I-PCDTFBT were also fabricated but all films were thinner than desired. Due to poor solubility, it was not possible to increase the concentration of the solution in order to obtain thicker films. No obvious difference is observed between the thin film absorption spectra C-PCDTFBT* and C-PCDTFBT (Figure 2-22a) or between H-PCDTFBT* and H-PCDTFBT (Figure S2-14a). The absorption maximum of the thin film is red-shifted in comparison with the solution absorption measurements. The onset of absorption and the absorption maximum shift toward longer wavelengths as the polymer molecular weight increases (Figure 2-22b). This trend agrees with our observations of these materials in solution.

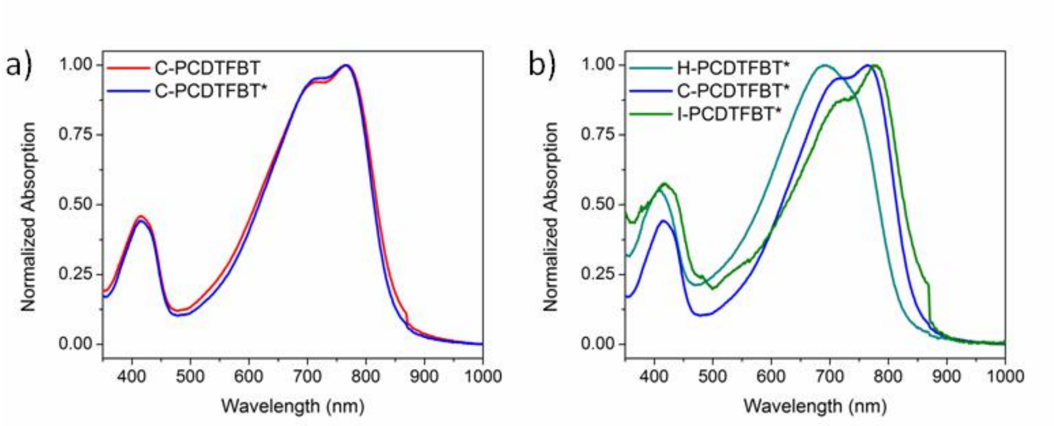

Figure 2-22. Normalized thin film optical absorption spectra of a) C-PCDTFBT (red) and C-PCDTFBT* (blue) and b) H-PCDTFBT* (cyan), C-PCDTFBT* (blue), and I-PCDTFBT* (green).

The CD spectra of H-PCDTFBT*, C-PCDTFBT*, and I-PCDTFBT* (Figure 2-23) suggest chiral organization in the solid state whereas the analogous racemic films provide no CD response, indicating that chiral organization in solution is translated to the solid state. The CD response in the thin film is composed of two bisignate Cotton effects in the case of all three molecular weights of PCDTFBT*, similar to the solution measurements. Despite containing a shorter polymer chain, H-PCDTFBT* still forms a chiral structure in the film. However the intensity of the CD response is smaller than the higher molecular weight samples. I-PCDTFBT* also shows a smaller CD signal compared to C-PCDTFBT*, likely due to differences in film thickness. I-PCDTFBT* also exhibits a red-shift in CD signal compared to C-PCDTFBT* in agreement with the red-shift observed in the optical absorption spectra. The difficulty in dissolving I-PCDTFBT* at concentrations sufficient for spin-coating combined with its tendency to dewet the glass substrate during drop-casting resulted in thinner films of I-PCDTFBT* compared to C-PCDTFBT*.

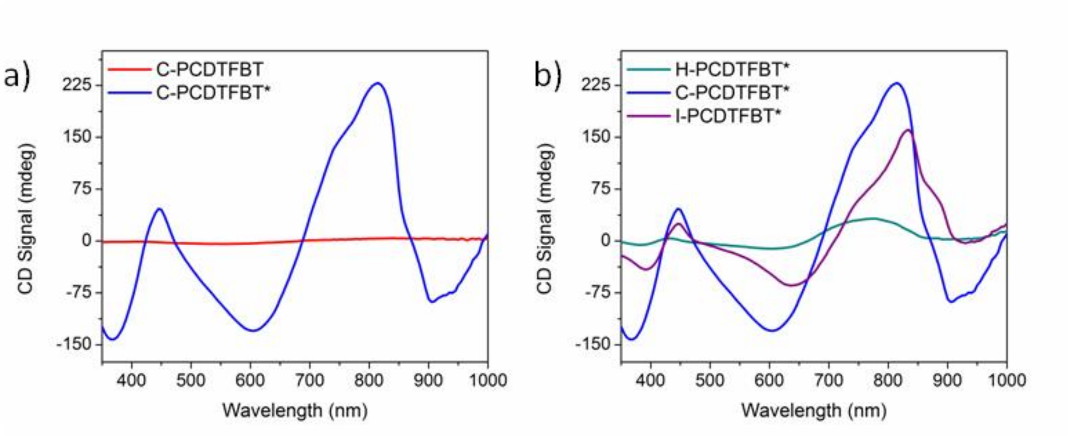

Figure 2-23. Thin film CD spectra of a) C-PCDTFBT (red) and C-PCDTFBT* (blue) and b) H-PCDTFBT (cyan), C-PCDTFBT* (blue), and I-PCDTFBT* (purple).

The average g_{abs} was calculated for the aggregate absorption peak of the thin film for each molecular weight of PCDTFBT* and summarized in Table 2-3. The average g_{abs} of H-PCDTFBT* is one order of magnitude smaller than C-PCDTFBT* and I-PCDTFBT*. H-PCDTFBT* and C-PCDTFBT* provide a slight increase in comparison to their solution values but retain the same order of magnitude. The thin film g_{abs} values of C-PCDTFBT* and I-PCDTFBT* are similar to PCPDTBT* (0.037).

Table 2-3. Average g_{abs} Values at the Thin Film Aggregate Absorption Peak

	G_{abs}	Wavelength (nm)
H-PCDTFBT*	0.0034	775
C-PCDTFBT*	0.028	815
I-PCDTFBT*	0.014	835

5. Conclusions

PCDTFBT* was synthesized at three different molecular weights via separation by GPC. The optical absorption spectra exhibit a red-shift in the absorption maximum as the molecular weight increases, in agreement with past work demonstrating an increase in electron delocalization with increasing molecular weight.[116-118] All three molecular weights of PCDTFBT* provide a CD response when aggregated in solution, however, the amount of poor solvent (DMSO) required for polymer chain aggregation increases with decreasing molecular weight. The chiral organization in solution is found to translate to the solid state. H-PCDTFBT* provides a g_{abs} value one order of magnitude lower than C-PCDTFBT* or I-PCDTFBT* both in solution and in the solid state. Likely either a smaller chiral aggregate or a lesser degree of twisting within the aggregate is responsible for the smaller CD response. More work is necessary to determine how a smaller polymer chain influences the resulting aggregate structure.

The rotational barrier of the CDT-FBT unit is lower than that of the CDT-PT unit. Based on the previous work covering PCPDTBT* and PCDTPT*, the lower rotational barrier of PCDTFBT* predicts a chiroptical response both in solution and the solid state. All three molecular weight fractions of PCDTFBT* confirm this prediction. Specifically, the g_{abs} values of C-PCDTFBT* and I-PCDTFBT* are similar to PCPDTBT*. The correlation between the rotational barrier and the ability of the conjugated polymer to provide a CD response suggests a degree of twisting of the conjugated backbone is required to form the final chiral aggregate structure. Further work on the influence of regioregularity and the replacement of the FBT unit with ffBT unit on the chiroptical properties of the resulting polymer may highlighter further structure-property relationships.

*D. Chiroptical Properties of PIPCP**

1. Introduction

The previous two sections of this chapter analyze structure-property relationships of conjugated D-A copolymers based on incremental changes of the acceptor unit. Changes in the donor unit also have potential to impact the secondary structure and thus the chiroptical properties of the copolymer through changes to the spacing and number of side chains, backbone planarity, and energy levels. One option is to change one CDT unit in the PCDTPT* monomer to an indacenodithiophene (IDT) unit to produce PIPCP*. As depicted in Figure 2-24, PIPCP* contains regioregular PT units with the nitrogen atoms oriented toward the CDT unit and away from the IDT unit. The CDT unit contains two chiral (*S*)-2-ethylhexyl side chains, similar to the previous three polymer structures. However, the IDT unit contains hexyl chains in the *para*-position on each branched phenyl unit rather than chiral (*S*)-2-ethylhexyl chains. Thus, the number of chiral substituents per monomer unit decreases from four to two.

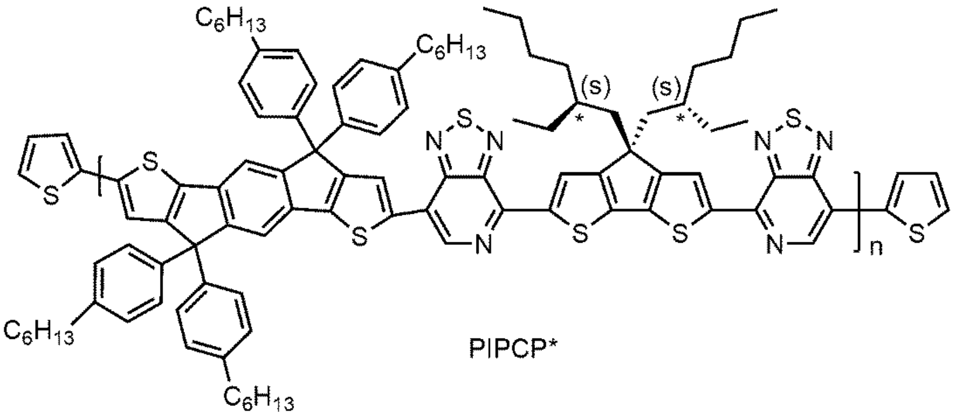

Figure 2-24. Sturcture of PIPCP*.

PIPCP containing racemic 2-ethylhexyl side chains on the CDT unit has previously been incorporated as the donor material in bulk heterojunction organic solar cells.[119-122] Molecular design suggested that the strong donor ability of the CPDT unit enhance the ICT character of the excited state and the IDT unit maintains a relatively deep HOMO energy level.[119] Solution absorption indicates PIPCP forms aggregates even in good solvents such chlorobenzene.[119] PIPCP, when blended with $PC_{60}BM$, achieves an average PCE of 5.86% with low V_{oc} loss.[119] The results achieved with PIPCP containing racemic 2-ethylhexyl side chains prompted their replacement with chiral (*S*)-2-ethylhexyl side chains with the goal of exploring the secondary structure and aggregation of the polymer chains.

2. Synthesis

The target polymer, PIPCP* is regioregular with the nitrogen atoms oriented toward the CDT unit, similar to PCPDTPT*, and is shown in Scheme 2-4. The synthesis of PT-EH-S-CDTSn$_2$-PT was carried out exactly as described in the section B.[95] The polymerization of PT-EH-S-CDTSn$_2$-PT and IDT-(SnMe$_3$)$_2$ was carried out by using microwave-assisted Stille-coupling polymerization conditions in a xylene:DMF solvent system with 0.052 eq. Pd(PPh$_3$)$_4$ as the catalyst as shown in Scheme 3-4.[119] The resulting polymer was purified by soxhlet extraction and the dichloromethane (DCM) fraction was collected. After running the DCM fraction through a silica gel column, the molecular weight was determined using GPC running chloroform as the eluent relative to PS standards. PIPCP* produced M_n = 47,600 and $Đ$ = 2.1. PIPCP, containing racemic 2-ethylhexyl side chains, was synthesized using the same procedure (Scheme S2-15). PIPCP produced M_n = 35,800 and $Đ$ = 2.1.

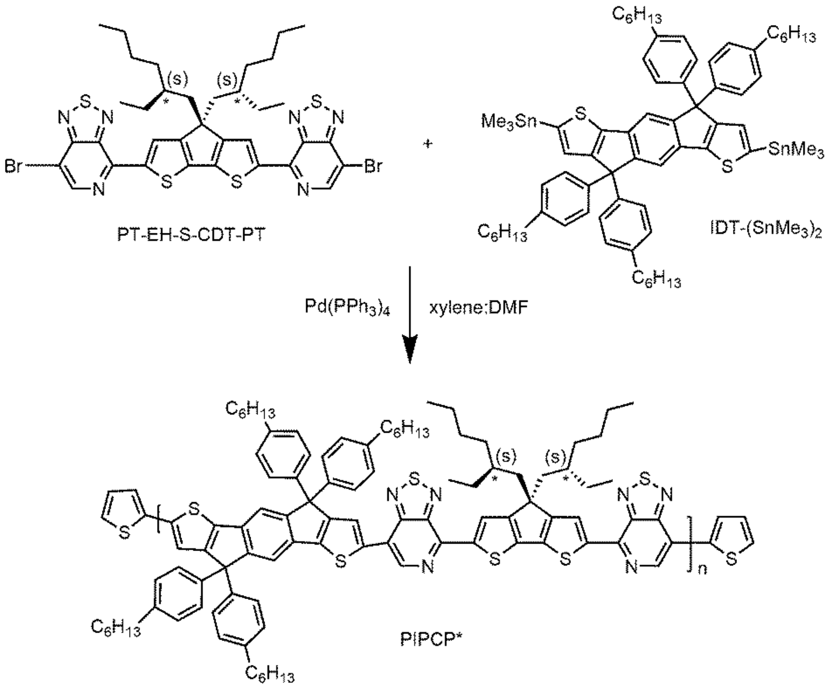

Scheme 2-4. Synthesis of PIPCP*.

3. Chiroptical Properties of PIPCP* in Solution

Similar strategies as described above were employed to study the chiroptical properties of PIPCP*. PIPCP* reveals aggregation even in solvents, such as chlorobenzene (CB), known to solubilize many conjugated polymers. This result is consistent with the literature on PIPCP with racemic side chains.[119] A comparison of PIPCP* and PIPCP is shown in Figure 2-25. The absorption profiles are the same with PIPCP exhibiting greater absorption compared to PIPCP*. The optical absorption profile as a function of temperature is shown in Figure 2-26. As the temperature is increased, the absorption maximum peak starts to decrease with a concomitant increase in absorption at shorter wavelengths. However, this change in absorption is minor compared to the disappearance of a shoulder peak for the polymers described above.

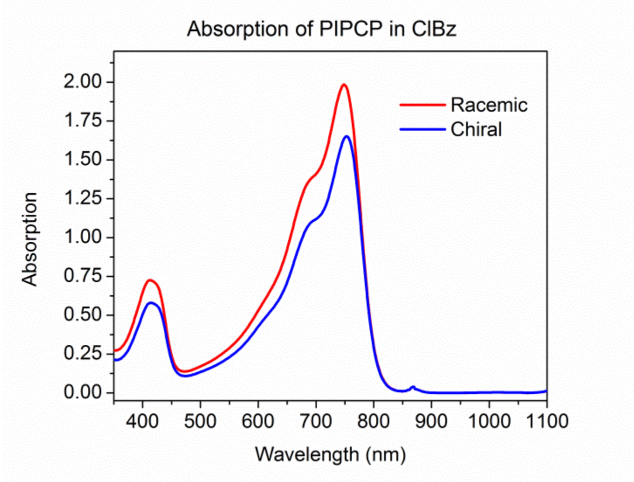

Figure 2-25. Optical absorption spectra of PIPCP (red) and PIPCP* (blue) in 0.03 mg/mL CB.

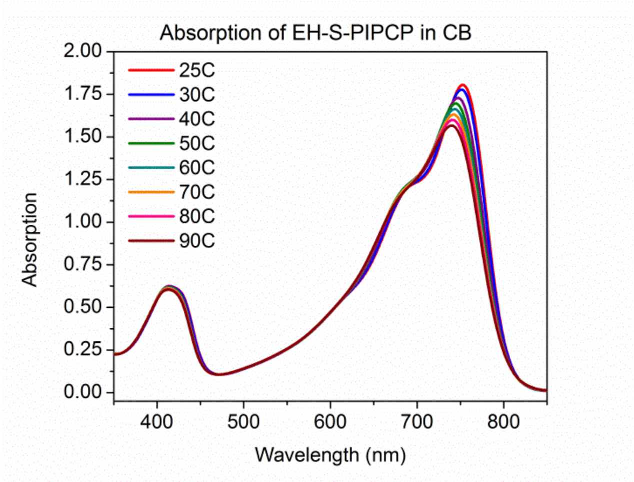

Figure 2-26. Optical absorption spectra of PIPCP* in CB as a function of temperature, from 25-90°C.

The CD spectrum of PIPCP* in CB is shown in Figure 2-27. The CD spectrum is roughly the first derivative of the absorption spectrum, as expected based on CD theory.[69] The absorption spectrum revealed aggregation in CB and the CD spectrum is correlates to the aggregation peaks. These data suggest that PIPCP* is chiral in the aggregated phase. When the CD spectrum is measured as a function of temperature, the CD signal decreases and eventually reaches the baseline at 60°C (Figure 2-28). The disappearance of the CD signal also suggests chirality in the aggregated phase.

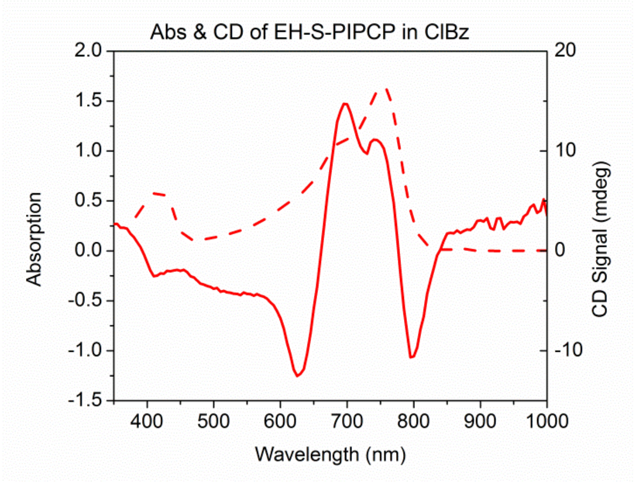

Figure 2-27. Absorption (dashed) and CD (solid) spectra of PIPCP* in 0.03 mg/mL CB at 25°C.

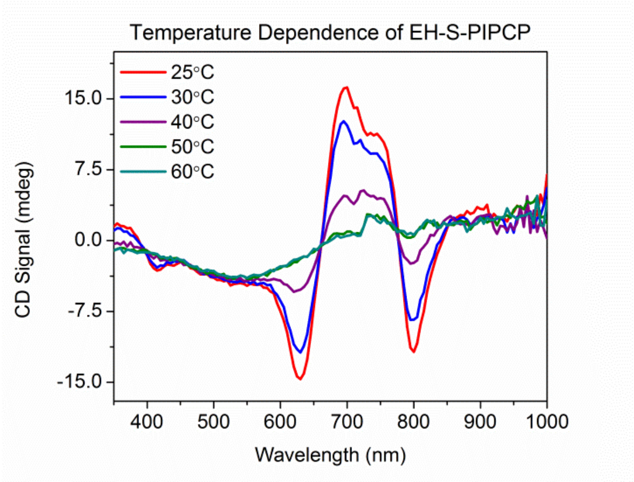

Figure 2-28. CD spectra of PIPCP* in 0.03 mg/mL CB as a function of temperature, from 25-60°C.

4. Chiroptical Properties of PIPCP* in the Solid State

Thin films of PIPCP and PIPCP* were obtained by spin-coating 5 mg/mL CB solutions onto clean glass substrates and characterized using optical absorption and CD spectroscopies. Thin film absorption measurements are shown in Figure 2-29. There is no significant difference in the absorption profiles of PIPCP and PIPCP*. The PIPCP film is likely thinner than the PIPCP* film, resulting in a lower maximum amount of absorption. Thermal annealing at 120°C for ten minutes has no effect on the absorption profile. CD spectra show a small signal for PIPCP* films but no signal for PIPCP films (Figure 2-30). Little to no change in the CD spectrum is observed upon thermal annealing. Compared to the magnitude of the signal for PCPDTBT* (~300), the CD signal of PIPCP* (~16) is not significant. This result is in agreement with PCDTPT* which also provided no significant CD signal in the thin film. The structural difference between PIPCP* and PCDTPT* is the replacement of one CDT unit for an IDT unit. The non-covalent interactions between the pyridal nitrogen on the PT group and the CDT group are still present and likely preventing the formation of chiral structures in the solid state.

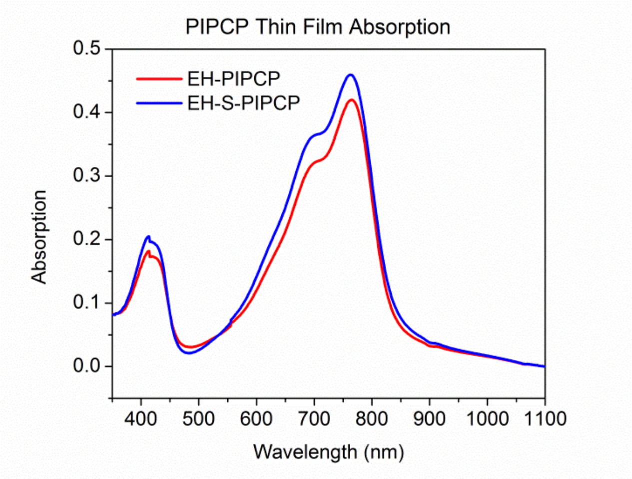

Figure 2-29. Thin film absorption of PIPCP (red) and PIPCP* (blue).

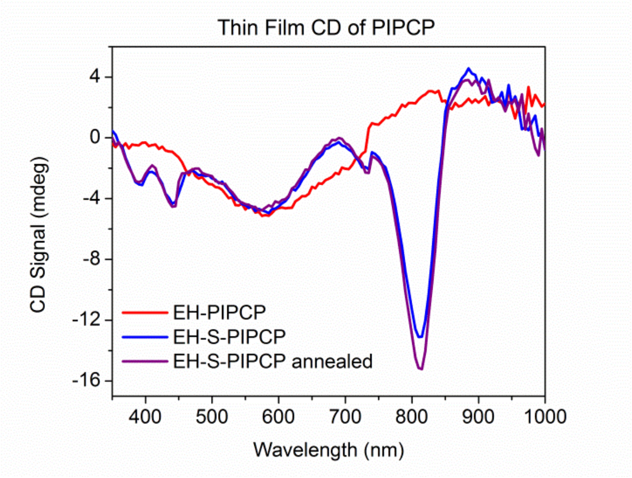

Figure 2-30. CD spectra of thin films of PIPCP (red), PIPCP* (blue), and PIPCP* after 10 minutes of annealing at 120°C (purple).

Conclusions

PIPCP* and PIPCP were synthesized and characterized for comparison with PCPDTBT* and PCDTPT*. PIPCP tends to strongly aggregate in solution, resulting in a CD signal when PIPCP* is dissolved in CB. The trend observed for the previous polymer containing chiral side chains continues with PIPCP*. A weak CD signal is observed for PIPCP* in solution in the aggregated phase. In the solid state, for similar absorption intensities, PIPCP* provides an almost insignificant CD signal compared to PCPDTBT*. The failure of PIPCP* to form significant chiral nanostructures in the solid state can be compared to the similar failure of PCDTPT*. Both polymers contain PT-CDT-PT units and the non-covalent interactions present in this monomer unit contribute to a high rotational barrier, preventing the twisting needed to form chiral structures.

E. Conclusions

A library of donor-acceptor copolymers containing a CDT unit with chiral side chains was synthesized and their chiroptical properties in solution and the solid state were characterized. These D-A copolymers containing chiral side chains produced chiral aggregates but their ability to form chiral structures within the aggregate cannot yet be proven. The rotational barrier of the monomer unit was found to influence the ability of the polymer to form chiral nanostructures. Higher rotational barriers promote the formation of planar conjugated backbones and prevent the twisting needed to form chiral structures, particularly in the solid state.

The structure-property relationships developed in this chapter add to the body of knowledge available for materials design of conjugated polymers for organic electronic applications. Achieving planar conformations is desirable in organic field effect transistor devices in promoting charge transport between and along polymer chains. Future work can utilize this understanding to design new polymer structures optimizing for planar backbone conformations.

F. Experimental and Supplementary Information

1. Materials and Methods

All reagents and solvents were purchased from Sigma Aldrich, BDM, Fisher Scientific, Alfa Aesar, or Acros Organics and used without further purification unless otherwise specified. Tetrakis(triphenylphosphine)palladium(0) [$Pd(PPh_3)_4$] was purchased from Strem Chemicals Inc. 4,7-dibromo-[1,2,5]thiadiazolo[3,4-c]pyridine (Br_2-PT) and 4,7-dibromo-[2,1,3]-benzothiadiazole (Br_2-BT) were purchased from Lumtec Co. *4H*-cyclopenta[2,1-*b*:3,4-*b*’]dithiophene (CDT) was purchased from WuXi AppTec Corporation. Deuterated solvents were purchased from Cambridge Isotopes Laboratories, Inc. Solvents used for air and/or water sensitive reactions (THF, toluene) were dried by passage through two columns of alumina and degassed by argon purge in a custom-built solvent purification system. Xylene at the ultra-dry grade was purchased from Acros Organics. Synthesis of EH-S-PCPDTBT and EH-S-PCDTPT were adapted from literature procedures.[84,88]

Microwave-assisted reactions were performed in a Biotage Initiator TM microwave reactor. ^{1}HNMR spectra were obtained on a Varian VNMRS 500 MHz or 600 MHz spectrometer at room temperature. GPC chromatographs were obtained using a Waters 2690 Separation Module with two Agilent PLGEL 5μm, MIXED-D columns running $CHCl_3$/0.25% triethylamine as eluent. Molecular weights were calculated relative to linear

PS standards. MALDI spectra were obtained on a Bruker Microflex series MALDI-TOF using a matrix of dithranol saturated chloroform.

2. Detailed Synthetic Procedures

Synthesis of (*S*)-2-ethylhexan-1-ol

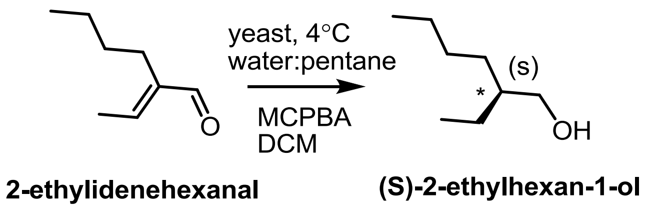

Scheme S2-1. Synthesis of (*S*)-2-ethylhexan-1-ol.

(*S*)-2-ethylhexan-1-ol was synthesized according to literature procedures.[96] HK_2PO_4 (16.647 g, 95.6 mmol), H_2KPO_4 (0.720 g, 5.29 mmol), and sucrose (10.280 g, 30.0 mmol) were dissolved in Millipore water (1000 mL). Yeast (200. g) was added slowly while stirring. The yeast mixture was allowed to stir for 2.5 hours. Pentane (1500 mL) was added. 2-ethylidene hexanal (10.254 g, 81.3 mmol) was added. The reaction was allowed to stir at 4°C for 1 week. The aqueous/yeast layer was removed by centrifugation. The resulting organic layer was filter through celite, concentrated under reduced pressure, and dried under vacuum. The resulting oil was dissolved in DCM (100 mL) and cooled to 0°C. MCPBA (7.904 g, 45.8 mmol) was added. The reaction was stirred for two hours. The reaction mixture was washed with water, dried over sodium sulfate, and concentrated under reduced pressure. The crude product was first purified by distillation. The product was then purified by column chromatography using 6:4 DCM:pentane as the eluent ($R_f \sim 0.25$). (S)-2-ethylhexan-1-ol was produced in 21% yield (2.181 g). ^{1}H NMR (500 MHz, $CDCl_3$) δ (ppm): 3.53 (d, 2H), 1.41-1.20 (m, 10H), 0.88 (t, 6H). ^{13}C NMR (600 MHz, $CDCl_3$) δ (ppm): 65.31, 41.95, 30.12, 29.09, 23.32, 23.08, 14.09, 11.12. GC/MS: calculated for

$C_8H_{18}O$ (m/z): 130.14, found 130. $[\alpha]_D$ = +2.954° (Concentration of 1.2 g/100 ml in acetone, 25 °C). ($[\alpha]_D$ = +3.1°,[97] e.e. = 95%).

Chiral Derivatization of (*S*)-2-ethylhexan-1-ol

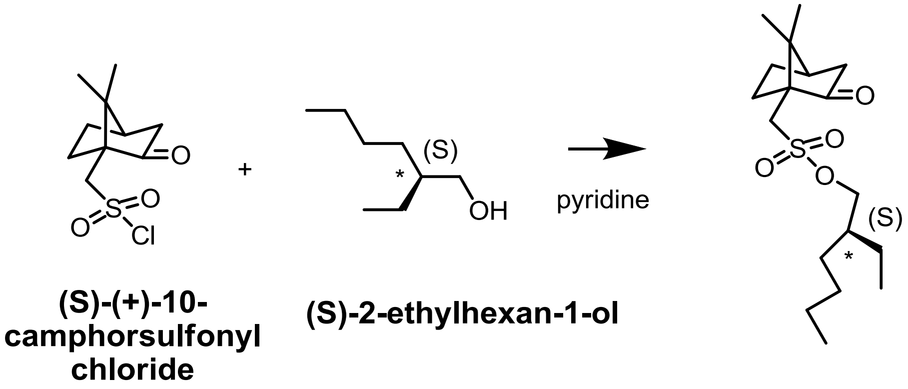

Scheme S2-2. Chiral derivatization reaction of (S)-(+)-10-camphorsulfonyl chloride and (S)-2-ethylhexan-1-ol.

(*S*)-2-ethylhexan-1-ol (0.0554 g, 0.425 mmol) and (*S*)-(+)-10-camphorsulfonyl chloride (0.1452 g, 0.579 mmol) were dissolved in pyridine (1 mL). The reaction was covered in aluminum foil and allowed to stir for about 16 hours. Pyridine was removed under reduced pressure. The mixture was separated using column chromatography with hexane:ethyl acetate (1:1) as the eluent ($R_f \sim 0.4$). The chiral adduct was produced at 79% yield (0.116 g). ^{1}H NMR (500 MHz, $CDCl_3$) δ (ppm): 4.16 (d, 2H), 3.57 (d, 1H), 2.96 (d, 1H), 2.48 (m, 1H), 2.36 (m, 1H), 2.10 (t, 1H), 2.01 (m, 1H), 1.92 (d, 1H), 1.66-1.57 (m, 2H), 1.46-1.34 (m, 3H), 1.33-1.19 (m, 6H), 1.10 (s, 3H), 0.87 (m, 9H).

Chiral Derivatization of 2-ethylhexan-1-ol

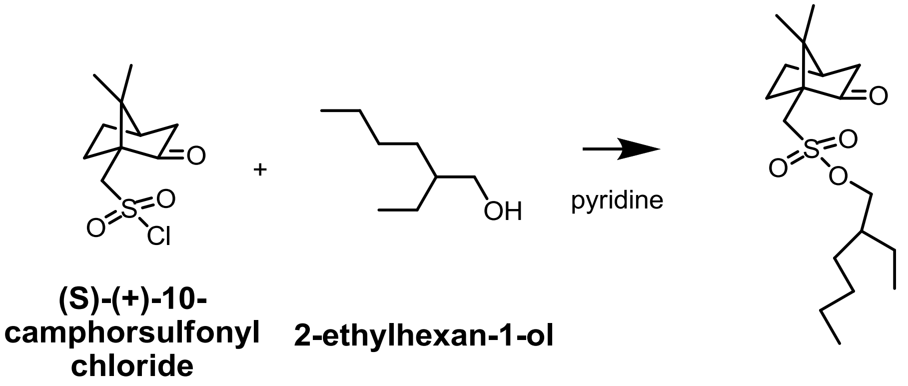

Scheme S2-3. Chiral derivatization reaction of (S)-(+)-10-camphorsulfonyl chloride and 2-ethylhexan-1-ol.

2-ethylhexan-1-ol (0.1149 g, 0.882 mmol) and (S)-(+)-10-camphorsulfonyl chloride (0.2895 g, 1.15 mmol) were dissolved in pyridine (2 mL). The reaction was covered in aluminum foil and allowed to stir for about 16 hours. Pyridine was removed under reduced pressure. The mixture was purified using column chromatography with hexane:ethyl acetate (8:2) as the eluent (R_f ~ 0.4). The racemic adduct was produced at 82% yield (0.249 g). ^{1}H NMR (500 MHz, $CDCl_3$) δ (ppm): 4.13 (m, 2H), 3.54 (d, 1H), 2.93 (d, 1H), 2.44 (m, 1H), 2.33 (m, 1H), 2.07 (t, 1H), 2.00 (m, 1H), 1.90 (d, 1H), 1.64-1.53 (m, 2H), 1.43-1.31 (m, 3H), 1.30-1.16 (m, 6H), 1.07 (s, 3H), 0.84 (m, 9H).

Synthesis of (*S*)-2-(bromomethyl)heptane

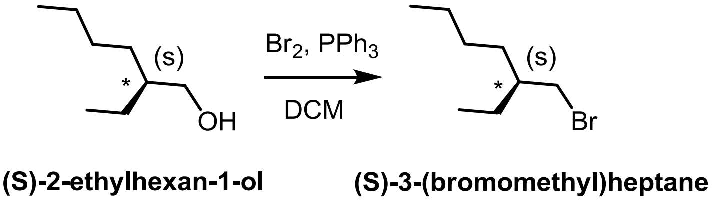

Scheme S2-4. Synthesis of (*S*)-3-(bromomethyl)heptane.

PPh_3 (2.7407 g, 10.4 mmol) was added to a 100 mL round bottom flask and dissolved in DCM (21 mL). The solution was cooled to 0°C. Elemental Br_2 (3.5408 g, 22.2 mmol) was added dropwise to the stirring solution. (*S*)-2-ethylhexan-1-ol (1.0559 g, 8.11 mmol) was dissolved in pyridine (1.54 mL) and added dropwise to the stirring reaction mixture. The reaction was allowed to stir for 1 hour at 0°C. The ice bath was then removed and the reaction was allowed to stir at room temperature for 1 hour. Na_2SO_3 (10% aq solution) was added to quench the reaction. The reaction mixture was washed with water and the organic layer was dried over sodium sulfate. The solvent was removed under reduced pressure. The resulting mixture was separated using column chromatography with hexane:DCM (8:2) as the eluent ($R_f \sim 0.8$). (*S*)-3-(bromomethyl)heptane was produced as a colorless oil with 69% yield (1.02 g). ^{1}H NMR (500 MHz, $CDCl_3$) δ (ppm): 3.46 (m, 2H), 1.54 (m, 1H), 1.46-1.22 (m, 8H), 0.90 (t, 6H). ^{13}C NMR (600 MHz, $CDCl_3$) δ (ppm): 41.06, 39.12, 31.86, 28.82, 25.14, 22.86, 14.06, 10.86. GC/MS: calculated for $C_8H_{17}Br$ (m/z): 192.05, found 192.

Synthesis of EH-S-CDT

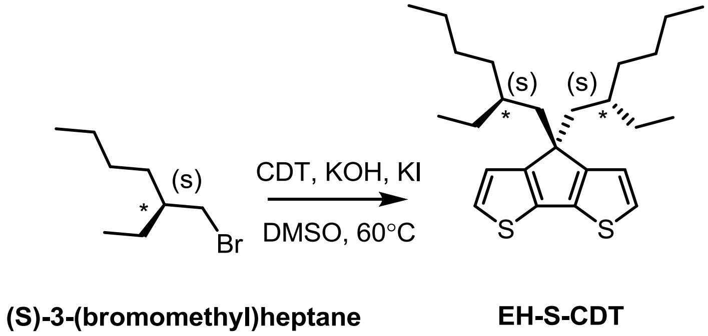

Scheme S2-5. Synthesis of EH-S-CDT.

Cyclopentadithiophene (0.4373 g, 2.45 mmol), potassium iodide (87.9 mg, cat.), and potassium hydroxide powder (0.499 g, 8.89 mmol) were dissolved in DMSO (10 mL). The solution was degassed with argon for 15 minutes. (*S*)-3-(bromomethyl)heptane (1.069 g, 5.54 mmol) was added via syringe. The reaction mixture was heated to 60°C and allowed to stir for about 16 hours. The reaction was cooled to room temperature and diluted with hexane. The reaction mixture was poured over DI water, washed with water, and dried over sodium sulfate. The solvent was removed under reduced pressure. The resulting red-brown oil was purified using column chromatography with hexane as the eluent (R_f ~ 0.8). EH-S-CDT was isolated as a colorless oil and produced at 88% yield. ^{1}H NMR (500 MHz, $CDCl_3$) δ (ppm): 7.09 (d, 2H), 6.91 (d, 2H), 1.86 (m, 4H), 1.05-0.82 (m, 16H), 0.74 (t, 4H), 0.58 (t, 6H). ^{13}C NMR (600 MHz, $CDCl_3$) δ (ppm): 157.65, 136.78, 123.95, 122.28, 53.26, 43.26, 34.98, 34.19, 28.55, 27.27, 22.73, 14.04, 10.65. GC/MS: calculated for $C_{25}H_{38}S_2$ (m/z): 402.25, found 402.

Stannylation of EH-S-CDT

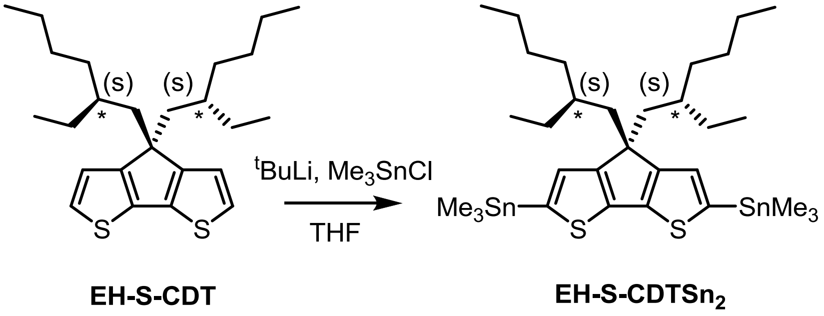

Scheme S2-6. Stannylation of EH-S-CDT.

In a nitrogen-filled glovebox, EH-S-CDT (0.1542 g, 0.383 mmol) was dissolved in THF (5 mL). ^{t}BuLi (0.90 mL, 1.7M in pentane) was added slowly and the reaction was allowed to stir for 1 hour. Me_3SnCl (0.4042 g, 2.03 mmol) was dissolved in THF (5 mL). The Me_3SnCl solution was slowly added and the reaction was allowed to stir for about 16 hours. The reaction was removed from the glovebox and water (5 mL) was added to quench. The reaction mixture was diluted with hexane, washed with water, and dried over sodium sulfate. The solvent was removed under reduced pressure to give a colorless oil. EH-S-CDTSn$_2$ was produced with an 82% yield (0.221 g). ^{1}H NMR (500 MHz, $CDCl_3$) δ (ppm): 7.00 (s, 2H), 1.87 (m, 4H), 1.03-0.84 (m, 18H), 0.75 (t, 6H), 0.60 (t, 6H), 0.37 (s, 18H). ^{13}C NMR (600

MHz, $CDCl_3$) δ (ppm): 159.66, 142.62, 136.17, 130.15, 104.98, 52.12, 43.18, 35.15, 34.45, 28.68, 27.59, 22.89, 16.90, 14.16, 10.73, -8.20.

Polymerization of $BT\text{-}Br_2$ and $EH\text{-}CDTSn_2$

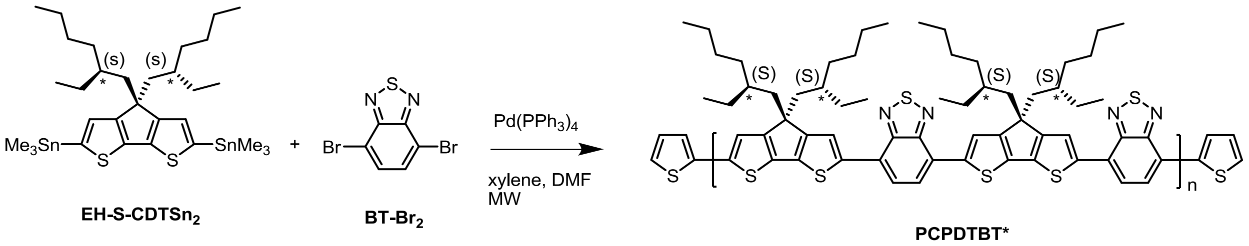

Scheme S2-7. Stille-coupling polymerization of $BT\text{-}Br_2$ and $EH\text{-}CDTSn_2$.

In a nitrogen-filled glovebox, $EH\text{-}S\text{-}CDTSn_2$ (0.055 g, 0.098 mmol), $BT\text{-}Br_2$ (0.0302 g, 0.103 mmol), and $Pd(PPh_3)_4$ (0.0113 g, 0.0098 mmol) were dissolved in dry xylenes (3 mL) in a microwave tube. DMF (0.2 mL) was added. The microwave tube was sealed and removed from the nitrogen glovebox. Microwave-assisted Stille-coupling was performed using the following procedure: 80°C for 5 minutes, 120°C for 5 minutes, 140°C for 5 minutes, and 170°C for 40 minutes. The reaction was allowed to cool to room temperature and returned to nitrogen atmosphere. 2-bromothiophene (0.15 mL, 0.155 mmol) and $Pd(PPh_3)_4$ (0.0043 g, 0.0037 mmol) were dissolved in xylene (1.5 mL) and added to the microwave tube. The reaction was allowed to stir at 150°C in an oil bath for about 16 hours. After cooling to room temperature, the polymer, PCPDTBT* was precipitated with methanol, filter, and dried under vacuum. The polymer was purified by Soxhlet extraction by washing successively with methanol (2 hours), acetone (6 hours), hexane (16 hours) and collected in chloroform (9 hours). The solvent was removed under reduced pressure to produce a black solid with 46% yield (0.024 g). ^1H NMR (500 MHz, $CDCl_3$) δ (ppm): 8.16 (s, 2H), 7.91 (s, 2H), 2.10 (s, 2H), 1.08 (m, 20H), 0.74 (m, 12H). GPC ($CHCl_3$): M_n = 23,132; M_w = 36,632; PDI = 1.6.

Stille-coupling of PT-Br_2 and EH-S-CDTSn_2

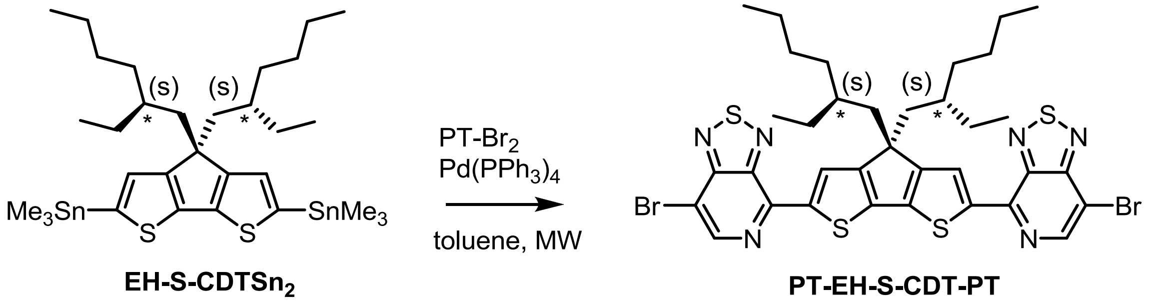

Scheme S2-8. Stille-coupling of PT-Br_2 and EH-S-CDTSn_2.

In a nitrogen-filled glovebox, EH-S-CDTSn_2 (0.3161 g, 0.434 mmol), PT-Br_2 (0.2625 g, 0.890 mmol), and $Pd(PPh_3)_4$ (0.050 g, 0.0433 mmol) were dissolved in dry toluene (11 mL) in a microwave tube. The microwave tube was sealed and removed from the nitrogen glovebox. Microwave-assisted Stille coupling was performed using the following procedure: 120°C for 10 minutes, 140°C for 10 minutes, 160°C for 10 minutes, and 170°C for 40 minutes. The reaction was cooled to room temperature and diluted with $CHCl_3$. The reaction mixture was extracted with $CHCl_3$, washed with water, and dried over sodium sulfate. The solvent was removed under reduced pressure. The resulting mixture was purified using column chromatography using a solvent gradient beginning with $CHCl_3$:hexane (1:1) and progressing to $CHCl_3$ (R_f ~ 0.3). The resulting purple solid was isolate with 67% yield (0.228 g). NMR and mass spec data. ^{1}H NMR (500 MHz, $CDCl_3$) δ (ppm): 8.68 (s, 2H), 8.62 (s, 2H), 2.11 (m, 4H), 1.08-0.91 (m, 16H), 0.83 (m, 2H), 0.66-0.57 (m, 12H). ^{13}C NMR (600 MHz, $CDCl_3$) δ (ppm): 161.76, 156.38, 147.88, 147.68, 146.00, 146.00, 143.20, 127.74, 107.44, 54.49, 43.13, 35.47, 34.29, 28.56, 27.59, 22.83, 14.06, 10.77. MALDI: calculated for $C_{35}H_{38}Br_2N_6S_4$ (m/z): 828.041, found 831.

Polymerization of PT-EH-S-CDT-PT and EH-S-CDTSn_2

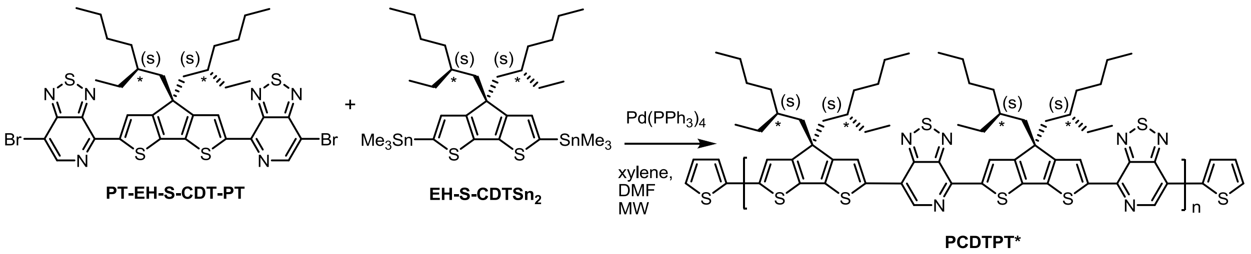

Scheme S2-9. Stille-coupling polymerization of PT-EH-S-CDT-PT and EH-S-CDTSn$_2$.

In a nitrogen-filled glovebox, EH-S-CDTSn$_2$ (0.0702 g, 0.0964 mmol), PT-EH-S-CDT-PT (0.075 g, 0.0903 mmol), and Pd(PPh$_3$)$_4$ (0.0063 g, 0.00545 mmol) were dissolved in dry xylenes (3.5 mL) in a microwave tube. DMF (0.2 mL) was added. The microwave tube was sealed and removed from the nitrogen glovebox. Microwave-assisted Stille coupling was performed using the following procedure: 80°C for 5 minutes, 130°C for 5 minutes, 170°C for 5 minutes, and 200°C for 40 minutes. The reaction was cooled to room temperature and returned to nitrogen atmosphere. 2-bromothiophene (0.15 mL, 1.55 mmol) and Pd(PPh$_3$)$_4$ (0.0040 g, 0.00346 mmol) were dissolved in xylenes (1.5 mL) and added to the microwave tube. The reaction was allowed to stir at 150°C in an oil bath for about 16 hours. After cooling to room temperature, the resulting polymer, PCDTPT* was precipitated with methanol, filtered, and dried under vacuum. The polymer was purified by Soxhlet extraction by washing successively with methanol (2 hours), acetone (6 hours), hexane (16 hours), and collected in chloroform (8 hours). The solvent was removed under reduced pressure to form a purple solid with 85% yield (0.082 g). ^{1}H NMR (600 MHz, CDCl$_3$) δ (ppm): 8.86 (s, 2H), 8.65 (s, 2H), 8.10 (s, 2H), 2.22-0.61 (m, 132H). GPC (CHCl$_3$): M$_n$ = 17,415; M$_w$ = 30,194; PDI = 1.7.

Synthesis of PCPDTBT

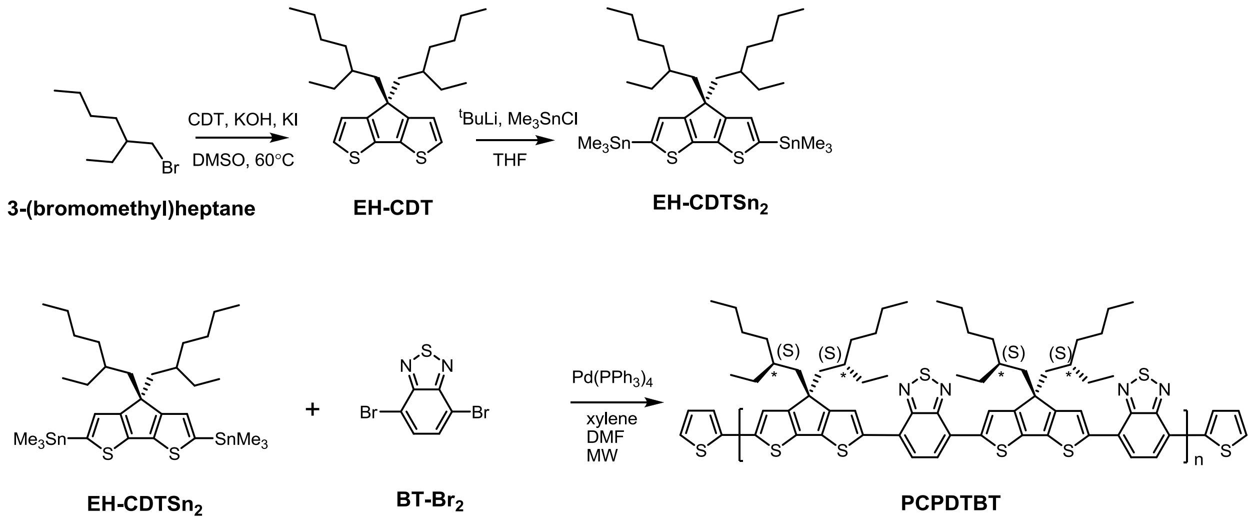

Scheme S2-10. Synthesis of PCPDTBT.

The procedure for synthesizing PCPDTBT is the same as that of PCPDTBT* where (S)-3-(bromomethyl)heptane is replaced by 3-(bromomethyl)heptane. GPC ($CHCl_3$): M_n = 31,553; M_w = 71,410; PDI = 2.3.

Synthesis of PCDTPT

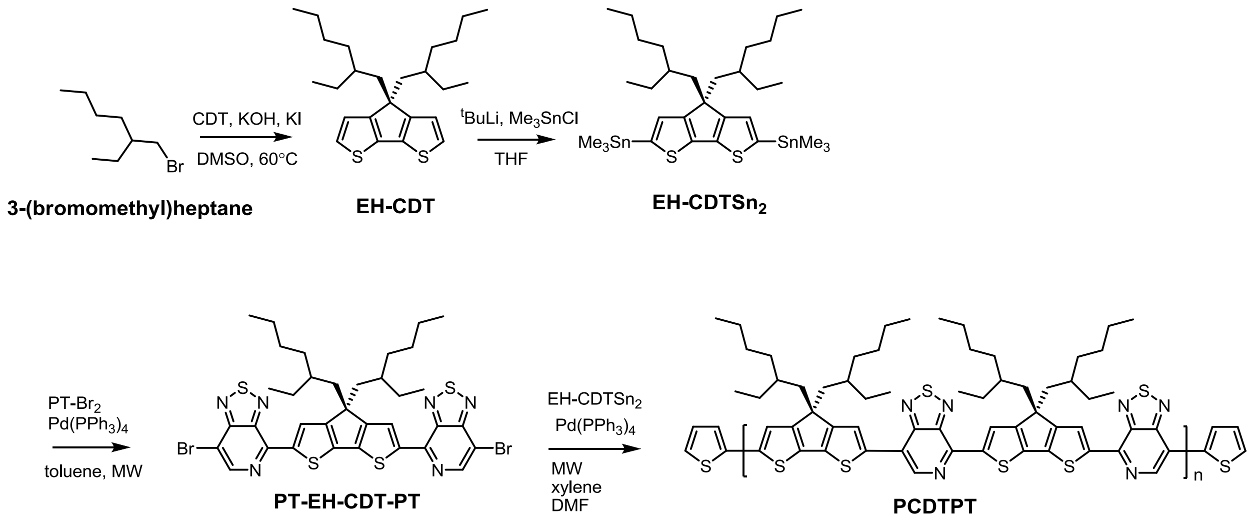

Scheme S2-11. Synthesis of PCDTPT.

The procedure for synthesizing EH-PCDTPT is the same as that of EH-S-PCDTPT where (S)-3-(bromomethyl)heptane is replaced by 3-(bromomethyl)heptane. GPC ($CHCl_3$): M_n = 22,506; M_w = 44,405; PDI = 2.0.

Synthesis of PCDTFBT*

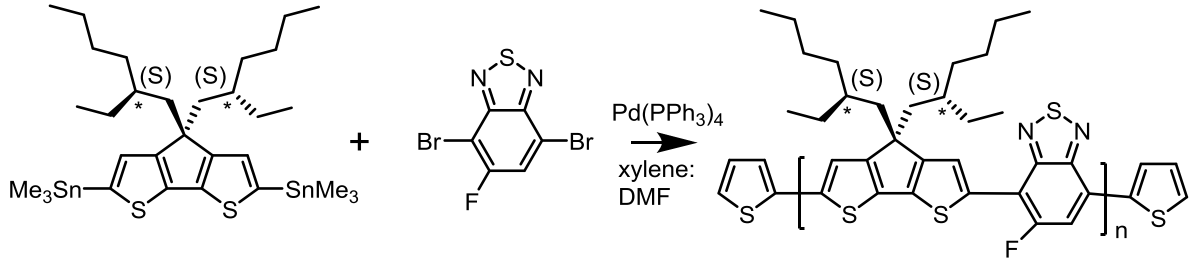

EH-S-CDT-(SnMe$_3$)$_2$

FBT-Br$_2$

PCDTFBT*

Scheme S2-12. Stille coupling polymerization of EH-S-CDT-Sn$_2$ and FBT-Br$_2$.

In a nitrogen-filled glovebox, EH-S-CDTSn$_2$ (0.0974 g, 0.134 mmol), FBT-Br$_2$ (0.0402 g, 0.127 mmol), and Pd(PPh$_3$)$_4$ (0.0077 g, 0.0066 mmol) were dissolved in dry xylenes (3.4 mL) in a microwave tube. DMF (0.35 mL) was added. The microwave tube was sealed and removed from the nitrogen glovebox. The reaction was heated in an oil bath at 144°C and allowed to stir for 24 hours. The reaction was allowed to cool to room temperature and returned to nitrogen atmosphere. 2-bromothiophene (0.15 mL, 0.155 mmol) and Pd(PPh$_3$)$_4$ (0.0043 g, 0.0037 mmol) were dissolved in xylene (1.0 mL) and added to the microwave tube. The reaction was allowed to stir at 144°C in an oil bath for about 16 hours. After cooling to room temperature, the polymer, PCDTFBT* was precipitated with methanol, filter, and dried under vacuum. The polymer was purified by Soxhlet extraction by washing successively with methanol acetone (2 hours), hexane (16 hours) and collected in chloroform (8 hours). The solvent was removed under reduced pressure to produce a black solid, PCDTFBT*. GPC (CHCl$_3$, chloroform fraction): M_n = 13940, M_w = 23392, PDI = 1.68. GPC (CHCl$_3$, hexane fraction): M_n = 2902, M_w = 3571, PDI = 1.23.

Synthesis of PCDTFBT

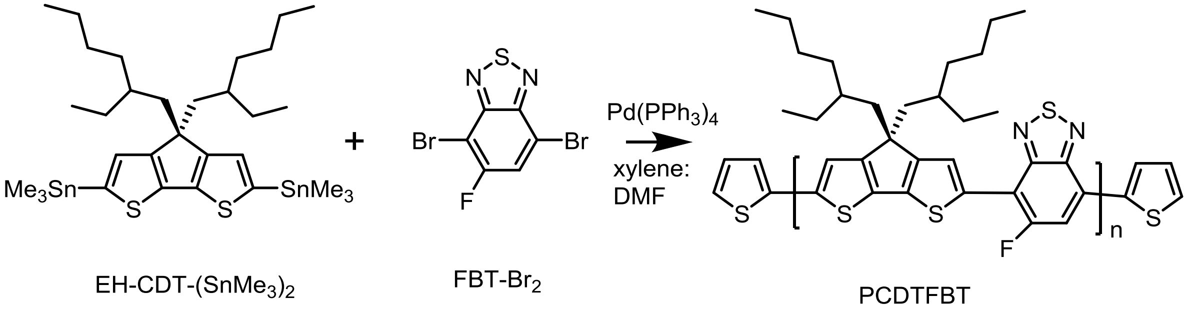

Scheme S2-13. Stille coupling polymerization of EH-CDT-Sn_2 and FBT-Br_2.

The procedure for synthesizing PCDTFBT is the same as that of PCDTFBT* where (S)-3-(bromomethyl)heptane is replaced by 3-(bromomethyl)heptane. GPC ($CHCl_3$, chloroform fraction): M_n = 13,430, M_w = 20,440, PDI = 1.52. GPC ($CHCl_3$, hexane fraction): M_n = 3190, M_w = 3910, PDI = 1.22.

Synthesis of PIPCP*

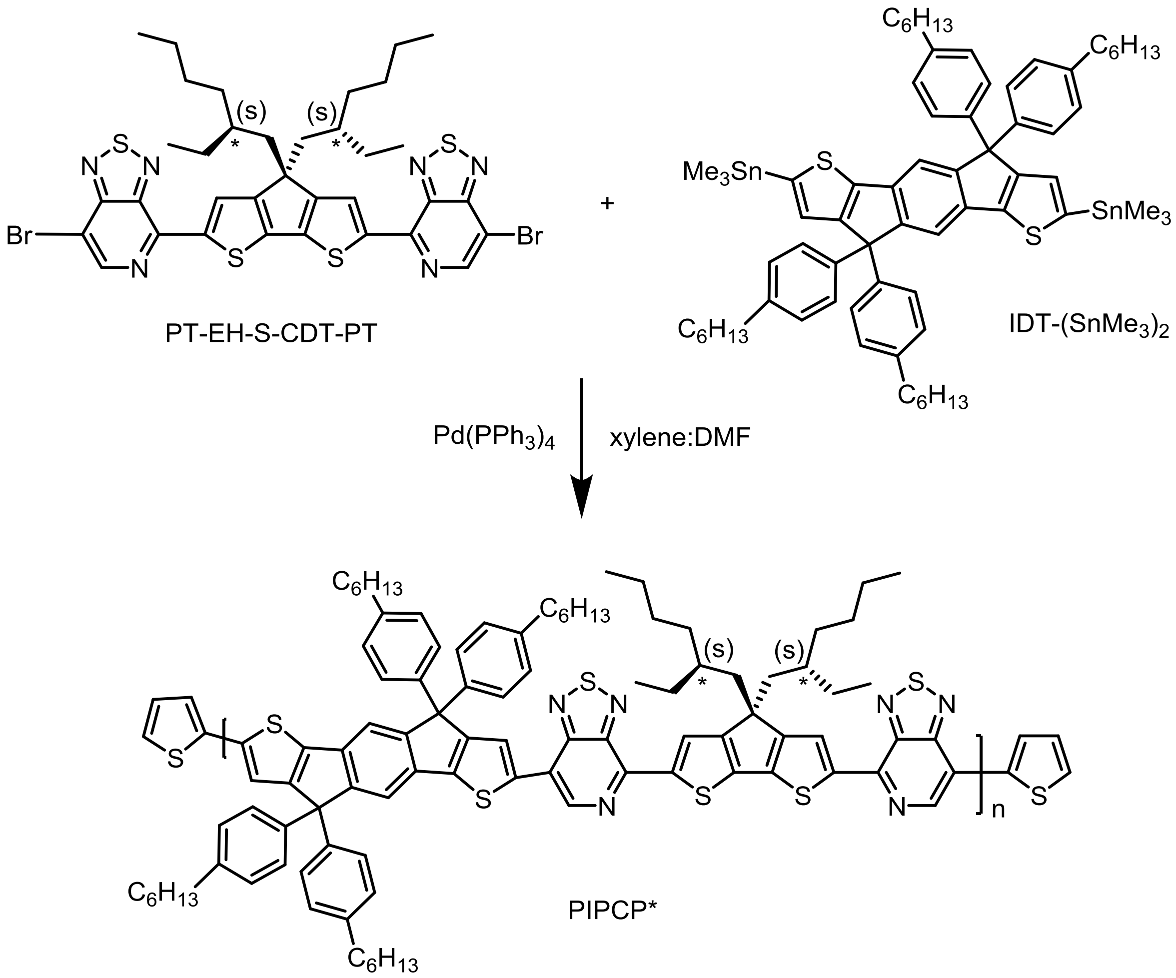

Scheme S2-14. Stille coupling polymerization of IDT-Sn_2 and PT-EH-S-CDT-PT.

In a nitrogen-filled glovebox, IDT-Sn_2 (0.0848 g, 0.0684 mmol), PT-EH-S-CDT-PT (0.0541 g, 0.0651 mmol), and $Pd(PPh_3)_4$ (0.0038 g, 0.00329 mmol) were dissolved in dry xylenes (2.5 mL) in a microwave tube. DMF (0.2 mL) was added. The microwave tube was sealed and removed from the nitrogen glovebox. Microwave-assisted Stille coupling was performed using the following procedure: 80°C for 2 minutes, 130°C for 2 minutes, 160°C for 2 minutes, 185°C for 2 minutes, and 200°C for 40 minutes. The reaction was cooled to room temperature and returned to nitrogen atmosphere. 2-bromothiophene (0.15 mL, 1.55 mmol) and $Pd(PPh_3)_4$ (0.0040 g, 0.00346 mmol) were dissolved in xylenes (0.55 mL) and added to the microwave tube. The reaction was allowed to stir at 150°C in an oil bath for about 16 hours. After cooling to room temperature, the resulting polymer, PCDTPT* was precipitated with methanol, filtered, and dried under vacuum. The polymer was purified by Soxhlet extraction by washing successively with acetone (2 hours), hexane (16 hours), DCM (24 hours) and collected in chloroform (5 hours). The solvent was removed under reduced pressure to form a purple solid with 99% yield (0.103 g). GPC ($CHCl_3$, DCM fraction): $M_n = 47,630$, $M_w = 98790$, PDI = 2.07.

Synthesis of PIPCP

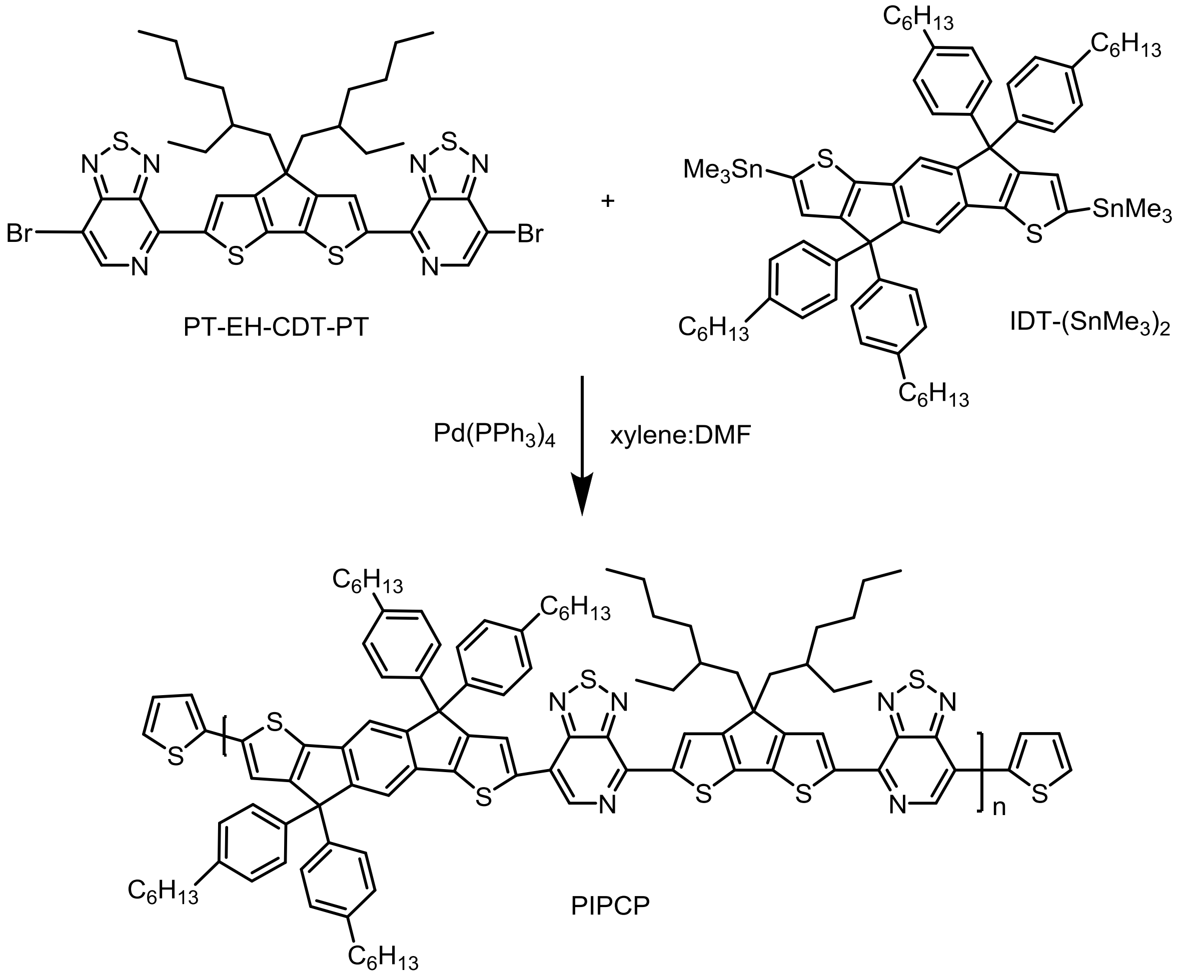

Scheme S2-15. Stille coupling polymerization of IDT-Sn_2 and PT-EH-CDT-PT.

The procedure for synthesizing PIPCP is the same as that of PIPCP* where (S)-3-(bromomethyl)heptane is replaced by 3-(bromomethyl)heptane. GPC ($CHCl_3$, DCM fraction): M_n = 33,880, M_w = 67,970, PDI = 2.01.

3. Additional Spectra and Graphs

^{1}HNMR spectra of chiral derivatization reactions

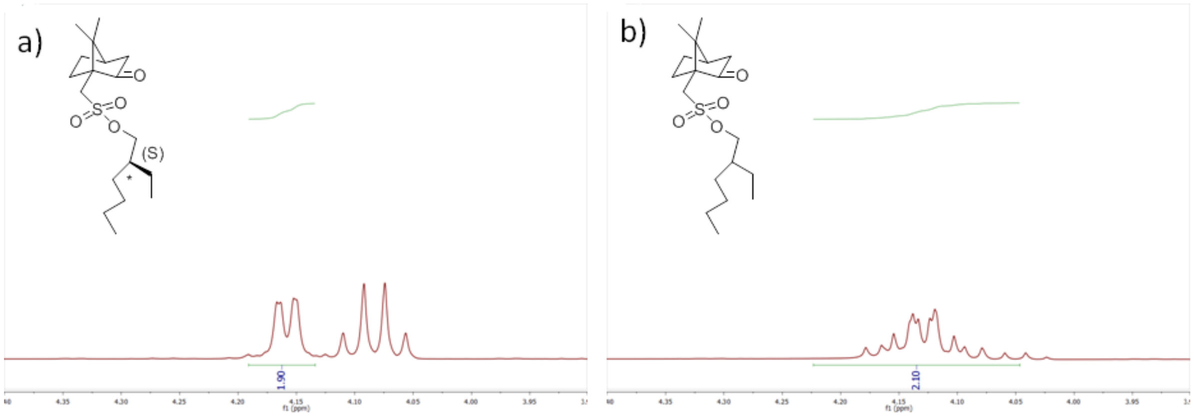

Figure S2-1. ^{1}HNMR spectra of a) chiral adduct and b) racemic adduct.

Differential Scanning Calorimetry

Differential scanning calorimetry (DSC) was measured a TA Instruments DSC (Model Q-20) with about 5 mg of polymer sample at a rate of 10°C/minute in the temperature range of 20°C to 300°C.

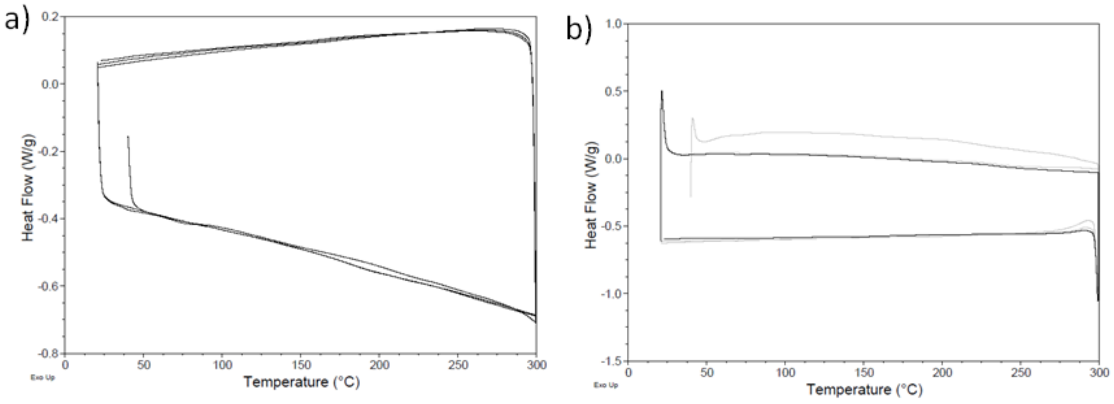

Figure S2-2. DSC curves of a) PCPDTBT and b) PCPDTBT*.

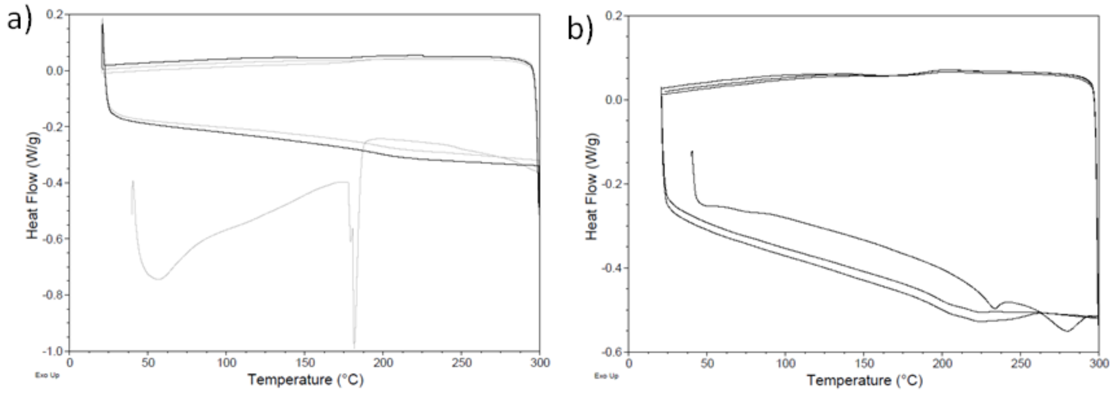

Figure S2-3. DSC curves of a) PCDTPT and b) PCDTPT*.

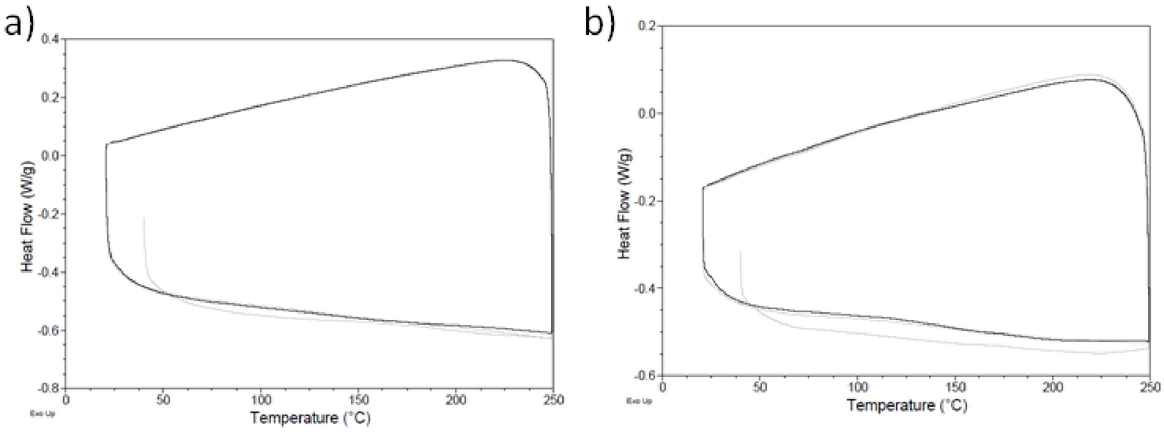

Figure S2-4. DSC curves of a) PIPCP and b) PIPCP*.

Optical Absorption Spectroscopy

Optical absorption spectra were measured using a Perkins Elmer Lambda 750 UV-Vis Spectrometer containing a STD detection module. Solvents for solution spectra were used without further purification. Solutions were measured using 10 mm path length quartz cuvettes. Solutions were prepared in CB, 1:1 CB:DIO, or 8:2 CB:DMSO at concentrations varying from 0.01 mg/mL to 0.07 mg/mL. Optical absorption measurements were taken at room temperature unless otherwise indicated. Thin films were fabricated using spin-coating in a nitrogen-filled glovebox at room temperature by depositing 20 μL of 8 mg/mL CB solution on a clean glass substrate and spinning for 120 seconds at 750 rpm.

Temperature-dependent optical absorption spectroscopy: Solutions were heating using a PolyScience Digital Temperature Controller. Solutions were heated to the desired temperature, allowed to equilibrate for 5 minutes, and then the optical absorption spectrum was measured.

The oscillator strength was calculated using the equation $f = (4.3X10^{-9})*\int \varepsilon dv$ where $\int \varepsilon dv$ is the integrated extinction coefficient with v in wave numbers. $\int \varepsilon dv$ was calculated by fitting the peaks with a Gaussian function to de-convolute the peaks and determine the area under the curve.

Table S2-1. Oscillator Strength of PCPDTBT and PCPDTBT*

Material	Solvent	$\pi \rightarrow \pi^*$	0-0
PCPDTBT	1:1 CB:DIO	13.2	11.7
PCPDTBT*	CB	26.6	9.4
PCPDTBT*	1:1 CB:DIO	7.3	1.7

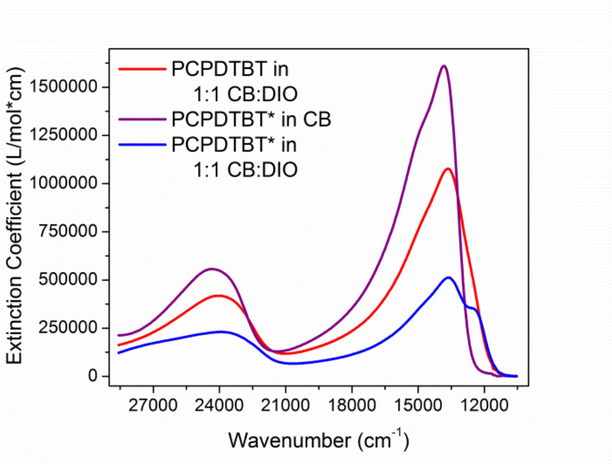

Figure S2-5. Extinction coefficients as a function of wave number for solutions of PCPDTBT in 1:1 CB:DIO (red) and PCPDTBT* in CB (purple) and 1:1 CB:DIO (blue).

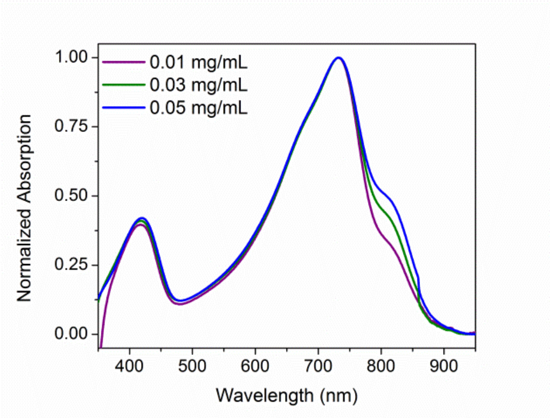

Figure S2-6. Concentration-dependent normalized absorption spectra of PCPDTBT* solutions at 0.01 mg/mL (purple), 0.03 mg/mL (green), and 0.05 mg/mL (blue) in 1:1 CB:DIO.

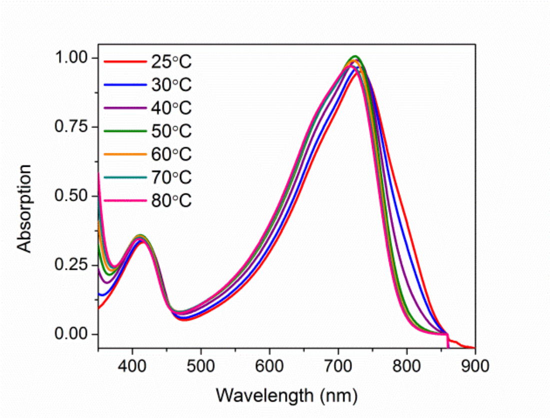

Figure S2-7. Temperature-dependent absorption of PCPDTBT at 0.03 mg/mL in 1:1 CB:DIO.

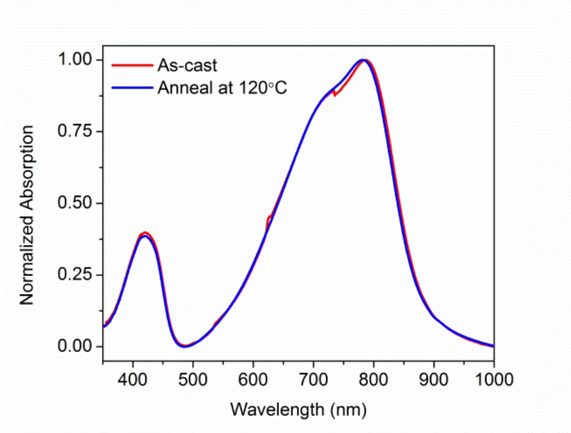

Figure S2-8. Normalized thin film absorption spectra of PCPDTBT* before (red) and after (blue) annealing at 120°C for 10 minutes.

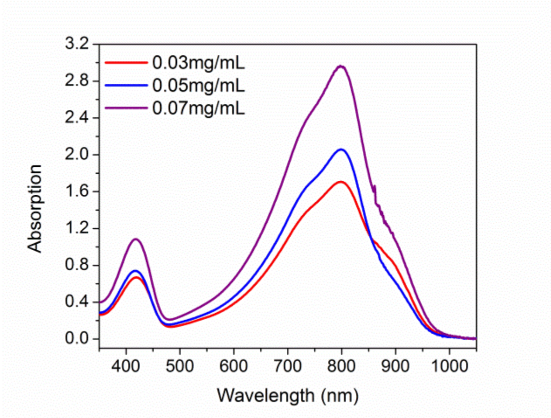

Figure S2-9. Concentration-dependent absorption of PCDTPT* at 0.03 mg/mL (red), 0.05 mg/mL (blue), and 0.07 mg/mL (purple) in 8:2 CB:DMSO.

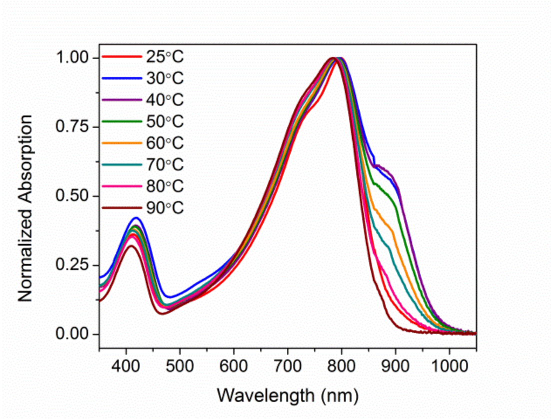

Figure S2-10. Temperature-dependent normalized absorption of PCDTPT at 0.01 mg/mL in 8:2 CB:DMSO.

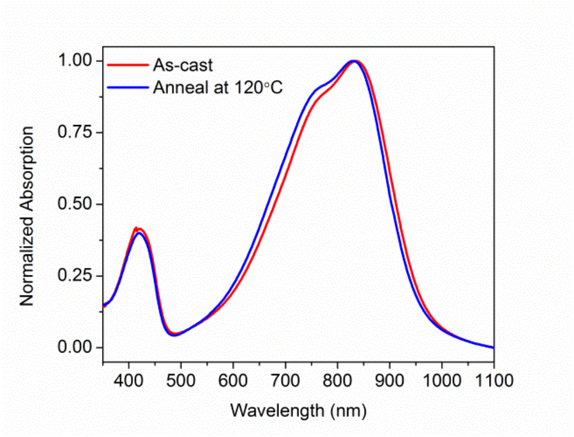

Figure S2-11. Normalized thin film absorption spectra of PCDTPT* before (red) and after (blue) annealing at 120°C for 10 minutes.

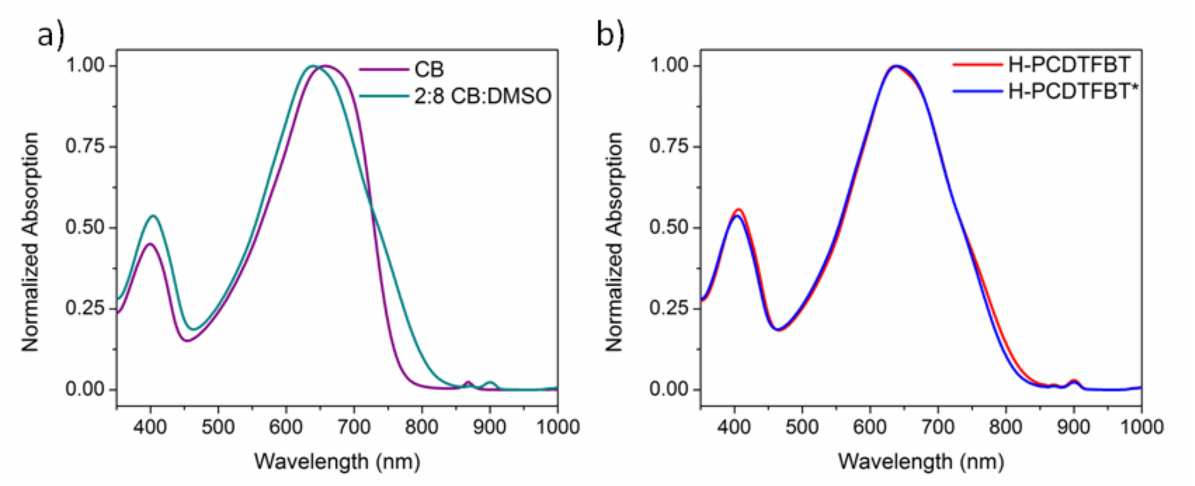

Figure S2-12. Optical absorption spectra of a) H-PCDTFBT* in CB (purple) and 2:8 CB:DMSO (teal) and b) H-PCDTFBT (red) and H-PCDTFBT* (blue) in 2:8 CB:DMSO.

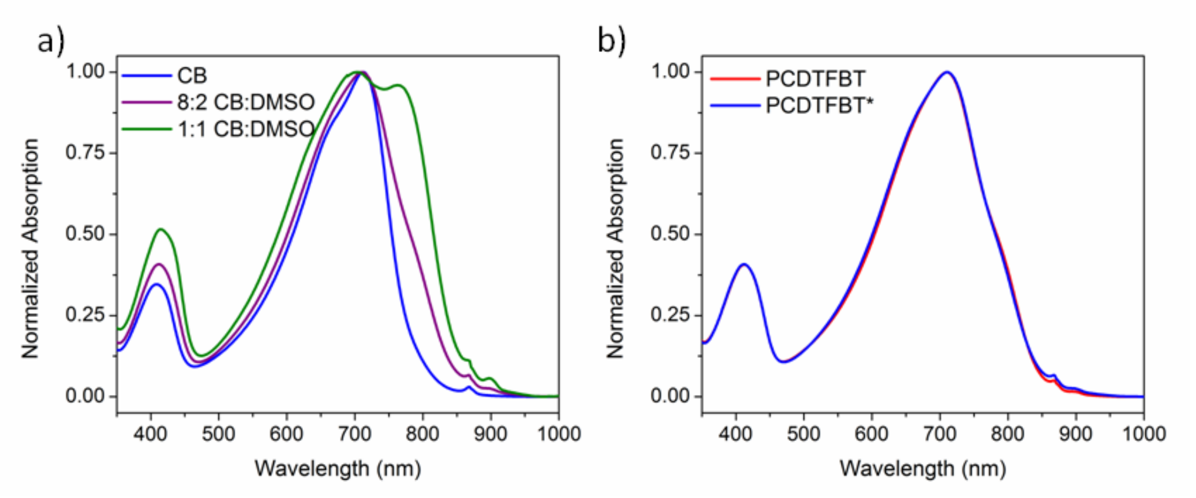

Figure S2-13. Optical absorption spectra of a) C-PCDTFBT* in CB (blue), 8:2 CB:DMSO (purple), and 1:1 CB:DMSO (green) and b) C-PCDTFBT* (blue) and C-PCDTFBT (red) in 8:2 CB:DMSO.

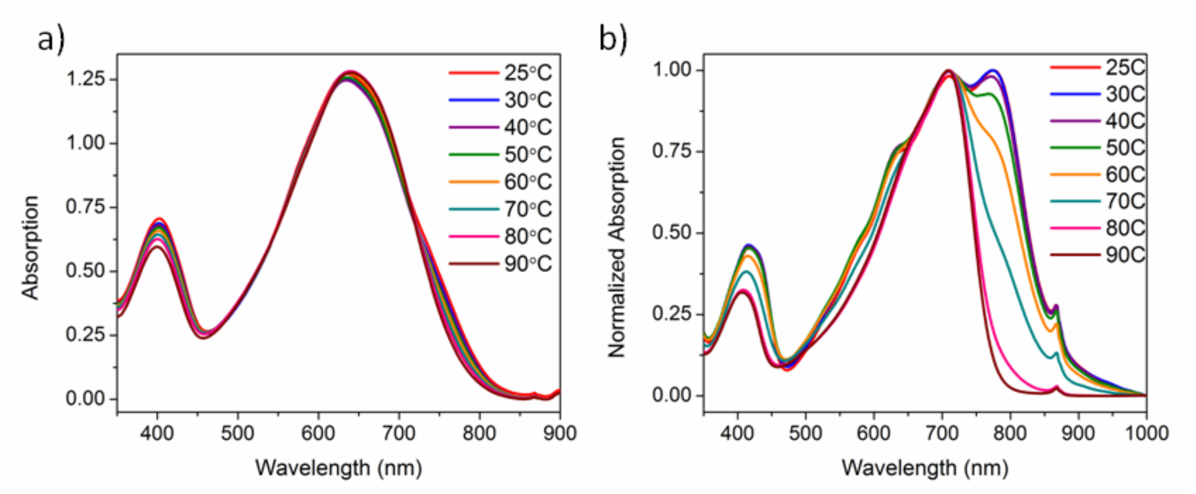

Figure S2-14. Optical absorption spectra of a) H-PCDTFBT* in 2:8 CB:DMSO and b) I-PCDTFT* in CB as a function of temperature, from 25-90°C.

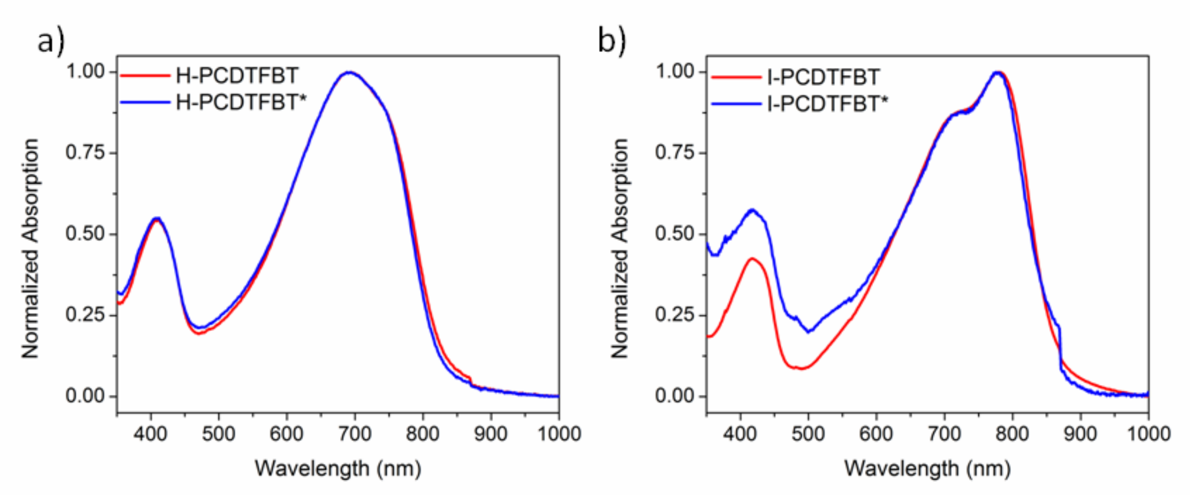

Figure S2-15. Thin film absorption of a) H-PCDTFBT (red) and H-PCDTFBT* (blue) and b) I-PCDTFBT (red) and I-PCDTFBT* (blue).

CD Spectroscopy

Circular dichroism spectra were measured using an Aviv Circular Dichroism Spectrometer, Model 202, which contains a Xenon lamp. Circularly polarized light is produced by a 50 kHz photoelastic modulator. Temperature is controlled via Peltier thermoelectric heating and cooling system. Solvents for solution spectra were used without further purification. Solutions were measured using 10 mm path length quartz cuvettes. Solutions were prepared in CB, 1:1 CB:DIO, or 8:2 CB:DMSO at concentrations varying from 0.01 mg/mL to 0.07 mg/mL. Thin films were fabricated using spin-coating in a nitrogen-filled glovebox at room temperature by depositing 20 µL of 8 mg/mL CB solution on a clean glass substrate and spinning for 120 seconds at 750 rpm.

Cooling kinetics: An initial CD spectrum was recorded at room temperature. The temperature was then increased at 5°C/min from 25°C to 90°C. The solution was held at 90°C for 15 minutes. The solution was cooled at a controlled rate of 1°C/min or 5°C/min from 90°C back down to 25°C. As soon as cooling began, the CD signal at 870 nm was monitored. CD signal was again measured one week after the cooling experiments.

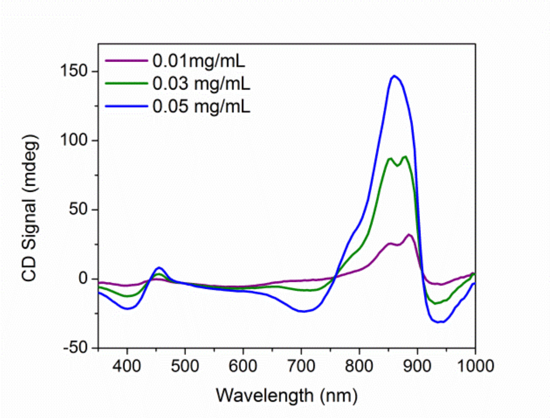

Figure S2-16. Concentration-dependent CD spectra of PCPDTBT* at 0.01 mg/mL (purple), 0.03 mg/mL (green), and 0.05 mg/mL (blue) in 1:1 CB:DIO.

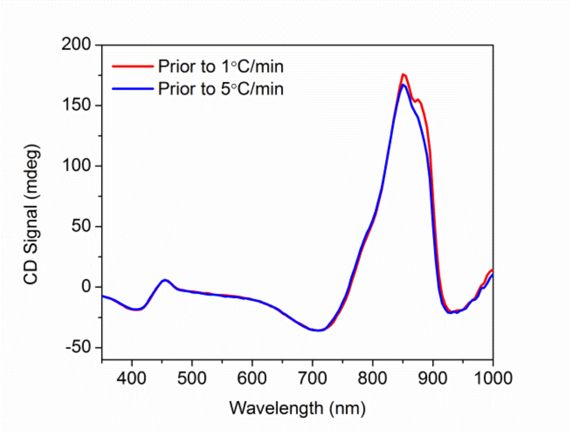

Figure S2-17. CD spectra of PCDTBT* prior to cooling at 1°C/minute (red) and 5°C/minute (blue).

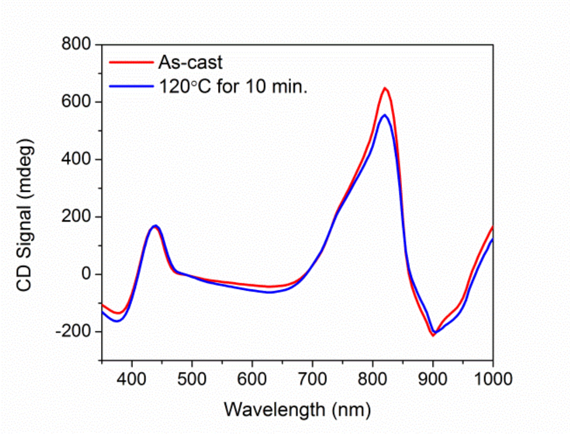

Figure S2-18. CD spectra of PCPDTBT* thin films before (red) and after (blue) annealing at 120°C for 10 minutes.

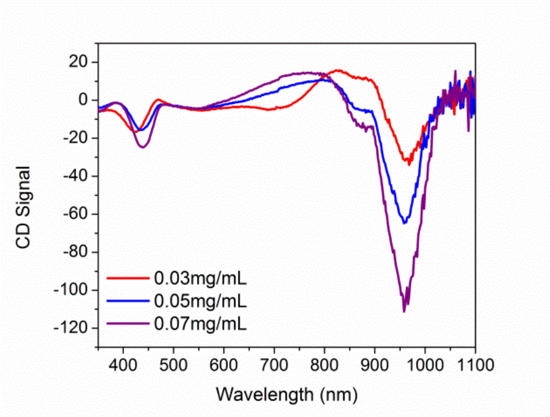

Figure S2-19. Concentration-dependent CD spectra of PCDTPT* at 0.03 mg/mL (red), 0.05 mg/mL (blue), and 0.07 mg/mL (purple) in 8:2 CB:DMSO.

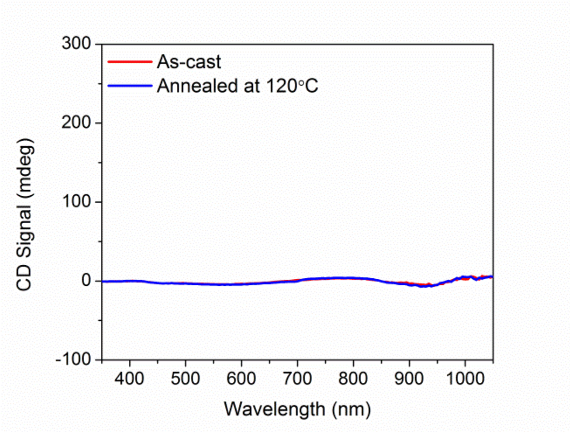

Figure S2-20. CD spectra of PCDTPT* thin films before (red) and after (blue) annealing at 120°C for 10 minutes.

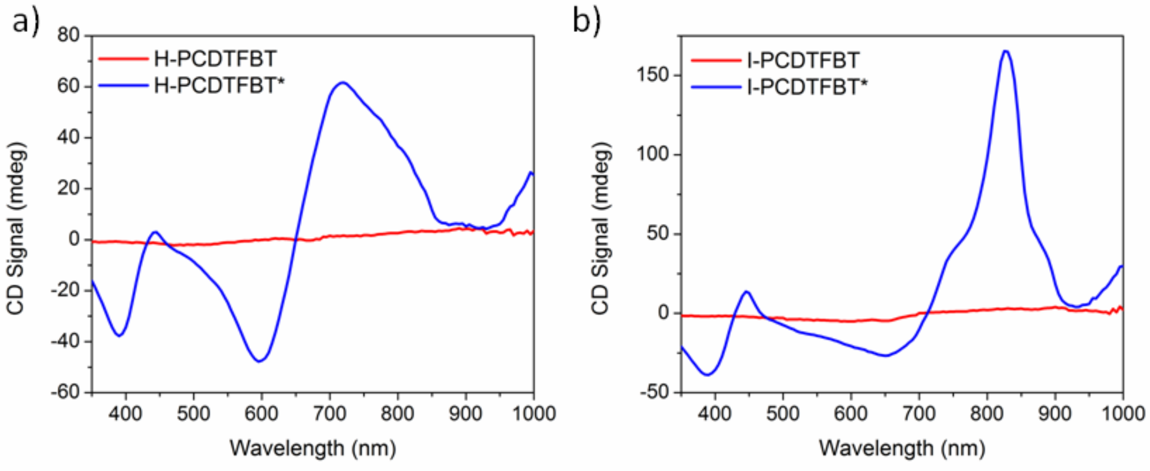

Figure S2-21. CD spectra of a) H-PCDTFBT (red) and H-PCDTFBT* (blue) in 2:8 CB:DMSO and b) I-PCDTFBT (red) and I-PCDTFBT* (blue) in CB.

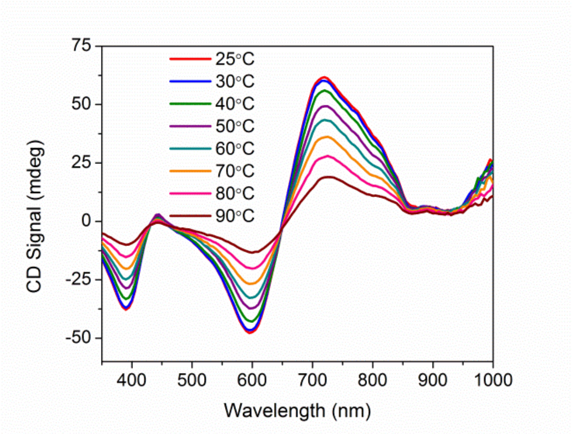

Figure S2-22. CD spectra of H-PCDTFBT* in 2:8 CB:DMSO as a function of temperature, from 25-90°C.

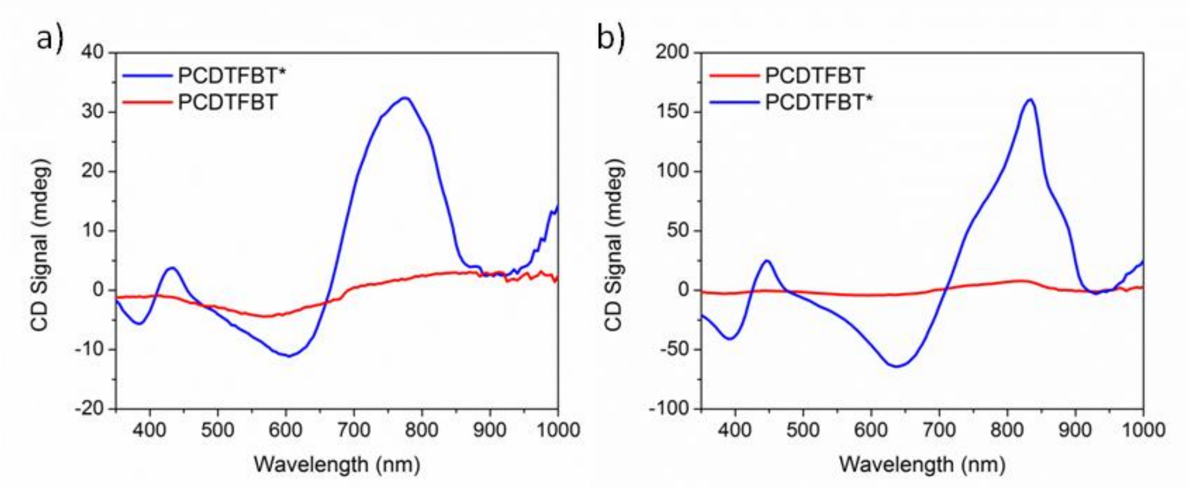

Figure S2-23. Thin film CD spectra of a) H-PCDTFBT (red) and H-PCDTFBT* (blue) and b) I-PCDTFBT (red) and I-PCDTFBT* (blue).

Atomic Force Microscopy (AFM)

Atomic force microscopy images were obtained using an Asylum MFP-3D AFM controlled through Igor Pro software. The AFM tips used were NanoWorld Pointprobe Al-coated, non-contact mode Si cantilevers, with a resonant frequency of 190 kHz and a spring constant of 48 N/m. All images were taken in air using AC mode. Thin films were fabricated using spin-coating in a nitrogen-filled glovebox at room temperature by depositing 20 µL of 8 mg/mL CB solution on a clean glass substrate and spinning for 120 seconds at 750 rpm.

Table S2-2. Average RMS Values for PCDTPT and PCDTPT* Films

Material	Avg. RMS (nm)	Error based on multiple measurements (nm)	Avg. error provided by AFM software (nm)
PCDTPT*	3.0	+/- 0.85	+/- 1.84
PCDTPT	1.4	+/- 0.55	+/- 0.81

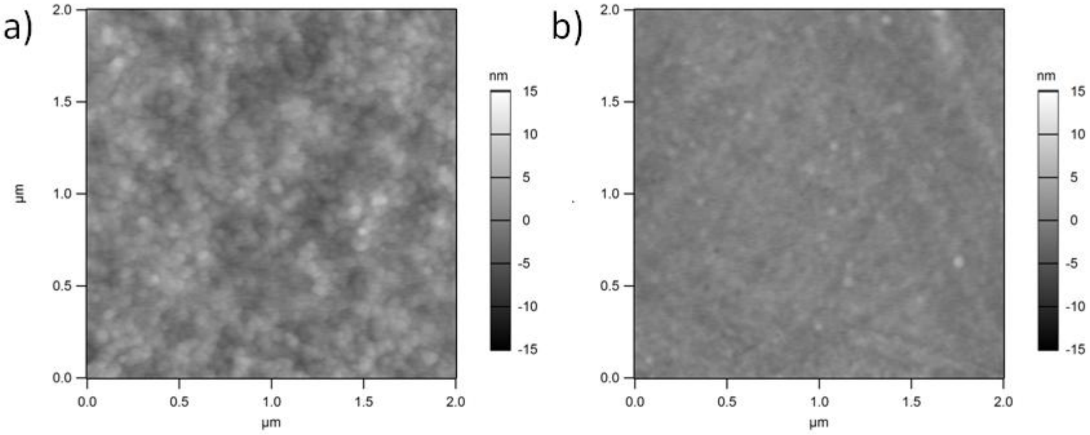

Figure S2-23. AFM topography images of a) PCDTPT* and b) PCDTPT.

GIWAXS

Samples were obtained as thin films by spin-coating 8 mg/mL CB solutions of PCDTBT* and PCDTBT onto silicon wafers. The one-dimensional and two-dimensional GIWAXS profiles were taken in the nominally in-plane and out-of-plane directions.

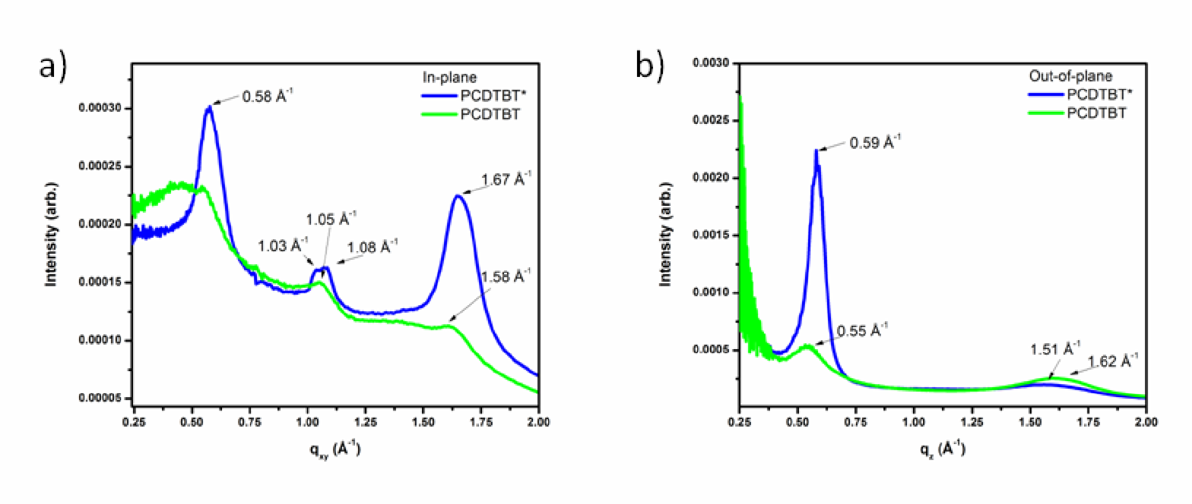

Figure S2-24. GIWAXS line cut profiles of PCDTBT* (blue) and PCDTBT (green) in the a) in-plane and b) out-of-plane directions. Relevant peaks have been labeled with their corresponding q values.

Density Functional Theory (DFT) Calculations

Calculations were done using the Gaussian 09 software suite.[123] The hybrid long range corrected CAM-B3LYP functional[124] with the basis set 6-31G(d,p) were used for the optimization of the geometry.

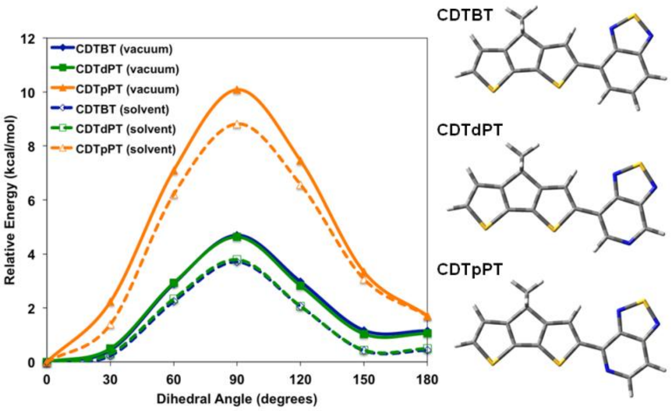

Figure S2-25. Calculated rotational barriers for CDTBT (blue), CDTdPT (green) and CDTpPT (orange) in vacuum (solid) and in chlorobenzene (dashed).

G. References

1. Xiao, S., Zhang, Q., You, W. Molecular Engineering of Conjugated Polymers for Solar Cells: An Updated Report. *Adv. Mater.* **2017**, DOI: 10.1002/adma.201601391.

2. Zhang, Z.-G., Wang, J. Structures and Properties of Donor-Acceptor Copolymers for Solar Cell Applications. *J. Mater. Chem.* **2012**, *22*, 4178-4187.

3. Bundgaard, E., Krebs, F. C. Low Band Gap Polymers for Organic Photovoltaics. *Sol. Energ. Mat. Sol. C,* **2007**, *91*, 954-985.

4. Scharber, M. C., Muhlbacher, D., Koppe, M., Denk, P., Waldauf, C., Heeger, A. J., Brabec, C. J. Design Rules for Donors in Bulk Heterojunction Solar Cells – Toward 10% Energy-Conversion Efficiency. *Adv. Mater.* **2006**, *18*, 789-794.

5. Henson, Z. B., Mullen, K., Bazan, G. C. Design Strategies for Organic Semiconductors Beyond the Molecular Formula. *Nat. Chem.* **2012**, *4*, 699-704.

6. Zhao, X., Zhan, X. Electron Transporting Semiconducting Polymers in Organic Electronics. *Chem. Soc. Rev.* **2011**, *40*, 3728-3743.

7. Allard, S., Forster, M., Souharce, B., Thiem, H., Scherf, U. Organic Semiconductors for Solution-Processable Field-Effect Transistors (OFETs). *Angew. Chem. Int. Ed.* **2008**, *47*, 4070-4098.

8. Holliday, S., Donaghey, J. E., McCulloch, I. Advances in Charge Carrier Mobilities of Semiconducting Polymers Used in Organic Transistors. *Mater. Chem.* **2014**, *26*, 647-663.

9. Li, Y. Molecular Design of Photovoltaic Materials for Polymer Solar Cells: Toward Suitable Electronic Energy Levels and Broad Absorption. *Acc. Chem. Res.* **2012**, *45*, 723-733.

10. Beaujuge, P. M., Amb, C. M., Reynolds, J. R. Spectral Engineering in π-Conjugated Polymers with Intramolecular Donor-Acceptor Interactions. *Acc. Chem. Res.* **2010**, *43*, 1396-1407.

11. van Mullekom, H. A. M., Vekemans, J. A. J. M., Havinga, E. E., Meijer, E. W. Developments in the Chemistry and Band Gap Engineering of Donor-Acceptor Substituted Conjugated Polymers. *Mater. Sci. Eng.* **2001**, *32*, 1-40.

12. Duan, C., Huang, F., Cao, Y. Recent Development of Push-Pull Conjugated Polymers for Bulk Heterojunction Photovoltaics: Rational Design and Fine Tailoring of Molecular Structures. *J. Mater. Chem.* **2012**, *22*, 10416-10434.

13. Liang, Y., Yu, L. A New Class of Semiconducting Polymers for Bulk Heterojunction Solar Cells with Exceptionally High Performance. *Acc. Chem. Res.* **2010**, *43*, 1227-1236.

14. Hoppe, H., Sariciftci, N. S. Organic Solar Cells: An Overview. *J. Mater. Res.* **2004**, *19*, 1924-1945.

15. Brabec, C. J., Sariciftci, N. S., Hummelen, J. C. Plastic Solar Cells. *Adv. Funct. Mater.* **2001**, *11*, 15-26.

16. Zhou, H., Yang, L., You, W. Rational Design of High Performance Conjugated Polymers for Organic Solar Cells. *Macromolecules,* **2012**, *45*, 607-632.

17. Cheng, Y.-J., Yang, S.-H., Hsu, C.-S. Synthesis of Conjugated Polymers for Organic Solar Cell Applications. *Chem. Rev.* **2009**, *109*, 5868-5923.

18. Liu, C., Wang, K., Gong, X., Heeger, A. J. Low Bandgap Semiconducting Polymers for Polymer Photovoltaics. *Chem. Soc. Rev.* **2016**, *45*, 4825-4846.

19. Coropceanu, V., Cornil, J., Filho, D. A. S., Olivier, Y., Silbey, R., Bredas, J.-L. Charge Transport in Organic Semiconductors. *Chem. Rev.* **2007**, *107*, 926-952.

20. Beaujuge, P. M., Frechet, J. M. J. Molecular Design and Ordering Effects in π-Functional Materials for Transistor and Solar Cell Applications. *J. Am. Chem. Soc.* **2011**, *133*, 200009-200029.

21. Huang, Y.-S., Gierschner, J., Schmidtke, J. P., Friend, R. H., Beljonne, D. Tuning Interchain and Intrachain Interactions in Polyfluorene Copolymers. *Phys. Rev. B,* **2011**, *84*, 205311.

22. Schwartz, B. J. Conjugated Polymers as Molecular Materials: How Chain Conformation and Film Morphology Influence Energy Transfer and Interchain Interactions. *Annu. Rev. Phys. Chem.* **2003**, *54*, 141-172.

23. Botiz, I., Stingelin, N. Influence of Molecular Conformations and Microstructure on the Optoelectronic Properties of Conjugated Polymers. *Materials*, **2014**, *7*, 2273-2300.

24. Mei, J., Bao, Z. Side Chain Engineering in Solution-Processable Conjugated Polymers. *Chem. Mater.* **2014**, *26*, 604-615.

25. Lei, T., Wang, J.-Y., Pei, J. Roles of Flexible Chains in Organic Semiconducting Materials. *Chem. Mater.* **2014**, *26*, 594-603.

26. Liu, Y., Zhao, J., Li, Z., Mu, C., Ma, W., Hu, H., Jiang, K., Lin, H., Ade, H., Yan, H. Aggregation and Morphology Control Enables Multiple Cases of High-Efficiency Polymer Solar Cells. *Nat. Commun.* **2014**, *5*, 5293.

27. Rivnay, J., Mannsfeld, S. C. B., Miller, C. E., Salleo, A., Toney, M. F. Quantitative Determination of Organic Semiconductor Microstructure from the Molecular to Device Scale. *Chem. Rev.* **2012**, *112*, 5488-5519.

28. Ayzner, A. L., Mei, J., Appleton, A., DeLongchamp, D., Nardes, A., Benight, S., Kopidakis, N., Toney, M. F., Bao, Z. Impact of the Crystallite Orientation Distribution on Exciton Transport in Donor-Acceptor Conjugated Polymers. *ACS Appl. Mater. Interfaces*, **2015**, *7*, 28035-28041.

29. Chen, M. S., Lee, O. P., Niskala, J. R., Yiu, A. T., Tassone, C. J., Schmidt, K., Beaujuge, P. M., Onishi, S. S., Toney, M. F., Zettl, A., Frechet, J. M. J. Enhanced Solid State Order and Field-Effect Hole Mobility through Control of Nanoscale Polymer Aggregation. *J. Am. Chem. Soc.* **2013**, *135*, 19229-19236.

30. Noriega, R., Salleo, A., Spakowitz, A. J. Chain Conformations Dictate Multiscale Charge Transport Phenomena in Disordered Semiconducting Polymers. *PNAS*, **2013**, *110*, 16315-16320.

31. Nguyen, T.-Q., Doan, V., Schwartz, B. J. Conjugated Polymer Aggregates in Solution: Control of Interchain Interactions. *J. Chem. Phys.* **1999**, *110*, 4068-4078.

32. Spano, F. C., Silva, C. H- and J-Aggregate Behavior in Polymeric Semiconductors. *Annu. Rev. Phys. Chem.* **2014**, *65*, 477-500.

33. Hu, H., Zhao, K., Fernandes, N., Boufflet, P., Bannock, J. H., Yu, L., de Mello, J. C., Stingelin, N., Heeney, M., Giannelis, E. P., Amassian, A. Entanglements in Marginal Solutions: A Means of Tuning Pre-Aggregation of Conjugated Polymers with Positive Implications for Charge Transport. *J. Mater. Chem. C*, **2015**, *3*, 7394-7404.

34. Yao, Y., Hou, J., Xu, Z., Li, G., Yang, Y. Effects of Solvent Mixtures on the Nanoscale Phase Separation in Polymer Solar Cells. *Adv. Funct. Mater.* **2008**, *18*, 1783-1789.

35. Peet, J., Cho, N. S., Lee, S. K., Bazan, G. C. Transition from Solution to the Solid State in Polymer Solar Cells Cast from Mixed Solvents. *Macromolecules*, **2008**, *41*, 8655-8659.

36. Ying, L., Hsu, B. B. Y., Zhan, H., Welch, G. C., Zalar, P., Perez, L. A., Kramer, E. J., Nguyen, T.-Q., Heeger, A. J., Wong, W.-Y., Bazan, G. C. Regioregular Pyridal[2,1,3]thiadiazole π-Conjugated Copolymers. *J. Am. Chem. Soc.* **2011**, *133*, 18538-18541.

37. Wang, D., Yuan, Y., Mardiyati, Y., Bubeck, C., Koynov, K. From Single Chains to Aggregates, How Conjugated Polymers Behave in Dilute Solutions. *Macromolecules*, **2013**, *46*, 6217-6224.

38. Brabec, C. J., Durrant, J. R. Solution-Processed Organic Solar Cells. *MRS Bulletin*, **2008**, *33*, 670-675.

39. Hiszpanski, A. M., Loo, Y.-L. Directing the Film Structure of Organic Semiconductors via Post-Deposition Processing for Transistor and Solar Cell Applications. *Energy Environ. Sci.* **2014**, *7*, 592-608.

40. Peet, J., Kim, J. Y., Coates, N. E., Ma, W. L., Moses, D., Heeger, A. J., Bazan, G. C. Efficiency Enhancement in Low Band-Gap Polymer Solar Cells by Processing with Alkane Dithiols. *Nature Mater.* **2007**, *6*, 497-500.

41. Kwon, S., Kang, H., Lee, J.-H., Lee, J., Hong, S., Kim, H., Lee, K. Effect of Processing Additives on Organic Photovoltaics: Recent Progress and Future Prospects. *Adv. Energy Mater.* **2016**, DOI: 10.1002/aenm.201601496.

42. Lee, J. K., Ma, W. L., Brabec, C. J., Yuen, J., Moon, J. S., Kim, J. Y., Lee, K., Bazan, G. C., Heeger, A. J. Processing Additives for Improved Efficiency from Bulk Heterojunction Solar Cells. *J. Am. Chem. Soc.* **2008**, *130*, 3619-3623.

43. Graham, K. R., Stalder, R., Wieruszewski, P. M., Patel, D. G., Salazar, D. H., Reynolds, J. R. Tailor-Made Additives for Morphology Control in Molecular Bulk Heterojunction Photovoltaics. *ACS Appl. Mater. Interfaces*, **2013**, *5*, 63-71.

44. Li, M., An, C., Marszalek, T., Baumgarten, M., Yan, H., Mullen, K., Pisula, W. Controlling the Surface Organization of Conjugated Donor-Acceptor Polymers by Their Aggregation in Solution. *Adv. Mater.* **2016**, *28*, 9430-9438.

45. Lee, J., Kim, M., Kang, B., Jo, S. B., Kim, H. G., Shin, J., Cho, K. Side-Chain Engineering for Fine-Tuning of Energy Levels and Nanoscale Morphology in Polymer Solar Cells. *Adv. Energy Mater.* **2014**, *4*, 1400087.

46. Dou, J.-H., Zheng, Y.-Q., Lei, T., Zhang, S.-D., Wang, Z., Zhang, W.-B., Wang, J.-Y., Pei, J. Systematic Investigation of Side-Chain Branching Position Effect on Electron Carrier Mobility in Conjugated Polymers. *Adv. Funct. Mater.* **2014**, *24*, 6270-6278.

47. Heintges, G. H. L., van Franeker, J. J., Wienk, M. M., Janssen, R. A. J. The Effect of Branching in a Semiconducting Polymer on the Efficiency of Polymer Photovoltaic Cells. *Chem. Commun.* **2016**, *52*, 92-95.

48. Himmelberger, S., Salleo, A. Engineering Semiconducting Polymers for Efficient Charge Transport. *MRS Communications*, **2015**, *5*, 383-395.

49. Hollinger, J., Seferos, D. S. Morphology Control of Selenophene-Thiophene Block Copolymers Through Side Chain Engineering. *Macromolecules*, **2014**, *47*, 5002-5009.

50. Zhang, F., Hu, Y., Schuettfort, T., Di, C., Gao, X., McNeill, C. R., Thomsen, R., Mannsfeld, S. C. B., Yuan, W., Sirringhaus, H., Zhu, D. Critical Role of Alkyl Chain Branching of Organic Semiconductors in Enabling Solution-Processed N-Channel Organic Thin Film Transistors with Mobility up to 3.50 $cm^2 V^{-1} s^{-1}$. *J. Am. Chem. Soc.* **2013**, *135*, 2338-2349.

51. Kang, B., Kim, R., Lee, S. B., Kwon, S.-K., Kim, Y.-H., Cho, K. Side-Chain-Induced Rigid Backbone Organization of Polymer Semiconductors through Semifluoroalkyl Side Chains. *J. Am. Chem. Soc.* **2016**, *138*, 3679-3686.

52. Fall, S., Biniek, L., Odarchenko, Y., Anokhin, D. V., de Tourneadre, G., Leveque, P., Leclerc, N., Ivanov, D. A., Simonetti, O., Giraudet, L., Heiser, T. Tailoring the Microstructure and Charge Transport in Conjugated Polymers by Alkyl Side-Chain Engineering. *J. Mater. Chem. C*, **2016**, *4*, 286-294.

53. Duan, C., Willems, R. E. M., van Franeker, J. J., Bruijnaers, B. J., Wienk, M. M., Janssen, R. A. J. Effect of Side Chain Length on Charge Transport, Morphology, and Photovoltaic Performance of Conjugated Polymers in Bulk Heterojunction Solar Cells. *J. Mater. Chem. A*, **2016**, *4*, 1855-1866.

54. Meng, B., Song, H., Chen, X., Xie, Z., Liu, J., Wang, L. Replacing Alkyl with Oligo(ethylene glycol) as Side Chains of Conjugated Polymers for Close π-π Stacking. *Macromolecules*, **2015**, *48*, 4357-4363.

55. Zhan, C., Yao, J. More Than Conformational "Twisting" or "Coplanarity": Molecular Strategies for Designing High Efficiency Non-Fullerene Organic Solar Cells. *Chem. Mater.* **2016**, *28*, 1948-1964.

56. Tsao, H. N., Mullen, K. Improving Polymer Transistor Performance via Morphology Control. *Chem. Soc. Rev.* **2010**, *39*, 2372-2386.

57. Livi, F., Zawacka, N. K., Angmo, D., Jorgensen, M., Krebs, F. C., Bundgaard, E. Influence of Side Chain Position on the Electrical Properties of Organic Solar Cells Based on Dithienylbenzothiadiazole-*alt*-phenylene Conjugated Polymers. *Macromolecules*, **2015**, *48*, 3481-3492.

58. Lee, J., Kim, J.-H., Moon, B., Kim, H. G., Kim, M., Shin, J., Hwang, H., Cho, K. Two-Dimensionally Extended π-Conjugation of Donor-Acceptor Copolymers via

Oligothienyl Side Chains for Efficient Polymer Solar Cells. *Macromolecules*, **2015**, *48*, 1723-1735.

59. Homyak, P., Liu, Y., Ferdous, S., Liu, F., Russell, T. P., Coughlin, E. B. Effect of Pendant Functionality in Thieno[3,4-b]thiophene-*alt*-benzodithiophene Polymers for OPVs. *Chem. Mater.* **2015**, *27*, 443-449.

60. Lui, B., Bazan, G. C. (Eds), *Conjugated Polyelectrolytes Fundamentals and Applications*. Wiley VCH: Weinheim (**2013**).

61. Hoven, C. V., Garcia, A., Bazan, G. C., Nguyen, T.-Q. Recent Applications of Conjugated Polyelectrolytes in Optoelectronic Devices. *Adv. Mater.* **2008**, *20*, 3793-3810.

62. Yang, T., Wang, M., Duan, C., Hu, X., Huang, L., Peng, J., Huang, F., Gong, X. Inverted Polymer Solar Cells with 8.4% Efficiency by Conjugated Polyelectrolyte. *Energy Enivron. Sci.* **2012**, *5*, 8208-8214.

63. Lee, W., Seo, J. H., Woo, H. Y. Conjugated Polyelectrolytes: A New Class of Semiconducting Material for Organic Electronic Devices. *Polymer,* **2013**, *54*, 5104-5121.

64. Watanabe, K., Suda, K., Akagi, K. Hierarchically Self-Assembled Helical Aromatic Conjugated Polymers. *J. Mater. Chem. C*, **2013**, *1*, 2797-2805.

65. Langeveld-Voss, B. M. W., Janssen, R. A. J., Christiaans, M. P. T., Meskers, S. C. J., Dekkers, H. P. J. M., Meijer, E. W. Circular Dichroism and Circular Polarization of Photoluminescence of Highly Ordered Poly{3,4}-di[(*S*)-2-methylbutoxy]thiophene}. *J. Am. Chem. Soc.* **1996**, *118*, 4908-4909.

66. Pu, L. The Study of Chiral Conjugated Polymers. *Acta Polymer*, **1997**, *48*, 116-141.

67. Rodgers, D. S. (Ed.), *Circular Dichroism: Theory and Spectroscopy*. Nova Press: Hauppauge (**2011**).

68. Wallace, B. A., Janes, R. W. (Eds.), *Modern Techniques for Circular Dichroism and Synchrotron Radiation Circular Dichroism Spectroscopy*. IOS Press: London (**2009**).

69. Berova, N., Nakanishi, K., Woody, R. W. (Eds), *Circular Dichroism: Principles and Applications, 2nd ed.*; Wiley-VCH: New York (**2000**).

70. Watanabe, K., Sun, Z., Akagi, K. Interchain Helically π-Stacked Assembly of Cationic Chiral Poly(*para*-phenylene) Derivatives Enforced by Anionic π-Conjugated Molecules through both Electrostatic and π-π Interactions. *Chem. Mater.* **2015**, *27*, 2895-2902.

71. Zhang, L., Wang, T., Shen, Z., Liu, M. Chiral Nanoarchitectonics: Toward the Design, Self-Assembly, and Function of Nanoscale Chiral Twists and Helices. *Adv. Mater.* **2016**, *28*, 1044-1059.

72. Kumar, J., Nakashima, T., Kawai, T. Circularly Polarized Luminescence in Chiral Molecules and Supramolecular Assemblies. *J. Phys. Chem. Lett.* **2015**, *6*, 3445-3452.

73. Freire, F., Quinoa, E., Riguera, R. Chiral Nanostructures in Polymers Under Different Deposition Conditions Observed by Atomic Force Microscopy of Monolayers: Poly(phenylacetylene)s as a Case Study. *Chem. Commun.* **2017**, *53*, 481-492.

74. Zhao, Y.; Rahim, N. A. A.; Xia, Y.; Fujiki, M.; Song, B.; Zhang, Z.; Zhang, W.; Zhu, X. Supramolecular Chirality in Achiral Polyfluorene: Chiral Gelation, Memory of Chirality, and Chiral Sensing Property. *Macromolecules* **2016**, *49*, 3214-3221.

75. Yu, Z-P.; Ma, C-H.; Wang, Q.; Liu, N.; Yin, J.; Wu, Z-Q. Polyallene-*block*-polythiophene-*block*-polyallene Copolymers: One-Pot Synthesis, Helical Assembly, and Multiresponsiveness. *Macromolecules* **2016**, *49*, 1180-1190.

76. Reuther, J. F.; Siriwardane, D. A.; Kulikov, O. V.; Batchelor, B. L.; Campos, R.; Novak, B. M. Facile Synthesis of Rod-Coil Block Copolymers with Chiral, Helical Polycarbodiimide Segments via Postpolymerization with CuAAC "Click" Coupling of Functional End Groups. *Macromolecules*, **2015**, *48*, 3207-3216.

77. Langeveld-Voss, B. M. W.; Janssen, R. A. J.; Meijer, E. W. On the Origin of Optical Activity in Polythiophenes. *J. Mol. Struct.* **2000**, *521*, 285-301.

78. Watanabe, K., Akagi, K. Helically Assembled π-Conjugated Polymers with Circularly Polarized Luminescence. *Sci. Technol. Adv. Mater.* **2014**, *15*, 044203.

79. Peeters, H., Koeckelberghs, G. Conformational Behavior of Conjugated Polymers with Oligo(Phenylene Vinylene) Side Chains. *Macromol. Chem. Phys.* **2013**, *214*, 538-546.

80. Zahn, S., Swager, T. M. Three Dimensional Electronic Delocalization in Chiral Conjugated Polymers. *Angew. Chem. Int. Ed.* **2002**, *41*, 4225-4230.

81. Koeckelberghs, G., Vangheluwe, M., Samyn, C., Persoons, A., Verbiest, T. Regioregular Poly(3-alkylthiophene)s: Toward Soluble, Chiral Conjugated Polymers with a Stable Oxidized State. *Macromolecules*, **2005**, *38*, 5554-5559.

82. Oda, M., Nothofer, H.-G., Scherf, U., Sunjic, V., Richter, D., Regenstein, W., Neher, D. Chiroptical Properties of Chiral Substituted Polyfluorenes. *Macromolecules*, **2002**, *35*, 6792-6798.

83. Satrijo, A., Swager, T. M. Facile Control of Chiral Packing in Poly(*p*-phenylenevinylene) Spin-Cast Films. *Macromolecules*, **2005**, *38*, 4054-4057.

84. Coffin, R. C., Peet, J., Rogers, J., Bazan, G. C. Streamlined Microwave Assisted Preparation of Narrow-Bandgap Conjugated Polymers for High-Performance Bulk Heterojunction Solar Cells. *Nature Chemistry*, **2009**, *1*, 657-661.

85. McCulloch, I., Heeney, M., Bailey, C., Genevicius, K., MacDonald, I., Shkunov, M., Sparrowe, D., Tierney, S., Wagner, R., Zhang, W., Chabinyc, M. L., Kline, R. J., McGehee, M. D., Toney, M. F. Liquid-Crystalline Semiconducting Polymers with High Charge Carrier Mobility. *Nature Mater.* **2006**, *5*, 328-333.

86. Muhlbacher, D., Scharber, M., Morana, M., Zhu, Z., Waller, D., Gaudiana, R., Brabec, C. High Photovoltaic Performance of a Low-Bandgap Polymer. *Adv. Mater.* **2006**, *18*, 2884-2889.

87. Kim, J. Y., Lee, K., Coates, N. E., Moses, D., Nguyen, T.-Q., Dante, M., Heeger, A. J. Efficient Tandem Polymer Solar Cells Fabricated by All-Solution Processing. *Science*, **2007**, *317*, 222-225.

88. Ying, L., Hsu, B. B. Y., Zhan, H., Welch, G. C., Zalar, P., Perez, L. A., Kramer, E. J., Nguyen, T.-Q., Heeger, A. J., Wong, W. Y., Bazan, G. C. Regioregular Pyridal[2,1,3]thiadiazole π-Conjugated Copolymers. *J. Am. Chem. Soc.* **2011**, *133*, 18538-18541.

89. Tseng, H. R., Phan, H., Luo, C., Wang, M., Perez, L. A., Patel, S. N., Ying, L., Kramer, E. J., Nguyen, T.-Q., Bazan, G. C., Heeger, A. J. High-Mobility Field-Effect Transistors Fabricated with Macroscopic Aligned Semiconducting Polymers. *Adv. Mater.* **2014**, *26*, 2993-2998.

90. Luo, C., Kyaw, A. K. K., Perez, L. A., Patel, S. N., Wang, M., Grimm, B., Bazan, G. C., Kramer, E. J., Heeger, A. J. General Strategy for Self-Assembly of Highly Oriented Nanocrystalline Semiconducting Polymers with High Mobility. *Nano Lett.* **2014**, *14*, 2764-2771.

91. Hou, J., Chen, T. L., Zhang, S., Chen, H.-Y., Yang, Y. Poly[4,4-bis(2-ethylhexyl)cyclopenta[2,1-b;3,4-b’]dithiophene-2,6-diyl-*alt*-2,1,3-benzoselenadiazole-4,7-diyl], a New Low Band Gap Polymer in Polymer Solar Cells. *J. Phys. Chem. C*, **2009**, *113*, 1601-1605.

92. Rogers, J. T., Schmidt, K., Toney, M. F., Kramer, E. J., Bazan, G. C. Structural Order in Bulk Heterojunction Films Prepared with Solvent Additives. *Adv. Mater.* **2011**, *23*, 2284-2288.

93. Jackson, N. E., Kohlstedt, K. L., Savoie, B. M., de la Cruz, M. O., Schatz, G. C., Chen, L. X., Ratner, M. A. Conformational Order in Aggregates of Conjugated Polymers. *J. Am. Chem. Soc.* **2015**, *137,* 6254-6262.

94. Hiszpanski, A. M., Loo, Y.-L. Directing the Film Structure of Organic Semiconductors via Post-Deposition Processing for Transistor and Solar Cell Applications. *Energy Environ. Sci.* **2014**, *7,* 592-608.

95. Fronk, S. L.; Wang, M.; Ford, M.; Coughlin, J.; Mai, C.-K.; Bazan, G. C. Effect of Chiral 2-ethylhexyl Side Chains on Chiroptical Properties of the Narrow Bandgap Conjugated Polymers PCPDTBT and PCDTPT. *Chem. Sci.* **2016**, *7,* 5313-5321.

96. Huang, Y., Zhang, F., Gong, Y. A Convenient Approach to (*S*)-2-ethylhexan-1-ol Mediated by Baker's Yeast. *Tetrahedron Letters.* **2005**, *46*, 7217-7219.

97. Grenier, C. R., George, S. J., Joncheray, T. J., Meijer, E. W., Reynolds, J. R. Chiral Ethylhexyl Substituents for Optically Active Aggregates of π-Conjugated Polymers. *J. Am. Chem. Soc.* **2007**, *129*, 10694-10699.

98. Parker, D. NMR Determination of Enantomeric Purity. *Chem. Rev.* **1991**, *91*, 1441-1457.

99. Latypov, S. K., Ferreiro, M. J., Quinoa, E., Riguera, R. Assignment of the Absolute Configuration of β-Chiral Primary Alcohols by NMR: Scope and Limitations. *J. Am. Chem. Soc.* **1998**, *120*, 4741-4751.

100. Harada, N., Watanabe, M., Kuwahara, S., Sugio, A., Kasai, Y., Ichikawa, A. 2-Methoxy-2-(1-naphthyl)propionic acid: A Powerful Chiral Auxiliary for Enantioresolution of Alcohols and Determination of their Absolute Configurations by the ^{1}H NMR Anisotropy Method. *Tetrahedron: Asymmetry*. **2000**, *11*, 1249-1253.

101. Bifulco, G., Dambruoso, P., Gomez-Paloma, L., Riccio, R. Determination of Relative Configuration in Organic Compounds in NMR Spectroscopy and Computational Methods. *Chem. Rev.* **2007**, *107*, 3744-3779.

102. Seco, J. M., Quinoa, E., Riguera, R. The Assignment of Absolute Configuration by NMR. *Chem. Rev.* **2004**, *104*, 17-117.

103. Zhu, Z., Waller, D., Gaudiana, R., Morana, M., Muhlbacher, D., Scharber, M., Brabec, C. Panchromatic Conjugated Polymers Containing Alternating

Donor/Acceptor Units for Photovoltaic Applications. *Macromolecules*, **2007**, *6*, 1981-1986.

104. Resta, C. C., Di Pietro, S., Maja Majerić Elenkov, M. M., Hameršak, Z., Pescitelli, G., Di Bari, L. Consequences of Chirality on the Aggregation Behavior of Poly[2-methoxy-5-(2'-ethylhexyloxy)-p-phenylenevinylene] (MEH-PPV). *Macromolecules*, **2014**, *47*, 4847-4850.

105. Yang, X., Seo, S., Park, C., Kim, E. Electrical Chiral Assembly Switching of Soluble Conjugated Polymers from Propylenedioxythiophene-Phenylene Copolymers. *Macromolecules.* **2014**, *47*, 7043-7051.

106. Kawashima, H., Kawabata, K., Goto, H. Intramolecular Charge Transfer (ICT) of Chiroptically Active Conjugated Polymer Showing Green Colour. *J. Mater. Chem. C.* **2015**, *3*, 1126-1133.

107. Satrijo, A., Meskers, S. C. J., Swager, T. M. Probing a Conjugated Polymer's Transfer of Organization-Dependent Properties from Solutions to Films. *J. Am. Chem. Soc.* **2006**, *128*, 9030-9031.

108. Goto, H., Okamoto, Y., Yashima, E. Solvent-Induced Chiroptical Changes in Supramolecular Assemblies of an Optically Active Regioregular Polythiophene. *Macromolecules.* **2002**, *35*, 4590-4601.

109. Langeveld-Voss, B. M. W., Christiaans, M. P. T., Janssen, R. A. J., Meijer, E. W. Inversion of Optical Activity of Chiral Polythiophene Aggregates by a Change of Solvent. *Macromolecules,* **1998**, *31*, 6702-6704.

110. Bidan, G., Guillerez, S., Sorokin, V. Chirality in Regioregular and Soluble Polythiophene: An Internal Probe of Conformational Changes Induced by Minute Solvation Variation. *Adv. Mater.* **1996**, *8*, 157-160.

111. Jackson, N. E., Savoie, B. M., Kohlstedt, K. L., de la Cruz, M. O., Schatz, G. C., Chen, L. X., Ratner, M. A. Controlling Conformations of Conjugated Polymers and Small Molecules: The Role of Nonbonding Interactions. *J. Am. Chem. Soc.* **2013**, *135*, 10475-10483.

112. Huang, H., Chen, Z., Ortiz, R. P., Newman, C., Usta, H., Lou, S., J. Youn, J., Noh, Y.-Y., Baeg, K.-J., Chen, L. X., Facchetti, A., Marks, T. Combining Electron-Neutral Building Blocks with Intramolecular "Conformational Locks" Affords Stable, High-Mobility P- and N-Channel Polymer Semiconductors. *J. Am. Chem. Soc.* **2012**, *134*, 10966-10973.

113. Coughlin, J. E., Zhugayevych, A., Bakus, R. C., van der Poll, T. S., Welch, G. C., Teat, S. J., Bazan, G. C., Tretiak, S. A Combined Experimental and

Theoretical Study of Conformational Preferences of Molecular Semiconductors. *J. Phys. Chem. C*, **2014**, *118*, 15610-15623.

114. Wang, M., Ford, M., Phan, H., Coughlin, J., Nguyen, T.-Q., Bazan, G. C. Fluorine Substitution Influence on Benzo[2,1,3]thiadiazole Based Polymers for Field-Effect Transistor Applications. *Chem. Commun.* **2016**, *52*, 3207-3210.

115. van der Poll, T. S., Love, J. A., Nguyen, T.-Q., Bazan, G. C. Non-Basic High-Performance Molecules for Solution-Processed Organic Solar Cells. *Adv. Mater.* **2012**, *24*, 3646-3649.

116. Xiao, Z., Sun, K., Subbiah, J., Qin, T., Lu, S., Purushothaman, B., Jones, D. J., Holmes, A. B., Wong, W. W. H. Effect of Molecular Weight on the Properties and Organic Solar Cell Performance of a Donor-Acceptor Conjugated Polymer. *Polym. Chem.* **2015**, *6*, 2312-2318.

117. Kang, H., Uddin, M. A., Lee, C., Kim, K.-H., Nguyen, T. L., Lee, W., Li, Y., Wang, C., Woo, H. Y., Kim, B. J. Determining the Role of Polymer Molecular Weight for High-Performance All-Polymer Solar Cells: Its Effect on Polymer Aggregation and Phase Separation. *J. Am. Chem. Soc.* **2015**, *137*, 2359-2365.

118. Li, W., Yang, L., Tumbleston, J. R., Yan, L., Ade, H., You, W. Controlling Molecular Weight of a High Efficiency Donor-Acceptor Conjugated Polymer and Understanding its Significant Impact on Photovoltaic Properties. *Adv. Mater.* **2014**, *26*, 4456-4462.

119. Wang, M., Wang, H., Yokoyama, T., Liu, X., Huang, Y., Zhang, Y., Nguyen, T.-Q., Aramaki, S., Bazan, G. C. High Open Circuit Voltage in Regioregular Narrow Band Gap Polymer Solar Cells. *J. Am. Chem. Soc.* **2014**, *136*, 12576-12579.

120. Wang, M., Wang, H., Ford, M., Yuan, J., Mai, C.-K., Fronk, S. L., Bazan, G. C. Influence of Molecular Structure on the Performance of Low V_{oc} Loss Polymer Solar Cells. *J. Mater. Chem. A*, **2016**, *4*, 15232-15239.

121. Ran, N. A., Love, J. A., Takacs, C. J., Sadhanala, A., Beavers, J. K., Collins, S. D., Huang, Y., Wang, M., Friend, R. H., Bazan, G. C., Nguyen, T.-Q. Harvesting the Full Potential of Photons with Organic Solar Cells. *Adv. Mater.* **2016**, *28*, 1482-1488.

122. Menke, S. M., Sadhanala, A., Nikolka, M., Ran, N. A., Ravva, M. K., Abdel-Azeim, S., Stern, H. L., Wang, M., Sirringhaus, H., Nguyen, T.-Q., Bredas, J.-L., Bazan, G. C., Friend, R. H. Limits for Recombination in a Low Energy Loss Organic Heterojunction. *ACS Nano*, **2016**, *10*, 10736-10744.

123. Frisch, M. J.; Trucks, G. W.; Schlegel, H. B.; Scuseria, G. E.; Robb, M. A.; Cheeseman, J. R.; Scalmani, G.; Barone, V.; Mennucci, B.; Petersson, G. A.;

Nakatsuji, H.; Caricato, M.; Li, X.; Hratchian, H. P.; Izmaylov, A. F.; Bloino, J.; Zheng, G.; Sonnenberg, J. L.; Hada, M.; Ehara, M.; Toyota, K.; Fukuda, R.; Hasegawa, J.; Ishida, M.; Nakajima, T.; Honda, Y.; Kitao, O.; Nakai, H.; Vreven, T.; Montgomery, J.; Peralta, J. E.; Ogliaro, F.; Bearpark, M.; Heyd, J. J.; Brothers, E.; Kudin, K. N.; Staroverov, V. N.; Kobayashi, R.; Normand, J.; Raghavachari, K.; Rendell, A.; Burant, J. C.; Iyengar, S. S.; Tomasi, J.; Cossi, M.; Rega, N.; Millam, J. M.; Klene, M.; Knox, J. E.; Cross, J. B.; Bakken, V.; Adamo, C.; Jaramillo, J.; Gomperts, R.; Stratmann, R. E.; Yazyev, O.; Austin, A. J.; Cammi, R.; Pomelli, C.; Ochterski, J. W.; Martin, R. L.; Morokuma, K.; Zakrzewski, V. G.; Voth, G. A.; Salvador, P.; Dannenberg, J. J.; Dapprich, S.; Daniels, A. D.; Farkas, Ö; Foresman, J. B.; Ortiz, J. V.; Cioslowski, J.; Fox, D. J. *Gaussian 09, Revision C.01*, Gaussian, Inc.: Wallingford, CT, **2010**.

124. Yanai, T.; Tew, D. P.; Handy, N. C. A New Hybrid Exchange-Correlation Functional Using the Coulomb Attenuating Method (CAM-B3LYP). *Chem. Phys. Lett.* **2004**, *393*, 51-57.

III. Aggregation Behavior of Benzotriazole-Based Polymers

A. Background

Conjugated polymers and small molecules containing chiral side-chains have generated recent interest based on their ability to self-assemble into novel nanostructures.[1-7] Recent work has focused on developing materials for chiral sensing applications,[1] synthesizing pH- and thermoresponsive triblock copolymers,[2] and designing liquid crystalline block copolymers with potential applications in drug delivery and as biological mimics.[3] Research has also explored the amount of chiral content necessary to induce helical structure formation.[8-10] In addition to novel nanostructures and possible applications, the presence of chiral side chains provides a design handle to investigate the secondary structure and aggregation of conjugated polymers.[11-15] Specifically, replacing the racemic 2-ethylhexyl substituents with (*S*)-2-ethylhexyl chains has previously been used to understand structure-property relationships of donor-acceptor (D-A) copolymers through chiroptical measurements.[16]

A better understanding of the aggregation properties of conjugated polymers is warranted due to the translation of organization in solution to the solid state.[17-19] Molecular design can be utilized to control aggregation and self-assembly in solution[20-22] through the choice of backbone structural units and side chain engineering.[23-29] Processing conditions, such as solvent,[30-31] solution temperature,[32-33] and solvent additives[34-36] among others, also influence the final bulk morphology. Conjugated polymers have previously been observed to self-assemble into aggregates even in “good” solvents such as chlorobenzene or chloroform.[33,37-38] Capitalizing on this capability has the potential to result in novel polymer organizations,[39-40] for example, helical nanostructures.[12-13]

Benzotriazole (BTz)-containing copolymers are relevant within the context of this discussion due to their previous use as donor materials in organic solar cells[41-44] and in organic field effect transistors (OFETs).[45-48] Polybenzotriazole homopolymers synthesized using novel catalysts show potential as n-type materials.[49-50] The benzotriazole monomer is a weakly electron-deficient unit that can be modified by an alkyl chain at one of the nitrogen atoms on the triazole ring.[45] The advantage of incorporating solubilizing chains onto the BTz unit when copolymerized with electron donating units such as carbazole,[43] fluorene,[43] and benzodithiophene[41,44] is a closer packing of polymer chains due to a more planarized backbone conformation.[45] Recent work also explored copolymerizing 2-hexyldecyl-benzotriazole monomers containing different functional groups at the 5- and 6-positions with a thiophene monomer in order to improve hole mobility in polymer OFETs through increased planarity of the conjugated backbone.[48] The effort demonstrated that noncovalent interactions, such as those between the nitrogen atom on the BTz and the hydrogen atom on the thiophene ring, act as “conformational locks” that favor coplanar configurations.[48]

Building on the previous chapter, this chapter aims to probe alternative molecular structures and further explore the possibility of chirality within an aggregate. Within this context, a better understanding of the aggregation properties of benzotriazole-based polymers is developed. Below an initial exploration of poly(benzotriazole) with ionic side chains is introduced followed by a more in-depth report on a benzotriazole-thiophene copolymer containing chiral side chains.

B. Optical Properties of Benzotriazole-Based Conjugated Polyelectrolytes

1. Introduction

Conjugated polyelectrolytes (CPEs) contain a conjugated polymer backbone and side chains with pendant ionic groups.[51-54] One advantage of the pendant ionic group is processability from environmentally-friendly solvents such as water while maintaining the semiconducting properties of the conjugated backbone.[52-54] These materials are of interest for organic electronic applications such as solar cells,[55-56] transistors,[57-58] and thermoelectric devices.[59-61] In particular, n-type CPEs have received limited attention.[62-66] Therefore, understanding the optical and aggregation properties of these CPEs provides valuable basic knowledge when designing new materials.

Benzotriazole homopolymers are of interested based on their strong electron affinity and therefore their n-type character.[67-72] Additional interested was generated when DFT calculations suggested that a benzotriazole-based homopolymer forms a twisted structure as shown in Figure 3-1. DFT calculations used vacuum as the medium and considered a molecule containing 15 benzotriazole units. Benzotriazole-based CPEs were synthesized using Yamamoto polymerization with a Ni(COD)$_2$ catalyst.[50] The structures of the three CPEs studied are shown in Figure 3-2. The optical and aggregation properties were studied using optical absorption spectroscopy, fluorescence spectroscopy, and dynamic light scattering.

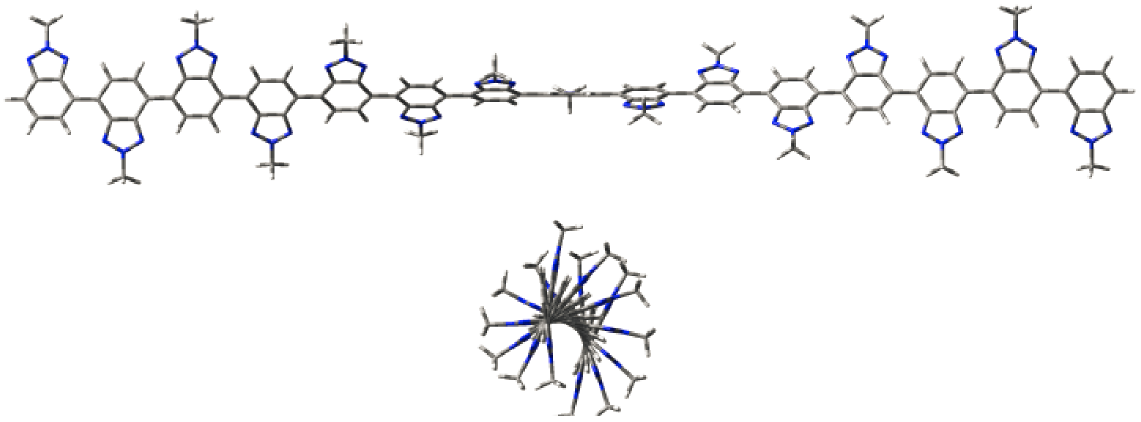

Figure 3-1. Structure of 15-mer benzotriazole molecule as calculated using DFT methods.

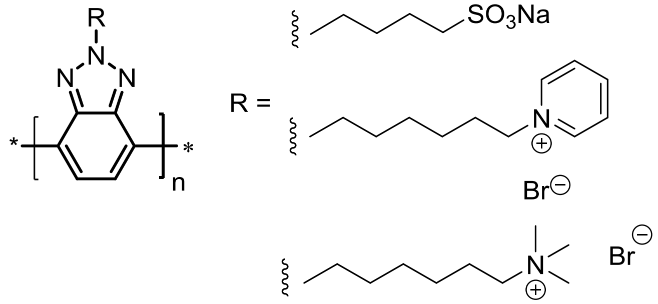

Figure 3-2. Structures of Benzotriazole-based CPEs.

2. Solution Characterization of PBTz-Based CPEs

Solution absorption spectra of PBTz-PyrBr and PBTz-TMABr were taken in three polar solvent systems (H_2O, 1:1 H_2O:MeOH, MeOH) and shown in Figure 3-3. Both CPEs exhibit absorption peaks in the expected range for a benzotriazole conjugated backbone.[49] Absorption spectra of PBTz-PyrBr are red-shifted compared to PBTz-TMABr. An increase in solvent polarity typically results in red-shifted absorption spectra for CPEs.[73-74] However, PBTz-PyrBr and PBTz-TMABr show the opposite trend with blue-shifted absorption with increasing solvent polarity.

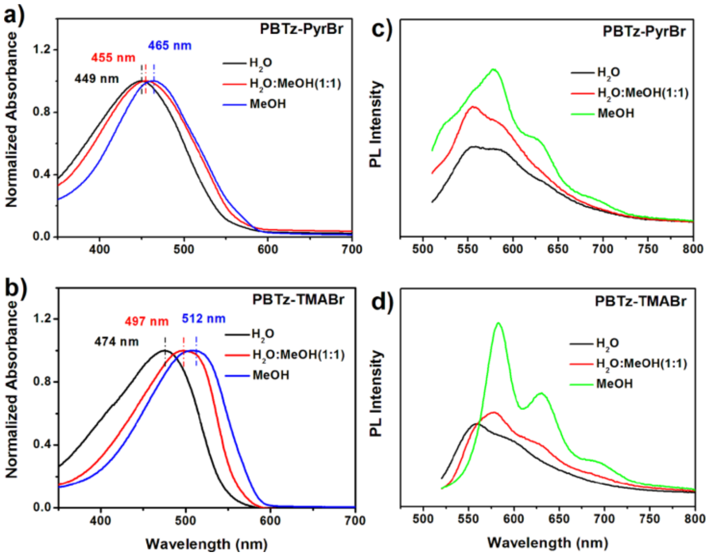

Figure 3-3. Optical absorption and PL intensity of PBTz-PyrBr and PBTz-TMABr solutions in polar solvents with a concentration of 0.0167 mg/mL. The value of λ_{Ex} corresponds to the maximum absorption peak.

Dynamic light scattering was used to estimate the particle size of PBTz-PyrBr and PBTz-TMABr under the same solvent conditions as the optical absorption measurements. Both PBTz-PyrBr and PBTz-TMABr provide bimodal distributions, indicating the co-existence of two different particle sizes. The data are presented in Table 3-1. Hydrodynamic radii (R_{hyd}) were on the order of tens and hundreds of nanometers for the small and large particles respectively. These data suggest the presence of small and large aggregates in solution. The peak percent by mass describes the relative proportions of the two components and allows comparison of similar samples. A comparison of the larger aggregates suggests that the peak percent by mass increases as the solvent polarity decreases for both PBTz-PyrBr and PBTz-TMABr. PBTz-TMABr consistently exhibits larger R_{hyd} with higher peak percent by mass than PBTz-PyrBr. These results are in agreement with the absorption spectra. Both CPEs are easily dissolved in water, such that aggregation is mediated by electrostatic pair of the ionic functionalities in lower dielectric media.

Table 3-1. R_{hyd} and fluorescence quantum yield for PBTz-PyrBr and PBTz-TMABr

Solvent	Avg. Hydrodynamic Radii (nm)		Fluorescence Quantum Yield	
	PBTz-PyrBr	PBTz-TMABr	PBTz-PryBr	PBTz-TMABr
H_2O	285 (24%)	369 (74%)	11%	16%
1:1 H_2O:MeOH	370 (68%)	409 (78%)	16%	25%
MeOH	345 (67%)	380 (88%)	53%	61%

Fluorescence spectra were collected under the same solvent conditions as optical absorption spectra. PBTz-PyrBr and PBTz-TMABr exhibit similar PL spectra in H_2O and 1:1 H_2O:MeOH. However, in MeOH, a red-shift in the emission maximum is observed along with more well-defined vibronic features. PL intensities can provide further information on aggregation as interchain aggregation often decreases PL intensity due to self-quenching.[73-75] Changes in PL intensity were quantified by determining the fluorescence quantum yields. Rhodamine 101 in MeOH was chosen as the reference and the results are shown in Table 3-1. As the solvent polarity decreases, the fluorescence quantum yield increases such that choosing MeOH as the solvent provides the highest quantum yields. These data, combined with the DLS results, suggest fluorescence intensity increases with aggregation.

Examining a benzotriazole-based CPE with an anionic functional group provides additional insight into the aggregation behaviors of benzotriazole-based CPEs. The optical absorption and emission spectra are shown in Figure 3-4. PBTz-Na exhibits the opposite trend as the cationic CPEs with a blue-shift in absorption maximum when the solvent is changed from 1:1 H_2O:DMF to H_2O. Similarly, DLS shows aggregation decreases with decreasing solvent polarity. In H_2O, the larger aggregate is 98 nm (29%) and in 1:1 H_2O:DMF, the larger aggregate is 103 nm (7%). This reversal in trends indicates that the identity of the ionic group influences polymer aggregation properties.

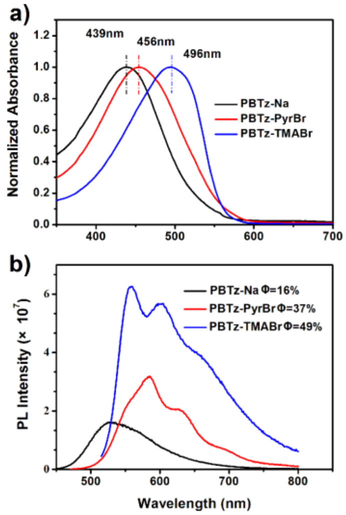

Figure 3-4. (a) Optical absorption and b) PL spectra of PBTz-Na, PBTz-PyrBr, and PBTz-TMABr in 0.0167 mg/mL 1:1 H_2O:DMF.

3. Conclusions

The aggregation properties of three benzotriazole-based CPEs were studied using optical absorption and fluorescence spectroscopies along with DLS. The identity of the pendant ionic group (tetraalkylammonium bromide, pyridinium bromide, sodium sulfonate) impact how the polymer chains aggregate in solution. PBTz-TMABr is the most aggregated based on having the largest aggregate size, the most red-shifted absorption, and the highest fluorescence quantum yield. Additionally, negative solvatochromic effects are observed for both cationic CPEs. This work provides a basis for further study of benzotriazole-based polymers where the ionic side chain is replaced with a chiral side chain.

C. Chiroptical Properties of a Benzotriazole-Thiophene Copolymer Bearing Chiral Ethylhexyl Side Chains

1. Introduction

In this section, the (*S*)-2-ethylhexyl chain is introduced on a BTz unit that is copolymerized with thiophene to form the D-A copolymer, PBTz-Th*. Thiophene was chosen as the electron donating unit based on the precedent for thiophene-containing D-A copolymers,[23,51-52] and the potential for chain planarity induced by noncovalent interactions between the two units.[48] Thus, it is possible to study the strength of these noncovalent interactions to induce planarity vs. the potential tendency of chiral-containing conjugated polymers to form helical structures. Compared to recent studies on the chiroptical properties of a cyclopentadithiophene-benzothiadiazole copolymer (PCPDTBT*) and a regioregular cyclopentadithiophene-pyridylthiadiazole copolymer (PCDTPT*), both containing (*S*)-2-ethylhexyl side chains,[16] the side-chain density on PBTz-Th* decreases from two chains per monomer unit to one and the distance between the backbone and the side chain increases, as shown in Figure 3-5. Initial synthetic attempts focused on the benzotriazole homopolymer. However, the poor solubility of the polymer prevented achieving a molecular weight sufficiently high to study its chiroptical properties, resulting in a shift in focus to synthesizing PBTz-Th*. The chiroptical properties of PBTz-Th* in solution and the thin film provide insight into the structure of the chain within aggregates in solution and the intramolecular forces that determine its secondary structure.

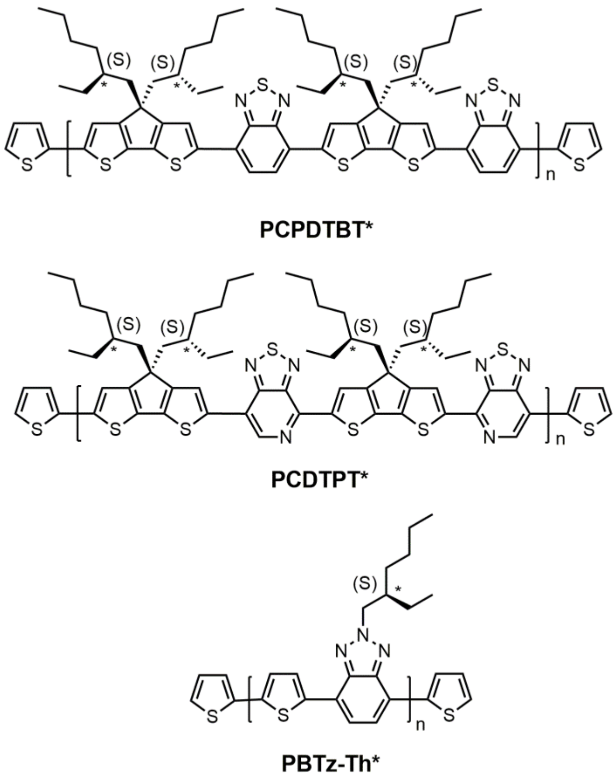

PCPDTBT*

PCDTPT*

PBTz-Th*

Figure 3-5. Structures of PCPDTBT* (top), PCDTPT* (middle), and PBTz-Th* (bottom).

2. Synthesis

As shown in Scheme 3-1, (*S*)-2-ethylhexan-1-ol was synthesized using a modification of literature procedures.[76] Reduction of the α,β-unsaturated aldehyde to the chiral alcohol is accomplished using Baker's yeast as a biocatalyst.[76] High chiral purity was deemed necessary to accentuate any changes in polymer structural characteristics. Optical rotation and a chiral derivatizing agent were used to confirm chiral purity as described previously[77-81] and reported in the Experimental and Supporting Information Section (SI). The remaining sequence of steps for the preparation of the target PBTz-Th* is outlined in Scheme 3-1. (*S*)-2-Ethylhexan-1-ol was converted to (*S*)-3-(bromomethyl)heptane via reaction with 2.7 eq. Br_2 and 1.4 eq. PPh_3 in dichloromethane. BTz-Br_2 was synthesized as reported before.[50] Attachment of the chiral side-chain to the benzotriazole framework yields EH-S-BTz by applying previously described alkylation protocols.[82] Polymerization of EH-S-BTz and bis(Me_3Sn)thiophene was carried out using conventional Stille coupling conditions.[83] One eq. EH-S-BTz, 1.05 eq. bis(Me_3Sn)thiophene, and 0.052 eq. $Pd(PPh_3)_4$ as the catalyst were dissolved in toluene and heated in an oil bath at 110 °C for 4 days. After precipitation, the resulting polymer, PBTz-Th*, was obtained with a number average molecular weight, M_n, of 6.2 K and a dispersity, $Đ$, of 1.1. The reference polymer (PBTz-Th) containing racemic 2-ethylhexyl side chains was prepared using the same procedure (Scheme S3-9). PBTz-Th was obtained with M_n = 6.2 K and $Đ$ = 1.1. It should be noted that poor solubility[49-50] limited the molecular weight achievable for both PBTz-Th* and PBTz-Th. Multiple solvent systems for polymerization were tested (xylene, THF, toluene, and dichlorobenzene) and toluene provided the highest molecular weights. Characterization by differential scanning calorimetry (DSC) reveals no phase transitions for either material in the range of 20 °C to 250 °C (Figure S3-2).

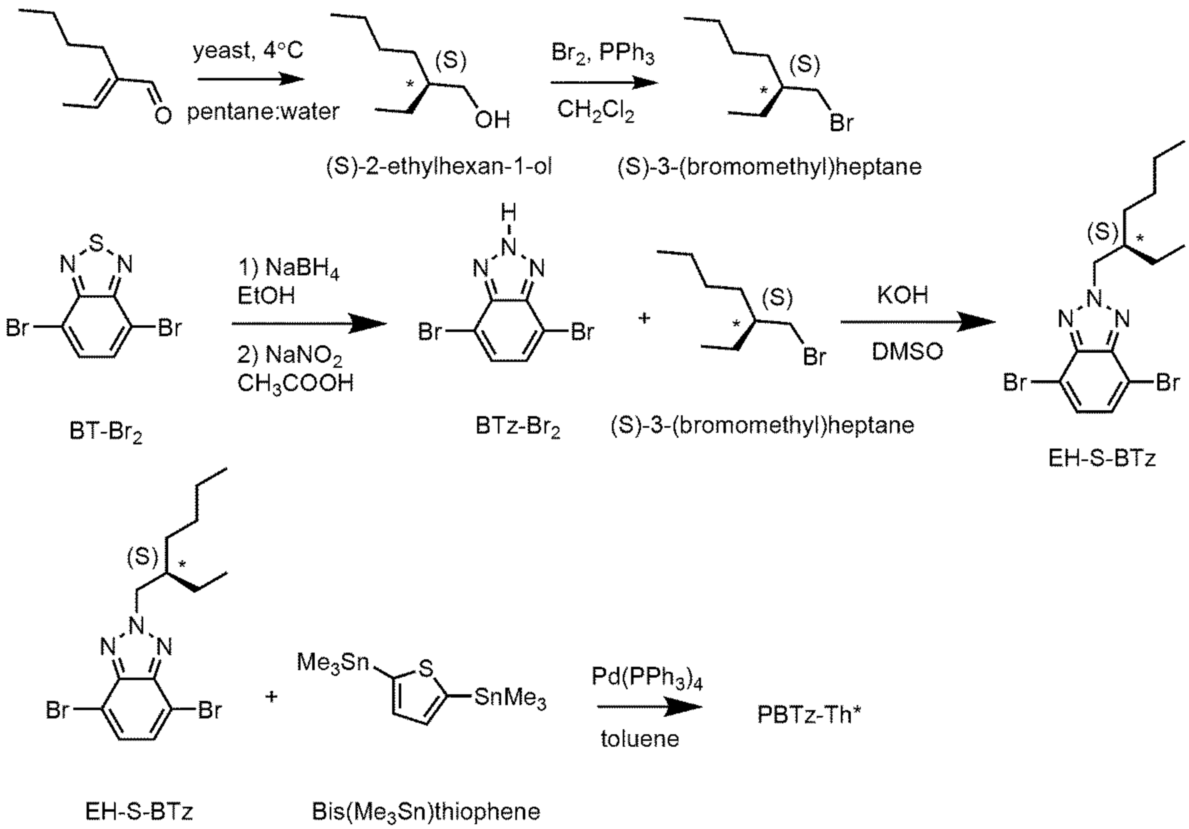

Scheme 3-1. Synthesis of PBTz-Th*

3. Chiroptical Properties of PBTz-Th* and PBTz-Th in Solution

Optical absorption and circular dichroism (CD) spectroscopies were measured for dilute solutions of PBTz-Th* and PBTz-Th in chlorobenzene (CB), ortho-dichlorobenzene (DCB), and toluene. Concentrations ranged from 0.0025 mg/mL to 0.1 mg/mL. The normalized optical absorption spectra of PBTz-Th* and PBTz-Th in dilute CB are shown in Figure 3-6a. No significant difference is evident between the two materials. Both materials show an absorption maximum at 573 nm and a second red-shifted peak at 622 nm. Vibronic-like features, such as those present in Figure 3-6a, are typically associated with the presence of aggregated chains.[84-90] The absorption band with a peak maximum at 573 nm corresponds to the intramolecular charge transfer band. In the case of PBTz-Th* and PBTz-Th, intramolecular charge transfer is observed from the thiophene unit to the benzotriazole unit. Absorption spectra of PBTz-Th* were measured in dilute DCB and toluene (Figure 3-6b). The absorption spectrum in DCB mirrors that in CB, however the spectrum in toluene exhibits a blueshift in the maximum (535 nm) and a decrease in relative shoulder peak intensity. Therefore, toluene likely contains a greater fraction of well-dissolved chains compared to CB and DCB. For the sake of thoroughness, we also include the emission spectrum of PBTz-Th* in CB in the SI (Figure S3-3).

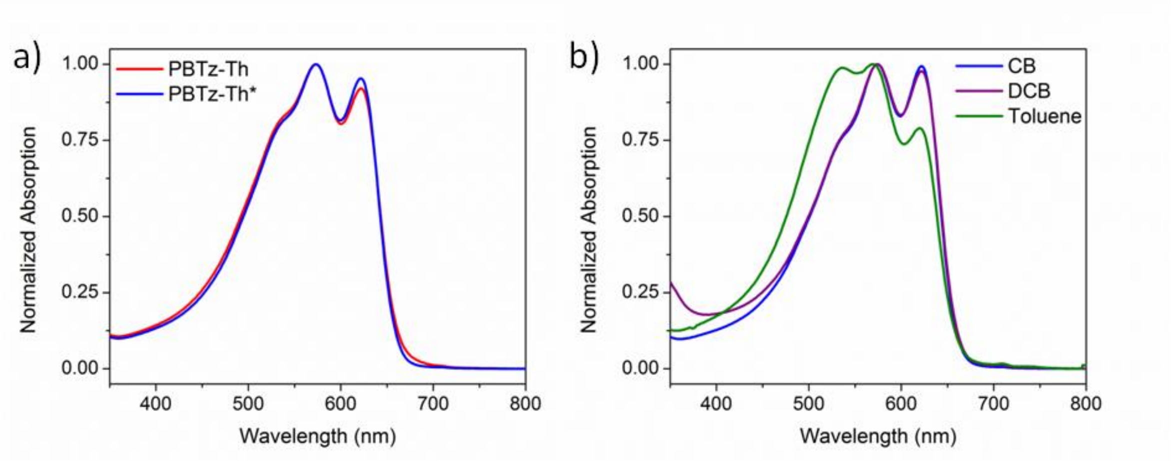

Figure 3-6. Normalized optical absorption spectra of a) PBTz-Th (red) and PBTz-Th* (blue) solutions in 0.01 mg/mL DCB and b) PBTz-Th* in 0.01 mg/mL CB (blue), DCB (purple), and toluene (green).

Temperature-dependent optical absorption spectra of PBTz-Th* were measured in dilute DCB solution at a concentration of 0.0025 mg/mL (Figure 3-7). In these experiments, solutions were heated from 25 °C to 110 °C and the spectra were measured every 10 °C. The resulting spectra show a progressive decrease in the red-most peak (622 nm) with increasing temperature. However, even at 110 °C, the vibronic structure has not fully disappeared. Temperature-dependent absorption of PBTz-Th was also measured and a similar decrease in the peak at 622 nm with increasing temperature is observed (Figure S3-

4). These results suggest a strong degree of interchain interactions in solution, such that a fraction of the chains remain in aggregates even at 110 °C. The poor solubility of this material reflects this pronounced tendency to aggregate.

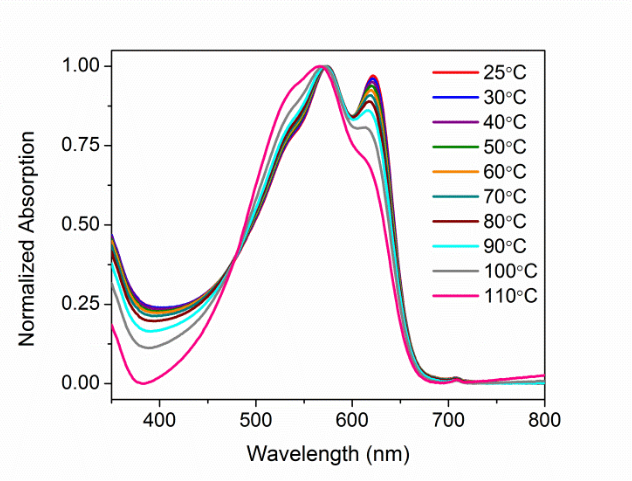

Figure 3-7. Normalized optical absorption spectra of PBTz-Th* solution in 0.0025 mg/mL DCB as a function of temperature, from 25-110 °C.

Figure 4-8a provides the room temperature CD spectra of PBTz-Th in 0.005 mg/mL DCB and of PBTz-Th* as a function of concentration in DCB. CD signals are present for PBTz-Th* but not PBTz-Th, which demonstrates the translation of optical activity from the chiral side chains to the chromophoric backbone. PBTz-Th* shows the expected bisignate Cotton effects such that the CD spectrum is roughly the first derivative of the absorption spectrum (Figure S3-6). The CD response is present in the absorption range of the aggregated PBTz-Th* chains and not in the absorption range of well-solvated chains. Thus, the well-solvated chains are not CD active. As the concentration of PBTz-Th* in DCB is increased, the ratio of the peak at 650 nm to the peak at 605 nm increases. For all solvents tested (toluene, CB, DCB), PBTz-Th* provides a CD signal at concentrations of 0.005 mg/mL (Figure S3-7). However, at the same concentration, solutions in CB and DCB provide a stronger CD signal compared to solutions in toluene. These observations are consistent with the optical absorption results, which suggest that there are more well-dissolved polymer chains in toluene. The reduction in CD signal in toluene, where less aggregation is observed in the optical absorption spectrum, indicates that the aggregated species is responsible for the CD signal. This explanation agrees with previous work on polymers bearing chiral (*S*)-2-ethylhexyl side chains where aggregated chains are the source of the chiral response.[16]

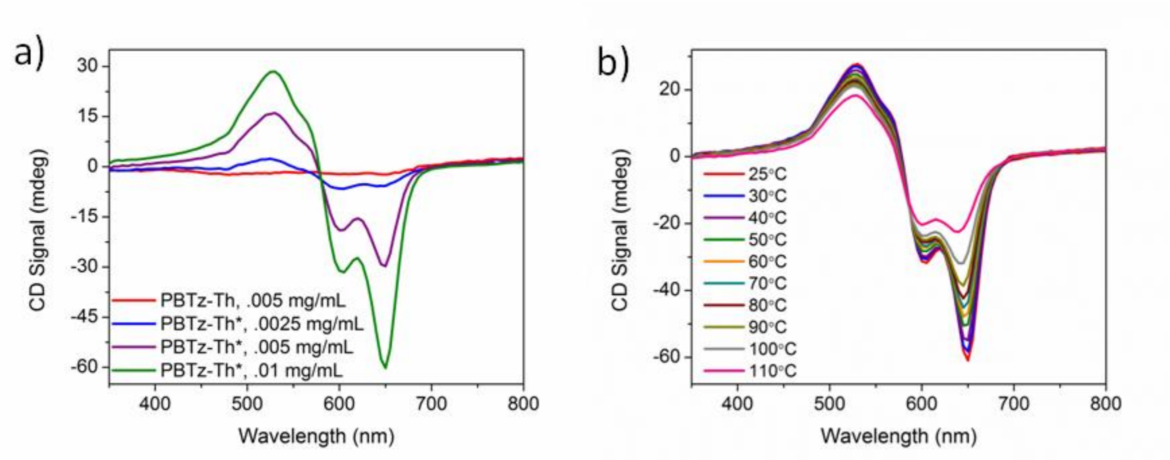

Figure 3-8. Solution CD spectra of a) PBTz-Th at 0.005 mg/mL (red) and PBTz-Th* at 0.0025 mg/mL (blue), 0.005 mg/mL (purple), and 0.01 mg/mL (green) in DCB and b) PBTz-Th* in 0.01 mg/mL DCB as a function of temperature, from 25-110 °C.

Temperature-dependent CD measurements were taken using the same conditions as temperature-dependent absorption measurements for solution concentrations of 0.0025 mg/mL (Figure S3-8) and 0.01 mg/mL DCB (Figure 3-8b). At both concentrations, the CD signal is observed to decrease with increasing temperature. At 110 °C, the presence of a CD signal suggests that not all polymer chains are fully solvated.

The dynamics of PBTz-Th* aggregate formation were studied by heating a 0.01 mg/mL solution of PBTz-Th* in DCB to 110 °C and allowing it to cool back down to 25 °C at a rate of 0.2 °C/minute. Optical absorption and CD spectra were measured before and after the heating/cooling cycle. The final optical absorption and CD measurements were taken about one week after cooling. After heating and then slowly cooling the solution, the optical absorption spectrum (Figure 3-9a) shows a blue shift in absorption maximum and a decrease in vibronic structure in comparison to the initial solution. The CD signal also does not recover completely after thermal treatment, as shown in Figure 3-9b. However, the signal strength at 25 °C after cooling is stronger than the signal strength at 110 °C. The initial aggregated state is typically recovered after cooling, such that thermal treatment is reversible.[32-33,88] Based on the optical absorption and CD results, aggregation of PBTz-Th* polymer chains is not completely reversible. Thus, order in the aggregates from the reaction and purification procedures is greater than can be achieved by spontaneous re-aggregation. The PBTz-Th* solution was subject to further heating/cooling cycles with CD spectra taken at 25 °C and 110 °C (Figure S3-9). After several temperature cycles, the PBTz-Th* solution equilibrates and there is no further change in subsequent CD spectra.

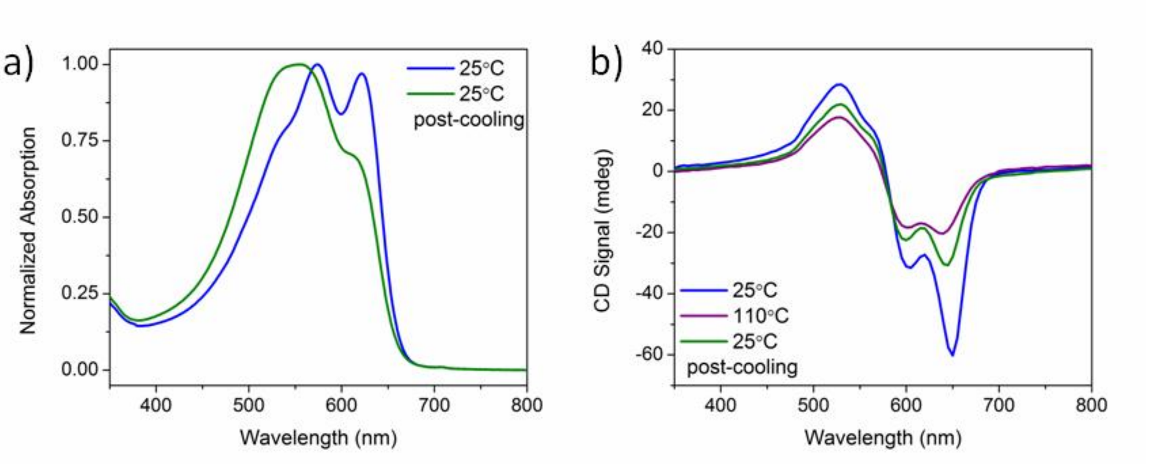

Figure 3-9. a) Normalized optical absorption spectra of PBTz-Th* in 0.01 mg/mL DCB at 25 °C before (blue) and after (green) thermal treatment and b) CD spectra of PBTz-Th* in 0.01 mg/mL DCB at 25 °C (blue), 110 °C (purple), and 25 °C 1 week after thermal treatment (green).

Dynamic light scattering (DLS) measurements were performed on solutions before and after thermal treatment to determine if a change in particle size would account for the failure of PBTz-Th* to recover its initial chiroptical properties. DLS measurements reveal a bimodal distribution both before and after the heating/cooling cycle. The hydrodynamic radius and percent by mass of both solutions are reported in Table 3-2 and are an average of 5 independent measurements. The smaller radius is denoted as “radius 1” with a corresponding “mass % 1.” The larger radius is denoted as “radius 2” with a corresponding “mass % 2.” Prior to the heating/cooling cycle, PBTz-Th* solutions at 0.01 mg/mL in DCB provide hydrodynamic radii of 8.8 nm and 81 nm with mass % of 72% and 27% respectively. Post heating/cooling, PBTz-Th* solutions provide hydrodynamic radii of 5.7 nm and 62 nm with mass % of 94% and 5.3% respectively. A decrease in both radius 1 and radius 2 is observed after thermal treatment.

Table 3-2. DLS Measurements of PBTz-Th* in 0.01 mg/mL DCB

	Radius 1 (nm)	Mass % 1	Radius 2 (nm)	Mass % 2
Initial Solution	8.8	72%	81	27%
Post-Thermal Treatment	5.7	94%	62	5.3%

DLS data suggest that the spontaneous re-aggregation during slow cooling leads to smaller aggregates relative to those produced by the reaction procedure (precipitating the polymer with methanol, a poor solvent, and re-dissolving in DCB, a good solvent). This difference in aggregate size is evident in the CD spectra, such that the ratio of CD response at the 650 nm to 605 nm peaks decreases after thermal treatment. Assuming the CD signal at 650 nm corresponds to a collective response, heating the solution to 110 °C likely breaks up the larger aggregates into a mixture of smaller aggregates and well-dissolved chains.

These small aggregates correlate to a lower collective response which results in the CD peaks at 605 nm and 650 nm being roughly equal in magnitude.

In order to study the CD response when the chiral chains are diluted in an aggregate containing predominately racemic polymers, a mixture of PBTz-Th and PBTz-Th* at a ratio of 8:2 was measured, and the resulting CD spectrum is shown in Figure 3-10a. As a control, the optical absorption spectra of pure PBTz-Th* and the mixture of 8:2 PBTz-Th:PBTz-Th* were measured and no significant difference was observed (Figure S3-5). The chiral response of the 8:2 mixture in 0.01 mg/mL toluene is about one-fourth that of pure PBTz-Th* in 0.01 mg/mL toluene, indicating that the CD response scales proportionally with PBTz-Th* content. A solution of the 8:2 mixture was heated at 90 °C overnight under argon and the CD response was measured after the solution was allowed to cool to room temperature (Figure 3-10b). The CD signal is observed to decrease after heating overnight. This observation is comparable to our observations when PBTz-Th* solutions were subjected to heating/cooling cycles as described above. In both experiments, the CD signal does not completely recover. We propose that heating overnight leads to scrambling of the chains, followed by re-aggregation at room temperature. These combined observations lead us to believe that the chiral response is unimolecular in nature and we propose a helical structure in the polymer chain.

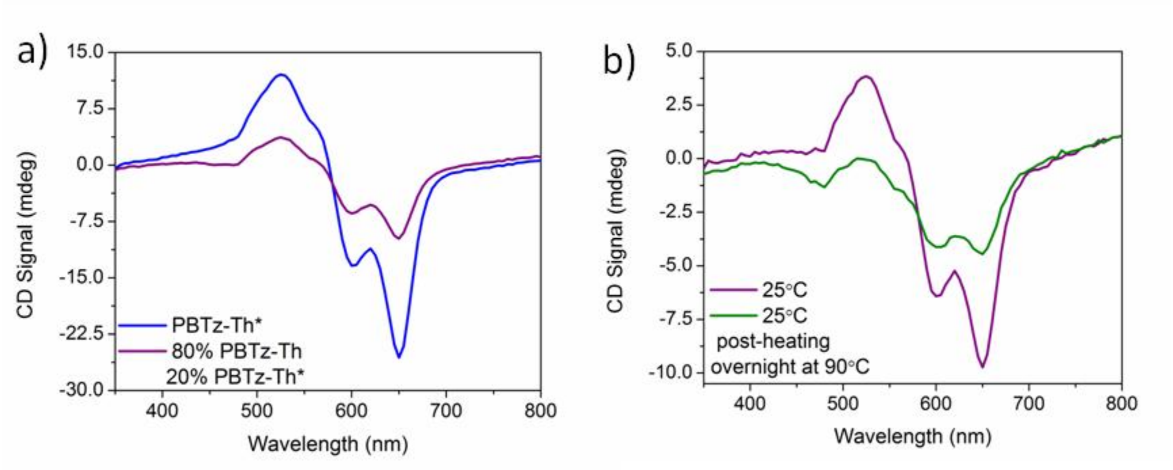

Figure 3-10. CD spectra of a) PBTz-Th* (blue) and a mixture of 8:2 PBTz-Th:PBTz-Th* (purple) in 0.01 mg/mL toluene and b) a mixture of 8:2 PBTz-Th:PBTz-Th* in 0.01 mg/mL toluene at 25 °C (purple) and at 25 °C after heating at 90 °C overnight (green).

4. Solid State Characterization of PBTz-Th* and PBTz-Th

Thin films of PBTz-Th* and PBTz-Th were obtained by drop-casting 0.5 mg/mL CB solutions onto clean glass substrates. This approach was chosen because the polymers were not sufficiently soluble to produce solution concentrations required for spin-casting films thick enough to provide a CD response. As shown in Figure 3-11a, the optical absorption of PBTz-Th* films reveals a shift in intensity from the shorter (577 nm) to the longer (626 nm) wavelengths, relative to absorption in solution. However, the similarity between the solution and thin film absorption for both materials provides further evidence of aggregation of polymer chains in solution. There is no discernible difference in absorption between PBTz-Th* and PBTz-Th films. As with the solution spectra, CD spectroscopy shows a chiral response for PBTz-Th* films and no response for PBTz-Th (Figure 3-11b).

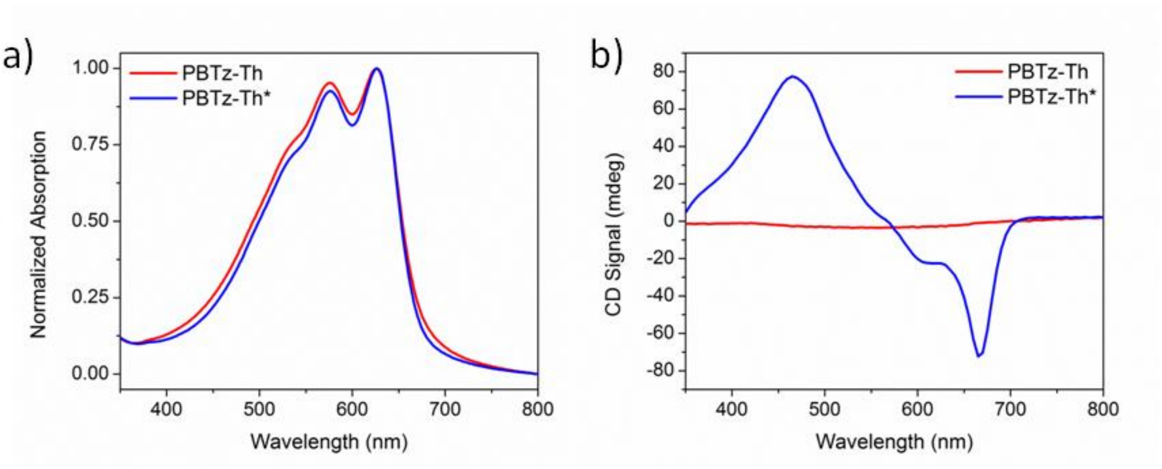

Figure 3-11. a) Normalized thin film absorption spectra and b) thin film CD spectra of PBTz-Th (red) and PBTz-Th* (blue).

It is worth mentioning that previous work found that films of PCPDTBT* and PCDTPT*, which are copolymers that also contain (*S*)-2-ethylhexyl side chains, see Figure 3-5, exhibit different chiroptical behaviors.[16] PCPDTBT* films provide a strong CD response, whereas PCDTPT* films lack any measurable CD signal. Like PCPDTBT*, the chiral response of PBTz-Th* translates from aggregates in solution to the thin film. The degree of circular polarized absorption in relation to linear optical absorption can be determined using the anisotropy factor, g_{abs} ($g_{abs} = (A_L - A_R)/A_{optical}$).[91] The g_{abs} values of these three polymers are reported in Table 3-3. The g_{abs} value for PBTz-Th* is negative based on the negative Cotton effect observed in the thin film CD spectra whereas the g_{abs} of PCPDTBT* exhibits a positive Cotton effect. The g_{abs} of PCPDTBT* is one order of magnitude greater than PBTz-Th*.

Table 3-3. Anisotropy Factor Comparison of Polymer Films

Polymer Film	Anisotropy Factor, g_{abs}	Wavelength (nm)
PCPDTBT*	0.037	830
PCDTPT*	0	n/a

PBTz-Th*	-0.008	665

Similar to the pyridyl nitrogen atom contained by PCDTPT*, PBTz-Th* contains nitrogen atoms in the triazole ring with potential for noncovalent hydrogen-bonding interactions that would favor a more planar backbone.[92-93] However, unlike PCDTPT*, PBTz-Th* is capable of forming a chiral structure in the solid state based on the CD data presented here. For a more quantitative comparison, the rotational barrier was calculated using density functional theory (DFT) for the BTz-Th monomer in vacuum and chlorobenzene (Figure S3-11). The rotational barrier in chlorobenzene of BTz-Th (3.6 kcal/mol) is more similar to CDT-BT (4 kcal/mol) than CDT-PT (9 kcal/mol). The lower rotational barrier indicates a more conformationally flexible backbone that could accommodate the distortions required to achieve a helical conformation.

5. Conclusions

In this contribution, we provide the synthesis and characterization of a D-A copolymer, PBTz-Th, containing either chiral or racemic 2-ethylhexyl side chains on the BTz unit. Both PBTz-Th* and its racemic counterpart show a propensity to aggregate based on their optical absorption spectra and the DLS data. PBTz-Th* provides a CD response in solution whereas, as expected, PBTz-Th does not. Examination of a solution containing an 8:2 ratio of PBTz-Th:PBTz-Th* suggests the existence of helical structures within aggregates, as the source of the CD response. Heating a solution above 110 °C and allowing the solution to cool to room temperature at 0.2 °C/minute results in smaller aggregates than originally obtained after the polymerization reaction and purification procedures which provide a less pronounced vibronic structure and a weaker CD response. These observations support the hypothesis of helical backbone structures within multichain aggregates. The chiral organization observed for aggregates in solution is found to translate to the solid state upon solution deposition as expected based on the relatively small calculated rotational barrier of the BTz-Th unit.

D. Chiroptical Properties of Poly(benzotriazole) Containing Chiral Ethylhexyl Side Chains

1. Introduction

The original goal of the study described in Part C was characterization of a benzotriazole homopolymer (PBTz) containing chiral side chains. The DFT described in Part B suggested an offset between each monomer unit of a given sequence. Difficulty in synthesizing the benzotriazole homopolymer containing chiral side chains (PBTz*) at a sufficiently high molecular weight resulted in the study of a benzotriazole-thiophene copolymer described above. Below initial results utilizing a low molecular weight PBTz* are reported.

2. Synthesis

PBTz* was synthesized using Yamamoto coupling (Scheme 3-2).[50] The dibromo-monomer synthesis is described above. Ni(COD)$_2$ was used as the catalyst with bipyridine and COD as additional ligands. A solvent system containing 6:1 THF:DMF was used in an attempt to balance polymer solubility and solvent polarity. Multiple solvent systems were tested but only low molecular weight polymers were achieved (Table 3-4). The highest molecular weight polymer was used in subsequent testing.

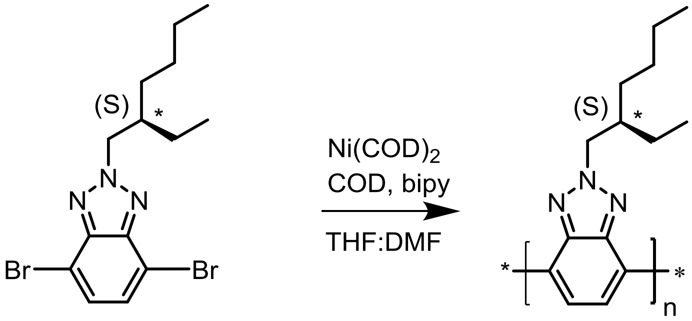

Scheme 3-2. Yamamoto coupling polymerization of EH-S-BTz.

Table 3-4. Molecular weight data for PBTz attempts

Solvent	M_n	M_w	PDI
2:1 xylene:DMF	n/a	n/a	n/a-insoluble
Toluene	1740	2250	1.3
Dichlorobenzene	1900	n/a	n/a
6:1 THF:DMF	2050	3000	1.5

3. Chiroptical Properties of PBTz* in Solution

The chiroptical properties of PBTz* and PBTz were studied using the method described above. Optical absorption spectra are shown in Figure 3-12. The absorption maximum of PBTz* is blue-shifted compared to PBTz in 0.05 mg/mL CB. When the solvent is changed to 3:7 CB:DMF (a poor solvent system for PBTz*), the absorption maximum also blue-shifts. Adding a poor solvent usually results in a red-shift in the absorption maximum and the appearance of a shoulder peak.[84-90] However, these data are consistent with the previous report of negative solvatochromic effects for PBTz with a cationic side chains.[94]

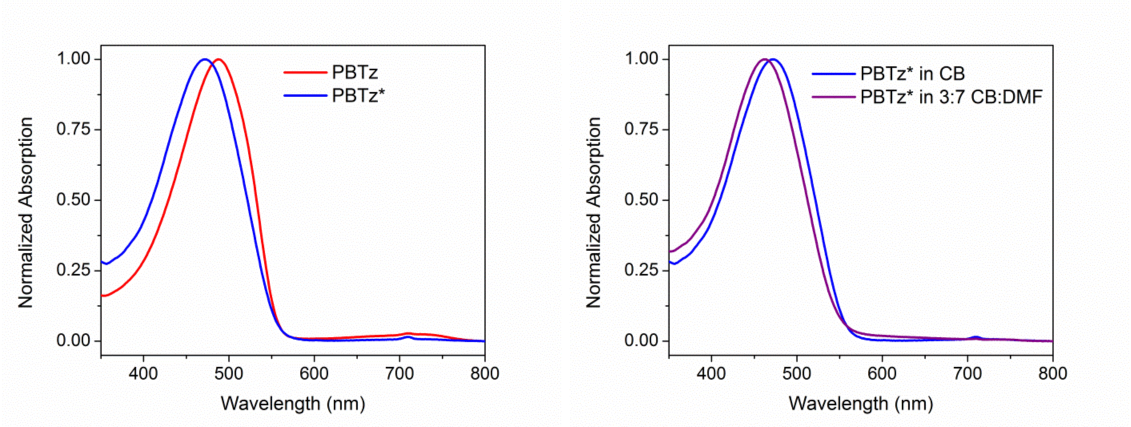

Figure 3-12. Optical absorption spectra at 25°C of PBTz (red) and PBTz* (blue) in CB (left) and PBTz* in 3:7 CB:DMF (purple) at 0.05 mg/mL.

CD spectroscopy reveals a signal for PBTz* but not PBTz in 0.05 mg/mL 3:7 CB:DMF (Figure 3-13). The dip in the spectrum of PBTz is noise from the spectrometer, confirmed by measuring the CD signal of a clean solvent. The CD spectrum of PBTz* is roughly the first derivative of the absorption spectrum. When the solution is heated from 25-50°C, the CD signal decreases. These data suggest the CD signal corresponds to a chiral aggregate.

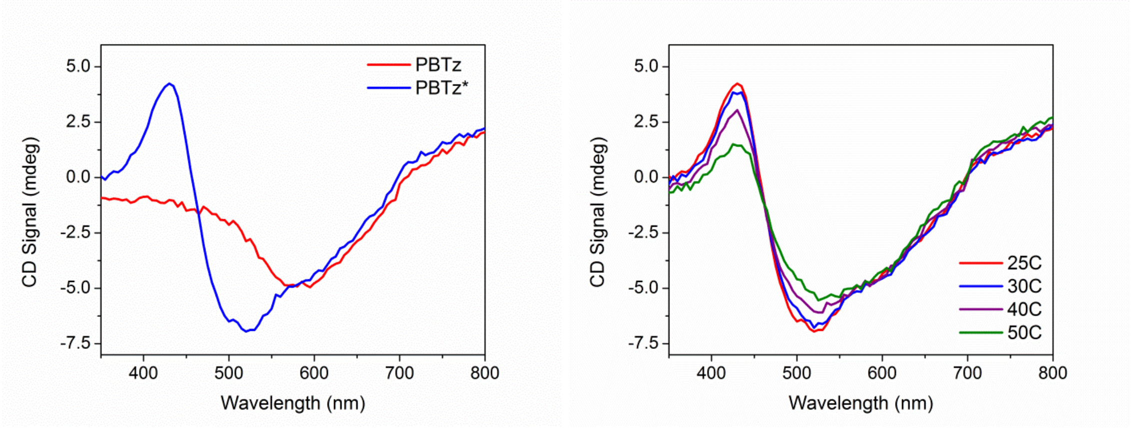

Figure 3-13. CD spectra of a) PBTz (red) and PBTz* (blue) in 3:7 CB:DMF and b) of PBTz* in 3:7 CB:DMF as a function of temperature, from 25-50°C.

Dynamic light scattering measurements were performed for PBTz-Th* dissolved at 1 mg/mL in CB. The average of three measurements provides a hydrodynamic radius of 20.6 ±4.7 nm. Measurements at lower concentrations failed to an acceptable signal-to-noise ratio for data collection. From these data, it is not possible to determine whether the chirality of PBTz* is only due to an aggregate structure or stems from twisting of a single polymer chain.

4. Conclusions

Difficulty in obtaining high molecular weight PBTz* and the related tendency of PBTz* to aggregate complicates testing the chirality of a single chain. The low molecular weight PBTz* provides a CD signal when aggregated in solution, indicating a differences in ordering compared to PBTz. However, in order to obtain the desired data, synthesizing a poly(benzotriazole) derivative with a longer chiral side chain is necessary for achieving sufficient solubility for these studies.

E. Conclusions

Benzotriazole-based polymers have the potential to form intrachain helical structures. The interesting optical properties of benzotriazole-based CPEs prompted DFT calculations which suggest a nonplanar polymer backbone. Efforts to probe the helical nature of these conjugated polymers through the incorporation of chiral side chains encountered obstacles due to the tendency of the polymer chains to aggregate.

A more successful approach to probing the helical nature of benzotriazole-based polymers may necessitate the synthesis of an alternative chiral side chain. As the Section B of this chapter shows, benzotriazole-based CPEs can achieve high molecular weight due to increased solubility. Developing a chiral ionic side chain offers a path forward in obtaining the higher molecular weight polymers needed to study these materials using spectroscopic methods.

F. Experimental and Supplementary Information

1. Materials and Methods

All reagents and solvents were purchased from Sigma Aldrich, BDM, Fisher Scientific, Alfa Aesar, or Acros Organics and used without further purification unless otherwise specified. Tetrakis(triphenylphosphine)palladium(0) [$Pd(PPh_3)_4$] was purchased from Strem Chemicals Inc. Deuterated solvents were purchased from Cambridge Isotopes Laboratories, Inc. Solvents used for air and/or water sensitive reactions (THF, toluene) were dried by passage through two columns of alumina and degassed by argon purge in a custom-built solvent purification system.

GPC chromatographs were obtained using a Waters 2690 Separation Module with two Agilent PLGEL 5μm, MIXED-D columns running $CHCl_3$/0.25% triethylamine as eluent. Molecular weights were calculated relative to linear PS standards. MALDI spectra were obtained on a Bruker Microflex series MALDI-TOF using a matrix of dithranol saturated chloroform.

Chiral Derivatizing Agents (CDAs) are used to determine stereochemistry and chiral purity using Mosher's method.[77-79] Diastereomers have different ^{1}H NMR chemical shifts, whereas enantiomers do not; thus a reaction to form a diastereomer allows for determination of enantiomeric purity.[80-81] Accordingly, (*S*)-2-ethylhexan-1-ol was reacted with (*S*)-(+)-10-camphorsulfonyl chloride (Scheme S3-2) to produce an adduct with a distinct doublet peak with at 4.16 ppm (Figure S3-1a). In contrast, the corresponding analogous adduct resulting from the reaction with racemic 2-ethylhexan-1-ol (Scheme S3-3) gave rise to a multiplet of peaks at 4.2-4.1 ppm (Figure S3-1b). This difference in chemical shifts of the chiral and racemic adducts confirms the chiral purity of (*S*)-2-ethylhexan-1-ol.

2. Detailed Synthetic Procedures

Synthesis of (*S*)-2-ethylhexan-1-ol

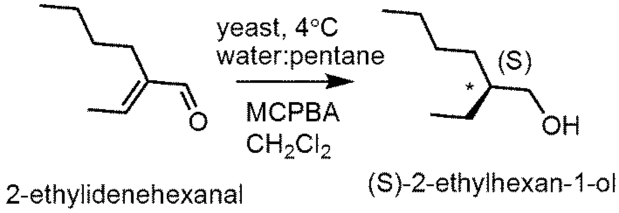

Scheme S3-1. Synthesis of (*S*)-2-ethylhexan-1-ol.

(*S*)-2-ethylhexan-1-ol was synthesized according to literature procedures.[76] HK_2PO_4 (16.647 g, 95.6 mmol), H_2KPO_4 (0.720 g, 5.29 mmol), and sucrose (10.280 g, 30.0 mmol) were dissolved in Millipore water (1000 mL). Yeast (200. g) was added slowly while stirring. The yeast mixture was allowed to stir for 2.5 hours. Pentane (1500 mL) was added. 2-ethylidene hexanal (10.254 g, 81.3 mmol) was added. The reaction was allowed to stir at 4°C for 1 week. The aqueous/yeast layer was removed by centrifugation. The resulting organic layer was filter through celite, concentrated under reduced pressure, and dried under vacuum. The resulting oil was dissolved in CH_2Cl_2 (100 mL) and cooled to 0°C. MCPBA (7.904 g, 45.8 mmol) was added. This reaction step allows the separation of an unwanted side product from (*S*)-ethylhexan-1-ol via column chromatography through the formation of an epoxide. The reaction was stirred for two hours. The reaction mixture was washed with water, dried over sodium sulfate, and concentrated under reduced pressure. The crude product was first purified by distillation. The product was then purified by column chromatography using 6:4 DCM:pentane as the eluent ($R_f \sim 0.25$). (*S*)-2-ethylhexan-1-ol was produced in 21% yield (2.181 g). ^{1}H NMR (500 MHz, $CDCl_3$) δ (ppm): 3.53 (d, 2H), 1.41-1.20 (m, 10H), 0.88 (t, 6H). ^{13}C NMR (600 MHz, $CDCl_3$) δ (ppm): 65.31, 41.95, 30.12, 29.09, 23.32, 23.08, 14.09, 11.12. GC/MS: calculated for $C_8H_{18}O$ (m/z): 130.14, found 130. $[\alpha]_D$ = +2.954° (Concentration of 1.2 g/100 ml in acetone, 25 ^{o}C). (Literature: $[\alpha]_D$ = +3.1°,[7] e.e. = 95%).

Chiral Derivatization of (*S*)-2-ethylhexanol

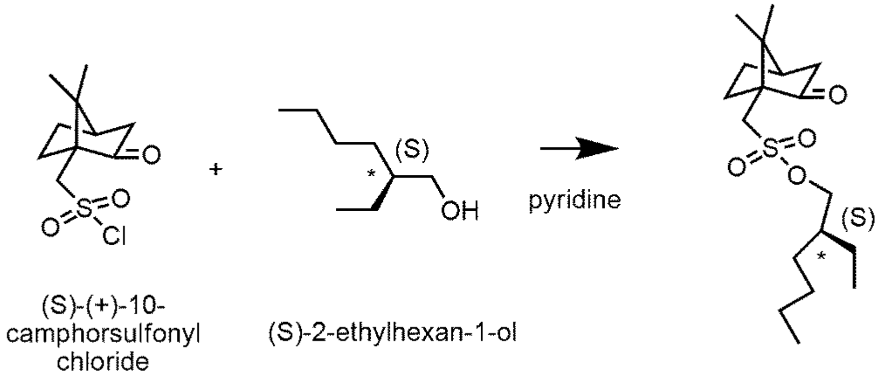

Scheme S3-2. Chiral derivatization reaction of (*S*)-(+)-10-camphorsulfonyl chloride and (*S*)-2-ethylhexan-1-ol.

(*S*)-2-ethylhexan-1-ol (0.0554 g, 0.425 mmol) and (*S*)-(+)-10-camphorsulfonyl chloride (0.1452 g, 0.579 mmol) were dissolved in pyridine (1 mL). The reaction was covered in aluminum foil and allowed to stir for about 16 hours. Pyridine was removed under reduced pressure. The mixture was separated using column chromatography with hexane:ethyl acetate (1:1) as the eluent (R_f ~ 0.4). The chiral adduct was produced at 79% yield (0.116 g). ^{1}H NMR (500 MHz, $CDCl_3$) δ (ppm): 4.16 (d, 2H), 3.57 (d, 1H), 2.96 (d, 1H), 2.48 (m, 1H), 2.36 (m, 1H), 2.10 (t, 1H), 2.01 (m, 1H), 1.92 (d, 1H), 1.66-1.57 (m, 2H), 1.46-1.34 (m, 3H), 1.33-1.19 (m, 6H), 1.10 (s, 3H), 0.87 (m, 9H).

Chiral Derivatization of 2-ethylhexan-1-ol

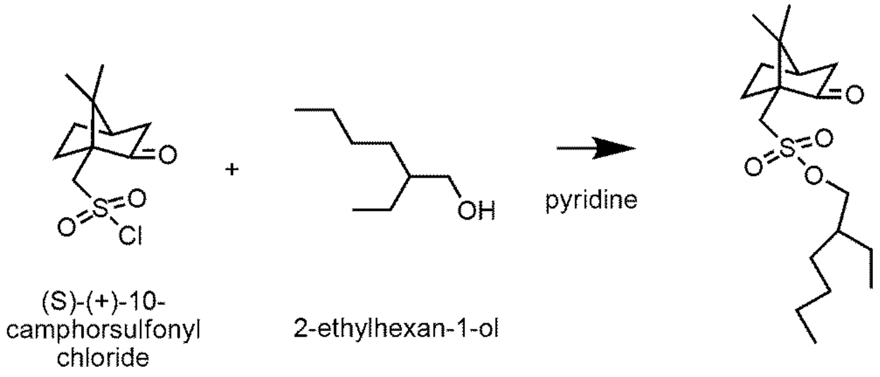

Scheme S3-3. Chiral derivatization reaction of (*S*)-(+)-10-camphorsulfonyl chloride and 2-ethylhexan-1-ol.

2-ethylhexan-1-ol (0.1149 g, 0.882 mmol) and (*S*)-(+)-10-camphorsulfonyl chloride (0.2895 g, 1.15 mmol) were dissolved in pyridine (2 mL). The reaction was covered in aluminum foil and allowed to stir for about 16 hours. Pyridine was removed under reduced pressure. The mixture was purified using column chromatography with hexane:ethyl acetate (8:2) as the eluent (R_f ~ 0.4). The racemic adduct was produced at 82% yield (0.249 g). ^{1}H NMR (500 MHz, $CDCl_3$) δ (ppm): 4.13 (m, 2H), 3.54 (d, 1H), 2.93 (d, 1H), 2.44 (m, 1H), 2.33 (m, 1H), 2.07 (t, 1H), 2.00 (m, 1H), 1.90 (d, 1H), 1.64-1.53 (m, 2H), 1.43-1.31 (m, 3H), 1.30-1.16 (m, 6H), 1.07 (s, 3H), 0.84 (m, 9H).

Synthesis of (*S*)-3-(bromomethyl)heptane

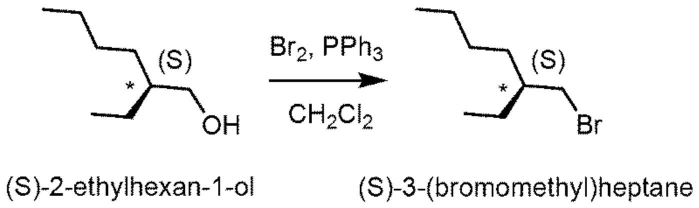

Scheme S3-4. Synthesis of (*S*)-3-(bromomethyl)heptane.

PPh_3 (2.7407 g, 10.4 mmol) was added to a 100 mL round bottom flask and dissolved in CH_2Cl_2 (21 mL). The solution was cooled to 0°C. Elemental Br_2 (3.5408 g, 22.2 mmol) was added dropwise to the stirring solution. (*S*)-2-ethylhexan-1-ol (1.0559 g, 8.11 mmol) was dissolved in pyridine (1.54 mL) and added dropwise to the stirring reaction mixture. The reaction was allowed to stir for 1 hour at 0°C. The ice bath was then removed and the reaction was allowed to stir at room temperature for 1 hour. Na_2SO_3 (10% aq solution) was added to quench the reaction. The reaction mixture was washed with water and the organic layer was dried over sodium sulfate. The solvent was removed under reduced pressure. The resulting mixture was separated using column chromatography with hexane: CH_2Cl_2 (8:2) as the eluent ($R_f \sim 0.8$). (*S*)-3-(bromomethyl)heptane was produced as a colorless oil with 69% yield (1.02 g). ^1H NMR (500 MHz, $CDCl_3$) δ (ppm): 3.46 (m, 2H), 1.54 (m, 1H), 1.46-1.22 (m, 8H), 0.90 (t, 6H). ^{13}C NMR (600 MHz, $CDCl_3$) δ (ppm): 41.06, 39.12, 31.86, 28.82, 25.14, 22.86, 14.06, 10.86. GC/MS: calculated for $C_8H_{17}Br$ (m/z): 192.05, found 192.

Synthesis of 1,2-diamino-3,6-dibromobenzene

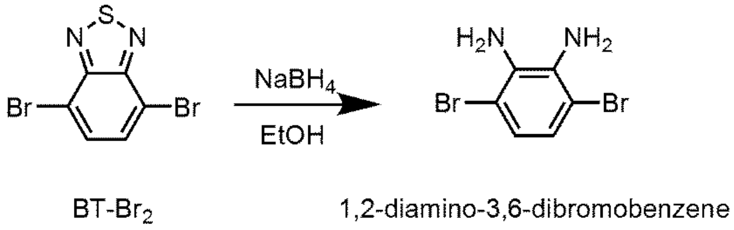

Scheme S3-5. Synthesis of 1,2-diamino-3,6-dibromobenzene.

1,2-diamino-3,6-dibromobenzene was synthesized according to the literature procedure.[50] $NaBH_4$ was added to a stirring solution of BT-Br_2 (2.0 mmol, 0.588 g) in ethanol (20 mL) at 0°C. The ice bath was removed after 1 hour and the reaction was allowed to proceed overnight at room temperature. The solvent was evaporated under reduced pressure. The residue was dissolved in ether and washed with water. The organic layer was collected, dried, and the solvent evaporated under reduced pressure. 1,2-diamino-3,6-dibromobenzene was obtained at 80% yield (0.426 g). ^1H NMR (500 MHz, CD_3OD) δ (ppm): 6.5 (s, 2H).

Synthesis of 4,7-dibromo-1,2,3-benzotriazole

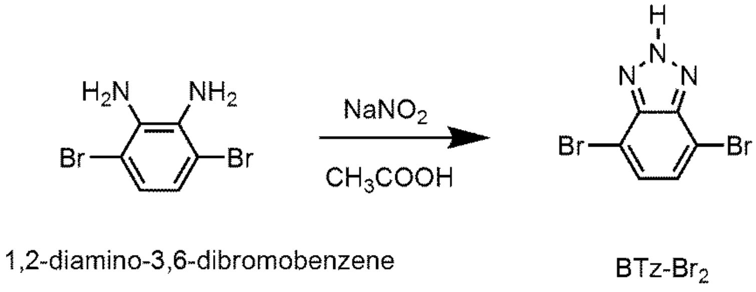

Scheme S3-6. Synthesis of 4,7-dibromo-1,2,3-benzotriazole.

BTz-Br$_2$ was synthesized according to the literature procedure.[50] A 3mL solution of NaNO$_2$ (0.15 g, 1.65 mmol) in water was added to a 6 mL solution of 1,2-diamino-3,6-dibromobenzene (0.40 g, 1.5 mmol) in acetic acid. The reaction was allowed to proceed for 30 minutes at room temperature. The resulting precipitate was filtered and washed with water. 4,7-dibromo-1,2,3-benzotriazole was produced as a pink powder at 85% yield (0.38 g). ^{1}H NMR (500 MHz, CDCl$_3$) δ (ppm): 7.56 (s, 2H).

Synthesis of EH-S-BTz

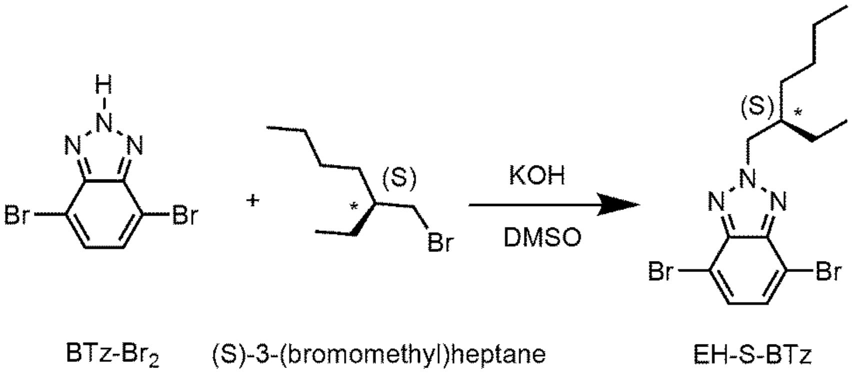

Scheme S3-7. Synthesis of EH-S-BTz.

BTz-Br$_2$ (0.3930 g, 1.42 mmol) and powdered KOH (0.097 g, 1.73 mmol) were added to a 25 mL conical flask and dissolved in DMSO (2.4 mL, 0.63M). The solution was capped with a septum and allowed to degas with argon for 15 minutes. Subsequently, (*S*)-3-

(bromomethyl)heptane (0.3409 g, 1.77 mmol) was added via syringe. The reaction was heated to 75°C and allowed to stir under argon for 16 hours. The reaction was then allowed to cool to room temperature and diluted with chloroform. The reaction was washed with water three times and the organic layer was dried over sodium sulfate. The solvent was removed under reduced pressure. The resulting mixture was separated using column chromatography with chloroform:hexane (2:1) as the eluent ($R_f \sim 0.8$). EH-S-BTz was produced as a colorless oil with a yield of 60% (0.334 g). ^1H NMR (500 MHz, $CDCl_3$) δ (ppm): 7.42 (s, 2H), 4.66 (d, 2H), 1.30 (m, 9H), 0.90 (t, 3H), 0.85 (t, 3H). ^{13}C NMR (600 MHz, $CDCl_3$) δ (ppm): 143.66, 129.41, 110.01, 60.83, 40.24, 30.16, 28.18, 23.69, 22.83, 13.94, 10.34. MS (FD) calculated for $C_{14}H_{19}Br_2N_3$ (m/z): 386.995, found 386.99.

Polymerization of EH-S-BTz and Bis(Me_3Sn)thiophene

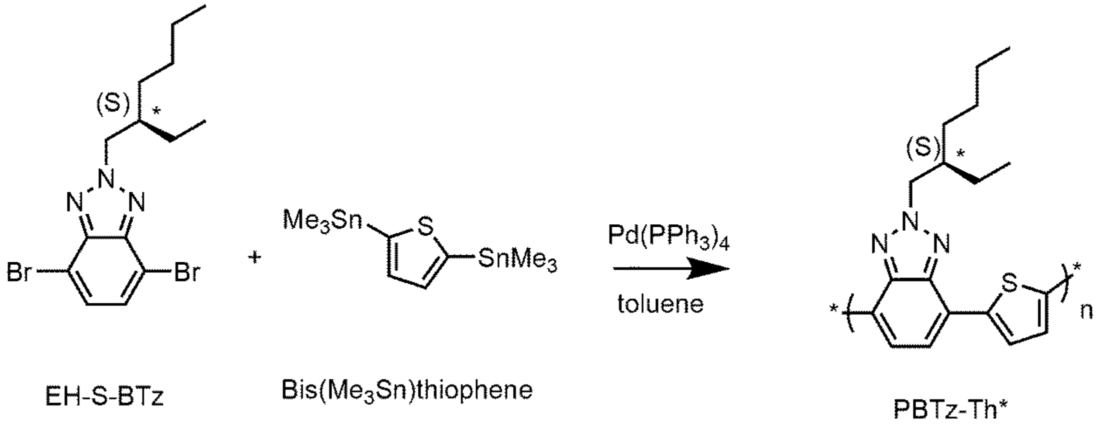

Scheme S3-8. Polymerization of EH-S-BTz and bis(Me_3Sn)thiophene.

In a nitrogen-filled glovebox, EH-S-BTz (0.1045g, 0.269 mmol), bis(Me_3Sn)thiophene (0.1168 g, 0.285 mmol), and $Pd(PPh_3)_4$ (15.2 mg, 0.0131 mmol) were added to a 10-20 mL microwave tube and dissolved in toluene (6.2 mL, 0.042M). The microwave tube was sealed under nitrogen and the reaction was removed from the nitrogen glovebox. The reaction was heated to 110°C in an oil bath and allowed to stir for 4 days. The reaction was cooled to room temperature and returned to a nitrogen atmosphere. 2-bromothiophene (0.21 mL, 2.2 mmol) and Pd(PPh$_3$)$_4$ (3.4 mg, 0.0029 mmol) were dissolved in toluene (0.5 mL) and added to the microwave tube. The reaction was allowed to stir at 110°C in an oil bath for about 16 hours. After cooling to room temperature, the resulting polymer, PBTz-Th*, was precipitated with MeOH, filtered, washed with acetone and MeOH, and dried under vacuum. This resulted in a purple solid with quantative yield (0.085 g). GPC (CHCl$_3$): M_n = 6242; M_w = 6611; PDI = 1.06.

Synthesis of PBTz-Th

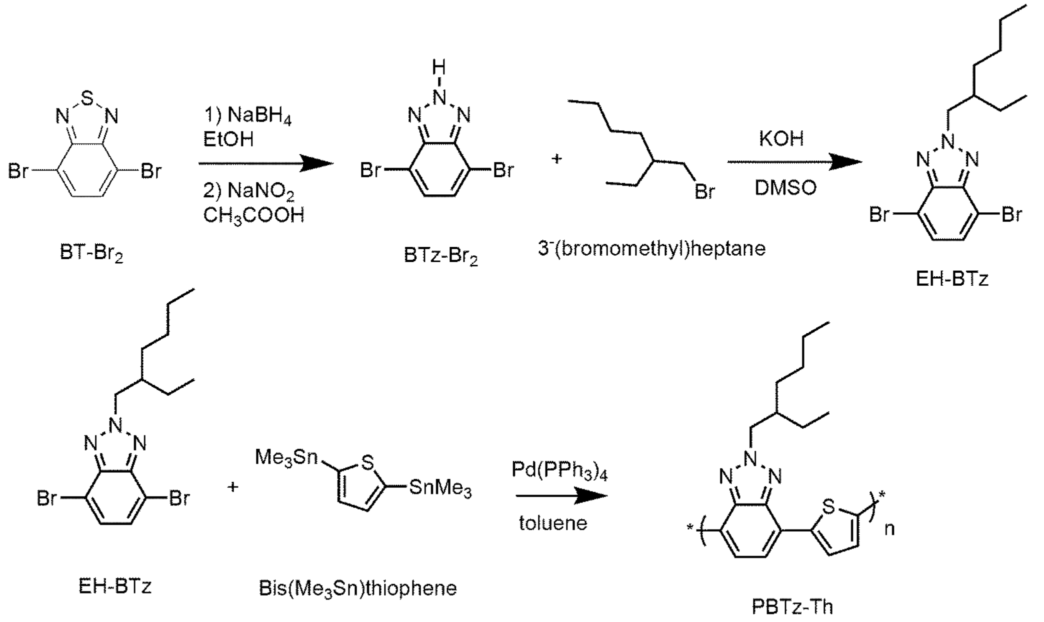

Scheme S3-9. Synthesis of PBTz-Th.

The procedure for synthesizing PBTz-Th is the same as that of PBTz-Th* where (S)-3-(bromomethyl)heptane is replaced by 3-(bromomethyl)heptane. GPC (CHCl$_3$): M_n = 6228; M_w = 6543; PDI = 1.05.

Synthesis of PBTz*

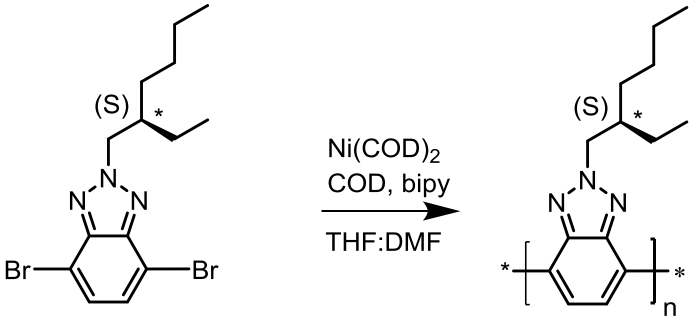

Scheme S3-10. Yamamoto coupling polymerization of EH-S-BTz.

In a nitrogen-filled glovebox, Ni(COD)$_2$ (0.0705 g, 0.258 mmol), bipyridine (0.0413 g, 0.260 mmol), COD (0.03 mL, 0.257 mmol), and 0.5 mL DMF were added to a microwave tube. EH-S-BTz was dissolved in 3 mL THF. The monomer solution was slowly added to the stirring catalyst. The microwave tube was capped and removed from the glovebox. The reaction was allowed to proceed at 40°C for one hour before cooling to room temperature. The reaction was allowed to proceed for about 48 hours. The resulting polymer was precipitated with methanol and washed with methanol before being dried under vacuum. The polymer was purified using Soxhlet extraction with acetone and chloroform. The chloroform fraction was saved and the solvent was removed under reduced pressure. GPC ($CHCl_3$): M_n = 2050; M_w = 3000; PDI = 1.46.

Synthesis of PBTz

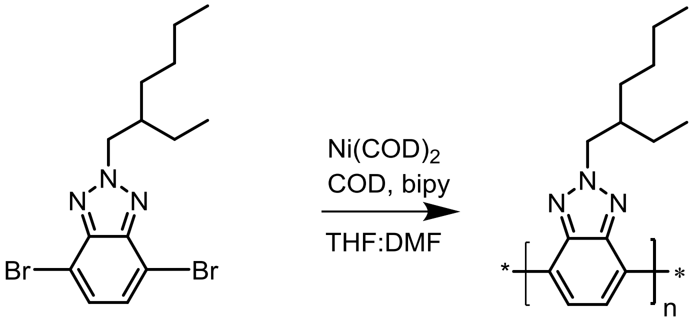

Scheme S3-11. Yamamoto coupling polymerization of EH-BTz.

The procedure for synthesizing PBTz is the same as that of PBTz where EH-S-BTz is replaced by EH-BTz. GPC ($CHCl_3$): $M_n = 2734$; $M_w = 3764$; PDI = 1.38.

3. Additional Spectra and Graphs

^{1}HNMR spectra of chiral derivatization reactions

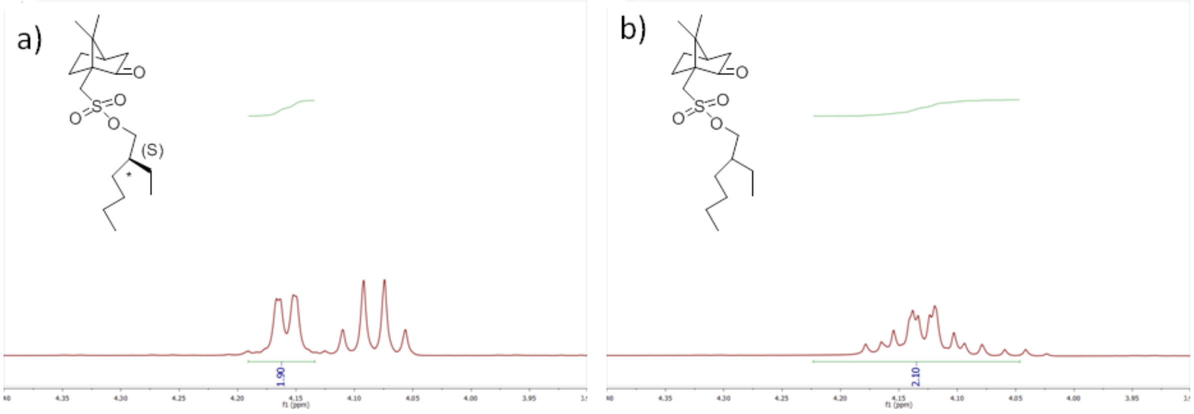

Figure S3-1. ^{1}HNMR spectra of a) chiral adduct and b) racemic adduct.

Differential Scanning Calorimetry

Differential scanning calorimetry (DSC) was measured a TA Instruments DSC (Model Q-20) with about 5 mg of polymer sample at a rate of 10°C/minute in the temperature range of 20°C to 250°C.

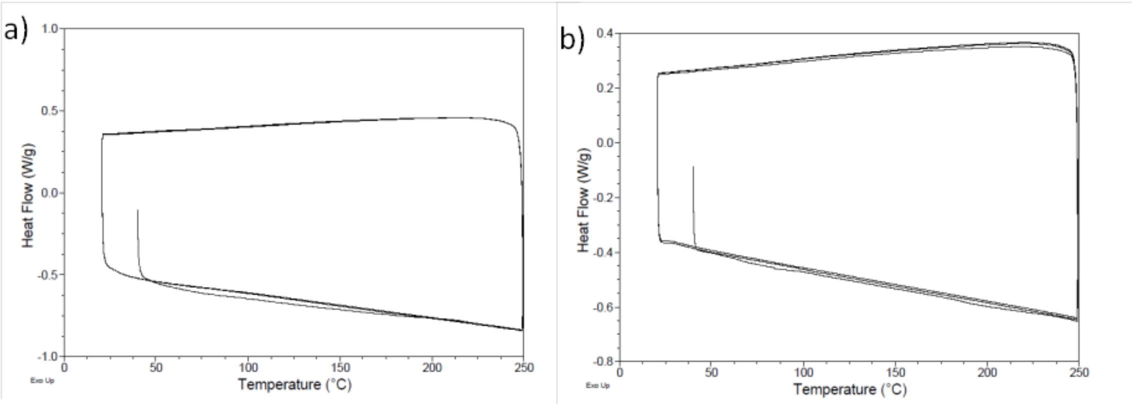

Figure S3-2. DSC curves of a) PBTz-Th* and b) PBTz-Th.

Optical Absorption and Photoluminescence Spectroscopy

Optical absorption spectra were measured using a Perkins Elmer Lambda 750 UV-Vis Spectrometer containing a STD detection module. Solvents for solution spectra were used without further purification. Solutions were measured using 10 mm path length quartz cuvettes. Solutions were prepared in CB, DCB, and toluene at concentrations of 0.0025, 0.005, 0.01, 0.015, 0.05, and 0.1 mg/mL. Optical absorption measurements were taken at room temperature unless otherwise indicated. Thin films were fabricated using drop-casting at ambient conditions by depositing 20 μL of 0.5 mg/mL CB solution on a clean glass substrate and allowing the solvent to evaporate.

Photoluminescence spectra were recorded on a PTI fluorimeter equipped with a Xenon lamp excitation source. Solvents were used without further purification. Solutions were measured in 10 nm path length quartz cuvettes. Solutions were prepared in CB at a concentration of 0.015mg/mL. The excitation wavelength used was 575 nm.

Temperature-dependent optical absorption spectroscopy: Solutions were heating using a PolyScience Digital Temperature Controller. Solutions were heated to the desired temperature, allowed to equilibrate for 5 minutes, and then the optical absorption spectrum was measured.

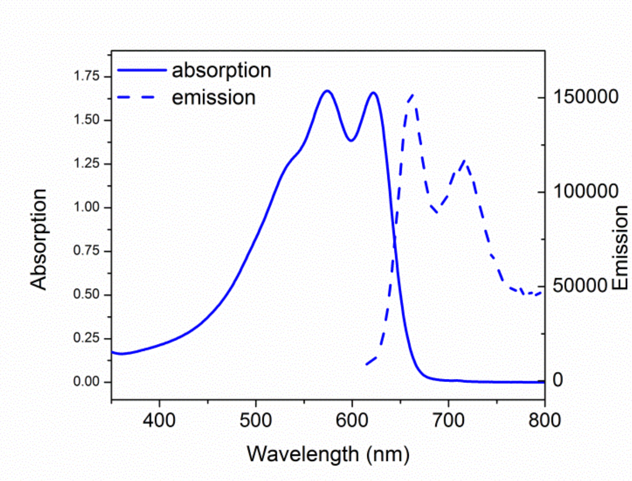

Figure S3-3. Optical absorption (solid) and emission (dashed) spectra of PBTz-Th* in 0.015 mg/mL CB.

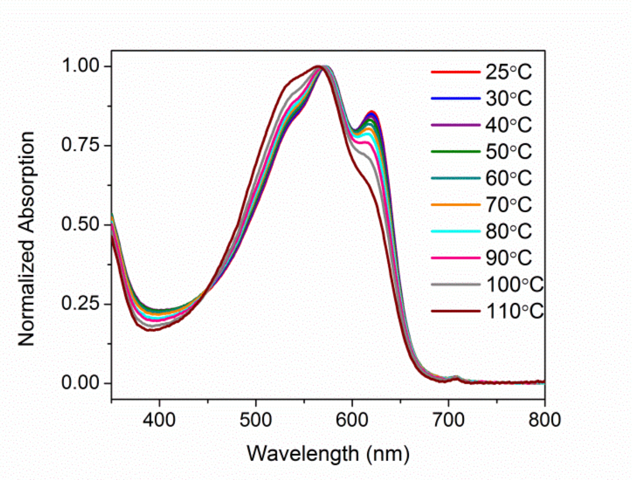

Figure S3-4. Normalized optical absorption spectra of PBTz-Th solution in 0.005 mg/mL DCB as a function of temperature, from 25-110°C.

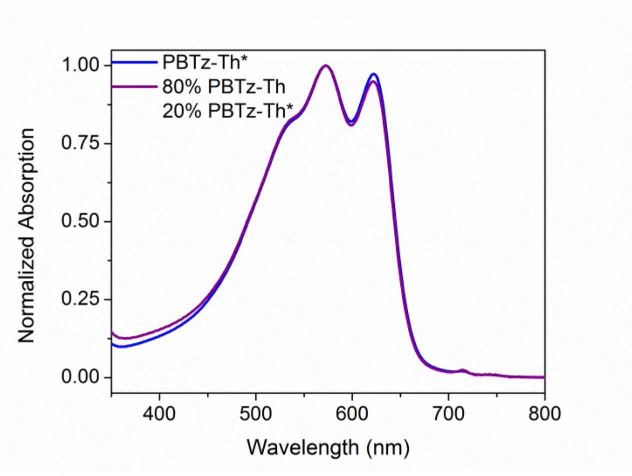

Figure S3-5. Normalized optical absorption spectra of PBTz-Th* (blue) and 8:2 PBTz-Th:PBTz-Th* (purple) in 0.01 mg/mL toluene.

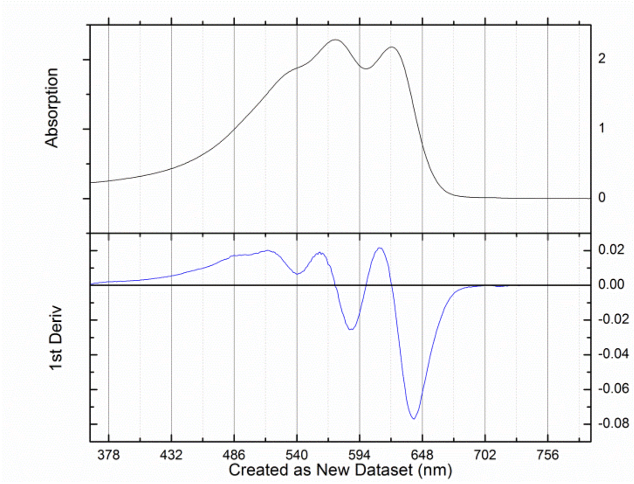

Figure S3-6. Optical absorption spectrum (top) and the first derivative of the optical absorption spectrum (bottom) of PBTz-Th* in 0.1 mg/mL CB as determined by Origin graphing software.

CD Spectroscopy

Circular dichroism spectra were measured using an Aviv Circular Dichroism Spectrometer, Model 202, which contains a Xenon lamp. Circularly polarized light is produced by a 50 kHz photoelastic modulator. Temperature is controlled via Peltier thermoelectric heating and cooling system. Solvents for solution spectra were used without further purification. Solutions were measured using 10 mm path length quartz cuvettes. Solutions were prepared in CB, DCB, and toluene at concentrations of 0.0025, 0.005, 0.01, 0.015, 0.05, and 0.1 mg/mL. Thin films were fabricated using drop-casting in ambient conditions by depositing 20 μL of 0.5 mg/mL CB solution on a clean glass substrate and allowing the solvent to evaporate.

Temperature-dependent circular dichroism spectroscopy: Solutions were heating using a Peltier thermoelectric heating system. Solutions were heated to the desired temperature, allowed to equilibrate for 5 minutes, and then the CD spectrum was measured.

Cooling kinetics: An initial CD spectrum was recorded at room temperature. The temperature was then increased at 5°C/min from 25°C to 110°C. The solution was held at 110°C for 30 minutes. The solution was cooled at a controlled rate of 0.2°C/min from 110°C back down to 25°C. The CD spectrum was recorded immediately after reaching 25°C and again 30 minutes and 1 week after 25°C.

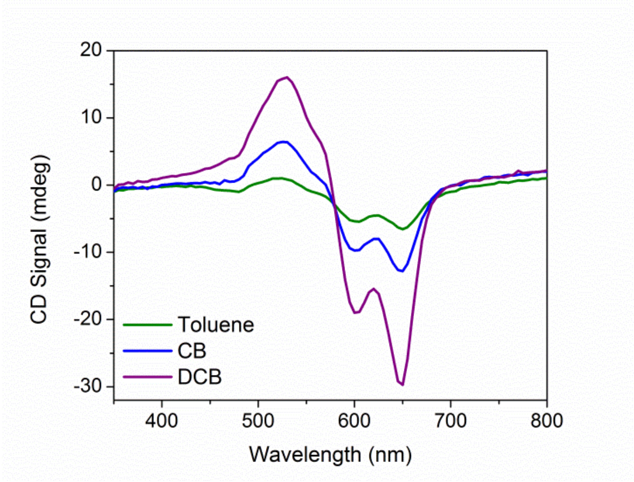

Figure S3-7. CD spectra of PBTz-Th* in 0.005 mg/mL toluene (green), CB (blue), and DCB (purple).

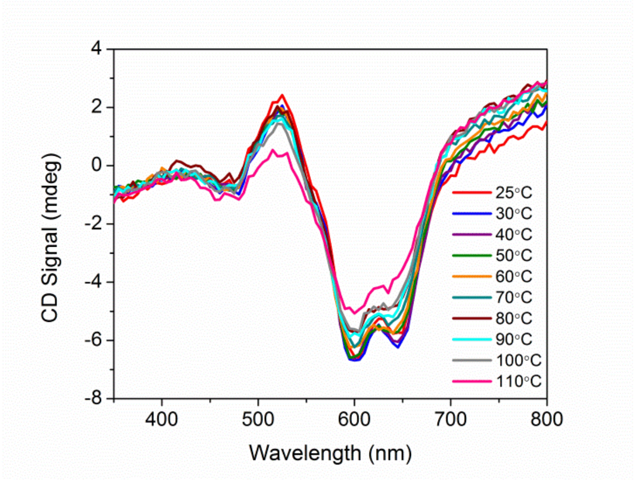

Figure S3-8. CD spectra of PBTz-Th* solution in 0.0025 mg/mL DCB as a function of temperature, from 25-110°C.

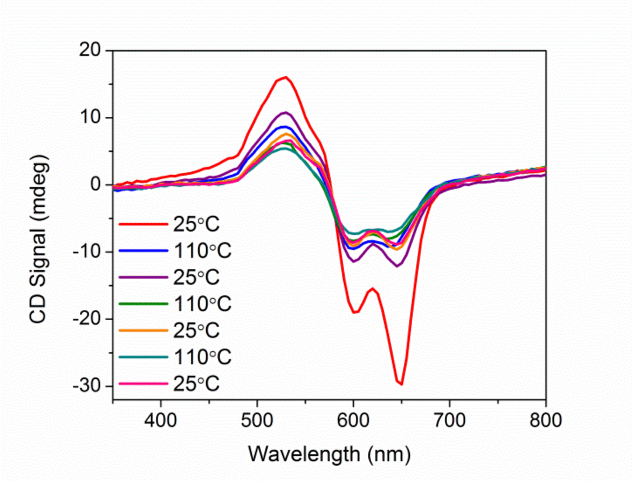

Figure S3-9. CD spectra of PBTz-Th* solution in 0.005 mg/mL DCB as a function of continuous cycles of heating to 110°C and cooling back to 25°C. The initial CD spectrum is shown in red and the final CD spectrum at 25°C is shown in pink.

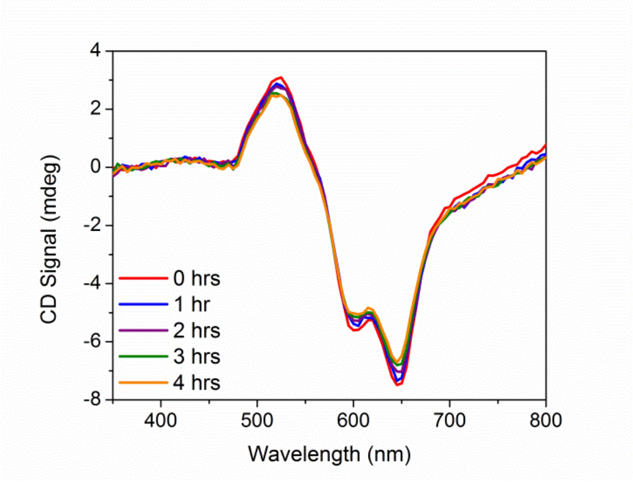

Figure S3-10. CD spectra of a mixture of 8:2 PBTz-Th:PBTz-Th* in .01 mg/mL toluene at 90°C after 0 hrs (red), 1 hr (blue), 2 hrs (purple), 3 hrs (green), and 4 hrs (orange).

Density Functional Theory (DFT) Calculations

Calculations were done using the Gaussian 09 software suite.[95] The hybrid long range corrected CAM-B3LYP functional[96] with the basis set 6-31G(d,p) were used for the optimization of the geometry.

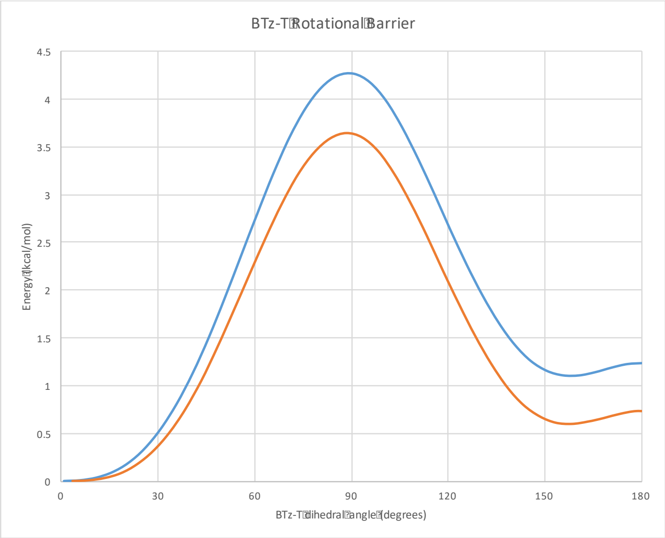

Figure S3-11. Calculated rotational barriers for BTz-Th in vacuum (blue) and chlorobenzene (orange).

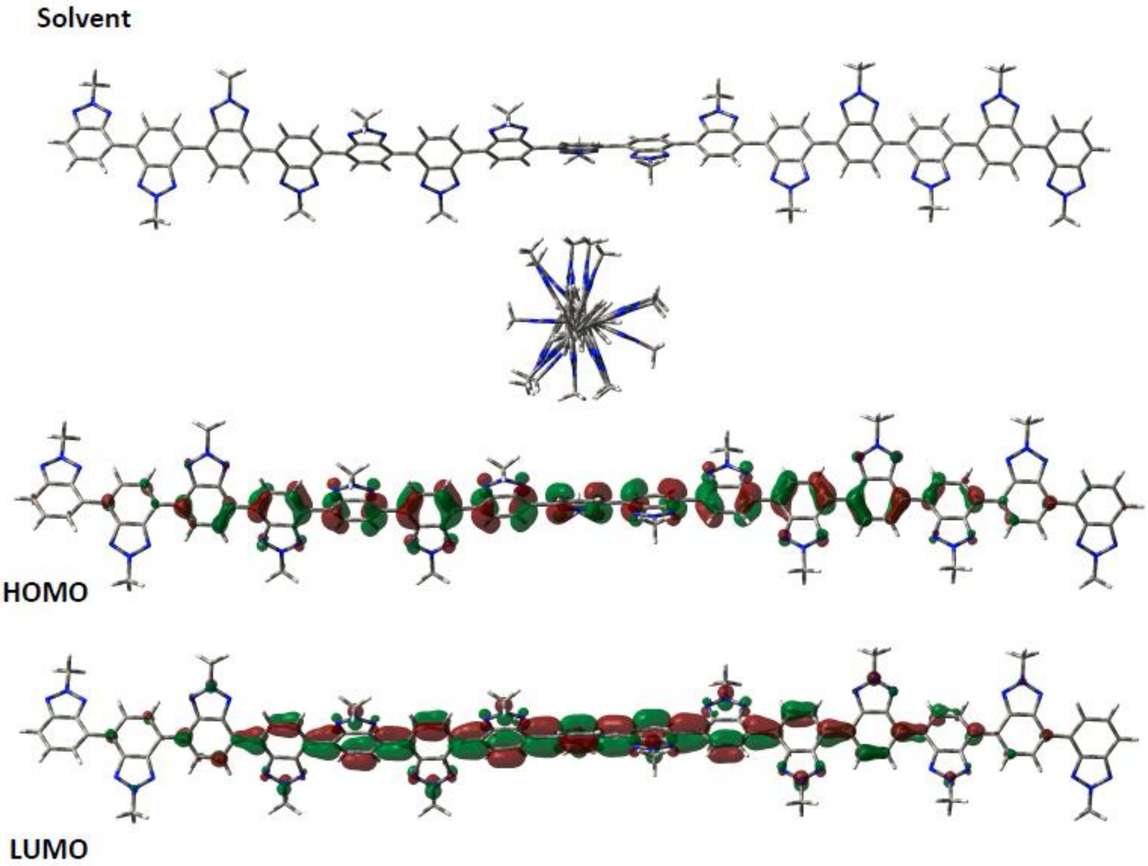

Figure S3-12. DFT calculated HOMO and LUMO levels of a 15-mer benzotriazole molecule.

Dynamic Light Scattering (DLS)

Dynamic light scattering measurements were taken using a DynaPro NanoStar with Dynamics software for data collection and analysis from Wyatt Technology. Measurements were carried out using a He-Ne laser at a wavelength of 662 nm at room temperature. The concentration used for each sample was 0.01 mg/mL DCB. An autocorrelation function is determined using the provided software to fit the data. The diffusion coefficient is extracted from the autocorrelation function such that the hydrodynamic radius is calculated using the Stokes-Einstein equation.

G. References

1. Zhao, Y.; Rahim, N. A. A.; Xia, Y.; Fujiki, M.; Song, B.; Zhang, Z.; Zhang, W.; Zhu, X. Supramolecular Chirality in Achiral Polyfluorene: Chiral Gelation, Memory of Chirality, and Chiral Sensing Property. *Macromolecules* **2016**, *49*, 3214-3221.

2. Yu, Z-P.; Ma, C-H.; Wang, Q.; Liu, N.; Yin, J.; Wu, Z-Q. Polyallene-*block*-polythiophene-*block*-polyallene Copolymers: One-Pot Synthesis, Helical Assembly, and Multiresponsiveness. *Macromolecules* **2016**, *49*, 1180-1190.

3. Reuther, J. F.; Siriwardane, D. A.; Kulikov, O. V.; Batchelor, B. L.; Campos, R.; Novak, B. M. Facile Synthesis of Rod-Coil Block Copolymers with Chiral, Helical Polycarbodiimide Segments via Postpolymerization with CuAAC “Click” Coupling of Functional End Groups. *Macromolecules* **2015**, *48*, 3207-3216.

4. Watanabe, K.; Sun, Z.; Akagi, K. Interchain Helically π-Stacked Assembly of Cationic Chiral Poly(*para*-phenylene) Derivatives Enforced by Anionic π-Conjugated Molecules through Both Electrostatic and π-π Interactions. *Chem. Mater.* **2015**, *27*, 2895-2902.

5. Rodriguez, R.; Quinoa, E.; Riguera, R.; Freira, F. Architecture of Chiral Poly(phenylacetylene)s: From Compressed/Highly Dynamic to Stretched/Quasi-Static Helices. *J. Am. Chem. Soc.* **2016**, DOI: 10.1021/jacs.6b04834.

6. Woo, E. M.; Lugito, G.; Tsai, J-H.; Muller, A. J. Hierarchically Diminishing Chirality Effects on Lamellar Assembly in Spherulites Comprising Chiral Polymers. *Macromolecules* **2016**, *49*, 2698-2708.

7. Kumar, J.; Nakashima, T.; Kawai, T. Circularly Polarized Luminescence in Chiral Molecules and Supramolecular Assemblies. *J. Phys. Chem. Lett.* **2015**, *6*, 3445-3452.

8. Kumazawa, S.; Castanon, J. R.; Shiotsuki, M.; Sato, T.; Sanda, F. Chirality Amplification in Helical Block Copolymers. Synthesis and Chiroptical Properties of Block Copolymers of Chiral/Achiral Acetylene Monomers. *Polym. Chem.* **2015**, *6*, 5931-5939.

9. Zhang, W.; Jin, W.; Fukushima, T.; Mori, T.; Aida, T. Helix Sense-Selective Supramolecular Polymerization Seeded by a One-Handed Helical Polymeric Assembly. *J. Am. Chem. Soc.* **2015**, *137*, 13792-13795.

10. Monnaie, F.; van den Eede, M-P.; Koeckelberghs, G. Expression of Chirality in a Conjugated Polymer without Any Excess of Chiral Centers. *Macromolecules* **2015**, *48*, 8121-8127.

11. Langeveld-Voss, B. M. W.; Janssen, R. A. J.; Meijer, E. W. On the Origin of Optical Activity in Polythiophenes. *J. Mol. Struct.* **2000**, *521*, 285-301.

12. Satrijo, A.; Meskers, S. C. J.; Swager, T. M.; Probing a Conjugated Polymer’s Transfer of Organization-Dependent Properties from Solutions to Films. *J. Am. Chem. Soc.* **2006**, *128*, 9030-9031.

13. Watanabe, K.; Suda, K.; Akagi, K. Hierarchically Self-Assembled Helical Aromatic Conjugated Polymers. *J. Mater. Chem. C* **2013**, *1*, 2797-2805.

14. Langeveld-Voss, B. M. W.; Beljonne, D.; Shuai, Z.; Janssen, R. A. J.; Meskers, S. C. J.; Meijer, E. W.; Bredas, J.-L. Investigation of Exciton Coupling in Oligothiophenes by Circular Dichroism Spectroscopy. *Adv. Mater.* **1998**, *10*, 1343-1348.

15. Oda, M.; Nothofer, H.-G.; Scherf, U.; Sunjic, V.; Richter, D.; Regenstein, W.; Neher, D. Chiroptical Properties of Chiral Substituted Polyfluorenes. *Macromolecules* **2002**, *35*, 6792-6798.

16. Fronk, S. L.; Wang, M.; Ford, M.; Coughlin, J.; Mai, C.-K.; Bazan, G. C. Effect of Chiral 2-ethylhexyl Side Chains on Chiroptical Properties of the Narrow Bandgap Conjugated Polymers PCPDTBT and PCDTPT. *Chem. Sci.* **2016**, *7*, 5313-5321.

17. Hu, H.; Zhao, K.; Fernandes, N.; Boufflet, P.; Bannock, J. H.; Yu, L.; de Mello, J. C.; Stingelin, N.; Heeney, M.; Giannelis, E. P.; Amassian, A. Entanglements in Marginal Solutions: a Means of Tuning Pre-Aggregation of Conjugated Polymers with Positive Implications for Charge Transport. *J. Mater. Chem. C* **2015**, *3*, 7394-7404.

18. Peet, J.; Cho, N. S.; Lee, S. K.; Bazan, G. C. Transition from Solution to the Solid State in Polymer Solar Cells Cast from Mixed Solvents. *Macromolecules* **2008**, *41*, 8655-8659.

19. Lee, J. K.; Ma, W. L.; Brabec, C. J.; Yuen, J.; Moon, J. S.; Kim, J. Y.; Lee, K.; Bazan, G. C., Heeger, A. J. Processing Additives for Improved Efficiency from Bulk Heterojunction Solar Cells. *J. Am. Chem. Soc.* **2008**, *130*, 3619-3623.

20. Nguyen, T.-Q.; Doan, V.; Schwartz, B. J. Conjugated Polymer Aggregates in Solution: Control of Interchain Interactions. *J. Chem. Phys.* **1999**, *110*, 4068-4078.

21. Li, L.; Lu, G.; Yang, X. Improving Performance of Polymer Photovoltaic Devices using an Annealing-Free Approach via Construction of Ordered Aggregates in Solution. *J. Mater. Chem.* **2008**, *18*, 1984-1990.

22. Scharsich, C.; Lohwasser, R. H.; Sommer, M.; Asawapirom, U.; Scherf, U.; Thelakkat, M.; Neher, D.; Kohler, A. Control of Aggregate Formation in Poly(3-hexylthiophene) by Solvent, Molecular Weight, and Synthetic Method. *J. Polym. Sci Pol. Phys.* **2012**, *50*, 442-453.

23. Guo, X.; Baumgarten, M.; Mullen, K. Designing π-Conjugated Polymers for Organic Electronics. *Prog. Polym. Sci*. **2013**, *38*, 1832-1908.

24. Marszalek, T.; Li, M.; Pisula, W. Design Directed Self-Assembly of Donor-Acceptor Polymers. *Chem. Commun.* **2016**, DOI: 10.1039/C6CC04523E.

25. Scharber, M. C.; Muhlbacher, Koppe, M.; Denk, P.; Waldauf, Heeger, A. J.; Brabec, C. J. Design Rules for Donors in Bulk-Heterojunction Solar Cells – Toward 10% Energy-Conversion Efficiency. *Adv. Mater.* **2006**, *18*, 789-794.

26. Henson, Z. B.; Mullen, K.; Bazan, G. C. Design Strategies for Organic Semiconductors Beyond the Molecular Formula. *Nature Chem.* **2012**, *4*, 699-704.

27. Beaujuge, P. M.; Frechet, J. M. J. Molecular Design and Ordering Effects in π-Functional Materials for Transistor and Solar Cell Applications. *J. Am. Chem. Soc.* **2011**, *133*, 20009-20029.

28. Fracchetti, A. π-Conjugated Polymers for Organic Electronics and Photovoltaic Cell Applications. *Chem. Mater*. **2011**, *23*, 733-758.

29. Gendron, D.; Leclerc, M. New Conjugated Polymers for Plastic Solar Cells. *Energy Environ. Sci.* **2011**, *4*, 1225-1237.

30. van Franeker, J. J.; Turbiez, M.; Li, W.; Wienk, M. M.; Janssen, R. A. J. A Real-Time Study of the Benefits of Co-Solvents in Polymer Solar Cell Processing. *Nature Commun.* **2015**, *6*, 6229.

31. Ho, P. K.-H.; Chua, L.-L.; Dipankar, M.; Gao, X.; Qi, D.; Wee, A. T.-S.; Chang, J.-F.; Friend, R. H. Solvent Effects on Chain Orientation and Interchain π-Interaction in Conjugated Polymer Thin Films: Direct Measurements of the Air and Substrate Interfaces by Near-Edge X-ray Absorption Spectroscopy. *Adv. Mater.* **2007**, *19*, 215-221.

32. Qian, D.; Ye, L.; Zhang, M.; Liang, Y.; Li, L.; Huang, Y.; Guo, X.; Zhang, S.; Tan, Z.; Hou, J. Design, Application, and Morphology Study of a New Photovoltaic Polymer with Strong Aggregation in Solution State. *Macromolecules* **2012**, *45*, 9611-9617.

33. Huang, J.; Zhu, Y.; Chen, J.; Zhang, L.; Peng, J.; Cao, Y. Dithienobenzothiadiazole-Based Conjugated Polymer: Processing Solvent-Relied Interchain Aggregation and Device Performances in Field-Effect Transistors and Polymer Solar Cells. *Macromol. Rapid Commun.* **2014**, *35*, 1960-1967.

34. Lou, S. J.; Szarko, J. M.; Xu, T.; Yu, L.; Marks, T. J.; Chen, L. X. Effects of Additives on the Morphology of Solution Phase Aggregates Formed by Active Layer Components of High-Efficiency Organic Solar Cells. *J. Am. Chem. Soc.* **2011**, *133*, 20661-20663.

35. Hoven, C. V.; Dang, X.-D.; Coffin, R. C.; Peet, J.; Nguyen, T.-Q.; Bazan, G. C. Improved Performance of Polymer Bulk Heterojunction Solar Cells Through the Reduction of Phase Separation via Solvent Additives. *Adv. Mater.* **2010**, *22*, E63-E66.

36. Yao, Y.; Hou, J.; Xu, Z.; Li, G.; Yang, Y. Effects of Solvent Mixtures on the Nanoscale Phase Separation in Polymer Solar Cells. *Adv. Funct. Mater.* **2008**, *18*, 1783-1789.

37. Wang, M.; Wang, H.; Yokoyama, T.; Liu, X.; Huang, Y.; Zhang, Y.; Nguyen, T.-Q.; Aramaki, S.; Bazan, G. C. High Open Circuit Voltage in Regioregular Narrow Band Gap Polymer Solar Cells. *J. Am. Chem. Soc.* **2014**, *136*, 12576-12579.

38. Wang, D.; Yuan, Y.; Mardiyati, Y.; Bubeck, C.; Koynov, K. From Single Chains to Aggregates, How Conjugated Polymers Behave in Dilute Solutions. *Macromolecules* **2013**, *46*, 6217-6224.

39. Hoeben, F. J. M.; Jonkheijm, P.; Meijer, E. W.; Schenning, A. P. H. J. About Supramolecular Assemblies of π-Conjugated Systems. *Chem. Rev.* **2005**, *105*, 1491-1546.

40. Kushida, S.; Braam, D.; Dao, T. D.; Saito, H.; Shibasaki, K.; Ishii, S.; Nagao, T.; Saeki, A.; Kuwabara, T.; Kijima, M.; Lorke, A.; Yamamoto, Y. Conjugated

Polymer Blend Microspheres for Efficient, Long-Range Light Energy Transfer. *ACS Nano* **2016**, *10*, 5543-5549.

41. Zhang, Z.; Peng, B.; Liu, B.; Pan, C.; Li, Y.; He, Y.; Zhou, K.; Zou, Y. Copolymers from Benzodithiophene and Benzotriazole: Synthesis and Photovoltaic Applications. *Polym. Chem.* **2010**, *1*, 1441-1447.

42. Min, J.; Zhang, Z.-G.; Zhang, S.; Zhang, M.; Zhang, J.; Li, Y. Synthesis and Photovoltaic Properties of D-A Copolymers Based on Dithienosilole and Benzotriazole. *Macromolecules* **2011**, *44*, 7632-7638.

43. Zhang, L.; He, C.; Chen, J.; Yuan, P.; Huang, L.; Zhang, C.; Cai, W.; Liu, Z.; Cao, Y. Bulk-Heterojunction Solar Cells with Benzotriazole-Based Copolymers as Electron Donors: Largely Improved Photovoltaic Parameters by Using PFN/Al Bilayer Cathode. *Macromolecules* **2010**, *43*, 9771-9778.

44. Unay, H.; Unlu, N. A.; Hizalan, G.; Hacioglu, S. O.; Yildiz, D. E.; Toppare, L.; Cirpan, A. Benzotriazole and Benzodithiophene Containing Medium Band Gap Polymer for Bulk Heterojunction Polymer Solar Cell Applications. *J. Polym. Sci. Polym. Chem.* **2015**, *53*, 528-535.

45. Gruber, M.; Jung, S.-H.; Schott, S.; Venkateshvaran, D.; Kronemeijer, A. J.; Andreasen, J. W.; McNeill, C. R.; Wong, W. W. H.; Shahid, M.; Heeney, M.; Lee, J.-K.; Sirringhaus, H. Enabling High-Mobility, Ambipolar Charge-Transport in a DPP-benzotriazole Copolymer by Side-Chain Engineering. *Chem. Sci.* **2015**, *6*, 6949-6960.

46. Lee, J.-K.; Gwinner, M. C.; Berger, R.; Newby, C.; Zentel, R.; Friend, R. H.; Sirringhaus, H.; Ober, C. K. High-Performance Electron-Transporting Polymers Derived from a Heteroaryl Bis(trifluoroborate). *J. Am. Chem. Soc.* **2011**, *133*, 9949-9951.

47. Yum, S.; An, T. K.; Wang, X.; Uddin, M. A.; Nguyen, T. L.; Xu, S.; Ryu, H.; Kim, Y. J.; Hwang, S.; Park, C. E.; Woo, H. Y. Thienothiophene-Benzotriazole-Based Semicrystalline Linear Copolymers for Organic Field Effect Transistors. *Pure Appl. Chem.* **2014**, *86*, 1293-1302.

48. Yum, S.; An, T. K.; Wang, X.; Lee, W.; Uddin, M. A.; Kim, Y. J.; Nguyen, T. L.; Xu, S.; Hwang, S.; Park, C. E.; Woo, H. Y. Benzotriazole-Containing Planar Conjugated Polymers with Noncovalent Conformational Locks for Thermally Stable and Efficient Polymer Field-Effect Transistors. *Chem. Mater.* **2014**, *26*, 2147-2154.

49. Bridges, C. R.; McCormick, T. M.; Gibson, G. L.; Hollinger, J.; Seferos, D. S. Designing and Refining Ni(II)diimine Catalysts Toward the Controlled Synthesis of Electron Deficient Conjugated Polymers. *J. Am. Chem. Soc.* **2013**, *135*, 13212-13219.

50. Tanimoto, A.; Yamamoto, T. Nickel-2,2’-Bipyridyl and Palladium-Triphenylphosphine Complex Promoted Synthesis of New π-Conjugated Poly(2-hexylbenzotriazole)s and Characterization of the Polymers. *Adv. Synth. Catal.* **2004**, *346*, 1818-1823.

51. Lui, B., Bazan, G. C. (Eds.), *Conjugated Polyelectrolytes Fundamentals and Applications*. Wiley VCH: Weinhein (**2013**).

52. Hoven, C. V., Garcia, A., Bazan, G. C., Nguyen, T.-Q. Recent Applications of Conjugated Polyelectrolytes in Optoelectronic Devices. *Adv. Mater.* **2008**, *20*, 3793-3810.

53. Yang, T., Wang, M., Duan, C., Hu, X., Huang, L., Peng, J., Huang, F., Gong, X. Inverted Polymer Solar Cells with 8.4% Efficiency by Conjugated Polyelectrolyte. *Energy Enivron. Sci.* **2012**, *5*, 8208-8214.

54. Lee, W., Seo, J. H., Woo, H. Y. Conjugated Polyelectrolytes: A New Class of Semiconducting Material for Organic Electronic Devices. *Polymer*, **2013**, *54*, 5104-5121.

55. He, Z., Zhong, C., Huang, X., Wong, W.-Y., Wu, H., Chen, L., Su, S., Cao, Y. Simultaneous Enhancement of Open Circuit Voltage, Short Circuit Current Density, and Fill Factor in Polymer Solar Cells. *Adv. Mater.* **2011**, *23*, 4636-4643.

56. Seo, J. H., Gutaker, A., Sun, Y., Wu, H., Huang, F., Cao, Y., Scherf, U., Heeger, A. J., Bazan, G. C. Improved High Efficiency Organic Solar Cells via Incorporation of a Conjugated Polyelectrolyte Interlayer. *J. Am. Chem. Soc.* **2011**, *133*, 8416-8419.

57. Hensen, Z. B., Zhang, Y., Nguyen, T.-Q., Seo, J. H., Bazan, G. C. Synthesis and Properties of Two Cationic Narrow Band Gap Conjugated Polyelectrolytes. *J. Am. Chem. Soc.* **2013**, *135*, 4163-4166.

58. Seo, J. H., Gutaker, A., Walker, B., Cho, S., Garcia, A., Yang, R., Nguyen, T.-Q., Heeger, A. J., Bazan, G. C. Improved Injection in n-Type Organic Transistors with Conjugated Polyelectrolytes. *J. Am. Chem. Soc.* **2009**, *131*, 18220-18221.

59. Mai, C.-K., Zhou, H., Zhang, Y., Hensen, Z. B., Nguyen, T.-Q., Heeger, A. J., Bazan, G. C. Facile Doping of Anionic Narrow-Band-Gap Polyelectrolytes During Dialysis. *Angew. Chem. Int. Ed.* **2013**, *52*, 12874-12878.

60. Mai, C.-K., Schlitz, R. A., Su, G. M., Spitzer, D., Wang, X., Fronk, S. L., Cahill, D. G., Chabinyc, M. L., Bazan, G. C. Side-Chain Effects on the Conductivity, Morphology, and Thermoelectric Properties of Self-Doped Narrow-Band-Gap Conjugated Polyelectrolytes. *J. Am. Chem. Soc.* **2014**, *136*, 13478-13481.

61. Mai, C.-K., Russ, B., Fronk, S. L., Hu, N., Chan-Park, M. B., Urban, J. J., Segalman, R. A., Chabinyc, M. L., Bazan, G. C. Varying the Ionic Functionalities of Conjugated Polyelectrolytes Leads to both p- and n-Type Carbon Nanotube Composites for Flexible Thermoelectrics. *Energy Environ. Sci.* **2015**, *8*, 2341-2346.

62. Hu, L., Wu, F., Li, C., Hu, A., Hu, X., Zhang, Y., Chen, L., Chen, Y. Alcohol-Soluble n-Type Conjugated Polyelectrolyte as Electron Transport Layer for Polymer Solar Cells. *Macromolecules,* **2015**, *48*, 5578-5586.

63. Wu, Z., Sun, C., Dong, S., Jiang, X.-F., Wu, S., Wu, H., Yip, H.-L., Huang, F., Cao, Y. n-Type Water/Alcohol-Soluble Napthalene Diimide-Based Conjugated Polymers for High-Performance Polymer Solar Cells. *J. Am. Chem. Soc.* **2016**, *138,* 2004-2013.

64. Zhang, K., Hu, Z., Xu, R., Jiang, X.-F., Yip, H.-L., Huang, F., Cao, Y. High-Performance Polymer Solar Cells with Electrostatic Layer-by-Layer Self-Assembled Conjugted Polyelectrolytes as the Cathode Interlayer. *Adv. Mater.* **2015**, *27*, 3607-3613.

65. Duan, C., Wang, L., Zhang, K., Guan, X., Huang, F. Conjugated Zwitterionic Polyelectrolytes and Their Neutral Precursor as Electron Injection Layer for High-Performance Light-Emitting Diodes. *Adv. Mater.* **2011**, *23*, 1665-1669.

66. Kim, B., Jung, I. H., Kang, M., Shim, H.-K., Woo, H. Y. Cationic Conjugated Polyelectrolytes-Triggered Conformational Change of Molecular Beacon Aptamer for Highly Sensitive and Selective Potassium Ion Detection. *J. Am. Chem. Soc.* **2012**, *134*, 3133-3138.

67. Cho, S., Lee, J., Tong, M., Seo, J. H., Yang, C. Poly(diketopyrrolopyrrole-benzothiadiazole) with Ambipolarity Approaching 100% Equivalency. *Adv. Funct. Mater.* **2011**, *21*, 1910-1916.

68. Kim, J., Han, A.-R., Hong, J., Kim, G., Lee, J., Shin, T. J., Oh, J. H., Yang, C. Ambipolar Semiconducting Polymers with π-Spacer Linked Bis-Benzothiadiazole Blocks as Strong Accepting Units. *Chem. Mater.* **2014**, *26*, 4933-4942.

69. Karakus, M., Balan, A., Baran, D., Toppare, L., Cirpan, A. Electrochemical and Optical Properties of Solution Processable Benzotriazole and Benzothiadiazole Containing Copolymers. *Synth. Met.* **2012**, *162*, 79-84.

70. Zhou, H., Yang, L., Stuart, A. C., Price, S. C., Liu, S., You, W. Development of Fluorinated Benzothiadiazole as a Structural Unit for a Polymer Solar Cell of 7% Efficiency. *Angew. Chem. Int. Ed.* **2011**, *50*, 2995-2998.

71. Hou, J., Chen, H.-Y., Zhang, S., Li, G., Yang, Y. Synthesis, Characterization, and Photovoltaic Properties of a Low Band Gap Polymer Based on Silole-Containing

Polythiophenes and 2,1,3-Benzothiadiazole. *J. Am. Chem. Soc.* **2008**, *130*, 16144-16145.

72. Peng, Q., Liu, X., Su, D., Fu, G., Xu, J., Dai, L. Novel Benzo[1,2b:4,5-b']dithiophene-Benzothiadiazole Derivatives with Variable Side Chains for High Performance Solar Cells. *Adv. Mater.* **2011**, *23*, 4554-4558.

73. Jiang, H., Taranekar, P., Reynolds, J. R., Schanze, K. S. Conjugated Polyelectrolytes: Synthesis, Photophysics, and Applications. *Angew. Chem. Int. Ed.* **2009**, *48*, 4300-4316.

74. Tan, C., Pinto, M. R., Kose, M. E., Ghiviriga, I., Schanze, K. S. Solvent-Induced Self-Assembly of a Meta-Linked Conjugated Polyelectrolyte. Helix Formation, Guest Intercalation, and Amplified Quenching. *Adv. Mater.* **2004**, *16*, 1208-1211.

75. Peng, H.-Q., Niu, L.-Y., Chen, Y.-Z., Wu, L.-Z., Tung, C.-H., Yang, Q.-Z. Biological Applications of Supramolecular Assemblies Designed for Excitation Energy Transfer. *Chem. Rev.* **2015**, *115*, 7502-7542.

76. Huang, Y.; Zhang, F.; Gong, Y. A Convenient Approach to (S)-2-ethylhexan-1-ol Mediated by Baker's Yeast. *Tetrahedron Lett.* **2005**, *46*, 7217-7219.

77. Parker, D. NMR Determination of Enantiomeric Purity. *Chem. Rev.* **1991**, *91*, 1441-1457.

78. Latypov, S. K.; Ferreiro, M. J.; Quinoa, E.; Riguera, R. Assignment of the Absolute Configuration of β-Chiral Primary Alcohols by NMR: Scope and Limitations. *J. Am. Chem. Soc.* **1998**, *120*, 4741-4751.

79. Harada, N.; Watanabe, M.; Kuwahara, S.; Sugio, A.; Kasai, Y.; Ichikawa, A. 2-Methoxy-2-(1-naphthyl)-propionic Acid, A Powerful Chiral Auxiliary for Enantioresolution of Alcohols and Determination of their Absolute Configurations by ^{1}HNMR Anisotropy Method. *Tetrahedron: Asymmetry* **2000**, *11*, 1249-1253.

80. Bifulco, G.; Dambruoso, P.; Gomez-Paloma, L.; Riccio, R. Determination of Relative Configuration in Organic Compounds by NMR Spectroscopy and Computational Methods. *Chem. Rev.* **2007**, *107*, 3744-3779.

81. Seco, J. M.; Quinoa, E.; Riguera, R. The Assignment of Absolute Configuration byNMR. *Chem. Rev.* **2004**, *104*, 17-117.

82. Coppo, P.; Cupertino, D. C.; Yeates, S. G.; Turner, M. L. Synthetic Routes to Solution Processable Polycyclopentadithiophenes. *Macromolecules* **2003**, *36*, 2705-2711.

83. Stille, J. K. Palladium-Catalyzed Cross-Coupling Reactions of Organotin Reagents with Organic Electrophiles. *Angew. Chem. Int. Ed.* **1986**, *25*, 508-524.

84. Kim, N.-K.; Jang, S.-Y.; Pace, G.; Caironi, M.; Park, W. T.; Khim, D.; Kim, J.; Kim, D.-Y.; Noh, Y. Y. High-Performance Organic Field-Effect Transistors with Directionally Aligned Conjugated Polymer Film Deposited from Pre-Aggregated Solution. *Chem. Mater.* **2015**, *27*, 8345-8353.

85. Clark, J.; Chang, J.-F.; Spano, F. C.; Friend, R. H.; Silva, C. Determining Exciton Bandwidth and Film Microstructure in Polythiophene Films Using Linear Absorption Spectroscopy. *Appl. Phys. Lett.* **2009**, *94*, 163306.

86. Clark, J.; Silva, C.; Friend, R. H.; Spano, F. C. Role of Intermolecular Coupling in the Photophysics of Disordered Organic Semiconductors: Aggregate Emission in Regioregular Polythiophene. *Phys. Rev.Lett.* **2007**, *98*, 206406.

87. Chen, Z.; Cai, P.; Chen, J.; Liu, X.; Zhang, L.; Lan, L.; Peng, J.; Ma, Y.; Cao, Y. Low Band-Gap Conjugated Polymers with Strong Interchain Aggregation and Very High Hole Mobility Toward Highly Efficient Thick-Film Polymer Solar Cells. *Adv. Mater.* **2014**, *26*, 2586-2591.

88. Zhang, Z. G.; Zhang, S.; Min, J.; Cui, C.; Geng, H.; Shuai, Z.; Li, Y. Side Chain Engineering of Polythiophene Derivatives with a Thienylene-Vinylene Conjugated Side Chain for Application in Polymer Solar Cells. *Macromolecules* **2012**, *45*, 2312-2320.

89. Zhang, S.; Ye, L.; Zhao, W.; Liu, D.; Yao, H.; Hou, J. Side Chain Selection for Designing Highly Efficient Photovoltaic Polymers with 2D Conjugated Structure. *Macromolecules* **2014**, *47*, 4653-4659.

90. Bencheikh, F.; Duche, D.; Ruiz, C. M.; Simon, J.-J.; Escoubas, L. Study of Optical Properties and Molecular Aggregation of Conjugated Low Band Gap Copolymers: PTB7 and PTB7-Th. *J. Phys. Chem. C* **2016**, DOI: 10.1021/acs.jpcc.5b07803.

91. Berova, N., Nakanishi, K., Woody, R. W. (Eds), *Circular Dichroism: Principles and Applications*, *2nd ed.* Wiley-VCH: New York (**2000**).

92. Jackson, N. E.; Savoie, B. M.; Kohlstedt, K. L.; de la Cruz, M. O.; Schatz, G. C.; Chen, L. X.; Ratner, M. A. Controlling Conformations of Conjugated Polymers and Small Molecules: The Role of Nonbonding Interactions. *J. Am. Chem. Soc.* **2013**, *135*, 10475-10483.

93. Huang, H.; Chen, Z.; Ortiz, R. P.; Newman, C.; Usta, H.; Lou, S.; Youn, J.; Noh, Y-Y.; Baeg, K-J.; Chen, L. X.; Facchetti, A.; Marks, T. Combining Electron-Neutral Building Blocks with Intramolecular “Conformational Locks” Affords Stable, High-

Mobility P- and N-Channel Polymer Semiconductors. *J. Am. Chem. Soc.* **2012**, *134*, 10966-10973.

94. Shi, Y., Mai, C.-K., Fronk, S. L., Chen, Y., Bazan, G. C. Optical Properties of Benzotriazole-Based Conjugated Polyelectrolytes. *Macromolecules*, **2016**, *49*, 6343-6349.

95. Frisch, M. J.; Trucks, G. W.; Schlegel, H. B.; Scuseria, G. E.; Robb, M. A.; Cheeseman, J. R.; Scalmani, G.; Barone, V.; Mennucci, B.; Petersson, G. A.; Nakatsuji, H.; Caricato, M.; Li, X.; Hratchian, H. P.; Izmaylov, A. F.; Bloino, J.; Zheng, G.; Sonnenberg, J. L.; Hada, M.; Ehara, M.; Toyota, K.; Fukuda, R.; Hasegawa, J.; Ishida, M.; Nakajima, T.; Honda, Y.; Kitao, O.; Nakai, H.; Vreven, T.; Montgomery, J.; Peralta, J. E.; Ogliaro, F.; Bearpark, M.; Heyd, J. J.; Brothers, E.; Kudin, K. N.; Staroverov, V. N.; Kobayashi, R.; Normand, J.; Raghavachari, K.; Rendell, A.; Burant, J. C.; Iyengar, S. S.; Tomasi, J.; Cossi, M.; Rega, N.; Millam, J. M.; Klene, M.; Knox, J. E.; Cross, J. B.; Bakken, V.; Adamo, C.; Jaramillo, J.; Gomperts, R.; Stratmann, R. E.; Yazyev, O.; Austin, A. J.; Cammi, R.; Pomelli, C.; Ochterski, J. W.; Martin, R. L.; Morokuma, K.; Zakrzewski, V. G.; Voth, G. A.; Salvador, P.; Dannenberg, J. J.; Dapprich, S.; Daniels, A. D.; Farkas, Ö; Foresman, J. B.; Ortiz, J. V.; Cioslowski, J.; Fox, D. J. *Gaussian 09, Revision C.01*, Gaussian, Inc.: Wallingford, CT, **2010**.

96. Yanai, T.; Tew, D. P.; Handy, N. C. A New Hybrid Exchange-Correlation Functional Using the Coulomb Attenuating Method (CAM-B3LYP). *Chem. Phys. Lett.* **2004**, *393*, 51-57.

IV. Acceleration of Biocatalysis with Conjugated Oligoelectrolytes

A. Background/Introduction

Biocatalysis generally refers to the application of enzymes or whole cells in chemical synthesis.[1-2] It provides a "green" method for synthesizing a variety of molecules.[3-4] A range of applications has been established including methods for small molecules relevant to the pharmaceutical industry, polymerization reactions, and nanomaterials.[5-8] Bioconversion processes provide advantages that include mild reaction conditions, the capability for multistep reactions, high stereo-,regio-, and chemoselectivity, and inexpensive purification.[9-13] However, the scope of reactions that can undergo biocatalysis can be limited by factors such as reactant and product solubility,[14-15] transport across the cell membrane,[16-17] and overall enzyme turn over rates.[18-19]

Cell membranes act as a barrier for molecules entering and leaving the cell.[20-22] While this property is beneficial to the cell as it prevents toxic compounds from entering and maintains structural integrity,[20-22] it can provide a hurdle in whole cell catalysis if substrates and/or products are unable to cross this barrier.[16-17] Methods to increase the membrane permeability to improve biocatalysis have been developed and include treating cells with surfactants,[23-24] genetic engineering,[25-27] and solvent treatments.[28-30] However, the latter is not an ideal permeabilization method as ethanol and similar alcohols are toxic to many microbes.[31] Surfactants present a similar challenge,[32] while genetic engineering requires a time-intensive screening process for each new reaction.[33]

Conjugated oligoelectrolytes (COEs) offer a potential alternative. Certain COEs are known to intercalate into the membranes of microorganisms such as *S. cerevisiae, E. coli*, and *Shewanella oneidensis*.[34-35] The molecular structures of several COEs capable of intercalation are shown in Figure 4-1. Initial interest in the exoelectrogenic actuation by these COEs showed that addition of DSSN+ to an *E. coli* microbial fuel cell (MFC) improved current collection[36] and addition to a mixed-culture wastewater MFC resulted in higher current production.[37] The observations prompted the synthesis and characterization of a library of COEs with varying backbone lengths, functional groups, and pendant ionic groups.[38] Mechanistic studies of COE-cell membrane interactions through enzyme assays revealed that DSSN+ permeabilizes the outer membrane of *E. coli* and accelerates the extracellular hydrolysis of ONPG.[39-40] These results suggested the potential for COEs to impact biocatalysis, particularly under conditions when substrate/product diffusion in/out of the cell contributes to the rate determining step.

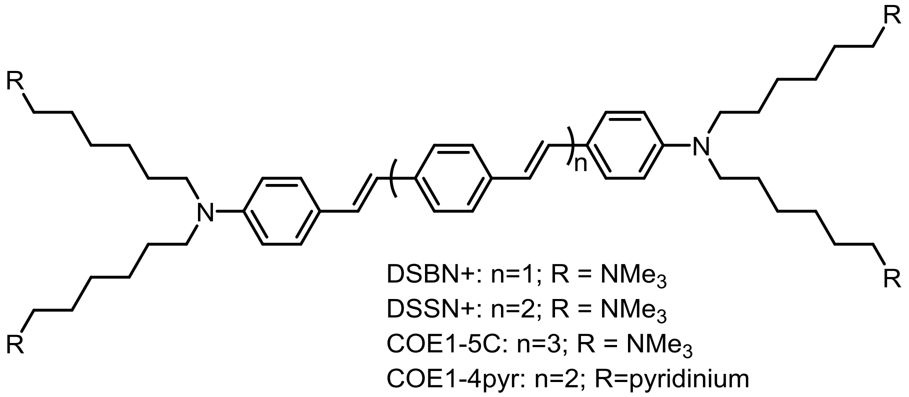

Figure 4-1. COEs used to permeabilize yeast cell membranes.

In this contribution, yeast cells were treated with four different COEs to study their influence on biocatalytic transformations, using the conversion of fumaric acid to L-malic acid by baker's yeast (*S. cerevisiae*)[41-43] as a model system. The COEs used in this study, shown in Figure 1, allow one to examine the impact on L-malic acid production by the differences in the length of the conjugated backbone and the identity of the ionic group. Hexadecyltrimethylammonium bromide (CTAB), a common surfactant used for cell membrane permeabilization,[23] was also tested for comparison. Cell association, confocal fluorescence microscopy (CFM), and minimum inhibitory concentration (MIC) experiments provide a deeper understanding of the effect of COEs on cells for biocatalytic activity.

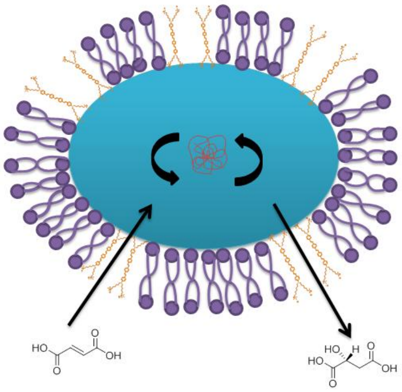

Figure 4-2. Cartoon illustration of COE intercalation into yeast membrane to accelerate the biocatalytic transformation of fumaric acid to L-malic acid.

B. Effect of COE Addition on Biocatalysis

1. Conversion by Yeast of Fumaric Acid to L-Malic Acid

The conversion of fumaric acid to L-malic acid utilizing baker's yeast, as shown in Figure 2, was chosen as a model reaction based on ease of product work-up, that only an aqueous medium is required, and literature precedent.[44-46] L-malic acid production has been studied based on its usefulness as a building block for larger molecules and polymers, and as a flavor additive in food.[47-48] Previous precedent also indicates that transportation across the cell membrane is a limiting factor for organic acids[49-50] and that surfactants increase the rate of product formation.[51-52] Fumarase, an enzyme located both in the cytosol and in the mitochondria of yeast cells, is the catalyst for this conversion.[53-54] Yeast cells used in our studies were cultured overnight and stained with COE. A 50 mM solution of fumaric acid was added and the reaction proceeded at 30°C for about a day. Reactions were run in triplicate and the results monitored by HPLC. Detailed experimental procedures and data can be found in the SI.

2. Effect of DSSN+

L-malic acid production using DSSN+ treated yeast cells was measured at four time points during the reaction (2.5 hrs, 5 hrs, 7.5 hrs, and 21 hrs) for six different DSSN+ concentrations (0, 10, 25, 50, 75, and 100 μM). As shown in Figure 4-3a, L-malic acid concentration increases with time for all reactions with [DSSN+] > 10 μM. The control reaction, using non-treated yeast, exhibits the lowest production of L-malic acid compared to yeast cells treated with 100 μM DSSN+, which provide the highest production. After 21 hours, the amount of L-malic acid is more than 3.6 times higher than the control reaction. Product formation curves indicate an initial steady increase in L-malic acid production for about the first five hours, after which production begins to level off. The rate of reaction (Figure 3b), estimated by the slope of [L-malic acid] vs. time during the first five hours, increases linearly with [DSSN+], thereby demonstrating enhancement of biocatalytic activity upon COE intercalation, as diagrammatically illustrated in Figure 4-2.

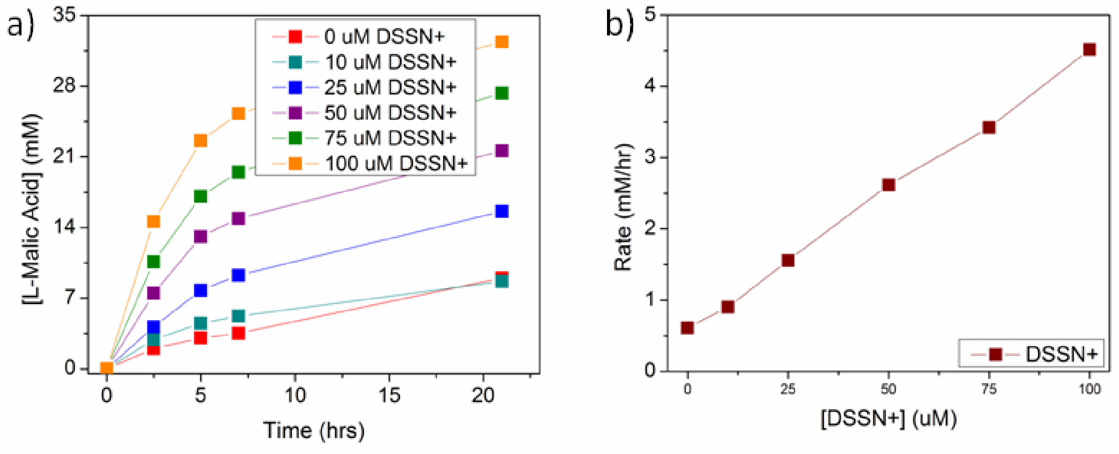

Figure 4-3. a) [L-malic acid] vs. time as a function of [DSSN+] and b) rate of L-malic acid production (mM/hr) during the first five hours of reaction time as a function of [DSSN+].

CFM and cell association experiments confirm DSSN+ association with the cell membrane. Cell association was determined using a UV-Vis absorption method in which the absorbance at 420 nm of the supernant from centrifuged stained yeast cells was compared to a fresh solution of DSSN+. Cell association for DSSN+ was greater than 50% for all concentrations. CFM images of yeast cells immediately after staining with 25 μM DSSN+ and 5 μM propidium iodide (PI), a dead stain, are shown in Figure 4-4. DSSN+ (green) successfully stains most of the yeast cells and is present in the cell membrane. One cell in this image is also stained with PI (red), indicating that this particular cell is no longer viable; similar to results for untreated cells (Figure S4-18). MIC experiments showed no evidence of toxicity by DSSN+ up to 128 μM (Figures S4-16, S4-17).

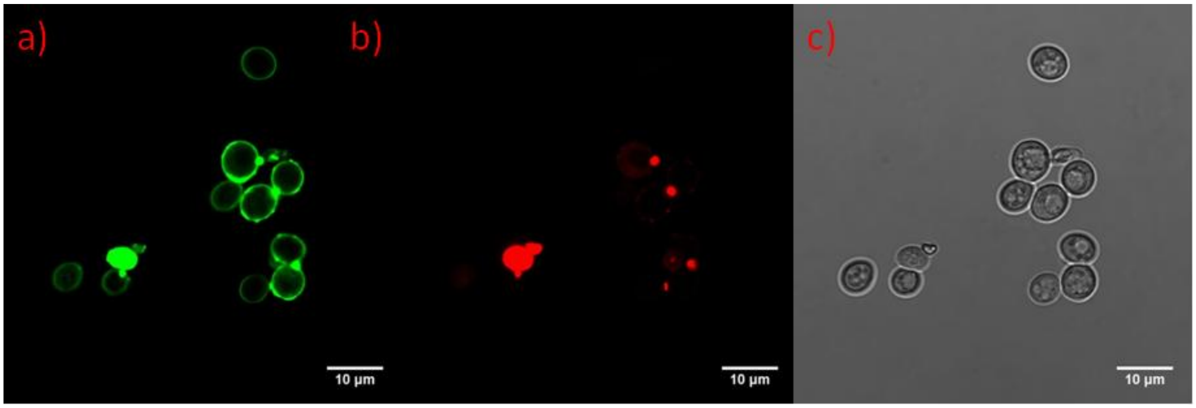

Figure 4-4. CFM images of yeast cells after staining with either 25 μM DSSN+ and 5 μM PI where a) shows the DSSN+ (green) channel, b) shows the PI (red) channel, and c) shows the bright field image.

In order to determine whether the relevant enzyme remains inside the cell or diffuses out to catalyze the reaction, yeast cells treated with 100 μM DSSN+ solutions were spun down and fumaric acid was added to the supernant to achieve a concentration of 50 mM. The reaction was run in triplicate and allowed to proceed for 21 hours. The concentration of L-malic remained at zero and the concentration of fumaric acid remained at 50 mM (Figure S4-13). Catalysis by fumarase thus does not occur outside the cells, thereby implicating membrane permeabilization by the DSSN+ as responsible for facilitating transport of the substrate and/or product.

3. Comparison to Conventional Surfactant, CTAB

The same procedures used for DSSN+ were used to examine the influence of CTAB and the results are provided in Figure 4-5. As established previously, CTAB increases L-malic acid production, such that at [CTAB] = 100 μM the yield is 2.9 times higher compared to controls. The rate during the first five hours of reaction time indicates no increase until [CTAB] = 50 μM. Compared to DSSN+ treated cells, the rate is consistently lower. Yeast cells treated with 100 μM CTAB and 5 μM PI were imaged using CFM, see Figure S4-19. Multiple yeast cells are stained red by PI and thus no longer viable. A comparison of multiple CFM images revealed that about 25% of cells treated with CTAB were not viable compared to 9% of cells treated with DSSN+. MIC experiments were also performed for CTAB concentrations from 1 μM to 128 μM using the same procedure as DSSN+ (Figure S4-16, S4-17). CTAB inhibits cell growth at concentrations of 16 μM and above. The MIC data are in agreement with literature reports of CTAB toxicity.[53]

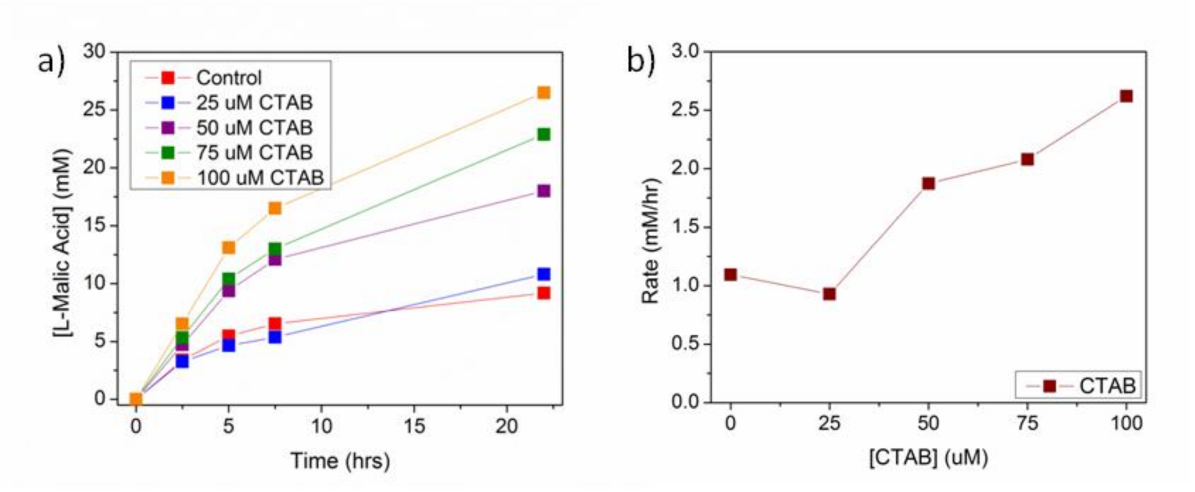

Figure 4-5. [L-malic acid] vs. time as a function of [CTAB] and b) rate of L-malic acid production (mM/hr) during the first five hours of reaction time as a function of [DSSN+].

Differences between CTAB and DSSN+ were further examined with a second addition of starting material. Beginning with the standard yeast growth conditions, cells were stained with 100 μM DSSN+ or 100 μM CTAB. The reaction was run using the method described above and the results are reported in Figure 4-6a. After allowing the reaction to proceed for 22 hours, the cells were centrifuged and the supernant discarded. A second addition of 50 mM fumaric acid was added to resuspended cells and the reaction was allowed to proceed under standard conditions. The results are shown in Figure 4-6b.

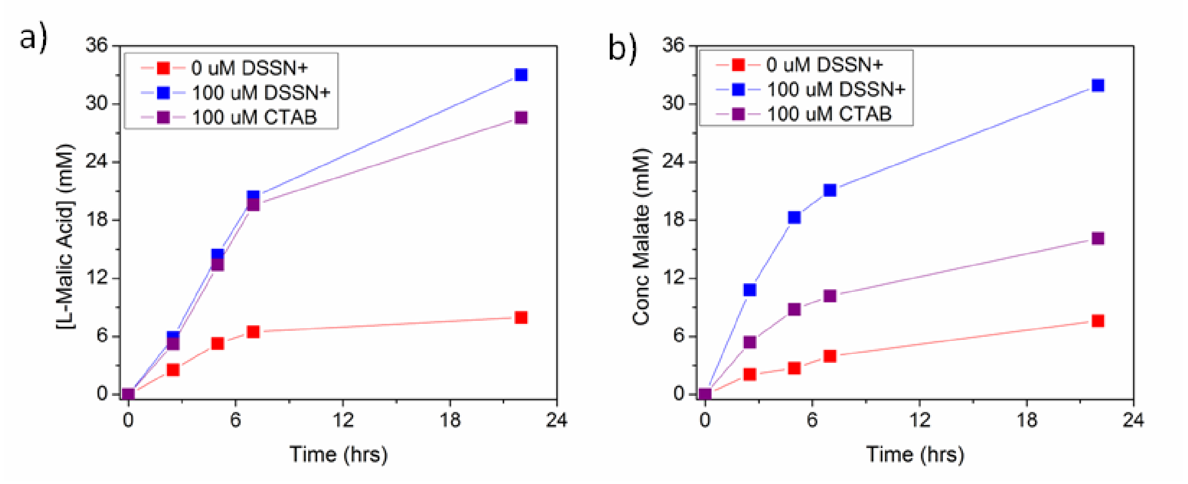

Figure 4-6. [L-malic acid] vs. time for a) the first and b) the second addition of fumaric acid added to the reactors for unstained yeast cells (red), cells stained with 100 μM DSSN+ (blue), and cells stained with 100 μM CTAB (purple).

The first addition of fumaric acid provides the expected results. However, Figure 4-6b shows that the second addition of fumaric acid reveals that cells with DSSN+ maintain their catalytic activity whereas CTAB treatment decreased activity, approximately 50% of their initial production. The difference in performance is attributed to the differences in toxicity toward yeast cells. CTAB is more toxic based on the MIC data, which suggests that fewer cells are still viable for catalysis. DSSN+ is non- toxic at this concentration and therefore gives rise to activated yeast cells that can be reused with only marginal decrease in their biocatalytic activity.

4. Influence of Conjugated Backbone Length

The effect of the conjugated backbone length on the ability of COEs to facilitate biocatalysis was explored by additionally testing DSBN+ and COE1-5C (Figure 4-1). DSBN+ contains one less phenylenevinylene unit compared to DSSN+, while COE1-5C contains one more. MIC experiments were performed on yeast cells for DSBN+ and COE1-5C using the procedure described for DSSN+ (Figures S4-16, S4-17). COE1-5C is non-toxic for all concentrations tested. DSBN+ inhibits cell growth at concentrations of 50 μM and above.

Compared to the control reaction, L-malic acid production increases when yeast cells are stained with DSBN+ for the concentrations tested and at all time intervals (Figure 4-7). Treatment with 100 μM DSBN+ solutions produces ~4.5 times more L-malic acid after 21 hours than control reactions. The rate of reaction for yeast cells treated with DSBN+ is also greater than untreated cells. The amount of L-malic acid produced saturates when [DSBN]

> 50 μM (Figure S6). Past work suggests that the maximum yield using free yeast cells in solution is 80%.[49] After 21 hours, yeast cells stained with the three highest concentrations of DSBN+ achieve yields of 75%, 71%, and 73% respectively. These data indicate that DSBN+ solutions sufficiently permeabilize yeast membranes for the effective biocatalytic conversion of fumaric acid to L-malic acid, such that diffusion across the membrane no longer contributes to the limiting step.

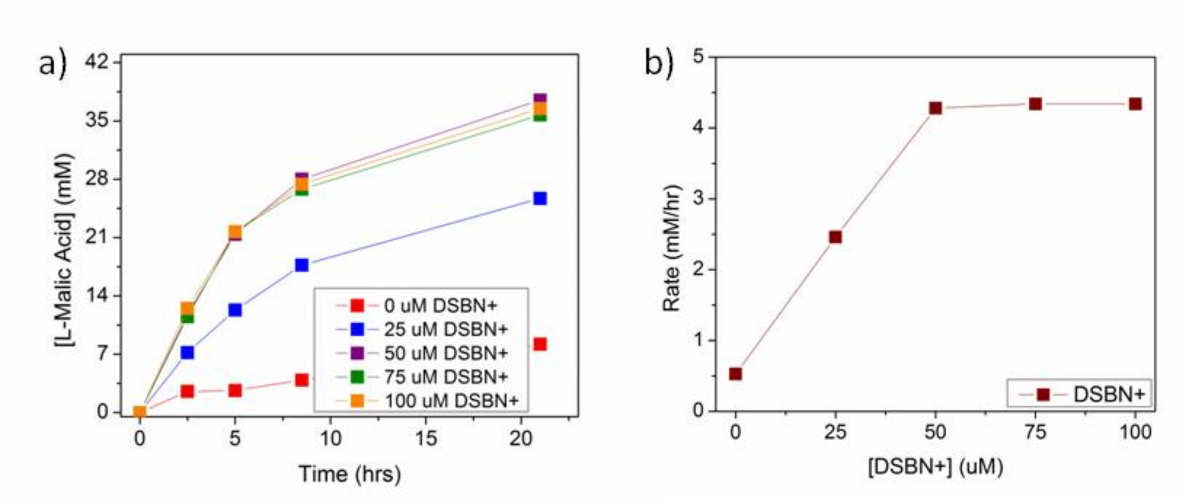

Figure 4-7. a) [L-malic acid] vs. time as a function of [DSBN+] and b) rate of L-malic acid production (mM/hr) during the first five hours of reaction time as a function of [DSBN+].

The influence of COE1-5C is summarized in Figure 4-8. One observes that there is little difference relative to the control reaction with unstained cells and the reactions containing yeast stained with COE1-5C. Even after about 22 hours, cells stained with COE1-5C produce less than or about equal to the amount of L-malic acid as the control reaction. Increasing the staining concentration from 25 μM to 100 μM COE1-5C does not result in significantly improved biocatalytic yield or rate.

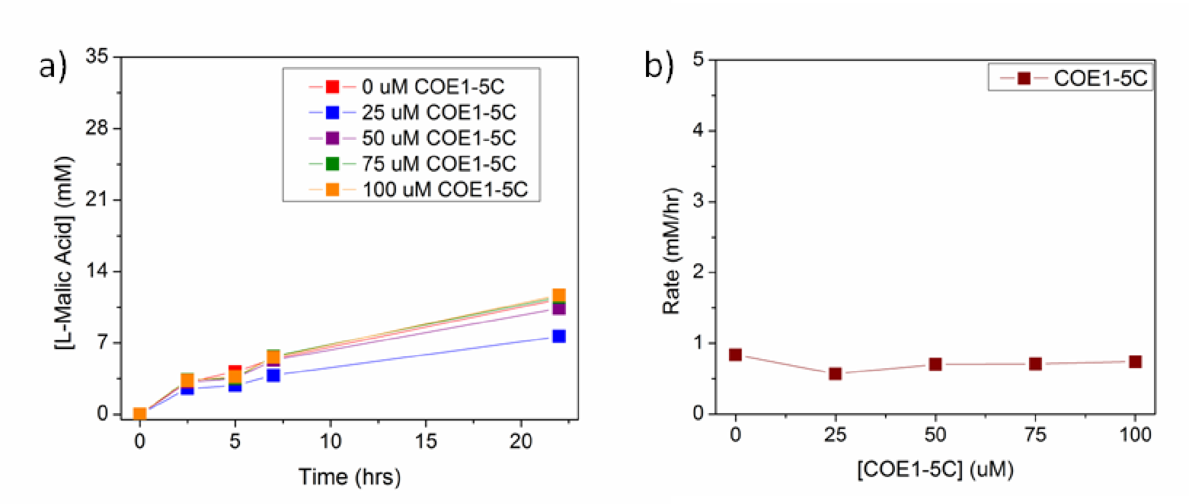

Figure 4-8. a) [L-malic acid] vs. time as a function of [COE1-5C] and b) rate of L-malic acid production (mM/hr) during the first five hours of reaction time as a function of [COE1-5C].

In order to confirm the presence of COE1-5C in the cell membrane, CFM measurements were preformed and the results are shown in Figure 4-9. CFM images of yeast stained with COE1-5C (green) provide evidence that COE1-5C is present in the cell membrane. Similar to DSSN+, staining with PI (red) indicates one nonviable cell within the image. Cell association of COE1-5C was determined to be 40%. The absence of biocatalytic enhancement is therefore not due to a failure of COE1-5C to insert into the yeast membrane or, as determined by MIC experiments, due to COE1-5C-containing cells being non-viable.

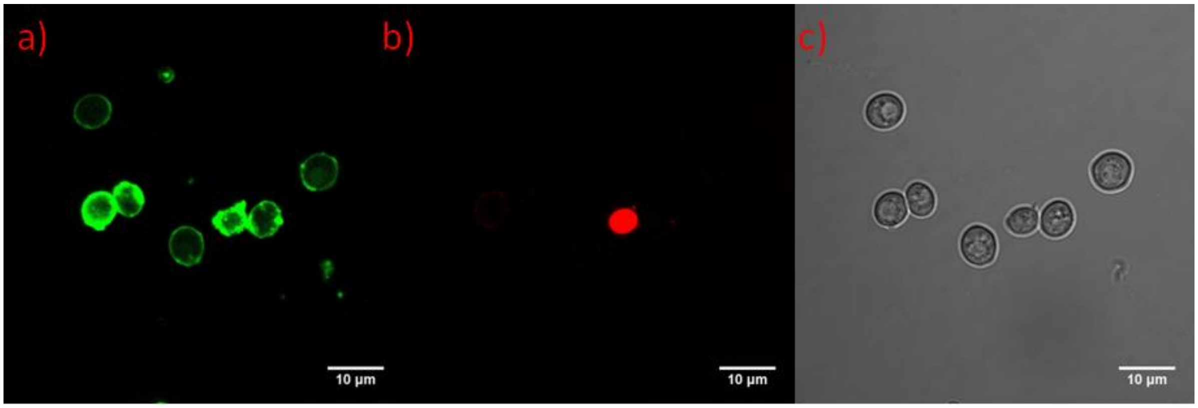

Figure 4-9. CFM images of yeast cells after staining with either 25 µM COE1-5C and 5 µM PI where a) shows the COE1-5C (green) channel, b) shows the PI (red) channel, and c) shows the bright field image.

As the length of the conjugated backbone increases, the ability of the COEs to permeabilize the membrane to enable the biocatalytic conversion of fumaric acid to L-malic acid decreases. DSBN+ treated yeast cells provide the highest yield of L-malic acid, whereas COE1-5C stained cells do not differ significantly from the control reaction. Similarly the rate of production is higher for DSBN+ than DSSN+ at lower COE concentrations. However; at 100 μM, DSBN+ and DSSN+ provide similar rates; indicating that diffusion across the membrane may no longer be a component of the rate determining step. It is worth noting that COE1-5C is known to *stabilize* the cell membrane of *E. coli*,[54] and a similar phenomenon may occur with yeast cell membranes – the membrane stabilizes such that there is no increase in the transport of reactants and products. In contrast, DSSN+ and DSBN+ are known to insert into cell membranes and subsequently permeabilize the membrane.[39,55] The shorter backbone length of DSBN+ results in increased membrane disruption compared to DSSN+ and likely greater membrane permeabilization.[55] Simulations in the literature show that the mismatch in the length of DSBN+ and the lipid bilayer causes cell membrane thinning and deformation at high concentrations.[55] At levels below those causing cell lysis, cell membrane disruption by DSBN+ facilitates biocatalysis.

5. Influence of Pendant Ionic Groups

Comparison of the catalytic activities with COE1-4pyr (Figure 4-1) and DSSN+ give insight into the influence of the pendant ionic group. DSSN+ contains tetraalkylammonium cations which are replaced with pyridinium in COE1-4pyr, while the length of the conjugated backbone is identical. Past work confirms the ability of COE1-4pyr to exhibit similar membrane insertion properties as DSSN+.[56]

L-malic acid production after COE1-4pyr staining is shown in Figure 4-10a. An increase in L-malic acid production is observed with increasing [COE1-4pyr], such at 100 μM COE1-4pyr one observes the highest biocatalytic yields. The trend is similar to that observed for DSSN+ stained yeast cells such that the rate of L-malic acid produced increases with increasing concentration of COE1-4pyr (Figure 4-10b). Cell association is also similar to DSSN+ with values greater than 50%, while MIC experiments result in no toxicity for all concentrations tested (Figures S4-16, S4-17). Thus switching the cationic group from tetraalkylammonium to pyridinium maintains accelerated biocatalytic activity and cell viability.

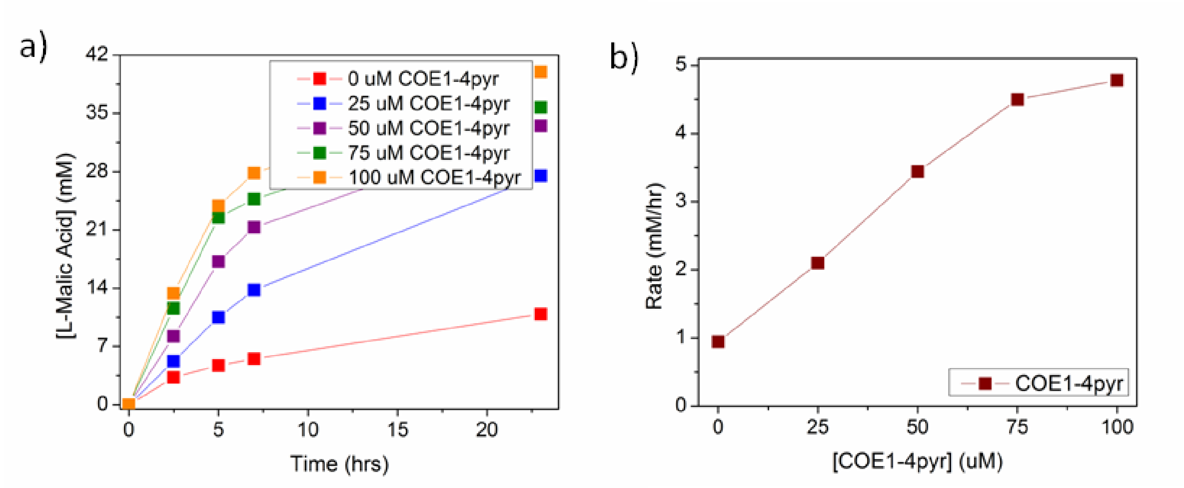

Figure 4-10. a) [L-malic acid] vs. time as a function of [COE1-4pyr] and b) rate of L-malic acid production during the first five hours of reaction time as a function of [COE1-4pyr].

6. Conclusions

COE incorporation within yeast membranes gives rise to an increase in the biocatalytic transformation of fumaric acid to L-malic acid. The increase in activity is modulated by the molecular structure of the COEs studied here, such that as the conjugated backbone length is increased from three to five phenylenevinylene units one observes a progressive increase in the overall activity. Our current thinking is that these rates correlate to the ability of the COE to permeabilize the cell membrane. DSBN+ provided the highest biocatalytic yield (37.5 mM) at the lowest staining concentration (50 μM). The rate of L-malic acid production saturates at 50 μM DSBN+; likely indicating that diffusion across the cell membrane is no longer contributing to the limiting step. Changing the pendant cationic group from methylammonium iodide (DSSN+) to pyridinium iodide (COE1-4pyr) maintains the trend of increasing L-malic acid production with increasing COE staining concentration. Compared to a conventional surfactant, CTAB, DSSN+ exhibits an improved ability to retain catalytic activity with a second addition of fumaric acid. The lower toxicity of DSSN+ compared to CTAB toward yeast indicates a greater potential to re-use cells for repeated transformations. This ability is desirable with respect to the goal of limited biowaste and decreases the amount of membrane-permeabilizing material used.

Altogether, the results presented provide a foundation for developing simple and easy-to-use methods for enabling biocatalysis with potentially wide-ranging applications. Structure-property relationships were developed based on changing only the length of the conjugated backbone and identity of the pendant cationic group. Designing molecules with similar molecular lengths but differing conjugated backbones and pendant ionic groups is worth exploring to find more tailored COE structures for enabling biocatalysis.

C. Experimental and Supplementary Information

1. Materials and Methods

All reagents and solvents were purchased from Sigma Aldrich, BDM, Fisher Scientific, Alfa Aesar, or Acros Organics and used without further purification unless otherwise specified. Baker's yeast was obtained from Vons (California, USA).

Confocal fluorescence microscope images were obtained using a FluoView 1000S (Olympus, Japan) with multialkali photocathodes detector, excited by a 405 nm laser and a 559 nm laser. HPLC measurements were obtained using a Shimadzu UFLC instrument; model SIL-20AHT, with the data collected using LCsolutions software. The FS column from Phenomenex was a Kinetex 2.6 μm FS 100 A, LC column 150 X 4.6 mm. The eluent used was 20 mM potassium phosphate with a pH = 2.0. The flow rate was 1.25 mL/minute at room temperature with 5 minutes per sample run. UV-Vis absorption spectra were obtained using a Beckman-Coulter DU800.

2. Cell Culture

Under sterile conditions, yeast pellets were suspended in standard growth media and incubated aerobically at 30°C on a shaker set to 120 rpm. Yeast cells were allowed to grow overnight (13-15 hours). Cells were spun down and washed once with a neutral phosphate buffer (0.1 M) before use in biocatalysis reactions.

3. COE Staining

Wet yeast cells were separated into 0.10 g samples using 15 mL Falcon tubes as reaction vessels and 4 mL of the appropriate COE solution was added to re-suspend the cells. Final COE concentrations of 25 μM, 50 μM, 75 μM, and 100 μM in phosphate buffer were tested. The yeast suspensions were incubated aerobically at 30°C on a shaker set to 120 rpm for 2 hours. The cells were spun-down and the supernant was discarded. The cells were then washed once with buffer.

4. CTAB Staining

CTAB was tested for comparison at concentrations of 25 μM, 50 μM, 75 μM, and 100 μM with a permeabilization time of 10 minutes as previously described.[49] After staining, cells were spun-down and washed once with buffer.

5. Conversion of Fumaric Acid to L-Malic Acid

After staining with the appropriate concentration of COE solution, 5 mL of a 50 mM solution of fumaric acid in buffer was added to each yeast cell sample along with a control containing unstained yeast cells. Based on extrapolation, the optical density of the cells for this reaction is about 21. The reaction was allowed to proceed aerobically in an incubator at 30°C with 120 rpm shaking. Aliquots were taken at four time intervals to measure reaction progress with the final sample taken after about 24 hours. The aliquot was filtered using a 0.2 μm PET filter. Samples were prepared for HPLC by combining 900 μL eluent with 100 μL aliquot solution. HPLC provided the concentrations of L-malic acid and fumaric acid. HPLC was measured three times per sample and the average values are reported. Each reaction was run three times in order to test for reproducibility and the results from the two remaining reactions are reported below.

6. Additional Graphs

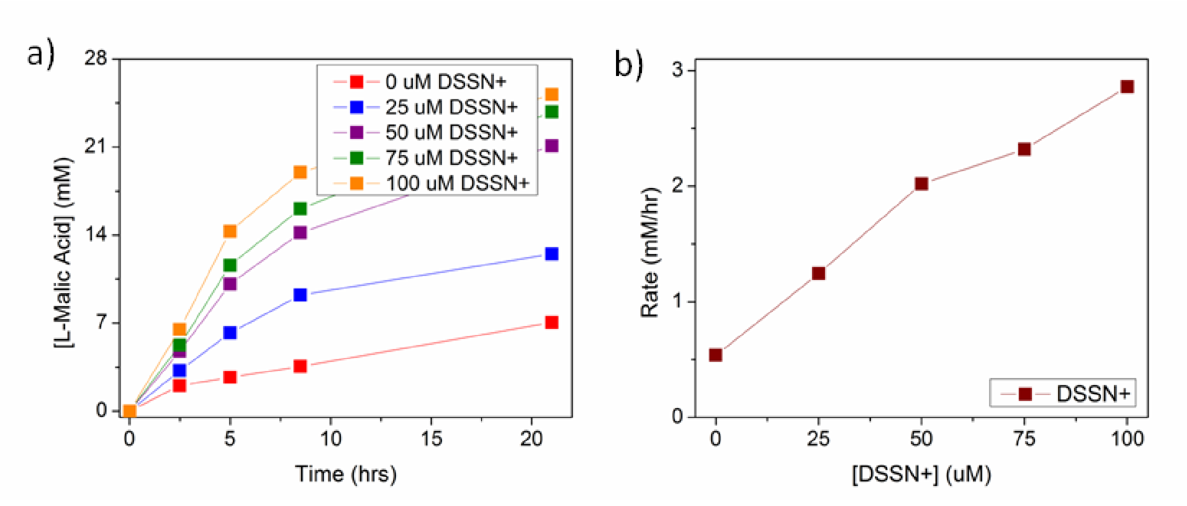

Figure S4-1. Trial 2: a) [L-malic acid] vs. time as a function of [DSSN+] and b) Rate of malate production (mM/hr) during the first five hours of reaction time as a function of [DSSN+].

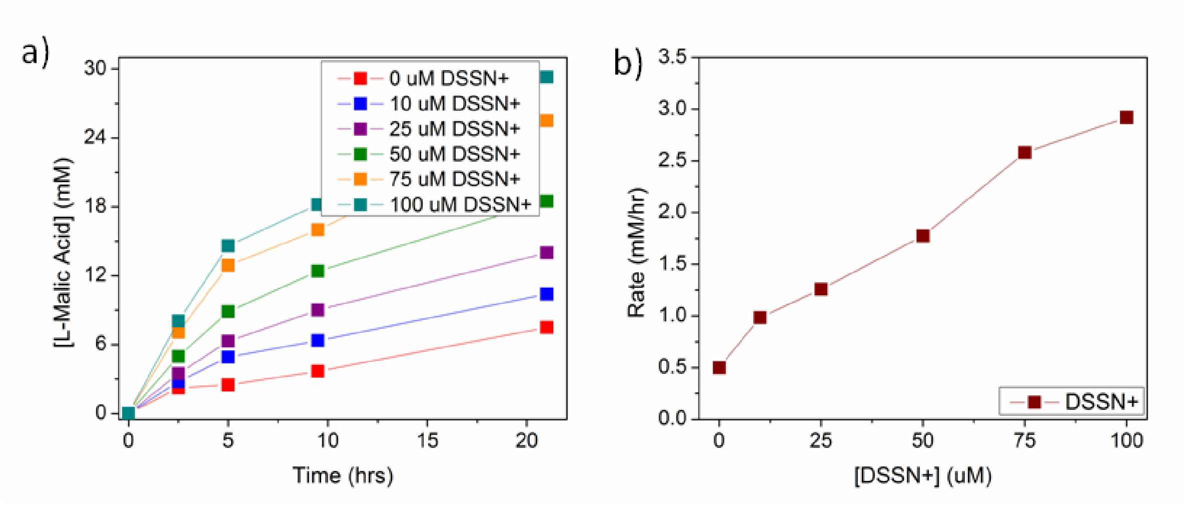

Figure S4-2. Trial 3: a) [L-malic acid] vs. time as a function of [DSSN+] and b) rate of L-malic acid production (mM/hr) during the first five hours of reaction time as a function of [DSSN+].

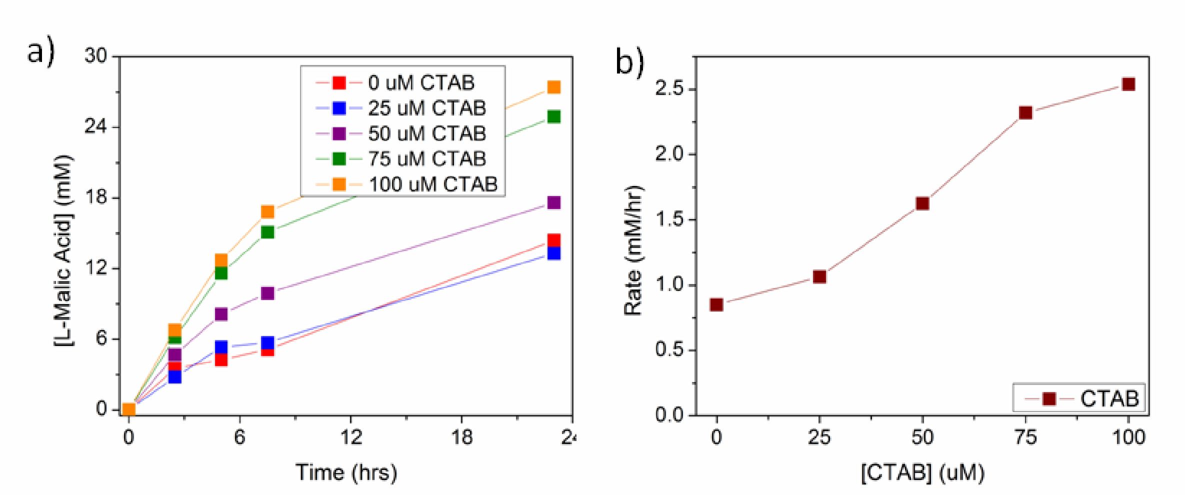

Figure S4-3. Trial 2: a) [L-malic acid] vs. time as a function of [CTAB] and b) rate of L-malic acid production (mM/hr) during the first five hours of reaction time as a function of [CTAB].

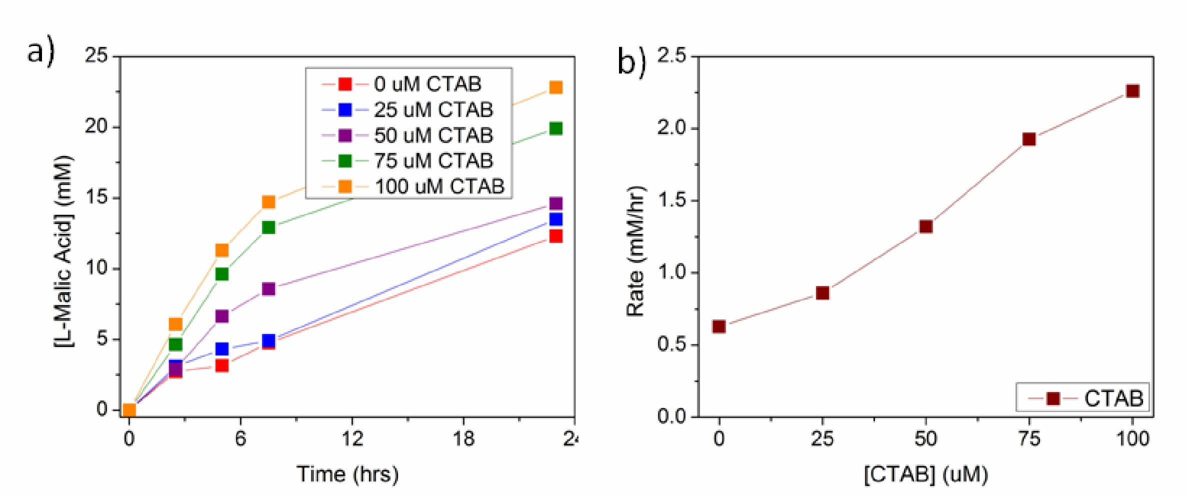

Figure S4-4. Trial 3: a) [L-malic acid] vs. time as a function of [CTAB] and b) rate of L-malic acid production (mM/hr) during the first five hours of reaction time as a function of [CTAB].

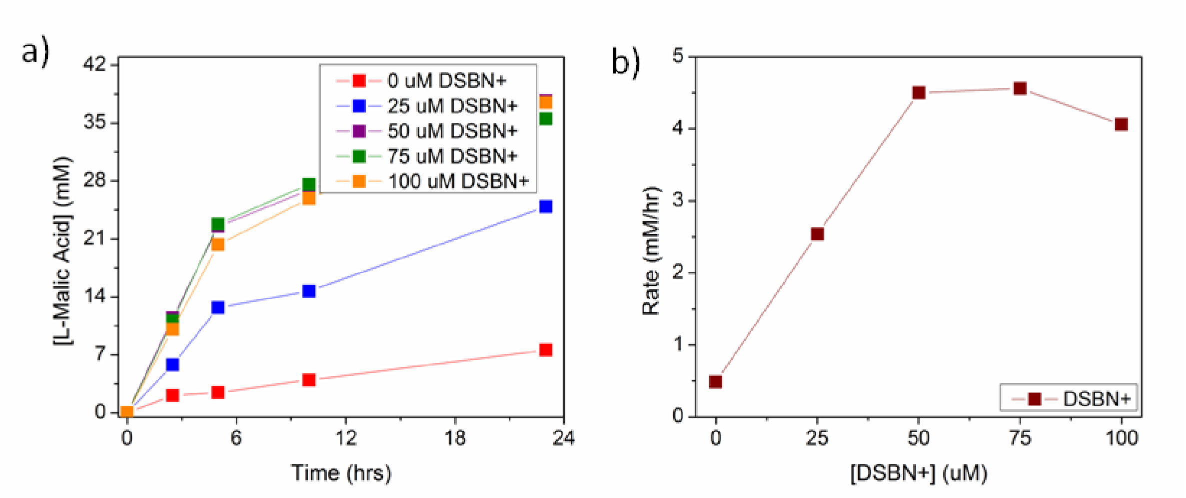

Figure S4-5. Trial 2: a) [L-malic acid] vs. time as a function of [DSBN+] and b) rate of L-malic acid production (mM/hr) during the first five hours of reaction time as a function of [DSBN+].

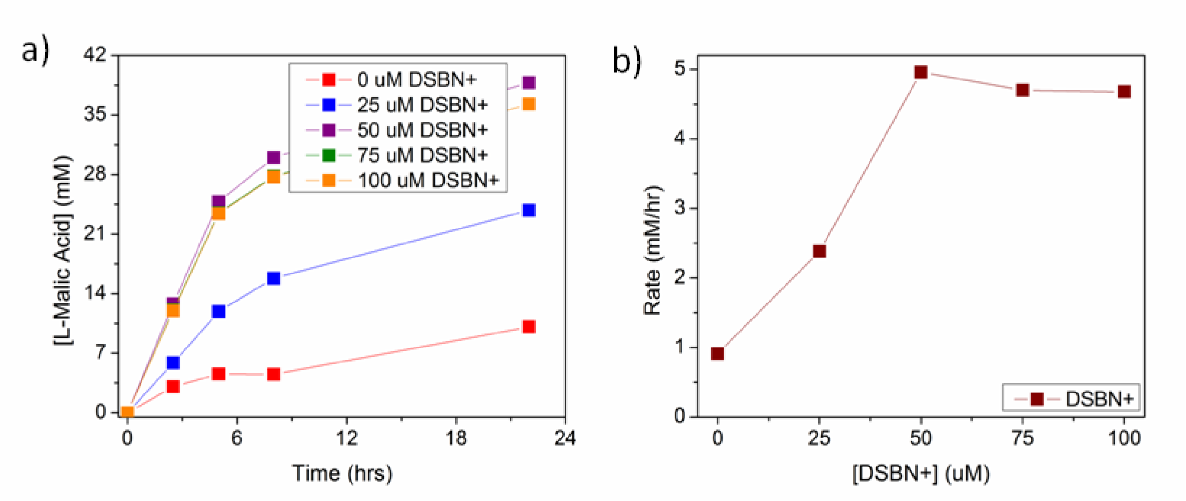

Figure S4-6. Trial 3: a) [L-malic acid] vs. time as a function of [DSBN+] and b) rate of L-malic acid production (mM/hr) during the first five hours of reaction time as a function of [DSBN+].

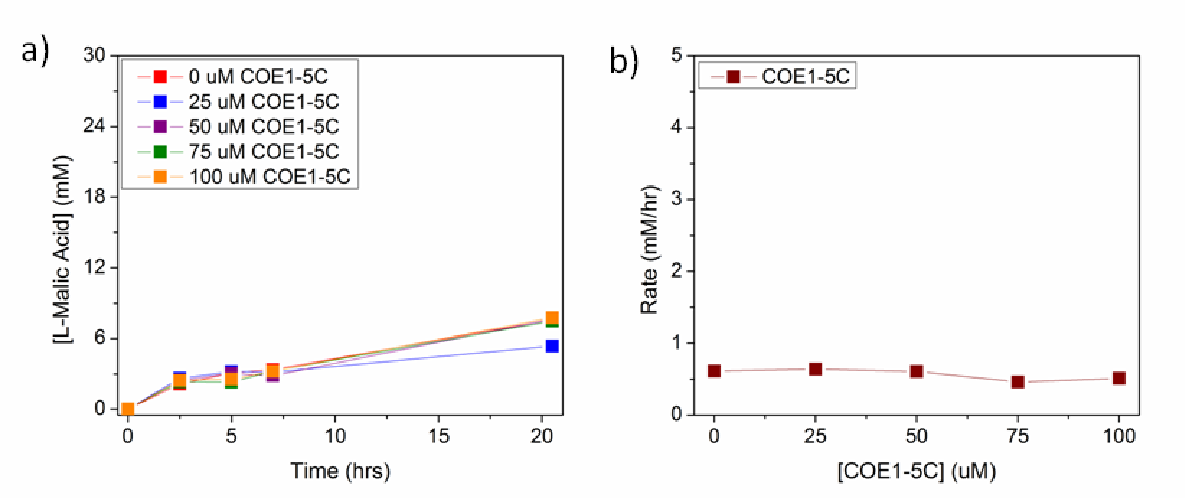

Figure S4-7. Trial 2: a) [L-malic acid] vs. time as a function of [COE1-5C] and b) rate of L-malic acid production (mM/hr) during the first five hours of reaction time as a function of [COE1-5C].

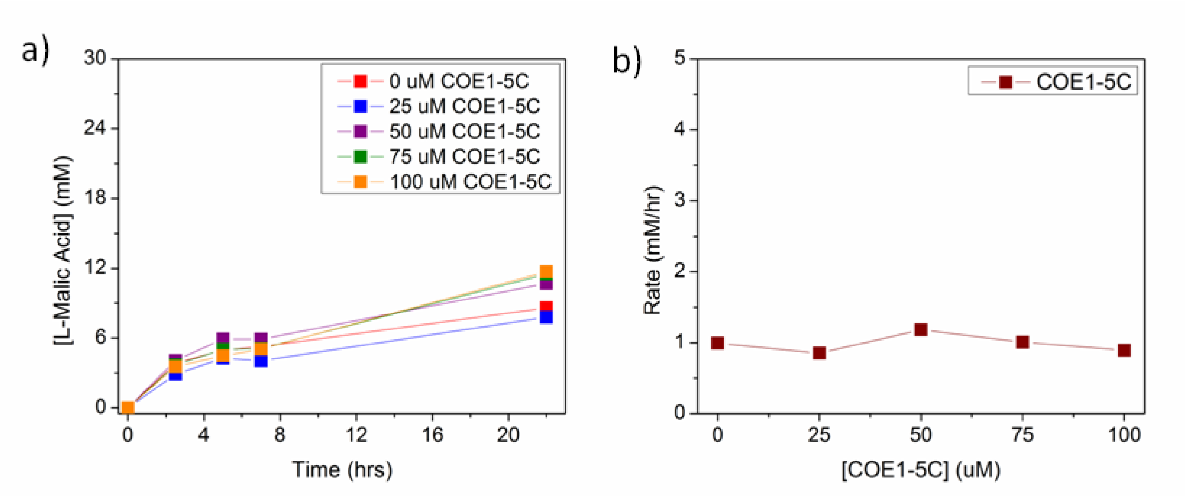

Figure S4-8. Trial 3: a) [L-malic acid] vs. time as a function of [COE1-5C] and b) rate of L-malic acid production (mM/hr) during the first five hours of reaction time as a function of [COE1-5C].

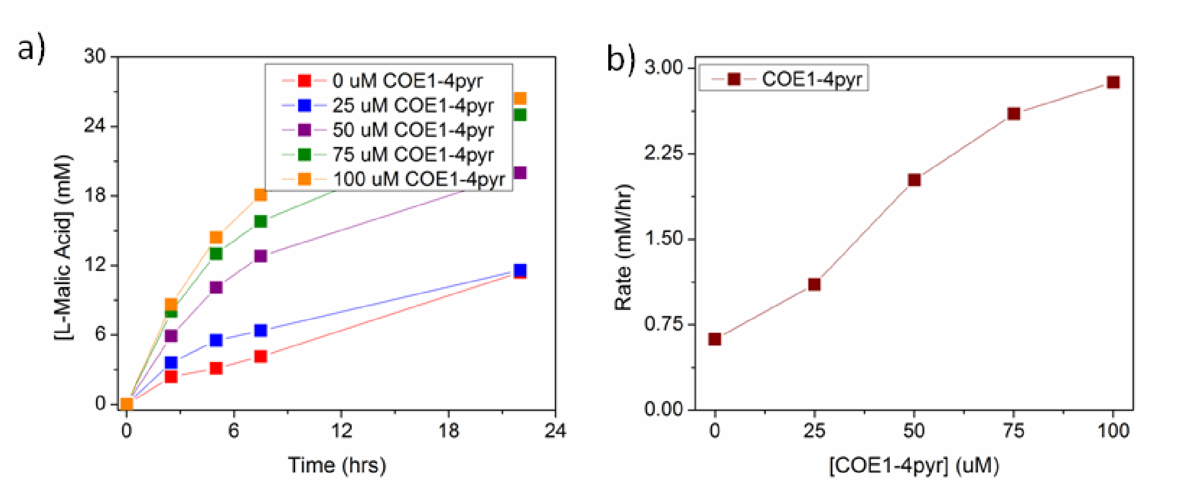

Figure S4-9. Trial 2: a) [L-malic acid] vs. time as a function of [COE1-4pyr] and b) rate of L-malic acid production (mM/hr) during the first five hours of reaction time as a function of [COE1-4pyr].

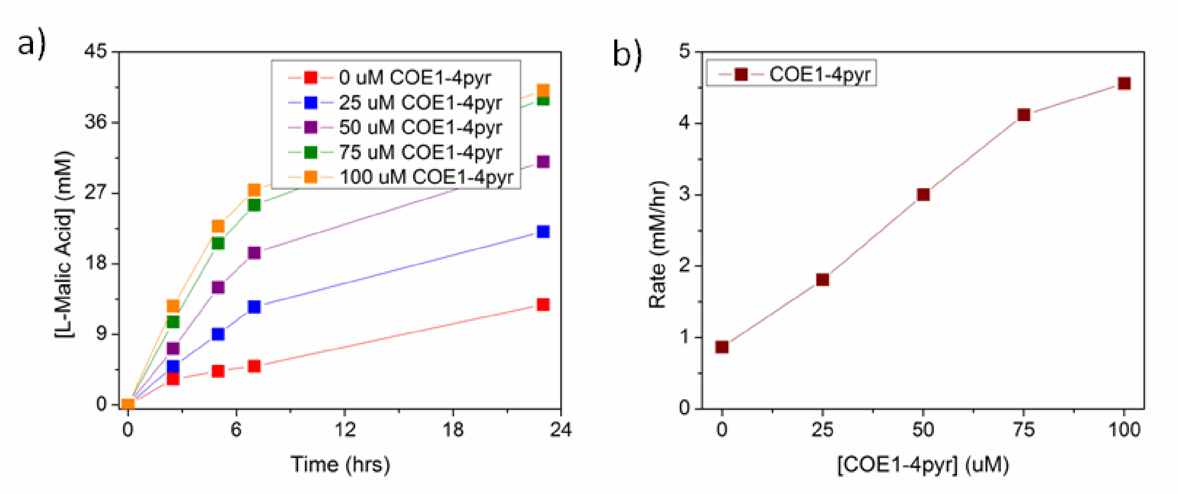

Figure S4-10. Trial 3: a) [L-malic acid] vs. time as a function of [COE1-4pyr] and b) rate of L-malic acid production (mM/hr) during the first five hours of reaction time as a function of [COE1-4pyr].

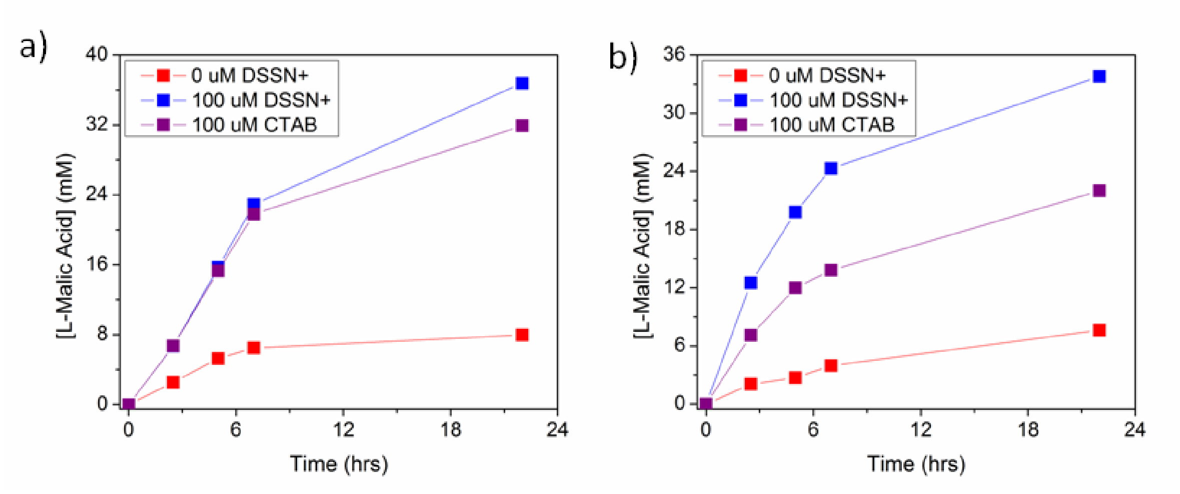

Figure S4-11. Trial 2: [L-malic acid] vs. time for a) the first and b) the second addition of fumaric acid added to the reactors for unstained yeast cells (red), cells stained with 100 μM DSSN+ (blue), and cells stained with 100 μM CTAB (purple).

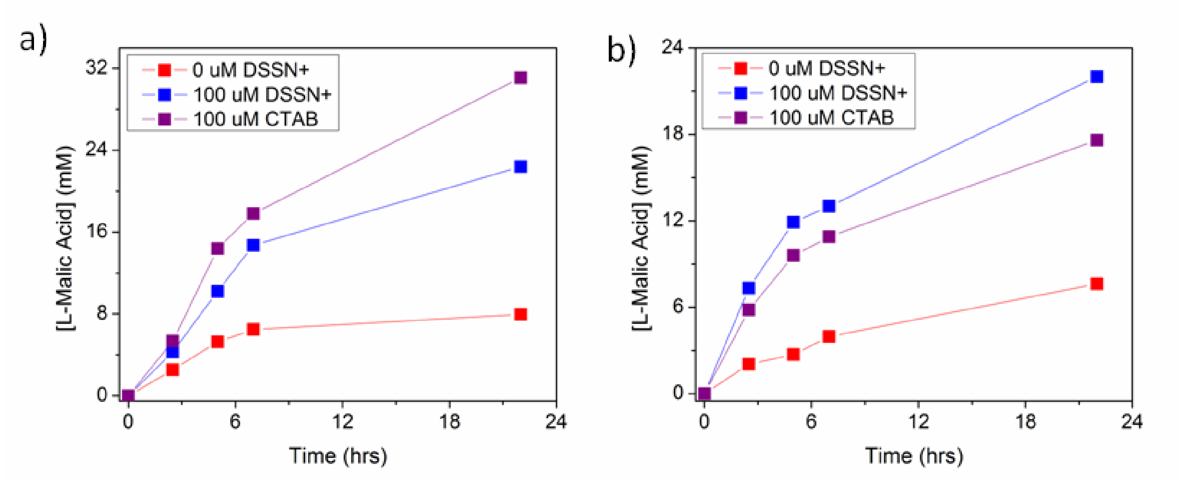

Figure S4-12. Trial 3: [L-malic acid] vs. time for a) the first and b) the second addition of fumaric acid added to the reactors for unstained yeast cells (red), cells stained with 100 μM DSSN+ (blue), and cells stained with 100 μM CTAB (purple).

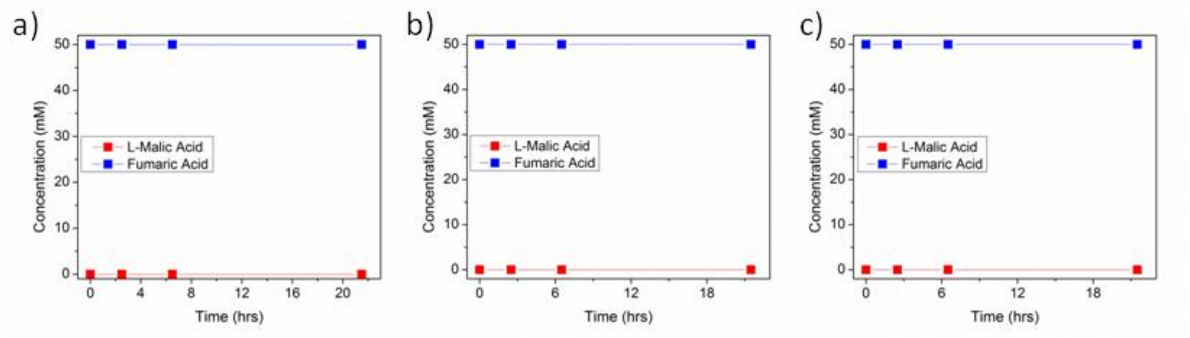

Figure S4-13. [L-malic acid] (red) and [fumaric acid] (blue) vs. time using supernant from cells stained with 100 μM DSSN+ for a) trial 1, b) trial 2, and c) trial 3.

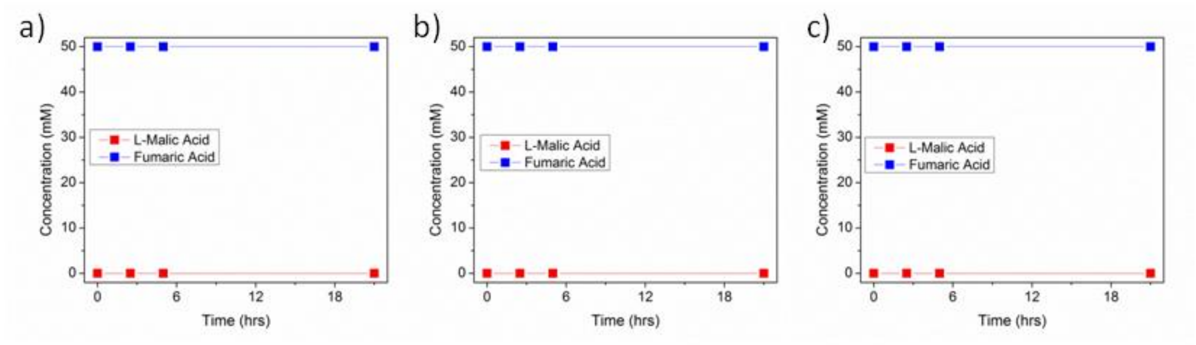

Figure S4-14. [L-malic acid] (red) and [fumaric acid] (blue) vs. time using supernant from cells stained with 100 μM CTAB for a) trial 1, b) trial 2, and c) trial 3.

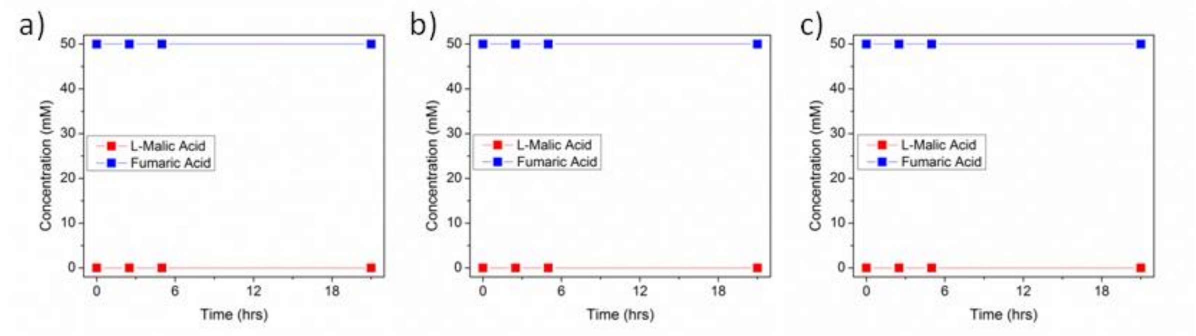

Figure S4-15. [L-malic acid] (red) and [fumaric acid] (blue) vs. time using supernant from cells stained with 100 μM DSBN+ for a) trial 1, b) trial 2, and c) trial 3.

7. Determining Cell Association

Cell association was determined using a UV-Vis absorption method. Yeast cells were stained with 25, 50, 75, or 100 μM COE solutions for two hours at 30°C with 120 rpm shaking. The cells were spun-down and the supernant was saved for further measurements. The absorption spectra of the supernant and of the fresh COE solutions were measured. Cell association was determined by comparing the absorption of the supernant to the absorption of the fresh COE solution at the wavelength of maximum absorption.

8. Minimum Inhibitory Concentration Experiments

MICs were performed using a broth-based method. Yeast cells were allowed to grow for 2 hours using the procedure described above. Yeast cells were diluted with yeast growth media to an optical density of 0.04. 96 well plates were used for MIC determination. 75 μL of COE or CTAB buffer solutions were added to the wells. Subsequently, 75 μL of suspended yeast cells were added. The final optical density was about 0.02 such that all solutions appeared clear. The final concentrations of COEs and CTAB studied were 1, 2, 4, 8, 16, 25, 50, 75, 100, and 128 μM. All concentrations were tested in triplicate.

The plates were wrapped in aluminum foil and secured to a 120 rpm shaker where they were allowed to incubate at 30°C for 3 days. The results are provided in Figures S34 and S35. Inhibited growth was determined based on whether or not the solution appeared cloudy after three days. Clear solutions indicated no yeast growth.

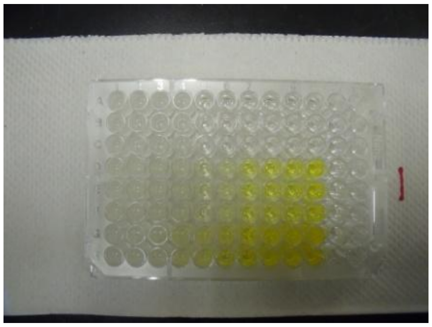

Figure S4-16. The top 3 rows contain CTAB, the next 3 rows contain DSBN+, and the last 2 rows contain COE1-4pyr with increasing concentration from left to right.

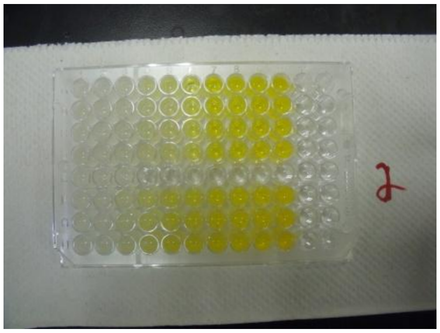

Figure S4-17. The top row contains COE1-4pyr, the next 3 rows contain DSSN+, the next row contains control samples, and the last three rows contain COE1-5C with increasing concentration from left to right.

9. Confocal Fluorescence Microscopy

Yeast cells were cultured and stained with 25 μM COE solution as described above. Cells were then stained with 5 μM propidium iodide (PI) for 30 minutes in an incubator at 30°C with 120 rpm shaking. The cells were spun-down and the supernant discarded. Cells were re-suspended in phosphate buffer and prepared on glass for confocal imaging. All images were processed using Image J. The emission of the COEs was assigned green as a false color and the emission of PI was assigned red.

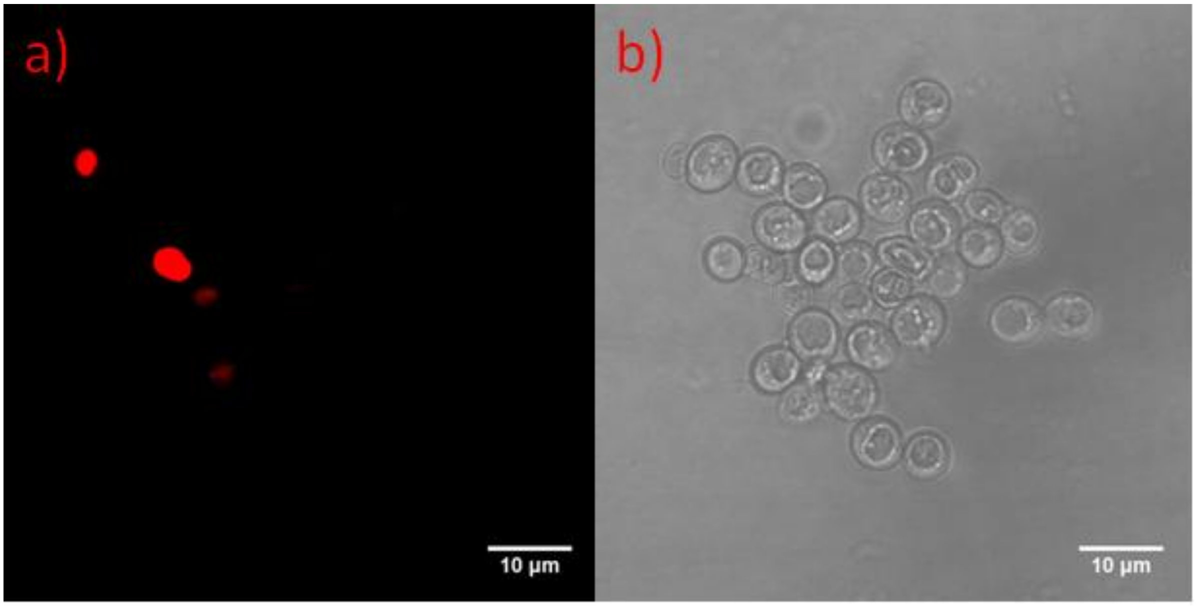

Figure S4-18. CFM images of yeast cells stained with 5 μM propidium iodide with the propidium iodide channel on the left and the confocal channel on the right.

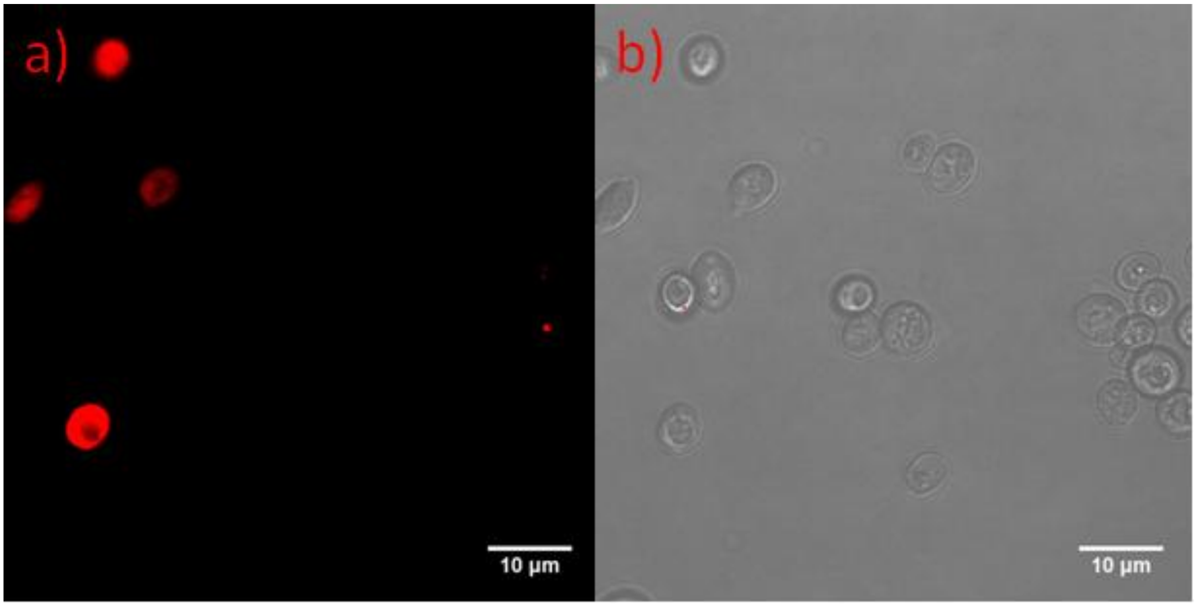

Figure S4-19. CFM images of yeast cells after permeabilizing with 100 μM CTAB and 5 μM PI (red) where a) shows the PI channel and b) shows the bright field image.

D. References

1. Bommarius, A. S.; Riebel-Bommarius, B. R. *Biocatalysis: Fundamentals and Applications* (Wiley-VCH, Weinheim, Germany, 2004).

2. Grunwald, P. *Biocatalysis: Biochemical Fundamentals and Applications* (Imperial College Press, 2009).

3. Fahrenkamp-Uppenbrink, J. "Chemistry Goes Green." *Science*, **2002**, *297*, 798.

4. Pantaleone, D. P. "Biotransformations: "Green" Processes for the Synthesis of Chiral Fine Chemicals." *Handbook of Chiral Chemicals* (ed. D. J. Ager), *Marcel Dekker Inc.* New York (1999): 245-286.

5. Schulze, B.; Wubbolts, M. G. "Biocatalysis for Industrial Production of Fine Chemicals." *Current Opinion in Biotechnology*, **1999**, *10*, 609-615.

6. Schmid, A.; Dordick, J. S.; Hauer, B.; Kiener, A.; Wubbolts, M.; Witholt, B. "Industrial Biocatalysis Today and Tomorrow." *Nature*, **2001**, *409*, 258-268.

7. Wenda, S.; Illner, S.; Mell, A.; Kragl, U. "Industrial Biotechnology – The Future of Green Chemistry?" *Green Chem.* **2011**, *13*, 3007-3047.

8. Reetz, M. T. "Biocatalysis in Organic Chemistry and Biotechnology: Past, Present, and Future." *J. Am. Chem. Soc.* **2013**, *135*, 12480-12496.

9. Carvalho, C. C. C. R. "Whole Cell Biocatalysts: Essential Workers from Nature to Industry." *Microbial Biotechnology*, **2017**, *10*, 250-263.

10. Clomburg, J. M.; Crumbley, A. M.; Gonzalez, R. "Industrial Biomanufacturing: The Future of Chemical Production." *Science*, **2017**, *355*, DOI: 10.1126/science.aag0804.

11. Yamada, H.; Shimizu, S. "Microbial and Enzymatic Processes for the Production of Biologically and Chemically Useful Compounds." *Angew. Chem. Int. Ed.* **1988**, *27*, 622-642.

12. Schoemaker, H. E.; Mink, D.; Wubbolts, M. G. "Dispelling the Myths – Biocatalysis in Industrial Synthesis." *Science*, **2003**, *299*, 1694-1697.

13. Pollard, D. J.; Woodley, J. M. "Biocatalysis for Pharmaceutical Intermediates: the Future is Now." *Trends Biotechnol.* **2006**, *25*, 66-73.

14. Ward, O. P. *Bioprocessing*. Van Nostrand Reinhold, New York, **1991**.

15. Nikolova, P.; Ward, O. P. "Whole Cell Yeast Biotransformations in Two Phase Systems: Effect of Solvent on Product Formation and Cell Structure." *J. Ind. Microbiol.* **1992**, *10*, 169-177.

16. Chen, R. R. "Permeability Issues in Whole-Cell Bioprocesses and Cellular Membrane Engineering." *Appl. Microbiol. Biotechnol.* **2007**, *74*, 730-738.

17. Felix, H. "Permeabilized Cells." *Anal. Biochem.* **1982**, *120*, 211-234.

18. Chica, R. A.; Doucet, N.; Pelletier, J. N. "Semi-Rational Approaches to Engineering Enzyme Activity: Combining the Benefits of Directed Evolution and Rational Design." *Curr. Opin. Biotech.* **2005**, *16*, 378-384.

19. Turner, N. J. "Directed Evolution Drives the Next Generation of Biocatalysts." *Nat. Chem. Biol.* **2009**, *5*, 567-573.

20. van der Rest, M. E.; Kamminga, A. H.; Nakano, A.; Anraku, Y.; Poolman, B.; Konings, W. N. "The Plasma Membrane of *Saccharomyces cerevisiae*: Structure, Function, and Biogenesis." *Microbiol. Rev.* **1995**, *59*, 304-322.

21. Sigler, K.; Hofer, M. "Biotechnological Aspects of Membrane Function." *Crit. Rev. Biotechnol.* **1997**, *17*, 69-86.

22. Nikaido, H. "Molecular Basis of Outer Membrane Permeability Revisited." *Microbiol. Mol. Biol. Rev.* **2003**, *67*, 593-656.

23. Gowda, L. R.; Bachhawat, N.; Bhat, S. G. "Permeabilization of Baker's Yeast by Cetyltrimethylammonium Bromide for Intracellular Enzyme Catalysis." *Enzyme Microb. Technol.* **1991**, *13*, 154-157.

24. Laouar, L.; Mulligan, B. J.; Lowe, K. C. "Yeast Permeabilization with Surfactants." *Biotechnol. Lett.* **1992**, *14*, 719-720.

25. Ni, Y.; Chen, R. R. "Accelerating Whole-Cell Biocatalysis by Reducing Outer Membrane Permeability Barrier." *Biotechn. Bioeng.* **2004**, *87,* 804-811.

26. Adamala, K. P., Martin-Alarcon, D. A., Guthrie-Honea, K. R., Boyden, E. S. Engineering Genetic Circuit Interactions within and Between Synthetic Minimal Cells. *Nat. Chem.* **2017**, *9*, 431-439.

27. Coward-Kelly, G.; Chen, R. R. "A Window into Biocatalysis and Biotransformations." *Biotechnol. Prog.* **2007**, *23,* 52-54.

28. Liu, Y.; Hama, H.; Fujita, Y.; Kondo, A.; Inoue, Y.; Kimura, A.; Fukuda, H. "Production of *S*-Lactoylglutathione by High Activity Whole Cell Biocatalysts Prepared by Permeabilization of Recombinant *Saccharomyces cerevisiae* with Alcohols." *Biotechn. Bioeng.* **1999**, *64*, 54-60.

29. Flores, M. V.; Voget, C. E.; Ertola, R. J. J. "Permeabilization of Yeast Cells (*Kluyveromyces lactis*) with Organic Solvents." *Enzyme Microb.Technol.* **1994**, *16,* 340-346.

30. Kondo, A.; Liu, Y.; Furuta, M.; Fujita, Y.; Matsumoto, T.; Fukuda, H. "Preparation of High Activity Whole Cell Biocatalyst by Permeabilization of Recombinant Flocculent Yeast with Alcohol." *Enzyme Microb. Technol.* **2000**, *27,* 806-811.

31. Yang, K. M.; Lee, N.-R.; Woo, J.-M.; Choi, W.; Zimmermann, M.; Blank, L. M.; Park, J.-B. "Ethanol Reduces Mitochondrial Membrane Integrity and Thereby Impacts Carbon Metabolism of *Saccharomyces cerevisiae*." *FEMS Yeast Res.* **2012**, *12,* 675-684.

32. Sirisattha, S.; Momose, Y.; Kitagawa, E.; Iwahashi, H. "Toxicity of Anionic Detergents Determined by *Sacchomyces cerevisiae* Microarray Analysis." *Water Research*, **2004**, *38*, 61-70.

33. Bornscheuer, U. T.; Huisman, G. W.; Kazlauskas, R. J.; Lutz, S.; Moore, J. C.; Robins, K. "Engineering the Third Wave of Biocatalysis." *Nature*, **2012**, *485,* 185-194.

34. Garner, L. E.; Park, J.; Dyar, S. M.; Chworos, A.; Sumner, J. J.; Bazan, G. C. "Modification of the Optoelectronic Properties of Membranes via Insertion of

Amphiphilic Phenylenevinylene Oligoelectrolytes." *J. Am. Chem. Soc.* **2010**, *132*, 10042-10052.

35. Yan, H.; Catania, C.; Bazan, G. C. "Membrane-Intercalating Conjugated Oligoelectrolytes: Impact on Bioelectrochemical Systems." *Adv. Mater.* **2015**, *27*, 2958-2973.

36. Wang, V. B.; Du, J.; Chen, X.; Thomas, A. W.; Kirchhofer, N. D.; Garner, L. E.; Maw, M. T.; Poh, W. H.; Hinks, J.; Wuertz, S.; Kjelleberg, S.; Zhang, Q.; Loo, J. S.; Bazan, G. C. "Improving Charge Collection in *Escherichia coli*-Carbon Electrode Devices with Conjugated Oligoelectrolytes." *Phys. Chem. Chem. Phys.* **2013**, *15*, 5867-5872.

37. Garner, L. E.; Thomas, A. W.; Sumner, J. J.; Harvey, S. P.; Bazan, G. C. "Conjugated Oligoelectrolytes Increase Current Response and Organic Contaminant Removal in Wastewater Microbial Fuel Cells." *Energy, Environ. Sci.* **2012**, *5*, 9449-9452.

38. Yan, H.; Rengert, Z. D.; Thomas, A. W.; Rehermann, C.; Hinks, J.; Bazan, G. C. "Influence of Molecular Structure on the Antimicrobial Function of Phenylenevinylene Conjugated Oligoelectrolytes." *Chem. Sci.* **2016**, *7*, 5714-5722.

39. Catania, C.; Ajo-Franklin, C. M.; Bazan, G. C. "Membrane Permeabilization by Conjugated Oligoelectrolytes Accelerates Whole-Cell Catalysis." *RCS Adv.* **2016**, *6*, 100300-100306.

40. Sivakumar, K.; Wang, V. B.; Chen, X.; Bazan, G. C.; Kjelleberg, S.; Loo, S. C. J.; Cao, B. "Membrane Permeabilization Underlies the Enhancement of Extracellular Bioactivity in *Shewanella oneidensis* by a Membrane-Spanning Conjugated Oligoelectrolyte." *Appl. Microbiol. Biotechnol.* **2014**, *98*, 9021-9031.

41. Zhou, Y. J.; Buijs, N. A.; Zhu, Z.; Qin, J.; Siewers, V.; Nielsen, J. "Production of Fatty Acid-Derived Oleochemicals and Biofuels by Synthetic Yeast Cell Factories." *Nat. Commun.* **2016**,*7*, DOI: 10.1038/ncomms11709.

42. Wang, X.; Gong, C. S.; Tsao, G. T. "L-Malic Acid Production from Fumaric Acid by a Laboratory *Saccharomyces cerevisiae* Strain SHY 2." *Biotechnol. Lett.* **1996**, *18*, 1441-1446.

43. Oliveira, E. A.; Costa, A. A. R.; Figueiredo, Z. M. B.; Carvalho, L. B. "L-Malic Acid Production by Entrapped *Saccharomyces cerevisiae* into Polyacrylamide Gel Beads." *Appl. Biochem. Biotech.* **1994**, *47*, 65-72.

44. Csuk, R.; Glanzer, B. I. "Baker's Yeast Mediated Transformations in Organic Chemistry." *Chem. Rev.* **1991**, *91*, 49-97.

45. Lee, J. W.; Kim, H. U.; Choi, S.; Yi, J.; Lee, S. Y. "Microbial Production of Building Block Chemicals and Polymers." *Curr. Opin. Biotech.* **2011**, *22*, 758-767.

46. Chibata, I.; Tosa, T.; Takata, I. "Continuous Production of L-Malic Acid by Immobilized Cells." *Trends Biotechnol.* **1983**, *1*, 9-11.

47. Sauer, M.; Porro, D.; Mattanovich, D.; Branduardi, P. "Microbial Production of Organic Acids: Expanding the Market." *Trends Biotechnol.* **2008**, *26*, 101-108.

48. Neufeld, R. J.; Peleg, Y.; Roken, J. S.; Pines, O.; Goldberg, I. "L-Malic Acid Formation by Immobilized *Saccharomyces cerevisiae* Amplified for Fumarase." *Enzyme Microb. Technol.* **1991**, *13*, 991-996.

49. Presecki, A. V.; Zelic, B.; Vasic-Racki, D. "Comparison of the L-Malic Acid Production by Isolated Fumarase and Fumarase in Permeabilized Baker's Yeast Cells." *Enzyme Microb. Technol.* **2007**, *41*, 605-612.

50. Stojkovic, G.; Znidarsic-Plazl, P. "Continuous Synthesis of L-Malic Acid Using Whole-Cell Microreactor." *Process Biochem.* **2012**, *47*, 1102-1107.

51. Pines, O.; Even-Ram, S.; Elnathan, N.; Battat, E.; Aharonov, O.; Gibson, D.; Goldberg, I. "The Cytosolic Pathway of L-Malic Acid Synthesis in *Saccharomyces cerevisiae*: the Role of Fumarase." *Appl. Microbiol. Technol.* **1996**, *46*, 393-399.

52. Krebs, H. A.; Gurin, S.; Eggleston, L. V. "The Pathway of Oxidation of Acetate in Baker's Yeast." *Biochem. J.* **1952**, *51*, 614-628.

53. White, J. "Effects of Common Bactericidal Substances and of Heat on Yeast Growth and Viability." *J. Inst. Brew.* **1953**, *59*, 470-479.

54. Hinks, J.; Wang, Y.; Matysik, A.; Kraut, R.; Kjelleberg, S.; Mu, Y.; Bazan, G. C.; Wuertz, S.; Seviour, T. "Increased Microbial Butanol Tolerance by Exogenous Membrane Insertion Molecules." *ChemSusChem*, **2015**, *8*, 3718-3726.

55. Hinks, J.; Wang, Y.; Poh, W. H.; Donose, B. C.; Thomas, A. W.; Wuertz, S.; Loo, S. C. J.; Bazan, G. C.; Kjelleberg, S.; Mu, Y.; Sevious, T. "Modeling Cell Membrane Perturbation by Molecules Designed for Transmembrane Electron Transfer." *Langmuir*, **2014**, *30*, 2429-2440.

56. Thomas, A. W.; Catania, C.; Garner, L. E.; Bazan, G. C. "Pendant Ionic Groups of Conjugated Oligoelectrolytes Govern their Ability to Intercalate into Microbial Membranes." *Chem. Commun.* **2015**, *51*, 9294-9297.